The First Multichroic Receiver and Results from ACTPol

by

Rahul Datta

A dissertation submitted in partial fulfillment
of the requirements for the degree of
Doctor of Philosophy
(Physics)
in the University of Michigan
2016

Doctoral Committee:

Professor Jeffrey J. McMahon, Chair
Professor August Evrard
Professor Dragan Huterer
Professor Roberto Merlin
Professor Christopher Miller

2016

To my parents,
Gautam and Gopa Datta,
and to the memory of my late grandparents,
Jatiswar and Mira Datta,
for their endless love, support and encouragement.

A C K N O W L E D G E M E N T S

This work would have been impossible without the support and guidance of many exceptional people I have been fortunate to meet and learn a lot from during my graduate school. I would like to thank first and foremost my fantastic advisor, Prof. Jeffrey McMahon, who has been a great guide over the last six years. He was always available to help me and I have learned a tremendous amount from him. I would also like to thank my thesis committee members, Professors August Evrard, Dragan Huterer, Roberto Merlin and Christopher Miller for their support and for the many valuable suggestions I received from them over the last few years. I learned a lot from the weekly astrophysics group meetings. The classes taught by Prof. Huterer and Prof. Merlin during the early years of my graduate school have been very useful for my research.

My association with the ACT collaboration has been a wonderful experience, and I owe a great amount of thanks to the entire collaboration, especially Johannes Hubmayr, Michael Niemack, Edward Wollack, Bob Thornton, Jason Austermann, Dan Becker, Laura Newburgh, Suzanne Staggs, Matthew Hasselfield, and Alessandro Schilacci for their help at different stages of my graduate school. None of the detector design work would have borne any fruit without the huge efforts and ingenuity of people at NIST. I would like to thank the entire NIST team for hosting me at NIST several times and teaching me a lot of interesting things. I would also like to thank Sherry Cho, Dale Li, Kent Irwin, Jim Beal, Gene Hilton, Shannon Duff, John Nibarger, Joseph Fowler, Jeff van Lanen, Frank Schima, Devin Crichton, and Benjamin Schmitt. I owe special thanks to Megan Gralla and Tobias Marriage, who got me started on the analysis of extragalactic point sources in the CMB maps during my visit to Johns Hopkins. I thank the Center for Cosmological Studies (CCS) for the fellowship that funded this visit. I would like to thank Lyman Page for his constant support.

I also want to thank Charles Munson, Kevin Coughlin, Taylor Baildon, Fletcher Boone, and Felicity Hills for being great lab mates and for all their help and support over the years. I owe my gratitude to several other friends inside and outside the department for their support: Joshua Gevirtz, Tom Cheng, Riddhiman Bhattacharyya, Arunabha Mohan Roy, and Pramathesh Maji.

I would like to thank the Michigan Physics Department staff who have always helped me with many administrative issues. I would like to thank the entire Machine Shop staff for their help during the many hours I spent working there. I also want to thank Marlin Whitaker for helping me with Linux and Server issues. I owe special thanks to our graduate coordinator Christina Zigulis. I would also like to thank the Rackham Graduate School for funding me for the past year through the Rackham Predoctoral Fellowship.

Finally, I want to thank my parents, Gautam and Gopa Datta, sister Ranjabati Datta, and late grandparents, Jatiswar and Mira Datta for their love and support through all times. I would not have made it this far without the constant support and care of my wife Mukta Barua, who has been a great friend over the last few years.

PREFACE

In the last two and a half decades since the first measurement of the CMB anisotropies by the COBE satellite, huge advances have been made in the field of CMB observations, ushering in the era of precision cosmology. While the CMB temperature anisotropies have been extensively measured, current and upcoming ground-based, balloon-borne, and satellite experiments are targeting the CMB-polarization signature of inflationary gravitational waves at large angular scales on the sky, which could provide a stunning confirmation of cosmic inflation. Ground-based instruments are gaining access to an increasing range of angular scales, with the potential to transform our understanding of the properties of dark energy and neutrinos.

This dissertation is based on my work at the University of Michigan during the past six years as part of the Atacama Cosmology Telescope Polarimeter (ACTPol) and Advanced ACTPol Collaborations. Most of this work has been published in peer-reviewed journals and conference proceedings. The chapters in this dissertation that contain already published content have been modified and/or expanded for this dissertation. Most of the Chapter 2 content has been published in Datta et al. [79]. My contributions as the first author of this paper included the design of novel metamaterial antireflection (AR) coatings, study of tolerance to manufacturing errors, working with a company to manufacture the first set of AR coatings, and measurement of the test wafers and finished AR-coated lenses, while my fellow graduate students developed the fabrication system and made the AR-coatings in the McMahon lab. Sections 2.4, 2.5, and 2.6 were written with collaborators from NIST Boulder, NASA Goddard, and Michigan, while the remaining figures and plots were almost entirely my contribution. Chapters 3 and 4 contain published material from McMahon et al. [85], Datta et al. [86], Datta et al. [87], Ho et al. [157], and Duff et al. [158]. The first ACTPol multichroic pixel was designed in our collaboration with NIST and further optimized my me. I designed the array of 255 pixels and the wiring layout.

I led the design of many of the pixel components for the AdvACT detectors. The detectors were fabricated by our collaborators at NIST and characterized at NIST, Princeton, Cornell, Michigan, and at the telescope site in Chile. I led the cryogenic detector testing efforts at Michigan as well as tested the prototype feedhorns fabricated at NIST. In Chapter 4, I have presented a method to characterize the passband of the deployed detectors in-situ on the telescope for which I designed an optical system to couple a Fourier transform spectrometer (FTS) to the ACTPol receiver. Chapter 5 contains a preliminary study of the impact of far-sidelobes in the ACTPol beam; a more thorough study was subsequently undertaken by our collaborators at PUC, Chile and presented in Rojas et al. [182]. In Chapter 6, I have described an ongoing analysis that I am working on using ACTPol data to study the polarization properties of extragalactic point sources in the ACTPol maps.

TABLE OF CONTENTS

Dedication . . . . . **ii**

Acknowledgements . . . . . **iii**

Preface . . . . . **v**

List of Figures . . . . . **x**

List of Tables . . . . . **xxv**

List of Appendices . . . . . **xxvi**

Abstract . . . . . **xxvii**

Chapter

1 Introduction **1**

1.1 Discovery of the CMB 1
1.2 History of the Universe and Origin of the CMB 1
1.3 CMB Temperature Anisotropy Power Spectrum 4
1.3.1 Primary Anisotropies 5
1.3.2 Secondary Anisotropies 8
1.4 CMB Polarization 11
1.5 Status of Observations and Current Challenges 16
1.6 The Atacama Cosmology Telescope Polarimeter (ACTPol) Experiment . . 19
1.6.1 ACTPol Science Goals 19
1.6.2 The Atacama Cosmology Telescope 21
1.6.3 Sky coverage and Scan strategy 22
1.6.4 Optics 23
1.6.5 Cryogenics 25
1.6.6 Detector Arrays 27
1.6.7 Readout 27
1.7 The Advanced ACTPol (AdvACT) Experiment 28
1.8 Outline of this Thesis 28

2 Large-aperture wide-bandwidth meta-material anti-reflection-coatings for millimeter wavelengths **31**

2.1 Introduction 31

2.2 Requirements . . . 33
2.3 AR Coating Design . . . 35
2.4 ACTPol Lenses . . . 44
2.5 Properties of Silicon . . . 46
2.6 Coating Fabrication . . . 49
2.7 Reflectometer Measurements . . . 53
2.8 Conclusion and Future work . . . 57

3 Multichroic Pixel Design and Array Optimization . . . 59

3.1 Introduction . . . 59
3.2 Detector Architecture . . . 61
3.3 Multichroic Array Optimization . . . 62
3.3.1 Ring-loaded Corrugated Feedhorns . . . 65
3.3.2 Co-Planar Waveguide (CPW) and Microstrip (MS) Transmission Lines . . . 68
3.3.3 Broadband OMT . . . 70
3.3.4 CPW to MS Transition . . . 72
3.3.5 Diplexer . . . 73
3.3.6 Hybrid Tee . . . 77
3.3.7 Nb-Au Transition . . . 78
3.3.8 TES bolometers . . . 79
3.3.9 Efficiency . . . 80
3.4 Design tolerances . . . 82
3.5 Study of alternative Filter types . . . 86
3.5.1 CPW Stub Filter . . . 86
3.5.2 Lumped Element Filter . . . 88
3.6 Lab measurement of Optical Efficiency using a Cold-load . . . 91
3.7 ACTPol 90/150 GHz Multichroic Array Wiring Layout . . . 97
3.8 Summary . . . 99

4 In-situ Passband Characterization of Deployed Detector Arrays . . . 101

4.1 Introduction . . . 101
4.2 Fourier Transform Spectrometer . . . 102
4.3 Design of the FTS Coupling Optics . . . 102
4.4 Frequency Calibration and Verification of the FTS Operation . . . 105
4.5 In-situ Passband Characterization . . . 109
4.5.1 On-site Measurements . . . 109
4.5.2 From Interferograms to Spectra: Analysis and Results . . . 111
4.5.3 Effective Array Central Frequencies and Bandwidth . . . 114
4.6 Conclusion . . . 119

5 Simulation of Diffractive Far-sidelobes resulting from Panel Gaps in the ACT Primary Mirror . . . 121

5.1 Introduction . . . 121
5.2 Simulations . . . 122

5.3 Estimates of Systematic Contamination . . . 124
5.4 Summary . . . 128

6 ACTPol: Polarized Point Sources at 148 GHz . . . 132

6.1 Introduction . . . 132
6.2 Observations . . . 134
6.3 Point Source Detection in Intensity maps . . . 134
6.3.1 Purity and Completeness . . . 137
6.4 Degree of Polarization . . . 139
6.4.1 Numerical Debiasing based on Simulations . . . 145
6.4.2 Distribution of Fractional Polarization . . . 148
6.5 Source Variability . . . 151
6.6 Comparison to Other Source Catalogs . . . 152
6.6.1 Source Spectra . . . 155
6.7 Discussion and Future Work . . . 158

7 Conclusion and Outlook . . . 161

7.1 Early Science Results from ACTPol . . . 161
7.2 ACTPol, AdvACT, and Beyond . . . 162

Appendices . . . 170

Bibliography . . . 191

LIST OF FIGURES

1.1 **History of the Universe** As the Universe came into existence, a period of rapid exponential expansion inflation amplified tiny quantum fluctuations in space-time to angular scales accessible to CMB experiments. At the end of Inflation, elementary particles started forming, but the Universe was still so hot that protons and electrons which formed atoms would be immediately separated by collisions with photons, and conversely the photon mean free path between scatters was negligibly small. The Universe gradually cooled and the intensity of radiation was low enough that atoms could form, allowing the photons to start their relatively unimpeded journey towards us. The matter, no longer tied to the photons by the electromagnetic force, clumped gravitationally and started forming the structures observed today. As the first stars formed, light from them partially reionized the Universe. On their way to us, the photons get scattered by electrons from the epoch of reionization, and hot electron gas clouds in clusters. They are aslo gravitationally deflected by massive galaxy clusters. Today, in the CMB photons, we can see the imprints of the above along with that of inflation and the primordial density perturbations that seeded the large scale structure. This helps improve our understanding of the birth and evolution of our Universe. 3

1.2 **Thomson Scattering** The schematic shows a local quadrupolar temperature anisotropy in the photons surrounding an electron. Photons are incident on the electron from two hot regions (to the left and right) and from two cold regions (up and down). The resulting scattered radiation has a net linear polarization in the vertical direction aligned with the cold axis of the quadrupole. 11

1.3 **A simplified illustration of the polarization patterns from photon diffusion between over-dense and under-dense regions** As a mode of wavevector undergoes compression (rarefaction), the photon-baryon fluid diffuses from hot crests (cold troughs) to cold troughs (hot crests). This motion is represented by the blue (red) arrows and produces a local quadrupole in the rest frame of a scattering electron with the hot (cold) axis parallel to the wavevector. The orientation of polarization of the scattered radiation represented by the brown bars is always parallel (perpendicular) to the wavevector, thus generating an E-mode pattern. B-modes are never produced by this mechanism. Figure inspired by [27]. 14

1.4 **A simplified illustration of the polarization patterns from velocity gradients** when the primordial plasma is accelerated towards an over-dense cold spot (bottom) or decelerated towards an under-dense hot spot (top). The black arrows in the left panel represent direction of fluid motion in the fluid rest frame with thicker arrows indicating higher velocity. The blue/red arrows in the center panel represent direction (converging/diverging) of fluid motion in the rest frame of the scattering electron. The orientation of polarization of the scattered radiation represented by the orange bars is parallel to the cold axis of the local quadrupole. Stacking on such local hot (cold) spots produces a pure radial (tangential) E-mode pattern around the center. B-modes are never produced by this mechanism. 14

1.5 **A simplified illustration of the polarization patterns from tensor perturbations (gravity waves)** The transverse contraction/expansion of a standing gravity wave generates a local quadrupole in the photon intensity field that sources net linear polarization of the CMB photons scattered off electrons. The projection of the cold quadrupole axis (along the orientation of the red lobes) on the last scattering surface defines the orientation of the polarization. *top*: In the case of a gravity wave with intrinsic plus (+) polarization, the pattern (denoted by orange bars) is always perpendicular or parallel to the wavevector, generating pure E-modes. *bottom*: In the case of a gravity wave with intrinsic cross (x) polarization, provided the angle at which the wavevector intersects the last scattering surface is not 90° (otherwise no net linear polarization), the pattern is always oriented at $\pm 45°$ to the wavevector, generating pure B-modes. Figure inspired by [27, 36] 17

1.6 *Left top:* Planck map of the 353 GHz dust polarization fraction p at 1° resolution. The color scale is linear and ranges from 0% to 20%. The grey areas are where the dust emission is not dominant [61]. Figure courtesy: Planck Collaboration. *Left bottom:* Amplitude of polarized dust power from extrapolation of Planck 353 GHz data to 150 GHz, normalized by the CMB expectation for tensor-to-scalar ratio $r = 1$. [54]. Figure courtesy: Lyman Page. *Right:* Signal strength of the CMB B-mode polarization compared to galactic foregrounds as a function of frequency. Figure adapted from David Spergel. 18

1.7 **Current status of CMB TT, EE, and BB anisotropy spectra measurements** as of May 2015. The CMB temperature (TT) anisotropy spectrum is shown for ACT, Planck, and SPT. The E-mode polarization (EE) anisotropy spectrum is shown for ACTPol, BICEP2/Keck Array, Planck, POLARBEAR, and SPTPol. Direct measurements of the B-mode polarization (BB) anisotropy spectrum are shown for ACTPol, BICEP2/Keck Array, Planck, POLARBEAR, and SPTPol. Indirect measurements of the BB signal, indicated with an 'i' below the data point, are shown for ACTPol, Planck, POLARBEAR, and SPTPol. Figure courtesy: Lyman Page. 20

1.8 Map of the sky at 353 GHz. The deep and wide patches surveyed during the 2013 (S1), 2014 (S2), and 2015 (S3) seasons by ACTPol are indicated. More than half the sky is accessible to ACTPol. Overlapping surveys include SDSS, BOSS, CFHTLS, XMM-XXL, Herschel, HSC, DES, GAMA, and KiDS. Figure courtesy: ACTPol Collaboration 23

1.9 Ray trace of ACT primary and secondary mirrors up to the entrance of the receiver. The major components of the telescope upper structure are shown, except for the inner ground screen and part of the receiver cabin wall, which have been removed for clarity. The telescope is shown in its service position (where the receiver cabin floor is level), corresponding to a viewing elevation of 60°. Figure courtesy: R. J. Thornton [104] 24

1.10 Ray trace of the cold optics. The upper trace shows the PA3 (multichroic) optical path and the lower trace shows the PA1 path. The PA2 optical path is a mirror image to that of PA1 and has been removed for clarity. The various filters, lenses, lyot stop and detector array are labelled. Figure courtesy: R. J. Thornton [104] 24
1.11 Model of the as-built cryostat. The length of the cryostat is 1.5 m. The PA3 optics tube and most of the radiation shields have been removed for clarity. A combination of flexible copper sheets and copper braid are used to reduce vibrational coupling between the pulse tubes and internal cryostat components. Figure courtesy: R. J. Thornton [104] 26

2.1 *Left:* A ray diagram of one set of ACTPol re-imaging optics, which includes three silicon lenses feeding a detector array. The AR coating developed here is optimized for this lens design but could be applied to a variety of similar problems in millimeter wave optics. *Right:* A histogram of the angles of incidence of rays at the surfaces of these three silicon lenses. . . 34
2.2 The geometry of the two layer metamaterial AR coating. The left side shows a cross section through the center of the pillars indicating the design parameters discussed in the text. The right side shows an isometric view of the structure resulting from making cuts along two perpendicular directions. In both drawings grey represents silicon and white represents vacuum. 35
2.3 A comparison of the reflectance calculated from HFSS numerical simulation of a pillar geometry to fits based on a model of a simple dielectric layer. The geometry is specified in the inset in the top. In the simulated geometry, p = 400 , t_{phys} = 220 , k = 180 and n_{Si} = 3.38. A comparison between fits where only the index n is free and where both the index n and thickness t are varied is shown. The HFFS simulation and the best fit curve differ by 5% normalized root-mean-square deviation at 220 GHz ($\sim$ 1.36 mm). This corresponds to the minimum wavelength, $\lambda_{5\%}$ (and a corresponding maximum frequency $f_{5\%}$) for the specified pitch, p below (above) which the coating no longer behaves as a simple dielectric layer. . . . 37
2.4 A summary of results from HFSS simulations of single layers of pillars with varying geometry. *Left:* The minimum wavelength $\lambda_{5\%}$ for which the single pillar layer is fit by an analytic model to 5% accuracy as a function of pitch p at normal incidence. *Center:* The effective index of refraction n_{eff} as a function of the volume fill factor v_f obtained by fitting the simulated reflectances upto the minimum wavelength $\lambda_{5\%}$ = 1360 for a pitch, p = 400 , 40 . The line labeled "Biber" is a prediction from the analytic Biber model [112], which corresponds to the quasi-static circuit approximation for the media. In the quasi static limit, the relation between v_f and n_{eff} extracted from simulation approaches the Biber approximation. *Right:* The thickness t_{eff} for a slab dielectric quarter-wave coating divided by the thickness t_{phys} of pillars forming an effective quarter wave coating at the same frequency (equivalent to the ratio of n_{eff} over $\sqrt{n_{Si}}$) as a function of p/λ. The simulated pillar geometries have pitch p = 200 , 400 , and 600 . A parabolic line (with offset of unity) is drawn through the points just to guide the eye. In the quasi-static limit, $p/\lambda << 1$, the metamaterial approximates a constant index material whereas for larger values of p/λ, the dielectric function becomes dispersive. 38
2.5 Maximum allowable pitch for diffraction-free operation at a given frequency given by Equation 2.1. The plotted curves are for normal and 30° oblique incidence. 39
2.6 *Left:* A simulation of the performance of the AR coating designed for the 150 GHz ACTPol lenses at a range of angles of incidence. *Right:* The unit cell geometry modeled using HFSS. . 40
2.7 *left:* HFSS simulation of a single-layer quarter-wave coating and analytic fit curve obtained by varying the layer thickness and index. *right:* 2-D plot of the chi-square for the fit. 41

2.8 Two-layer AR coating modeled as two dielectric layers between air and silicon with thickness and index given by l_1, n_1, l_2, n_2. 41
2.9 The geometry of the three layer metamaterial AR coating. The left side shows a cross section through the center of the pillars indicating the design parameters shown in Table 2.3. Grey represents silicon and white represents vacuum. The right side shows a photo of a mechanical prototype. 43
2.10 *Left:* A simulation of the performance of the AR coating designed for the 90/150 GHz ACTPol lenses at a range of angles of incidence. *Right:* The unit cell geometry modeled using HFSS. . 44
2.11 Cross-section of the perimeter of the ACTPol lens 2, which is designed to enable machining of the AR coating and clamping the lens without damaging the AR coating. Figure courtesy: Michael Niemack 45
2.12 Measured silicon transmission at room-temperature (upper panels) and 4.5 K (lower panels). The left and right columns in the panel are for samples specified as $1 < \rho < 5$ Ω-cm and $\rho > 500$ Ω-cm respectively, the sample thickness is ∼180 thick. The figure contains the measured FTS data (red), model (dashed blue), and residual (green). Figure courtesy: Edward Wollack 47
2.13 Summary of findings from metrology performed on a two-layer coating cut on a silicon test wafer at NIST, Boulder. Figure courtesy: John Nibarger 49
2.14 *left:* VNA measurements of reflection from a 2 mm thick silicon test wafer, on which a single layer of rectangular grooves were cut in perpendicular directions with a commercially available dicing saw blade, compared to HFSS simulations. *right:* VNA measurements of reflection from a 4 mm thick silicon test wafer, two-layer AR-coated on both sides, compared to HFSS simulations. The measurements were carried out by Michael Niemack and Joseph Fowler at NIST, Boulder. 50
2.15 The custom, micron accurate, three axis silicon dicing system used to fabricate coatings on the lenses. The labels identify the key components and axes described in the Section 2.6. Figure courtesy: Charles Munson 51
2.16 *Left:* Photograph of the curved front surface of a two-layer AR coated 150 GHz (PA1/PA2) ACTPol silicon lens (lens 2) with zoomed view of a small patch. *Right:* Photographs taken with side looking metrology microscope. By focusing on the top, middle, and bottom of the pillars it is possible to determine the depth of the grooves including measuring asymmetries between left/right and up/down grooves, which in this case are less than 4 . Measurement of the profile of the grooves requires cutting a vertical section from the silicon substrate. Since creating these sections damages the substrate, the vertical section measurements were only performed on cuts made on a reference wafer before (pre-cut) and after (post-cut) cutting the lens. The measurements were made by Charles Munson. 53
2.17 *top:* Photos of different reflectometer setups used for measuring reflections from the small AR coated silicon test wafers. A white sheet of HDPE (for setup verification) is shown being measured in the photos. *bottom left:* The left panel shows a comparison between simulation and measurements of reflection from the HDPE sheet with the three setups shown above. *bottom right:* Two test wafers were two-layer AR-coated on one side of each and stuck back-to-back. The reflection was measured and compared to simulations of an equivalent two-layer two-sided AR coating with and without a hypothetical 10 air gap between the two test wafers sandwiched together. 54

2.18 A photo of the reflectometer setup used for measuring reflections from the ACTPol lenses. The lens being measured sits on the plate with the circular hole cut out. The two feedhorns are the transmit and receive horns, and the angle and distance of each feedhorn from the lens under test are adjustable. The black material is Eccosorb HR-10, which is a very good absorber of microwave radiation, and is used to mitigate stray reflections in the setup. 55
2.19 Comparison between simulations and measurements of the fabricated lens. The two sided simulations include the AR coating on both sides of a flat silicon sample of thickness equal to that of the lens at its center. The single sided simulations are for AR coating on only one side of a flat silicon sample. 56
2.20 *Left:* Photo of a three-layer AR-coated lens. *Right:* Comparison between simulations and measurements of the fabricated lens. The simulations are for a single-sided AR coating on a flat silicon sample of thickness equal to that of the lens at its center, illuminated at 15° angle of incidence. The two-sided simulations are not shown for preserving clarity. 57
2.21 *bottom*: Practically feasible (manufacturable) multiple-layer AR coatings, assuming a kerf width of 20 for the thinnest blade. n_i's refer to the effective indices of the layers, p refers to the pitch and an approximate total coating thickness is shown. *top*: Simulated reflections for the corresponding geometries, showing maximum achievable bandwidths. 58

3.1 A linearly polarized electromagnetic wave with an electric field vector $\vec{E}$ (*left*) traveling in the z-direction can be decomposed into two orthogonal linearly polarized components along the x- and y-direction (*middle*). *right*: the locus of the points of the tip of $\vec{E}$. 60
3.2 The Stokes parameters I, Q, and U on the sky can be fully mapped by combining measurements from multiple polarimeters rotated 45° relative to each other. Schematics of two polarimeters rotated 45° with respect to each other are shown here. Incident radiation couples to the planar detector wafer through the OMT (Ortho-Mode Transducer described in detail in Section 3.3.3) fins. The mutually perpendicular pair of fins pick up the two orthogonal components of linear polarization. 61
3.3 A simulation of the mapping speed as a function of horn aperture for a six inch detector array with 1.4:1 ratio bandwidth detectors with the band centers as labeled. For a multichroic array with two wide bands (centered at 90 and 150 GHz for example) it is possible to achieve sensitivity equivalent to 1.7 single frequency arrays with a 5 mm horn aperture diameter. Adding additional frequency bands leads to diminishing returns in sensitivity as these are sub-optimally coupled to the telescope. Figure courtesy: Suzanne Staggs 62
3.4 *Left:* design of a single horn coupled multichroic polarimeter with labels on the major components. *Center:* A photograph of a cross-section of a broad-band ring-loaded corrugated feed horn fabricated by gold plating a stack of etched silicon platelets. *Right:* A photograph of a prototype 90/150 multichroic detector with the major components labeled. A description of these components is in the text. For clarity, the path light follows to reach the bolometer corresponding to Y polarization in the 150 GHz band has been highlighted. 64
3.5 Simulated properties of the ring-loaded corrugated feedhorn. The bottom right panel shows a schematic of the cross-section of the feed. 66

3.6 *a:* A photo of a single prototype gold-plated stacked silicon feed fabricated at NIST, Boulder, *d:* a photo of the warm beam-mapping setup in our lab to measure the beam pattern of the prototype feed, *b, c and e:* zoomed in sections of the beam-mapper set-up showing the horn under test and the transmit horn, *top right:* comparison between measurements and simulations of the half power beamwidth over a range of frequencies. *bottom:* Measurements and simulations of the beam pattern of the ring loaded corrugated feed horn. These measurements of the E-, H-, and X-pol beams were made using a room temperature beam mapping system. The angles at which the beams hit the ACTPol aperture stop are greyed out. 67
3.7 A photograph of the ACTPol PA3 feed-horn array fabricated at NIST, Boulder along with measurements of return loss and insertion loss performed at different locations on the array using a Vector Network Analyzer (VNA). Plot Courtesy: Justus Brevik 68
3.8 Schematics of the CPW and MS lines implemented in our pixel design. The dielectric layers along with the thicknesses are noted. 68
3.9 *top left:* A schematic of the ACTPol PA3 OMT with the fin dimensions shown in the inset. The AdvACT MF (90/150 GHz) OMT is identical to this one. *top right:* Scaling down the PA3 OMT dimensions by a factor of 1.61 gives the OMT used for the AdvACT HF (150/230 GHz) array. *bottom:* The OMT Coupling for ACTPol 90/150 pixel (blue) and AdvACT 150/230 pixel (green). 71
3.10 CPW-to-MS transition design for ACTPol PA3, AdvACT MF, and AdvACT HF pixels, consisting of alternating sections of CPW and MS (length of each section shown in the tables). It behaves as a low pass filter as shown in the plot. 72
3.11 Designs of the PA3 five-pole resonant stub filters. The combined diplexer response is simulated for two different values of SiO_x loss tangent, 0.002 and 0.005. 74
3.12 Design of the AdvACT HF diplexer along with the simulated passbands. 75
3.13 Design of the AdvACT HF diplexer along with the simulated passbands. 76
3.14 A schematic of the hybrid tee consisting of sections of microstrip lines of given lengths as shown and carefully optimized widths [149]. 78
3.15 Designs of the Hybrids for AdvACT MF and HF pixels. The detailed dimensions are excluded for clarity. The sum port output is terminated while the difference port output (red and black lines) of each hybrid is routed to a TES. The difference port, odd-mode output (solid lines) represent our desired signal while the power in the difference port, even-mode output (dashed red and black lines) is suppressed by the on-chip bandpass filters before the hybrid. 79
3.16 Designs of the stepped-impedance Nb-Au transition for AdvACT MF and HF pixels consisting of alternating sections of Nb and Au. The detailed dimensions are excluded for clarity. The simulated reflections for different values of conductivity of Au (our best estimate lies within the range of simulated values) are shown. 80
3.17 *left:* Simulated passbands for ACTPol PA3 and AdvACT MF pixels. The ACTPol PA3 passband is plotted for two different values of SiO_x loss tangent. *right:* Simulated passbands for the AdvACT HF pixel. 81

3.18 *left:* FTS measurements and simulations of the ACTPol prototype Multichroic (90/150 GHz) detector pass-bands. For the 90 and 150 GHz channels, measurements of both linear polarizations as well as the terminated sum port were carried out. The agreement between the sum port measurements and simulations show that these detectors are properly rejecting unwanted waveguide modes. The agreement between the measured and simulated pass-band for the nominal X and Y polarized pixels is good, but has a 2% shift in the band edges. *right:* The prototype detector beams as measured by raster scanning with a hot thermal source in the lab at NIST. 82
3.19 *left:* Optical microscope image of one high frequency 150/230 GHz multichroic AdvACT HF single pixel. *right:* Zoomed images of the major pixel components: a) the planar OMT, b) the CPW-to-MS transition, c) the in-line diplexer composed of two five-pole resonant stub filters, d) the 180° hybrid tee, and e) one of the AlMn TESs, which is thermally isolated on a SiN_x membrane suspended with four narrow legs. Figure courtesy: Shannon Duff 83
3.20 Comparison between dielectric losses using SiO_2 and SiN_x dielectrics. 84
3.21 AdvACT MF (left) and HF (right) diplexer passbands for fiducial and worst case shifted values of dielectric constant and thickness. 85
3.22 Frequency response of the post-OMT microwave components in the AdvACT HF pixel for different values of Nb London penetration depth. 85
3.23 Unit cell of the CPW stub filter consisting of open-circuit quarter-wavelength long stubs. The top layer conductor traces and the ground plane are shown. The equivalent lumped element circuit model is shown. 87
3.24 The response of the bandpass CPW stub filter comprising two series-connected unit cells optimized for the 90 GHz band. The first odd-order harmonic is shown. 87
3.25 Lumped element bandpass filter design. *top left:* ladder circuit for a low pass filter prototype consisting of three normalized elements. *bottom left:* transformation to a bandpass filter with series LC and shunt parallel LC. *top right:* five-pole bandpass filter with impedance inverter blocks replacing the shunt inductors. *bottom right:* Final five-pole lumped-element bandpass filter circuit. 88
3.26 Implementation of a section of the lumped element bandpass filter using CPW and MS transmission lines. 89
3.27 Lumped element filter designs for the 150/230 GHz multichroic pixel. The 150 GHz filter is a five-pole design whereas the 230 GHz filter is a six-pole design. The two filters are connected to the two ends of a microstrip T-junction via a 5 long microstrip which is 5 wide. The input microstrip line to the T-junction is 4 wide and the output of the filters are also 4 wide microstrip lines. 90
3.28 Measured passbands of AdvACT HF prototype pixels (using MS stub filters (left) and lumped element filters (right)) compared to predictions. The measured passbands match predictions quite well for the pixel containing stub filters. The pixel with lumped element filters have passbands shifted by ∼5%. 91
3.29 The split-block brass module on which the detectors are mounted. *top*: Schematics showing the top and bottom parts of the module. *bottom*: A photo of 2 single pixels mounted on two such modules on a PCB. 92

3.30 *a*: A photo of the cold load. *b*: 2 single pixels mounted on a PCB with 2 copper horns. *c*: The PCB on which the pixels are mounted are screwed on to a copper board that is heat sunk to the cryostat cold stage. The two prototype ring-loaded corrugated silicon platelet single feeds are visible. Super-insulating mylar is used to prevent radiative heating of the PCB and the pixels. *d*: A photo showing the different cryostat stages and the aluminum cold load, enclosed in a copper box heat sunk to the 4 K stage via a G-10 tube, facing the detector board. A free-space low-pass filter (not visible here) is taped to the copper board in between the cold load and the feeds. 93
3.31 Emissive loading expected from heating of the free-space low-pass filter between the cold load and the detectors. 95
3.32 *top:* Assumed passbands for computing the optical efficiency. *bottom:* The respective measured dark-subtracted optical efficiencies. When assuming the simulated passband (left), we would ideally expect the optical efficiency to be equal to 1. 95
3.33 *top:* The differential Incident load power and detector powers for the 230 (left) and 150 (right) GHz prototype AdvACT HF pixels assuming top-hat passbands. *bottom:* The respective measured dark-subtracted optical efficiencies. The gradual rise in measured efficiency with cold load temperature indicates that some unwanted systematic is affecting our measurement. We are investigating this. 96
3.34 Each semihex sub-array consists of 24 pixels. *left*: The distribution of the two pixel types within the sub-array is indicated by the yellow and green filled circles. *right*: A group of upto 8 pixels (32 detectors) can be read-out via one multiplexing (mux) chip, the pixel routing scheme based on this is indicated by the three different types of colored circles. All read-out traces are routed to two groups of bond-pads along two edges of the hex. 97
3.35 Each hex sub-array consists of 61 pixels. *left*: The distribution of the two pixel types within the sub-array is indicated by the yellow and green filled circles. *right*: A group of upto 8 pixels (32 detectors) can be read-out via one multiplexing (mux) chip, the pixel routing scheme based on this is indicated by the eight different types of colored circles. All read-out traces are routed to a group of bond-pads along an edge of the semi-hex. 98
3.36 The ACTPol multichroic array comprises three $3''$ diameter hex sub-arrays (61 pixels each) and three $3''$ diameter semi-hex sub-arrays (24 pixels each). *Left:* Schematic of two semihex sub-array layouts. *right:* Schematic of a hex sub-array layout. 98
3.37 Separate rows of bondpads for the 90 and 150 detectors enable differential TES biasing. . . . 99
3.38 The PA3 full array consists of 255 pixels distributed between hex and semihex sub-arrays. . . 100

4.1 A schematic of the optics which couple the FTS output port to the ACTPol receiver. 102
4.2 A schematic of the L-shaped mount (made of aluminum) for the coupling optics attached to the FTS. 103
4.3 *left:* A schematic of the cross-section of the AR coating geometry. *right:* Simulated (HFSS [122]) reflection from a single-sided AR-coating on HDPE. 105
4.4 *left:* Side-view drawings of the three HDPE lenses. *right:* Surface profiles of the 6 lens surfaces. Three of these surfaces are spheric and three are aspheric. The lenses were cut in the Princeton Physics machine shop. 105

4.5 *top:* A 150 GHz microwave transmitter was used as a source for frequency calibration of the FTS. A diode detector was placed at the focus of the coupling optics. Resulting interferograms and Fourier transformed spectra obtained by operating the FTS in the step-and-integrate mode with two different step sizes. *bottom:* The lab setup for measuring prototype detector passbands. The FTS is pointing into a cryostat with a downward facing window. The three photos show different FTS sources (a blackbody emitter, a LN2 dewar, and an IR lamp) used for the measurement and testing/verification of the test setup. 107
4.6 Lab testing of the FTS: measuring the spectrum of a prototype 150 GHz ACTPol pixel. *top:* Raw data acquired with the ADC (Labjack T7) at 500 samples/second at an arbitrary position of the FTS dihedral mirror. *middle:* A cosine apodization function. *bottom:* Software demodulated signal amplitude. 108
4.7 *Left:* A photograph of the FTS setup in front of the ACTPol receiver to measure the instrument passbands; using an IR lamp as the source and pointing into the PA3 array, and *Right:* using an Eccosorb HR-10 immersed in LN2 as the source and pointing into the PA1 array. 109
4.8 Comparison between the spectra measured using two different types of FTS sources (IR lamp and LN2) and AR coated/non-coated HDPE lens in the coupling optics. Apart from the higher signal-to-noise with the hot IR lamp source, no noticeable differences were observed between the various spectra. 110
4.9 The left column shows some raw interferograms. The zero-path-difference (ZPD) point is not at the center because the throw of the movable mirror was not equal on either side of the center. The step size and throw combination of the dihedral mirrors was (Δl = 0.15mm, L = 100mm) for this higher resolution ($\Delta\nu$ = 0.75 GHz, ν_{UL} = 250 GHz) scanning. The middle column shows the same interferograms after phase correction. The right column shows the recovered spectra from the measured interferograms. 113
4.10 The left column shows some raw interferograms. The zero-path-difference (ZPD) point is not at the center because the throw of the movable mirror was not equal on either side of the center. The step size and throw combination of the dihedral mirrors was (Δl = 0.03mm, L = 20mm) for this lower resolution ($\Delta\nu$ = 3.75 GHz), high bandwidth (ν_{UL} = 1250 GHz) scanning. The middle column shows the same interferograms after phase correction. The right column shows the recovered spectra from the measured interferograms. 114
4.11 The left column shows schematics of the ACTPol arrays, with each circle representing a pixel and the filled circles representing the detectors whose measured passbands are over-plotted in each row. The 'good' detectors (red) refer to ones whose measured passband approximately matches the design, whereas the 'band-shifted' detectors refer to those which have a shifted passband with respect to design. Dividing by the RJ source spectrum blows up the noise at low frequencies. 115

4.12 The left column shows schematics of the ACTPol arrays, with each circle representing a pixel and the filled circles representing the detectors whose measured passbands are averaged and plotted in each row. The subsequent columns show averaged high resolution and low resolution spectra. The detectors, represented by the green filled circles, have passbands shifted down in frequency (for the PA3 array, these are detectors on the FH4 hex wafer). The lowest band edge, defined by the feedhorn waveguide section, is not affected by this. The dotted lines (over-plotted with the PA3 spectra) are from simulations of the multichroic pixel, including the feedhorn and the OMT. However, the simulations do not include the filters in the optical path. The sharper roll-off (than design) in the lowest PA3 90 GHz band edge is a result of a design flaw in PA3 that the waveguide section of the feedhorn was much shorter than required, which has been rectified for the subsequent dichroic arrays. Dividing by the RJ source spectrum blows up the noise at low frequencies. No evidence for out-of-band leakage was found. 116

4.13 Plotted along each row are the per measured detector effective central frequencies to compact sources (left column), diffuse sources (middle column), and effective bandwidths (right column). The four rows correspond to the PA1 148 GHz array, PA2 148 GHz array, PA3 150 GHz array, and PA3 90 GHz array, respectively. All measured detectors (including the ones with shifted passbands are plotted here). Error bars are excluded to preserve readability. . . . 118

4.14 A histogram plot of the 90 and 150 GHz PA3 (dichroic array) detector efficiencies, relative to the simulated passband shown in dotted lines in Figure 4.12. FH4, FH3 and FH2 represent the three hex sub-arrays and SH1a, SH1b and SH8b represent the three semi-hex sub-arrays. Figure courtesy: Christine Pappas 119

5.1 *left:* A schematic of the ACT primary mirror showing the 71 panels (courtesy: Swetz et. al. [76]). *right:* Model of the primary illumination pattern with the panel gaps, which is also the aperture field for our simulation. 122

5.2 Grayscale images of the simulated near and far field beams plotted in log scale. The square patches represent a 120° x 120° region on the sky. The panel gaps were assumed to be not covered for these simulations. 123

5.3 *top:* Filled contour plots of the simulated far-field beam zoomed in to 2° x 2° and 4° x 4° patches. *bottom:* 1D cuts across the center of the beam plotted in logarithmic dB scale. 124

5.4 Grayscale images of the simulated near and far field beams plotted in log scale along with 1-D cuts (x-, y-, y-) across the center plotted below. The square patches represent a 120° x 120° region on the sky. The panel gaps were assumed to be covered with aluminum tapes for these simulations. 125

5.5 A panoramic view of the landscape surrounding the telescope. 125

5.6 A photo of the telescope showing the major sources of ground pick-up. 126

5.7 *top left:* Model of the emission from the stationary ground screen encompassing 90° in azimuth. *top right:* Convolved map with the simulated near-field beam at a distance of 12 m. *bottom:* 1-D constant-elevation cuts of the convolved map showing the amplitude of the contamination when the telescope is pointed to different elevations 127

5.8 *top left:* Model of the emission from the lightning rods encompassing 90° in azimuth. *top right:* Convolved map with the simulated near-field beam at a distance of 12 m. *bottom:* 1-D constant-elevation cuts of the convolved map showing the amplitude of the contamination when the telescope is pointed to different elevations 128

5.9 *top left:* Model of the emission from the mountain peaks encompassing 90° in azimuth. *top right:* Convolved map with the simulated beam at a distance of 6 km. *bottom:* 1-D constant-elevation cuts of the convolved map showing the amplitude of the contamination when the telescope is pointed to different elevations 129
5.10 *top row:* Map of the Sun convolved with the simulated far-field beam, coordinate-transformed to polar coordinates with the Sun at the center and plotted in logarithmic dB scale. The white circles are spaced at 5° intervals away from the center. *middle row:* Sun-centered ACTPol maps made by S. K. Naess. The radial stripes are a result of Sun contamination. *bottom row:* Simulated contamination superimposed on the map. The left column plots are with uncovered panel gaps while the right column plots assume aluminum tapes covering the gaps. 131

6.1 Intensity map of a selected region within the ACTPol Deep56 patch. The color scale is restricted to $\pm 200\ \mu K$. 135
6.2 Match filtered map of the region shown in Figure 6.1. The bright spots in this map correspond to galaxies. The color scale is restricted to $\pm 40000\ \mu K$. 136
6.3 The ACTPol beam used in the point-source detection algorithm shown in the ACTPol pixelization of 0.5' (the non-circular appearance is a result of pixelization artifacts). 137
6.4 Example of three irregular or extended sources, removal of which require a two-step matched-filtering method. The left column shows thumbnails of the original sources, the middle column shows the residuals after the first run of the source removal algorithm, and the right column shows the residuals after applying the source removal algorithm the second time. 138
6.5 Histogram of the number of detected sources in the ACTPol Deep56 Intensity map plotted against the signal-to-noise ratio of the detections binned in log space. 139
6.6 I, Q, and U maps of the ACTPol Deep56 patch. The color scale is restricted to $\pm 250\ \mu K$ in the T map and to $\pm 125\ \mu K$ in the Q and U maps. 140
6.7 Thumbnails of some of the intensity detected sources that have the largest polarization signal in the corresponding Q and U maps. 141
6.8 Inverse variance weighted maps of the region shown in Figure 6.6. These constitute the per pixel covariance matrix. 142
6.9 Examples of the maximum likelihood estimation of the true values of Q and U in the presence of correlated noise for two of the brightest sources. *top:* 2D maximum likelihood contour and Gaussian estimates of the true value of Q/U obtained by marginalizing over the other variable. *bottom:* Data, model and residuals showing that the maximum likelihood estimation works. . . 143
6.10 Stacking polarization signal (from Q and U maps) on sources detected in temperature with signal-to-noise ratio between 5 and 50 (top), 50 and 500 (bottom). 144
6.11 *top left:* ACTPol intensity (T) noise map obtained by differencing one half of a 2-way data split from the other. *top right:* Map of the constructed noise model. *middle left:* 2D spectrum of the ACTPol noise map in l space. *middle right:* 2D spectrum of the noise model in l space. *bottom:* Comparison between ACTPol and modeled T, Q, U noise power spectra. 146
6.12 Comparison between ACTPol Deep56 detected source counts and simulated source counts. . . 147
6.13 Polarization fraction simulations. The blue dots represent the polarization fraction of the simulated sources and the red curve is the polarization fraction binned in intensity. 148
6.14 Polarization fraction simulations. The blue dots represent the polarization fraction of the simulated sources and the red curve is the polarization fraction binned in intensity. 149

6.15 Polarization fraction plotted against intensity (total flux) for the ACTPol sources brighter than 25 mJy in the Deep56 region. The error bars encompass the 95% confidence interval. 149
6.16 Best fit model for distribution of source polarization fraction with the green band representing the $\pm 1\sigma$ standard deviation. 151
6.17 Simulations of TT (blue) and EE (green) power spectra with *top left:* no extragalactic sources, *top right:* without source removal, and *bottom:* sources with flux greater than 0.5 mJy removed. The dashed line shows the upper limit of the error bars. 152
6.18 A comparison of the average Season 1 and Season 2 flux for sources with >10% variability. The length of the bars along each axis are equal to the $\pm 1\sigma$ deviation in measured flux between the 11-day maps within the respective season. The inset shows the plot in log scale. 153
6.19 Histogram plot of the number of sources as a function of source variability index computed as per Equation 6.8 based on ten, 11-day maps made from Season 1 data (left panel) and twelve, 11-day maps made from Season 2 data (right panel). 153
6.20 Positional offsets between ACTPol catalog and VLA First catalog obtained by comparing the positions of ACTPol sources detected with flux greater than 100 mJy and their VLA First counterparts. The cross is centered on the mean offset with lengths along either axis indicating the rms offset. 154
6.21 Source spectral indices. In this color-color diagram, 1.4-20 GHz and 20-148 GHz spectral indices are shown for ACTPol-AT20G-NVSS cross-identified sources with 148GHz flux density greater than 25 mJy (the darker blue dots represent sources with 148 GHz flux greater than 50 mJy). The population is dominated by sources which are peaked (lower right quadrant) or falling (lower left quadrant). The low flux sample is incomplete and suffers from selection bias that favors sources with more negative spectral indices. The left panel shows the color-color diagram for source flux estimated from the intensity map, while the right panel is for polarized flux. 156
6.22 1.4 GHz NVSS flux (green dots) and 20 GHz AT20G flux (blue dots) are plotted against 148 GHz flux for ACTPol-AT20G-NVSS cross-identified sources with 148GHz flux density greater than 25 mJy. The left panel shows the source flux estimated from the Intensity map, while the right panel is for polarized flux. The darker dots are sources with 148 GHz flux greater than 50 mJy. 157
6.23 1.4-148 GHz spectral indices are plotted against 148 GHz flux for ACTPol-NVSS cross-identified sources with 148 GHz flux density greater than 25 mJy. The blue dots are source flux derived from the intensity map while the green dots represent polarized flux (the darker blue and green dots are sources with 148 GHz flux greater than 50 mJy). 157
6.24 Fractional Polarization versus total source flux. *top:* sources differentiated according to steepening (falling) and peaked spectra based on total flux. *bottom:* sources with total flux variability >10% differentiated from the rest. 159
6.25 1.4-148 GHz spectral indices are plotted against 148 GHz flux for ACTPol-VLA First cross-identified sources with 148 GHz flux density greater than 3 mJy. The low flux sample is incomplete and suffers from selection bias that favors sources with more negative spectral indices. 160

7.1 Example maps from the region 29.65° < RA < 40.49°, -7.60° < Dec < -0.68°, in the center of ACTPol patch D6. Panels 1,2,3,5,6 (left to right, top to bottom) show T, Q, U, E and B respectively. Panel 4 is a zoom on a 2.79° x 1.73° subregion of the T map, showing the full map resolution. The maps have been bandpass filtered to maximize signal-to-noise ($240 < l$ for temperature, $260 < l < 1370$ for polarization). The visible patterns in the Q and U maps are consistent with a sky dominated by E-mode polarization, as can be seen in the derived E and B maps. The B map is consistent with noise except for a faint m = 0 (constant declination) ground residual. The circled galaxy cluster candidate, ACT-CL J0205.2-0439, is within 2' of a CFHTLS cluster candidate with photometric redshift z = 1.1 and three concordant galaxies with spectroscopic z = 0.97 found in the VIMOS Public Extragalactic Survey. The circled point source may be associated with FBQS J0209-0438, a quasar at z = 1.128. Figure taken from S.K. Naess et al [237]. 162

7.2 The ACTPol TT, TE, and EE power spectra, together with the best-fitting ΛCDM cosmological model and foreground components. Six acoustic peaks are seen in the E-mode polarization, out of phase with the temperature peaks and with the TE correlation pattern predicted by the standard model. Figure taken from S.K. Naess et al [237]. 163

7.3 *left:* ACTPol PA3 multichroic array NEP (Noise Equivalent Power). Figure courtesy: S. P. Ho. *right:* Temperature maps of Centaurus A made from six hours of PA3 data Figure courtesy: M. Lungu. 164

7.4 Sky coverage of AdvACT. The yellow boxes are the tentative patches to be mapped by AdvACT during the current observing season. Sky coverage of some other astronomical surveys are shown by the shaded regions to highlight the overlap. Figure courtesy: AdvACT Collaboration. 165

7.5 Preliminary 90 GHz (left) and 150 GHz (right) maps of a 15° × 15° patch centered at RA ∼36° and Dec ∼-3° made from observations with the ACTPol multichroic array. The color scale is restricted to ±250 μK. Figure courtesy: S.K. Naess 167

7.6 Example simulated passbands for some four-color pixels as described in text. The filter designs can be easily adjusted to allow varying extents of overlap between the bands which could enable better spectral characterization of complicated foregrounds that are not defined by a simple power law. For a ground observatory, the atmospheric lines need to be avoided, whereas a space mission would have no such constraints. 168

A.1 This figure shows the families of machining errors considered in the tolerance analysis and described in the text. The dashed lines show the target shape for the grooves and that for the pillars while the white space in the grey represents the material as actually cut. Therefore difference between the dashed region and the white region represent machining errors. For the asymmetric depth and damaged row errors the sketches show the geometry of the errors. . 171

A.2 The band averaged reflectance at a 15° angle of incidence as a function of changes in the pitch. The grey region shows range for which the performance is within 3 dB of the fiducial design. 171

A.3 This figure shows the impact of errors in the kerf, slopes in the sidewalls, overall depth errors, and asymmetric differences in depth between the two orthogonal cuts. The color scale presents the degradation in reflection at 15° incidence compared to the simulations in Figure 2.6. The fiducial design is at the coordinate (0,0) in all the plots as highlighted by a "+" or arrow. The outer edge of the light blue contour (see label) represents 3 dB degradation. The horizontal (vertical) axis represents errors in the inner (outer) layer of the coating for the labeled parameters. 172
A.4 *Left:* The simulated impact of having the surface of the lens tilted by 10°. *Right:* The simulated impact of variation in the refractive index of the silicon substrate. 173

B.1 *left*: parameters for a Gaussian beam diverging from a feed horn *right* a Gaussian beam propagating through a lens. Figures taken from Quasioptical Systems: Gaussian Beam Quasioptical Propogation and Applications, Paul F. Goldsmith [135] 176

C.1 *left:* Measured reflection from a ∼380 thick sheet of the Zitex used for AR-coating the UHMWPE vacuum window compared to simulations with different index and thickness parameters. The blue, green, and black curves correspond to three different measurements. *right:* Measured reflection from the ACTPol PA3 vacuum window made of UHMWPE and AR-coated with Zitex. Simulated reflection (assuming $n_{zitex} = 1.32$) is also plotted for comparison. 179
C.2 Simulated reflection from a two-layer AR coating on HDPE composed of teflon and Zitex . . 179
C.3 *top left:* Cross-section of a custom drill bit for drilling holes on HDPE to make an AR-coating. *top middle:* Zoomed-in photo of a prototype made at the Princeton Physics machine shop with a pitch of 32 mils. *top right:* Zoomed-in photo of a prototype made at the Princeton Physics machine shop with a pitch of 22 mils. *bottom left:* Simulated model in HFSS. *bottom middle:* Photo of a 2x2 inch square section of the prototype with the 22 mil pitch. *bottom right:* Measured reflection of the same, when compared to simulation, is significantly higher. . . . 180
C.4 Three alternative AR coating designs for HDPE along with simulated reflections: (*top left:*) design1: a two-layer coating very similar to that for the silicon lenses, (*bottom left:*) design2: cutting grooves in perpendicular directions with a tool having a triangular cross-section might be easier. (*right:*) design3: conical holes drilled into HDPE. 181

D.1 Mitering of 90° bends in our CPW and MS lines. 183
D.2 Mitering of acute angle bends in our CPW and MS lines. 184

E.1 *Left:* Two neighboring pairs of traces (blue and green). Each pair consists of two traces - one each on the two wiring layers on the wafer. *Right:* A simplified case of the figure on the left where the separation between the two wiring layers is ignored. This is an assumption to simplify the calculation of the mutual inductance between the two pairs. 186
E.2 A circuit model of the TES biasing circuit with the criss-crossed traces. 187
E.3 A circuit model of the TES biasing circuit without the criss-cross. The two neighboring pairs of traces between which the crosstalk is calculated are marked purple and green. For ease of computation, the voltage drop across the variable TES resistance is approximated as: product of a constant resistance, R_{TES} times the current i_{TES} plus a time varying voltage $v_{1s}e^{j\omega t}$ as shown in the inset. 188

E.4 Ratio of induced current to the time varying component of the current in the neighboring pair as a function of frequency. 190

LIST OF TABLES

2.1 The parameters for the 150 GHz ACTPol two-layer AR coating design. 40
2.2 Effective layer indices and thicknesses for the 150 GHz ACTPol two-layer AR coating. 42
2.3 The parameters for the 90/150 GHz ACTPol three-layer AR coating design. . . 43
2.4 Effective layer indices and thicknesses for the 90/150 GHz ACTPol three-layer AR coating. 44
2.5 Silicon Drude Model Fit Parameters. 49

3.1 Co-Planar Waveguide and Microstrip Transmission Line Properties 70
3.2 Total Losses in post-OMT microwave components assuming SiO_x loss tangent = 0.005 81
3.3 Dielectric Losses in post-OMT microwave components in the AdvACT HF Pixel 83
3.4 Stub Filter Design Tolerances 84
3.5 Lumped Element Filter Design Tolerances 91

4.1 Surface Profiles of Lenses for the Coupling Optics 106
4.2 ACTPol effective central frequencies and bandwidth (from Dec 2014 and May 2015 on-site FTS measurements) 120

6.1 Completeness and Purity of the ACTPol sources 137

A.1 A summary of the 3 dB sensitivities for all parameters described in the text. . 175

LIST OF APPENDICES

A Design Tolerances for the Two-layer AR Coating 170

B Design of the plastic lenses for the reflectometer setup 176

C AR coatings on plastic 178

D Mitered Bends in CPW and MS Transmission Lines 182

E Crosstalk between pairs of traces in the array wiring layout 185

ABSTRACT

The Cosmic Microwave Background (CMB) is a unique and powerful tool for the study of cosmology and fundamental physics. The next frontier of CMB research is to extract the wealth of cosmological information available from its polarization. Accurate measurement of this polarization signal will enable us to probe inflation, provide an alternative means to measure the neutrino mass sum and number of neutrino species; improve our understanding of dark energy; explore the reionization history of our Universe; probe the large scale structure through gravitational lensing; and enable a multitude of other astrophysical studies. The polarized signatures of the early universe are extremely weak, dominated by foregrounds, and its measurement is susceptible to instrumental effects. Extracting the information contained in these faint signals requires instruments with high sensitivity, excellent control over systematic errors, and careful data analysis.

The Atacama Cosmology Telescope Polarimeter (ACTPol) is a state-of-the-art experiment that measures CMB polarization over finer angular scales from the Atacama desert in Chile. In this thesis, I present an overview of this project and then describe my work on the project including development of a new polarization sensitive dichroic camera for ACTPol designed to increase the sensitivity of CMB telescopes and enable high precision measurements of CMB polarization; the development of novel metamaterial antireflection coatings for silicon lenses; diffraction from panel gaps; calibration of detector pass-bands; and a detailed description of my analysis of the polarization properties of extragalactic point sources discovered with the ACTPol data. I conclude with a discussion of the science of ACTPol, and the impact of my technical work on future CMB experiments.

CHAPTER 1

Introduction

1.1 Discovery of the CMB

The Cosmic Microwave Background (CMB) provides a snapshot of the early Universe. In fact, it is the oldest measurable light in our Universe. In 1948, George Gamow and his students Ralph Alpher and Robert Herman first predicted the existence of the CMB [1] by extrapolating the observed expansion of the present Universe backwards in time. They showed that the abundances of the light elements could be explained by a hot, dense phase beginning some 10-20 billion years ago. They predicted that this would leave the Universe with radiation temperature of ~ 5 K today [2], though two years later they re-estimated it at ~ 28 K [3]. It was not until 1965 that the CMB was accidentally discovered when Arno Penzias and Robert Wilson of Bell Laboratories pointed a horn antenna in the sky sensitive to a communication frequency $\nu = 4.080$ GHz and detected an excess radiation with a brightness temperature of 3.5 K $\pm$ 1.0 K that was isotropic in nature [4]. The discovery of the CMB and explanation of its origin by Dicke, Peebles, and Wilkinson [5] gave credence to the hot big bang model and laid the seeds of observational cosmology. For their discovery of the CMB, Penzias and Wilson received the 1978 Nobel Prize in Physics.

1.2 History of the Universe and Origin of the CMB

The Universe is believed to have been created by the hot Big Bang [6] beginning with a period of rapid exponential expansion [7, 8] that lasted only a tiny fraction of a second. Not long after Inflation, the first particles formed and the Universe was relatively simple, comprised of baryons bound, photons, and dark matter [9, 1]. The Universe was still relatively hot, which imparted the photons with enough energy to ionize neutral atoms and kept the photons in thermal equilibrium with the baryonic matter. The scattering cross-section be-

tween photons and electrons is such that the mean free path of the photons was very small and the Universe was a hot opaque soup of plasma. This is often referred to as the primordial or photon-baryon plasma. The Universe cooled over the next ∼380,000 years [10] to the point that the energy of the photons was no longer sufficient to ionize neutral atoms and protons and electrons combined to form neutral hydrogen. The Universe gradually transformed to a transparent space filled with neutral atoms with photons decoupled from the plasma, the rapid re-scattering of photons off electrons came to a halt, and the photons could now free-stream in every direction. This era is known as the epoch of recombination. The CMB photons which fill our sky come from this surface of last scattering, which is a spherical slice through the Universe at the epoch of decoupling. Since the photons and baryons were in thermal equilibrium prior to this, the energy spectrum of the photons arriving at our detectors today from the last scattering surface is a black body spectrum redshifted to much lower energies by the expansion of the Universe. By the end of the 20th century, the CMB had been measured to be isotropic on large scales with a spectrum spectacularly consistent with Planck's black body law. Measurements from the Far InfraRed Absolute Spectrophotometer (FIRAS) instrument aboard the COsmic Background Explorer (COBE) satellite [11, 12] showed that the isotropic component of the CMB could be characterized by a 2.728 ± 0.004 K blackbody, constraining the thermal history of the hot big bang and ushering in an era of precision cosmology.

The frequency spectrum of the CMB and its angular variation in temperature and polarization contain a wealth of information about the origin of the Universe and the evolution of large scale structure. The incredible temperature isotropy of the CMB indicates that at the time of decoupling the universe was in thermal equilibrium over distances greater than that light could travel since the big bang. This observation strongly supports the theory of inflation, that would have separated regions that were previously in causal contact. Probing this inflationary paradigm is one of the primary goals of CMB experiments today.

Because photons and baryonic matter were tightly coupled in a plasma state between inflation and decoupling, small temperature fluctuations in the CMB indicate density fluctuations in the matter density of the universe at decoupling. Dark matter which, having no electromagnetic interactions, interacted with this primordial plasma through gravity. At decoupling, the protons and electrons, which combined to form neutral atoms, were no longer perturbed by collisions with photons and were able to gravitationally collapse along with the dark matter into the structures observed in the Universe today. In addition to providing information about the universe at the time of decoupling, the fluctuations in the CMB are

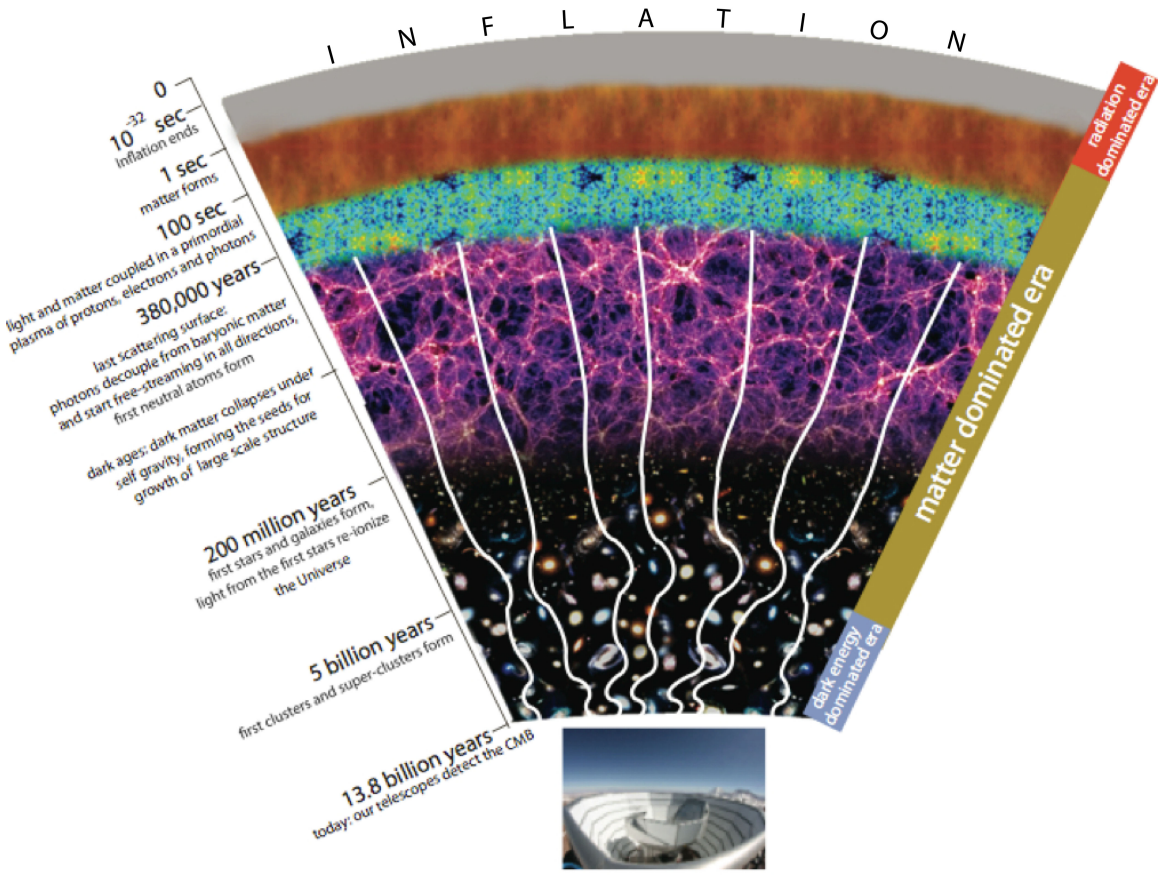

Figure 1.1: **History of the Universe** As the Universe came into existence, a period of rapid exponential expansion inflation amplified tiny quantum fluctuations in space-time to angular scales accessible to CMB experiments. At the end of Inflation, elementary particles started forming, but the Universe was still so hot that protons and electrons which formed atoms would be immediately separated by collisions with photons, and conversely the photon mean free path between scatters was negligibly small. The Universe gradually cooled and the intensity of radiation was low enough that atoms could form, allowing the photons to start their relatively unimpeded journey towards us. The matter, no longer tied to the photons by the electromagnetic force, clumped gravitationally and started forming the structures observed today. As the first stars formed, light from them partially reionized the Universe. On their way to us, the photons get scattered by electrons from the epoch of reionization, and hot electron gas clouds in clusters. They are aslo gravitationally deflected by massive galaxy clusters. Today, in the CMB photons, we can see the imprints of the above along with that of inflation and the primordial density perturbations that seeded the large scale structure. This helps improve our understanding of the birth and evolution of our Universe.

also indicators of physics before decoupling (see Figure 1.1). In particular, the CMB can give us information about the seed perturbations in energy and space that were in place at the very beginning of the universe and therefore provide essential clues as to the physical means by which the Universe, as we know it, was created. The CMB also serves as a backlight to the evolution of large scale structure in the universe between recombination and the current epoch.

1.3 CMB Temperature Anisotropy Power Spectrum

The CMB can be considered to be a field on a 2D spherical surface, whose temperature distribution on the sky may be represented as:

$$\frac{\Delta T(\theta,\phi)}{T} = \sum_{l=0}^{m=\infty} \sum_{m=-l}^{m=+l} a_{lm} Y_{lm}(\theta,\phi) \tag{1.1}$$

where each spherical harmonic Y_{lm} represents a mode with fluctuations of a characteristic angular size. The Fourier coefficients a_{lm} are a set of random variables whose distribution defines the temperature anisotropies. Initial density perturbations are expected to be Gaussian in nature, hence $\frac{\Delta T(\theta,\phi)}{T}$ is a Gaussian random variable, and subsequently the magnitudes $|a_{lm}|$ are expected to be drawn randomly from a Gaussian distribution at each l. The different a_{lm} are independent random variables, so that the variance of the coefficients:

$$\langle a^*_{lm} a_{l'm'} \rangle = \delta_{ll'} \delta mm' C_l^{TT} \tag{1.2}$$

where the above average is taken over many ensembles and the delta functions arise from isotropy. The C_l's represent the temperature angular power spectrum. It can be inferred from the homogeneity and isotropy of the Universe that the temperature fluctuations should have no preferred directionality. The power spectrum of the fluctuations is indexed in terms of the multipole l, while taking an ensemble average over the azimuthal coordinate, m:

$$C_l^{TT} = \frac{1}{2l+1} \sum_{m=-l}^{m=+l} |a_{lm}|^2 \tag{1.3}$$

The l = 0, 1, and 2 components represent the average temperature on the sky, the dipole (l = 1), and quadrupole (l = 2) components, respectively. Thus, the information about fluctuations on various angular scales can be encoded in the CMB angular power spectrum with increasing l corresponding to decreasing angular scales. The linear perturbation theory

for the generation of CMB anisotropy leads to independent evolution of different Fourier modes. Thus, the C_l's completely specify the distribution of the a_{lm}'s, and contain the total information content of the temperature anisotropies. The fundamental measurement limit due to cosmic variance arises from the fact that the number of multipole modes or $m's$ corresponding to a given l is limited, and the limit decreases with l as $1/\sqrt{2l+1}$. The variance of the temperature fluctuations smoothed over an angle θ is approximately given by:

$$\left(\frac{\Delta T}{T}\right)^2_\theta \sim l(l+1)C_l/2\pi \tag{1.4}$$

where, $l \sim 180^\circ/\theta$. The redshifting of CMB photons due to the Earth's velocity through space relative to the CMB rest frame imparts the largest measurable deviation of the CMB from isotropy. This deviation, approximately of the order of 10^{-3} T_{CMB}, appears as a dipole on the celestial sphere. After subtracting this dipole, T_{CMB} measured in all directions on the sky is uniform to almost a part in 10^5. The tiny fluctuations of the temperature about the mean are described as the CMB temperature anisotropies. The angular correlation between these fluctuations represented as an angular power spectrum, is sensitive to a variety of fundamental parameters that describe our universe, including the age and geometry of the universe, the total energy density, the total matter density, and the baryonic matter density. The standard model gives a rich set of predictions for the variation of anisotropy power with angular scale [13]. A second instrument onboard COBE called the Differential Microwave Radiometer (DMR), observing on angular scales larger than 7°, was the first to detect anisotropies at smaller scales than the dipole at a level of 10^{-5} [14]. These scales today correspond to regions of the Universe that were not yet in causal contact at the epoch of recombination, and thus reflect the primordial super-horizon inhomogeneities which set the initial conditions for structure formation. Observations since the DMR detection have focused on smaller angular scales, where gravitationally-driven evolution of the primordial inhomogeneities can enhance or suppress the temperature anisotropies generated at last scattering.

1.3.1 Primary Anisotropies

Three effects are primarily responsible for the generation of the primary temperature anisotropies, up to the time of decoupling: (1) local gravitational potential wells resulting from fluctuations in the density of the photon-baryon plasma at the last scattering surface imprint temperature variations due to gravitational redshift of CMB photons, (2) these density fluc-

tuations also directly result in temperature variations of the local monopole radiation field at the last scattering surface, and (3) Doppler shifts due to perturbations of the photon-baryon velocity field (the local dipole) at the last scattering surface.

Dominant on the largest angular scales ($l <\sim 10-20$) is the Sachs-Wolfe (SW) effect [15] which refers to the gravitational redshifting of CMB photons from over-dense regions as they lose energy climbing out of gravitational potential wells generated by super-horizon scale density fluctuations at the last scattering surface. This gives the photons a redshift and a consequent temperature decrease given by $\Delta T/T = -\Delta\phi/c^2$, where $\Delta\phi = -G\Delta M/R$ is the gravitational potential shift associated with a mass fluctuation ΔM of physical radius R. The wavelength of radiation is also stretched by the expansion of space, which should also be taken into account while estimating the SW effect. The radiation density, $\rho_{rad} \propto a^{-4}$, where a is the scale factor and from Stefan Boltzmann Law, $\rho_{rad} \propto T^4$, where T is temperature. Hence $a \propto T^{-1}$, i.e., $\Delta T/T = -\Delta a/a$. Considering radiation as a perfect fluid described by the stress-energy tensor and applying conservation of energy-momentum, we have $\rho \propto a^{-3(1+w)}$. Plugging this into the Friedmann equation for a flat universe,

$$\left(\frac{\dot{a}}{a}\right)^2 = \frac{8\pi G\rho}{3} \tag{1.5}$$

we get $\Delta a/a = -2/(3+3w)(\Delta\phi/c^2)$. Therefore, the net temperature fluctuation associated with the SW effect is given by:

$$\left(\frac{\Delta T}{T}\right)_{SW} = -\frac{\Delta\phi}{c^2} + \frac{2}{3(1+w)}\frac{\Delta\phi}{c^2} \sim -\frac{1}{3}\frac{\Delta\phi}{c^2} \tag{1.6}$$

The time evolution of density and curvature fluctuations along the line of sight of the photon produce further net gravitational redshifts which can generate temperature anisotropies well after last scattering. This is known as the integrated Sachs-Wolfe (ISW) effect.

On sub-horizon scales, the opposing forces of gravitational collapse of the primordial photon-baryon plasma and photon pressure resisting the infall drives acoustic oscillations of the plasma into over-dense and under-dense regions creating compressions and rarefactions. At the time of decoupling, some of these oscillations are at their peak minima or maxima resulting in larger temperature anisotropies and producing an excess of power at angular scales corresponding to the wavelength of those modes, while those that have returned to the average density of the Universe produce a dearth of power at the corre-

sponding angular scales and show up as troughs in the power spectrum. These show up at intermediate angular scales ($\sim 50 < l <\sim 1000$). The first couple of peaks in the CMB temperature angular power spectrum are thus a result of interactions between gravitational potential wells formed by dark matter and the photon-baryon plasma. Careful measurements of the peak amplitudes allow us to constrain the different types (dark and baryonic) of matter densities in the universe, while the location of the first peak constrains the geometry of the Universe as is explained below.

The angle (in radians) subtended on the sky today by a physical process of a characteristic length scale, L at some given redshift, z is given by:

$$\theta(L) \sim \frac{L}{d_a(z)} \tag{1.7}$$

where $d_a(z)$ is the angular diameter distance which is a function of redshift and is defined as $d_a(z) = a_z r = a_o r/(1+z)$, where $a_z(a_o)$ is the scale factor at a redshift z (today), r is the comoving or coordinate distance and $a_z r$ is the physical distance. The Friedmann-Robertson-Walker (FRW) spacetime metric (in polar coordinates) for an isotropic and homogeneous Universe is:

$$ds^2 = -dt^2 + a^2(t)\left[\frac{dr^2}{1-kr^2} + r^2 d\theta^2 + r^2 sin^2\theta d\phi^2\right] \tag{1.8}$$

where k denotes the spatial curvature of the Universe. It can be shown that for a matter dominated Universe where Ω_{tot} is the ratio of total density of the Universe over the critical density required for a flat Universe (k = 0), $r \sim 2/(H_o a_o \Omega_{tot})$ for sufficiently large z, i.e., $d_a(z) \sim 2/(H_o \Omega_{tot} z)$ and:

$$\theta(L) \sim \frac{1}{2}(L\Omega_{tot} z H_o) \tag{1.9}$$

At the present epoch, the physical size L will have stretched to $La_o/a_z = L(1+z) \sim Lz$. We will estimate the angular scale in the sky associated with a physical process with a 'characteristic Hubble distance' at the last scattering surface. We know from General Relativity,

$$H(z) = H_o\sqrt{\Omega_\Lambda + \Omega_M a_z^{-3} + \Omega_R a_z^{-4} + \Omega_k a_z^{-2}} \tag{1.10}$$

where $\Omega_R, \Omega_M, \Omega_\Lambda$ are the radiation density, matter (dark plus baryonic) density, and the cosmological constant or vacuum density today and $\Omega_k = 1 - \Omega_{tot}$ is the spatial curvature

density today. At decoupling, the Universe was matter dominated, therefore,

$$\begin{aligned} H(z = z_{LSS}) &\sim H_o \sqrt{\Omega_M a_{z_{LSS}}^{-3}} \sim H_o \sqrt{\Omega_M a_{z_{LSS}}^{-3}} \\ &= H_o \sqrt{\Omega_M (\frac{a_o}{1+z_{LSS}})^{-3}} \sim H_o \Omega_M^{\frac{1}{2}} z_{LSS}^{\frac{3}{2}} a_o^{\frac{-3}{2}} \\ &= H_o \Omega_M^{1/2} z_{LSS}^{3/2} a_o^{\frac{-3}{2}} \end{aligned} \tag{1.11}$$

For $z_{LSS} = 1100$ and $\Omega_{tot} = \Omega_M = 1$ and $a_o = 1$ (today), we have

$$\theta(L = H(z = z_{LSS})^{-1}) \sim \frac{1}{2}(H_o^{-1} z_{LSS}^{-\frac{3}{2}})\, z_{LSS}\, H_o \sim \frac{1}{2} z_{LSS}^{-1/2} \sim 0.87^\circ \tag{1.12}$$

Using the approximation $l \sim 180/\theta$ to translate from degrees to multipole l, the first peak in the spectrum corresponds to temperature anisotropies at $l \sim 208$. An important assumption regarding the geometry of the Universe that has been made here is its flatness, i.e., $\Omega_{tot} = 1$. Thus the location of the first peak in the CMB temperature angular power spectrum constrains the geometry of our Universe and provides a very good test for its flatness.

At smaller angular scales ($l > 1000$), exponential damping caused by photon diffusion during decoupling wipes out the anisotropy signatures of the acoustic oscillations (Silk damping) [16], thus reducing the anisotropy power on scales smaller than the photon random-walk diffusion length. The scale of this damping effect is determined by the thickness of the surface of last scattering, i.e., the period of time over which decoupling occurs.

1.3.2 Secondary Anisotropies

After decoupling, non-linear gravitational and scattering phenomena give rise to a variety of additional temperature anisotropies [17]. Though the CMB photons start free-streaming to us from the last scattering surface, a fraction of these will scatter again on their way to our detectors from intervening ionized matter between us and the CMB. Phenomena like reionization (the ultraviolet radiation from the first stars dissociating neutral hydrogen) and the Sunyaev-Zel'dovich effect (scattering by hot gas clouds containing electrons in galaxy clusters) [18] imprint signatures upon the CMB. Gravitational lensing imprints large scale structure. These effects are discussed below.

There are two components to the Sunyaev-Zel'dovich (SZ) effect: the thermal SZ (tSZ)

and the kinetic SZ (kSZ) effects. The tSZ is a non-thermal distortion of the CMB spectrum by inverse Compton scattering through free electrons in a hot intra-cluster gas cloud. The effect has a spectral signature:

$$\begin{gathered}\frac{\Delta B_\nu}{B_\nu} = h(x)\frac{\Delta T_{CMB}}{T_{CMB}} = h(x)f(x)y, \\ \text{where, } x = \frac{h\nu}{kT_{CMB}},\ h(x) = \frac{xe_x}{e^x-1},\ f(x) = x\frac{e^x+1}{e^x-1} - 4, \\ y = \int_{LOS} n_e \frac{kT_e}{m_e c^2}\sigma_T dl, \\ B_\nu(x) = 2kT_{CMB}\frac{\nu^2}{c^2}\frac{x}{e^x-1}\end{gathered} \tag{1.13}$$

where m_e, n_e, T_e are mass, number density and temperature of electrons, B_ν is the surface brightness, σ_T is the Thomson scattering cross section and the integral for the Comptonization parameter, y, is along the line of sight. A typical temperature of the hot intracluster gas is $\sim$5 keV with a range from $\sim$2 to 14 keV, and the central gas density is $\sim 10^{-3}$ electrons/cm^3. The Thomson scattering cross section is given by:

$$\sigma_T = \frac{8\pi}{3}\left(\frac{\alpha\lambda_c}{2\pi}\right)^2 \sim 6.6\times10^{-29} m^2 \tag{1.14}$$

where, α is the fine structure constant and λ_c is the Compton wavelength. Assuming average electron density $n_e \sim 10^{-3}$ cm^{-3}, a volume number density of clusters $\sim 10^{-6}$ h^3 Mpc^{-3} converted to a line-of-sight density $\sim 10^{-2}$ h Mpc^{-1} and typical cluster radius $\sim$1 h^{-1} Mpc, we arrive at a value of $\sim 1.7\times10^{-3}$ for the Comptonization parameter, y. At an observation frequency of 150 GHz, this yields a temperature anisotropy of the order of:

$$\left(\frac{\Delta T_{CMB}}{T_{CMB}}\right)_{tSZ} \sim -10^{-3} \tag{1.15}$$

A unique feature of the tSZ effect, in general, is that its strength is independent of the redshift of the cluster. In addition, conservation of number of photons implies that the tSZ has an easily distinguishable characteristic spectral signature with a decrement in energy at lower frequencies compensated by an increment at higher frequencies. Thus, a SZ survey has the potential to detect galaxy clusters above a given mass threshold without bias at high redshifts [19]. When combined with X-ray measurements of the cluster temperature and optical/infrared redshift data, it will produce an unbiased catalogue of galaxy clusters at a wide range of redshifts enhancing the scope of cluster cosmology.

The kSZ effect arises due to the scattering medium relative to the CMB rest frame. The scattered radiation experiences a Doppler shift, which causes a thermal distortion of the CMB spectrum given by:

$$\frac{\Delta B_\nu}{B_\nu} = h(x)\frac{\Delta T_{CMB}}{T_{CMB}} = -h(x)\frac{v}{c}\tau \tag{1.16}$$

where, v is the peculiar velocity of galaxies, and $\tau = \int n_e \sigma_T dl$ is the optical depth for Thompson scattering in the ionized medium. However, this temperature fluctuation is independent of frequency and is hence spectrally indistinguishable from other CMB fluctuations. The galaxies in rich clusters typically move with random peculiar velocities of ~ 750 km/s and those in poor clusters have peculiar velocities of ~ 250 km/s. Since rich clusters are less common, we assume $v \sim 600$ km/s, which yields a temperature anisotropy of the order of:

$$\left(\frac{\Delta T_{CMB}}{T_{CMB}}\right)_{kSZ} \sim -10^{-5} \tag{1.17}$$

The tSZ and kSZ effects are a result of processes operating over an intracluster scale $\sim$ 2 h^{-1} Mpc, with the clusters being spread over a range of redshifts, z. Cross-correlating CMB with large scale structure provides an exciting way to get around the spectral degeneracy of the kSZ signal with the CMB and extract useful information from the kSZ [20].

On their way to us, the CMB photons are deflected many times through gravitational interactions with massive galaxy clusters, that results in a net deflection. In general, the deflection field can be written down as:

$$d(\hat{n}) = \nabla\phi(\hat{n}) \tag{1.18}$$

where ϕ is the line of sight integral of the gravitational potential from the observer to the surface of last scattering. Lensing smears out the acoustic peaks in the TT power spectrum. Measuring the deflection field allows a probe of the amplitude of matter fluctuations over a range of redshifts with particular sensitivity to z $\sim$ 2-4 providing insight into the distribution of dark matter. This measurement is sensitive to the sum of neutrino masses due to the suppression of small scale clustering caused by higher neutrino mass. Cross-correlation of the lensing signal with lower redshift optical lensing observations can improve constraints on the properties of dark energy and neutrinos.

A rough estimate of the angular scale at which the effect of gravitational lensing is expected can be made by noting that the angle β (in radians) by which a light ray grazing a massive object is deflected by its gravitational potential is given by $\beta = 4GM/Rc^2$. Assuming a typical cluster mass of 10^{14} h^{-1} M_s and size of 1 h^{-1} Mpc, we have $\beta \sim$4 arcseconds. As before for the SZ effect, we estimate the number of such clusters a CMB photon encounters along its line of sight from the last scattering surface to our detectors today to be ~ 100. This gives an approximate upper limit for the net deflection of a CMB photon to be ~ 6 arcminutes. This would correspond to a multipole index $l >\sim \pi/\theta_{rad} \sim 2000$ where the effect of lensing is expected to peak.

1.4 CMB Polarization

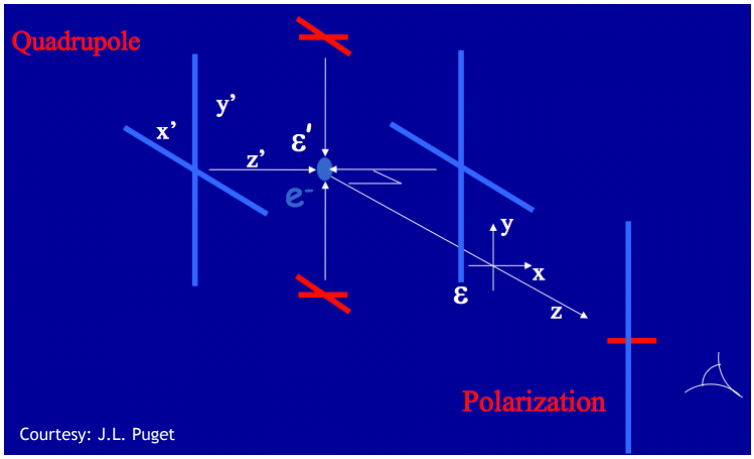

Figure 1.2: **Thomson Scattering** The schematic shows a local quadrupolar temperature anisotropy in the photons surrounding an electron. Photons are incident on the electron from two hot regions (to the left and right) and from two cold regions (up and down). The resulting scattered radiation has a net linear polarization in the vertical direction aligned with the cold axis of the quadrupole.

CMB polarization, unlike temperature anisotropies, arises from a single mechanism: a local quadrupolar temperature anisotropy in the photons around a scattering electron in the last scattering surface [21]. The total scattering cross section σ_T has a directional dependence [22, 23]:

$$\frac{d\sigma}{d\Omega} = \frac{3}{8\pi}|\hat{\varepsilon}_{in} \cdot \hat{\varepsilon}_{out}|^2 \sigma_T \tag{1.19}$$

where Ω_T is the total Thomson cross section and the unit vectors $\hat{\varepsilon}_{in}$ and $\hat{\varepsilon}_{out}$ are in the planes perpendicular to the propagation directions which are aligned with the incoming and outgoing linear polarization, respectively. The incident photons trigger oscillations of

the electron in the direction of the electric field of the photons. The scattered radiation intensity thus peaks in the direction normal to the incident polarization, with an outgoing net linear (only) polarization perpendicular (parallel) to the hot (cold) quadrupole axis (see Figure 1.2).

Polarized light is commonly described using the Stokes parameters. Since the CMB is linearly polarized, we only need the Stokes parameters Q and U. These depend on a choice of basis and measure the intensity difference between two orthogonal polarization directions, measured at each point on the sky, aligned with the basis directions (Q) or at 45° to them (U). Q and U transform as spin-2 variables. Hence the harmonic decomposition of polarization maps on the celestial sphere is written in terms of combinations of spin-2 spherical harmonics ${}_{\pm2}Y_{lm}$ as:

$$(Q \pm iU)(\theta,\phi) = \sum_{l,m} a_{lm}^{\pm2}({}_{\pm2}Y_{lm}(\theta,\phi)) \tag{1.20}$$

Though these Stokes parameters are a natural choice for measuring the polarization, their coordinate dependence makes them rather inconvenient for cosmological interpretation. Instead, linear polarization can be decomposed in terms of two scalar fields, E and B. Equation 1.20 can be written down as a sum of two distinct sets of harmonic modes [24, 25] :

$$\begin{aligned}(Q \pm iU)(\theta,\phi) &= \sum_{l,m} -(a_{lm}^{E} \pm i a_{lm}^{B})({}_{\pm2}Y_{lm}(\theta,\phi)) \\ = -\left(\sum_{l,m} -\frac{1}{2}(a_{lm}^{+2} + a_{lm}^{-2})({}_{\pm2}Y_{lm}(\theta,\phi)) \pm i \sum_{l,m} -\frac{1}{2i}(a_{lm}^{+2} - a_{lm}^{-2})({}_{\pm2}Y_{lm}(\theta,\phi))\right) \\ &= -(E(\theta,\phi) \pm iB(\theta,\phi))\end{aligned} \tag{1.21}$$

These so-called E and B-modes together form a coordinate independent complete basis for polarization maps. This decomposition is on the basis of parities. The even parity (symmetric) pattern is called the E-mode and the odd parity (anti-symmetric) pattern the B-mode.

The polarization auto power spectra and all possible cross-spectra between temperature and polarization are defined as:

$$\begin{aligned} C_l^{EE} = \langle a_{lm}^{E^*} a_{lm}^{E} \rangle \quad C_l^{BB} = \langle a_{lm}^{B^*} a_{lm}^{B} \rangle \\ C_l^{TE} = \langle a_{lm}^{T^*} a_{lm}^{E} \rangle \quad C_l^{TB} = \langle a_{lm}^{T^*} a_{lm}^{B} \rangle \quad C_l^{EB} = \langle a_{lm}^{E^*} a_{lm}^{B} \rangle \end{aligned} \tag{1.22}$$

However, because the B-modes have opposite parity from E and T, parity conservation demands that C_l^{TB} and C_l^{EB} vanish. The effect of secondary anisotropies generated after the recombination epoch, such as reionization, can significantly change the large-scale anisotropies and lead to non-vanishing TB- and EB-mode power spectra [26]. Since the primordial density perturbations are expected to be Gaussian, the above spectra along with C_l^{TT} specify the complete statistics of the primordial CMB temperature and polarization fields.

The local quadrupole in temperature that generates polarization can be sourced by two different physical processes: acoustic density oscillations resulting from primordial fluctuations in the curvature or the scalar component of the space-time metric [27], and inflationary gravitational waves resulting from tensor perturbations in the space-time metric [28] contraction/expansion space as they propagate. In the primordial plasma, the local quadrupole is initially suppressed as any polarization gets averaged out by successive rescatterings, keeping the photon field randomly polarized and isotropic in the rest frame of the electrons. As recombination proceeds, the rapid growth of the mean free path allows the local photon field to probe spatial variations and we only observe polarization from the last scattering event, at the end of recombination. The scale of the fluctuations we can observe is of the order of the mean free path of photons when the last scattering occurs and cannot be larger than the thickness of the last scattering surface. The same acoustic oscillations in the photon-baryon plasma that generate temperature fluctuations in the CMB also impart a polarization to the photons [27] in two different ways: the most common mode of producing a local quadrupole is photon diffusion between overdense (cold) and underdense (hot) regions (see Figure 1.3).

In addition, acoustic density oscillations create a local quadrupole from the Doppler shift due to the photon-baryon velocity field as the photons fall into the gravitational potential well formed by overdense regions. In the photon baryon fluid rest frame, the velocities of neighboring particles tend to diverge radially from and converge transversely to the scattering point when the fluid is accelerated from a hot spot to a cold spot. The reverse velocity scheme applies when the fluid is decelerated away from a cold spot. By Doppler shift, this induces a quadrupole flux anisotropy around the last scattering electron, leading to a radial polarization pattern in the first case and to a tangential polarization pattern in the second case (see Figure 1.4). The E-mode polarization at large scales ($l < 10$) arises from scattering during reionization rather than recombination because of the larger horizon size at these later times, providing an independent probe of the optical depth to reionization, τ.

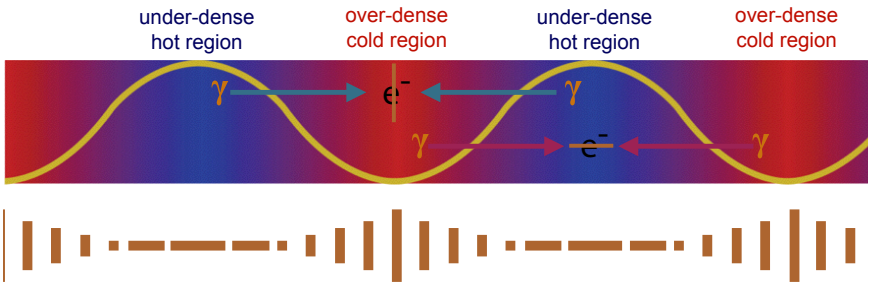

Figure 1.3: **A simplified illustration of the polarization patterns from photon diffusion between over-dense and under-dense regions** As a mode of wavevector undergoes compression (rarefaction), the photon-baryon fluid diffuses from hot crests (cold troughs) to cold troughs (hot crests). This motion is represented by the blue (red) arrows and produces a local quadrupole in the rest frame of a scattering electron with the hot (cold) axis parallel to the wavevector. The orientation of polarization of the scattered radiation represented by the brown bars is always parallel (perpendicular) to the wavevector, thus generating an E-mode pattern. B-modes are never produced by this mechanism. Figure inspired by [27].

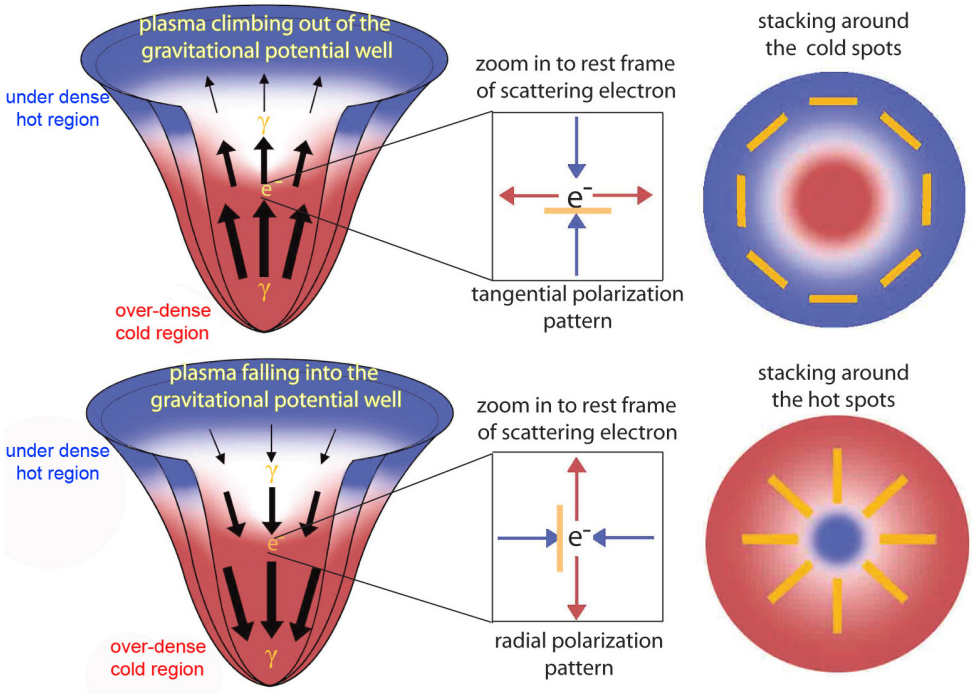

Figure 1.4: **A simplified illustration of the polarization patterns from velocity gradients** when the primordial plasma is accelerated towards an over-dense cold spot (bottom) or decelerated towards an under-dense hot spot (top). The black arrows in the left panel represent direction of fluid motion in the fluid rest frame with thicker arrows indicating higher velocity. The blue/red arrows in the center panel represent direction (converging/diverging) of fluid motion in the rest frame of the scattering electron. The orientation of polarization of the scattered radiation represented by the orange bars is parallel to the cold axis of the local quadrupole. Stacking on such local hot (cold) spots produces a pure radial (tangential) E-mode pattern around the center. B-modes are never produced by this mechanism.

Going back to the E and B mode patterns, a simple way to understand these is to consider a local intensity extremum. The wave vectors of the plane wave perturbations producing the intensity extremum are aligned along the radial direction towards the extremum center. Now an E-mode pattern is observed when the orientation of the polarization is either perpendicular or parallel to the wave vector, i.e., the polarization bars are oriented either in a tangential or a radial pattern around the peak, as is the case in Figures 1.3 and 1.4. A B-mode pattern, on the other hand, is observed when the polarization is oriented at 45 degrees to the wave vector or relative to rays emanating from the local extremum. A reflection of the sky about any line through the temperature extremum leaves the E-mode unchanged (even parity), while the B-mode changes sign (odd parity).

Till now, we have only seen how E-modes are generated. The only source of B-modes prior to decoupling is inflationary gravitational waves. Inflationary expansion generates a primordial spectrum of tensor perturbations which can be viewed as standing gravitational waves. The transverse contraction/expansion of space by a gravitational wave generates a quadrupole in the local photon field. Figure 1.5 illustrates how the intrinsic polarization of the gravitational waves leads to the generation of both E and B-mode CMB polarization patterns [29, 30]. The tensor E modes are generated by gravitational waves with plus (+) polarization while the tensor B modes are only generated by cross (x) polarization gravitational waves. The E-mode signal generated by gravitational waves is an order of magnitude smaller than that generated from scalar perturbations over comparable angular scales and will be difficult to detect. However, the B-modes in CMB polarization are a unique probe of long wavelength inflationary gravitational waves [31, 29], which would manifest as a characteristic peak near $l \sim 80$ in the BB power spectrum. The amplitude of this peak is directly related to the ratio (r) of the amplitude of tensor-to-scalar perturbations generated during inflation. Detection of these inflationary B-modes, often recognized as a "smoking gun" signature of inflation, will produce a confirmation of the same, providing a window into the first instants after the birth of our universe and enable us to probe quantum gravity and GUT scale physics a trillion times higher in energy than accessible to terrestrial particle accelerators. It will also provide a means to test specific inflationary models. This signal, though, is very weak compared to the unpolarized CMB and the dominant E-mode polarization signal. B-mode patterns may also have been created during the epoch of reionization, which would produce a similar peak, but near $l \sim 10$. Though there are several ongoing experiments targeting the B-mode "recombination peak", there are only a few planned experiments (e.g. CLASS [32], PIPER [33]) that will be capable of measuring the B-mode power spectrum over angular scales encompassing both the "recombination peak" at $l \sim 80$

and the "reionization bump" at $l < 10$.

Further, the late-time distortion of scalar E-modes by gravitational lensing from intervening large scale structure could convert some E-mode power to B-mode power (in addition to smearing out the acoustic peaks in the EE power spectrum), which would dominate the inflationary gravitational wave signal, though at higher multipoles, $l > 100$, with an envelope that roughly traces the shape of the scalar E spectrum [34]. The detailed mapping of these lensing B modes could allow separation of a primordial B mode signal down to a minimum detectable inflationary energy scale of $\sim 10^{15}$ GeV [35]. In addition, it will also allow accurate reconstruction of the lensing potential field, offering a powerful probe of the dark matter- and dark energy-dependent growth of structure. This could help constrain the neutrino mass [37] and, using cross-correlation with the ISW effect, test properties of the dark energy [38]. Hence the decomposition of CMB polarization into E and B modes is of special cosmological significance.

It is clear that the CMB temperature and E mode polarization anisotropy should be correlated at some level, because they are sourced by the same scalar density perturbations [39]. However, the peaks of the EE spectrum are 180° out of phase with those of the TT spectrum because, unlike temperature, the polarization amplitude scales with the velocity of the fluid rather than the density. Since the velocities at last scattering are the source of this CMB polarization, the acoustic peak structure of the EE spectrum captures the evolution of these velocities on different scales associated with the spatial Fourier modes of the wavevector. The tensor polarization spectra rise like the scalar EE spectrum at large angular scales. Gravitational waves behave like massless particles with $w = 1/3$. Hence, upon entering the horizon, their energy density decreased as a^{-4}. Thus, unlike the scalar modes that stabilized upon entering the horizon, the amplitude of the tensor modes were adiabatically damped going to smaller angular scales.

1.5 Status of Observations and Current Challenges

Over the last three decades, the CMB has been measured with increasing sensitivity at a large range of angular scales and frequencies, ushering in an era of precision cosmology. After the success of the COBE mission, the acoustic peak structure of the temperature anisotropy was confirmed in the late 90's and early 2000's by several balloon-borne and ground-based experiments operating from North America, Chile, and the South Pole such

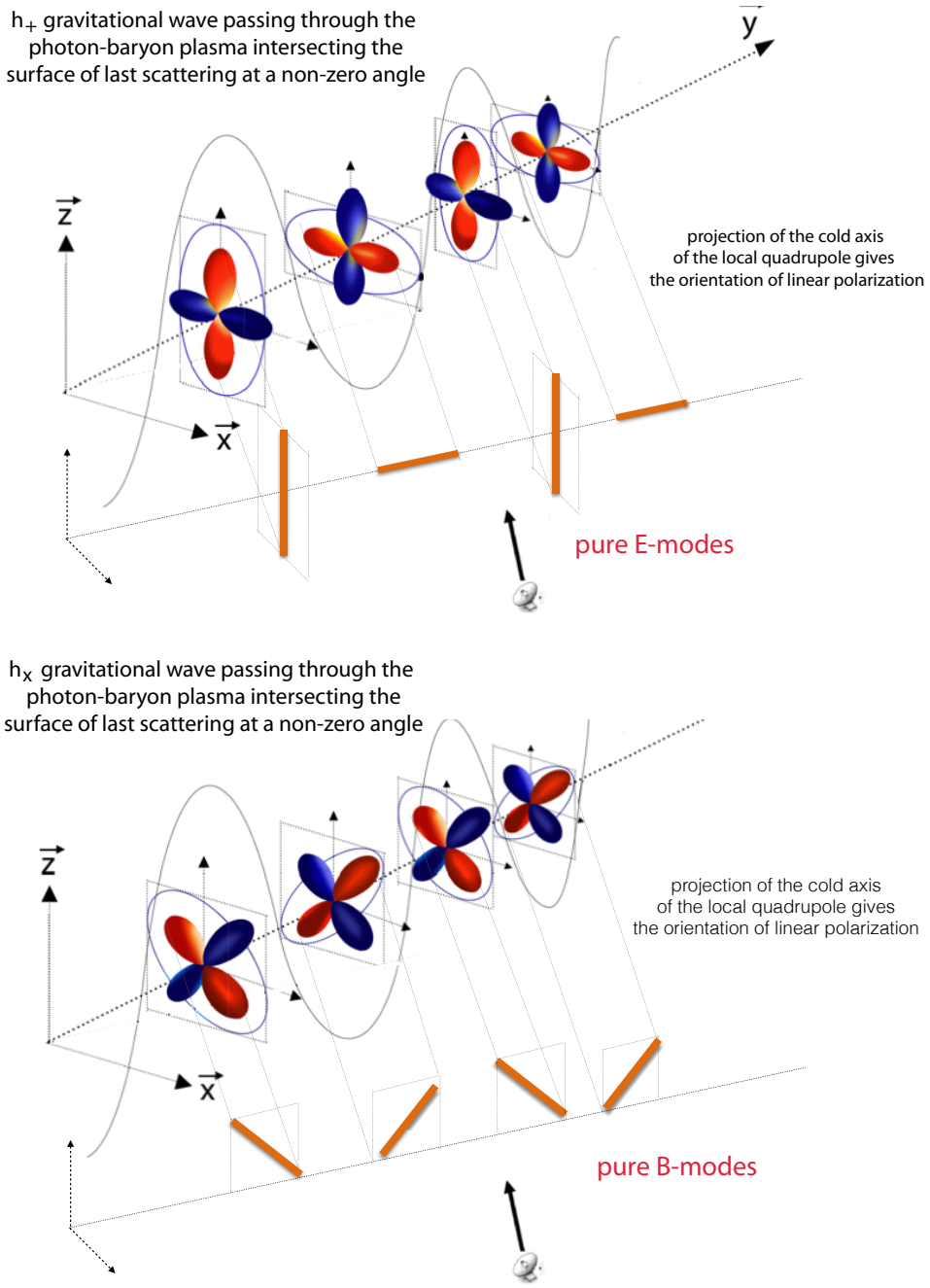

Figure 1.5: **A simplified illustration of the polarization patterns from tensor perturbations (gravity waves)** The transverse contraction/expansion of a standing gravity wave generates a local quadrupole in the photon intensity field that sources net linear polarization of the CMB photons scattered off electrons. The projection of the cold quadrupole axis (along the orientation of the red lobes) on the last scattering surface defines the orientation of the polarization. *top*: In the case of a gravity wave with intrinsic plus (+) polarization, the pattern (denoted by orange bars) is always perpendicular or parallel to the wavevector, generating pure E-modes. *bottom*: In the case of a gravity wave with intrinsic cross (x) polarization, provided the angle at which the wavevector intersects the last scattering surface is not 90° (otherwise no net linear polarization), the pattern is always oriented at $\pm 45°$ to the wavevector, generating pure B-modes. Figure inspired by [27, 36]

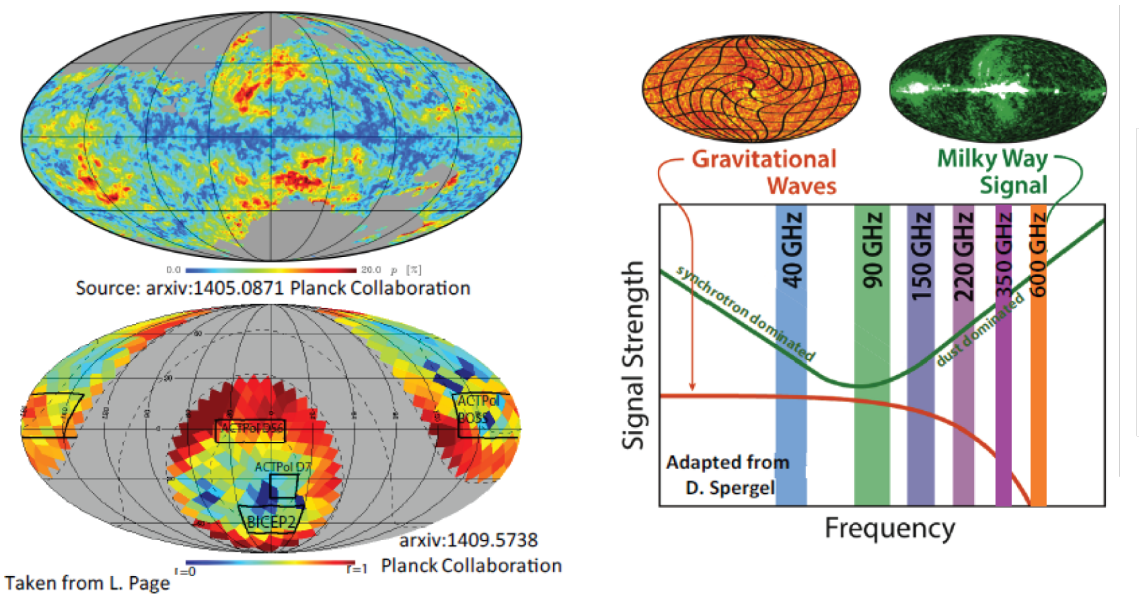

Figure 1.6: *Left top:* Planck map of the 353 GHz dust polarization fraction p at 1° resolution. The color scale is linear and ranges from 0% to 20%. The grey areas are where the dust emission is not dominant [61]. Figure courtesy: Planck Collaboration. *Left bottom:* Amplitude of polarized dust power from extrapolation of Planck 353 GHz data to 150 GHz, normalized by the CMB expectation for tensor-to-scalar ratio $r = 1$. [54]. Figure courtesy: Lyman Page. *Right:* Signal strength of the CMB B-mode polarization compared to galactic foregrounds as a function of frequency. Figure adapted from David Spergel.

as Saskatoon [40], MAXIMA [41], DASI [42], TOCO [43], and BOOMERANG [44]. Since then, the CMB temperature anisotropies have been well measured by a large number of experiments at both large and small angular scales. Full-sky measurements of the anisotropies were produced by the Wilkinson Microwave Anisotropy Probe (WMAP) [45] and Planck [46] satellites.

Current CMB experiments are focusing their efforts on observations of the polarized signal, which was first detected in the CMB by the DASI experiment [47] in 2002. While the E-mode power spectrum has now been extensively characterized down to very small angular scales by a number of experiments over the years from space (e.g. WMAP [45]) and ground (e.g. CAPMAP [48], QUAD [49], BICEP [50], QUIET [51, 52], SPTPol [53], and ACTPol [237]), the field has only recently entered the era of B-mode measurements. The B-mode signal, especially the primordial B-mode signature of inflationary gravitational waves, is very weak compared to the unpolarized CMB and the dominant E-mode polarization and even smaller with respect to instrumental and astrophysical contaminants. Further, it is comparable to the polarized Galactic synchrotron and dust foregrounds in the cleanest parts of the sky (see Figure 1.6). Even in the faintest dust-emitting regions there

are no "clean" windows in the sky where primordial CMB B-mode polarization measurements could be reliably made without subtraction of foreground emission [54]. It is thus necessary to map the sky in multiple carefully chosen spectral frequency bands in order to extensively characterize the foregrounds and subsequently allow the maps to be cleaned of foregrounds. This measurement requires excellent control over systematics and high sensitivity to integrate down to the required $\sim$nK scale.

The lensing B-mode signal has been detected in the last few years by the ACT, ACTPol [55], POLARBEAR [56], SPT, SPTPol [57], Planck [46], and BICEP/KECK [58, 59] collaborations. Figure 1.7 shows the current status of CMB measurements. While BICEP2 announced a detection of B-modes at scales relevant for the inflationary gravitational wave signal in 2014, it was later found to be consistent with foreground emission by a combined BICEP2, KECK, and Planck analysis [60]. The most recent BICEP2/KECK analysis in combination with the Planck high frequency dust maps currently place the most stringent limits on the tensor-to-scalar ratio with $r < 0.07$ [62].

1.6 The Atacama Cosmology Telescope Polarimeter (ACTPol) Experiment

Precision measurements of the primordial CMB temperature anisotropies by experiments such as WMAP [45], Planck [46], SPT [70], and ACT [71] have constrained the cosmological parameters of the ΛCDM model to high accuracy. However, there are still many aspects of the model that are not yet well understood, for example the nature of dark energy and dark matter, and properties of neutrinos. By measuring the primordial CMB temperature and polarization anisotropies at high l, ACTPol aims to constrain the number of neutrino species, the sum of the neutrino masses, the primordial helium abundance, and the running of the spectral index, n_s [68]. The primordial CMB temperature and polarization spectra, shown in Figure 1.7, are sensitive to each of these parameters at high l. A measurement of these signals provide an independent probe of the cosmological model and its parameters.

1.6.1 ACTPol Science Goals

In this section, we describe the ACTPol and Advanced ACTPol experiments; two experiments I worked on that are in the process of dramatically improving cosmological mea-

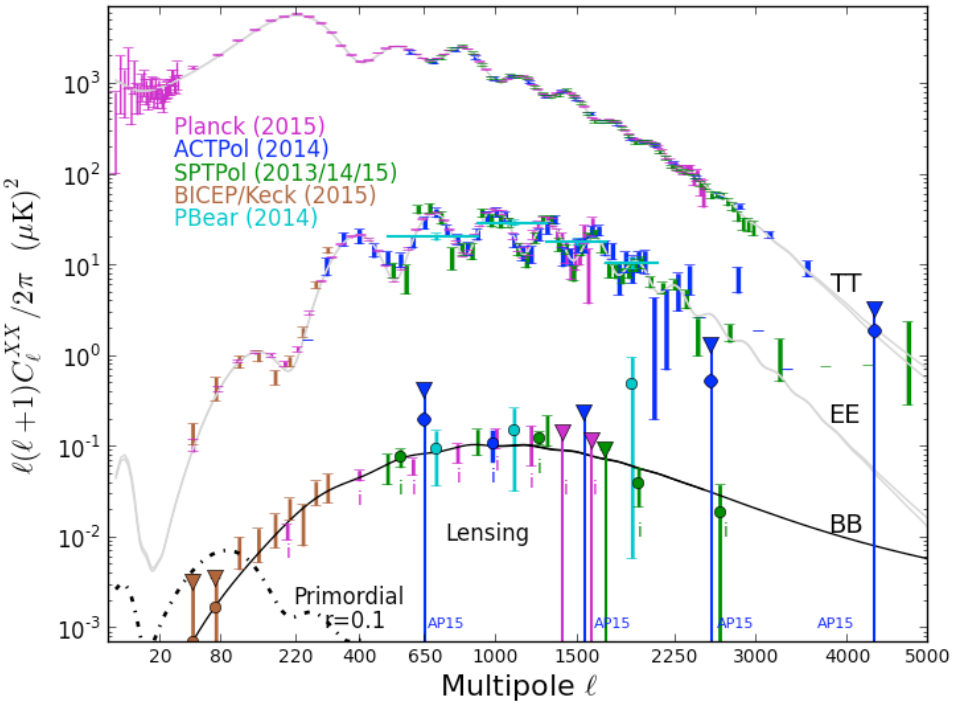

Figure 1.7: **Current status of CMB TT, EE, and BB anisotropy spectra measurements** as of May 2015. The CMB temperature (TT) anisotropy spectrum is shown for ACT, Planck, and SPT. The E-mode polarization (EE) anisotropy spectrum is shown for ACTPol, BICEP2/Keck Array, Planck, POLARBEAR, and SPTPol. Direct measurements of the B-mode polarization (BB) anisotropy spectrum are shown for ACTPol, BICEP2/Keck Array, Planck, POLARBEAR, and SPTPol. Indirect measurements of the BB signal, indicated with an 'i' below the data point, are shown for ACTPol, Planck, POLARBEAR, and SPTPol. Figure courtesy: Lyman Page.

surements with the CMB. ACTPol is designed to achieve high sensitivity at small angular scales, which makes it an ideal instrument for precision measurements of the secondary CMB anisotropies such as those induced by gravitational lensing and the tSZ and kSZ effects. The lensing measurements will enable probing the growth of structure, putting constraints on early dark energy [72, 38] and the sum of the neutrino masses [37]. The SZ measurements will lead to the discovery of many clusters [184], [73], probe dark energy [74] as well as help constrain the optical depth to reionization [20, 240]. Large sky accessibility from the ACT location opens up exciting avenues for cross correlating the CMB lensing, tSZ, and kSZ measurements with large optical surveys such as SDSS BOSS [75], increasing the statistical significance of the findings of each experiment alone. The optical surveys can in turn provide estimates of redshifts and masses of large numbers of ACTPol detected SZ clusters, broadening the scope for cluster cosmology.

1.6.2 The Atacama Cosmology Telescope

The Atacama Cosmology Telescope (ACT) is a six-meter off-axis Gregorian telescope located on Cerro Toco at an elevation of 5190 meters in the Atacama Desert in Chile. The site's high elevation and low atmospheric water vapor content (precipitable water vapor or PWV) are excellent for millimeter and sub-millimeter wavelength observations, with optimum observing during the Austral winter and spring between April and December, when the weather is the driest. ACT is neighbor to a number of millimeter and sub-millimeter observatories including Atacama Pathfinder Experiment (APEX) [63], Atacama Large Millimeter Array (ALMA) [64], POLARBEAR [65], Atacama B-Mode Search (ABS) [66], and Cosmology Large Angular Scale Surveyor (CLASS) [32].

The Atacama Cosmology Telescope Polarimeter (ACTPol) [67], the second generation receiver for the ACT telescope, is a polarization sensitive camera designed to make observations of the CMB anisotropies with arcminute resolution [68]. ACTPol can observe with up to three optics tubes cooled to cryogenic temperatures, each with its own polarization-sensitive transition-edge sensor (TES) bolometer detector array. The staged deployment of the ACTPol receiver started in 2013 with the first detector array, PA1; PA2 was added before the 2014 observing season began; and PA3 was added in 2015. PA1 and PA2 measure radiation in a band centered at 148 GHz, while PA3 features dichroic pixels that are sensitive to both 90 and 150 GHz bands simultaneously. Each of these arrays had $\sim$ 1000 detectors at its focal plane. In June 2016, PA1 was replaced by a dichroic high frequency

(HF) Advanced ACTPol (AdvACT) detector array [69], with higher detector packing density, simultaneously sensitive to the 150 and 230 GHz bands. The plan is to eventually replace all the ACTPol arrays with dichroic AdvACT arrays spanning five frequency bands in aggregate ranging from 25 to 280 GHz. AdvACT will have excellent angular resolution and increased polarization and temperature sensitivity aided by almost a two-fold increase in the number of detectors per array relative to ACTPol in the respective frequency bands.

1.6.3 Sky coverage and Scan strategy

ACT's mid-latitude location at 23°S provides access to the majority of the southern sky and a portion of the northern sky from 73°S to 27°S for a total of $25,000$ deg^2 which is $\sim 60\%$ of the sky. This allows overlap with a number of other astronomical surveys at a range of wavelengths enabling a broad set of cross-correlation studies that are key to the ACTPol and AdvACT science program. The systematic effects caused by elevation dependent atmospheric airmass variation that modulates the instrumental gain and optical loading of the bolometric detectors are avoided by scanning the ACT telescope in azimuth at a fixed elevation. The elevation is stepped between scans to follow the motion of the target on the sky, typically between 30° and 60°. Each target is observed both as it rises in the east and again as it sets in the west. This cross-linking scan strategy allows each field to be observed at multiple parallactic angles, which is important for minimizing scan related systematic effects such as striping in the maps.

Two types of survey strategies, '*wide*' and '*deep*' have been implemented with ACTPol. The deep observing strategy targeted four 70 deg^2 regions (see Figure 1.8) for very high sensitivity observations during Season 1 (2013) of ACTPol operation. These deep fields are near the equator and spaced a few hours apart, enabling rising and setting observations of the different regions to be interspersed. The wide observing strategies implemented in Season 2 (2014) and Season 3 (2015) cover a total of ~ 4000 deg^2 (see Figure 1.8) and primarily overlap with the SDSS Baryon Oscillation Spectroscopic Survey (BOSS) and other equatorial observations. Southern regions with lower galactic foreground emission have also been observed, especially during the daytime when the Sun traverses the equatorial fields. The data and results from Season 1 have been published [237], while the analysis of the subsequent data is underway.

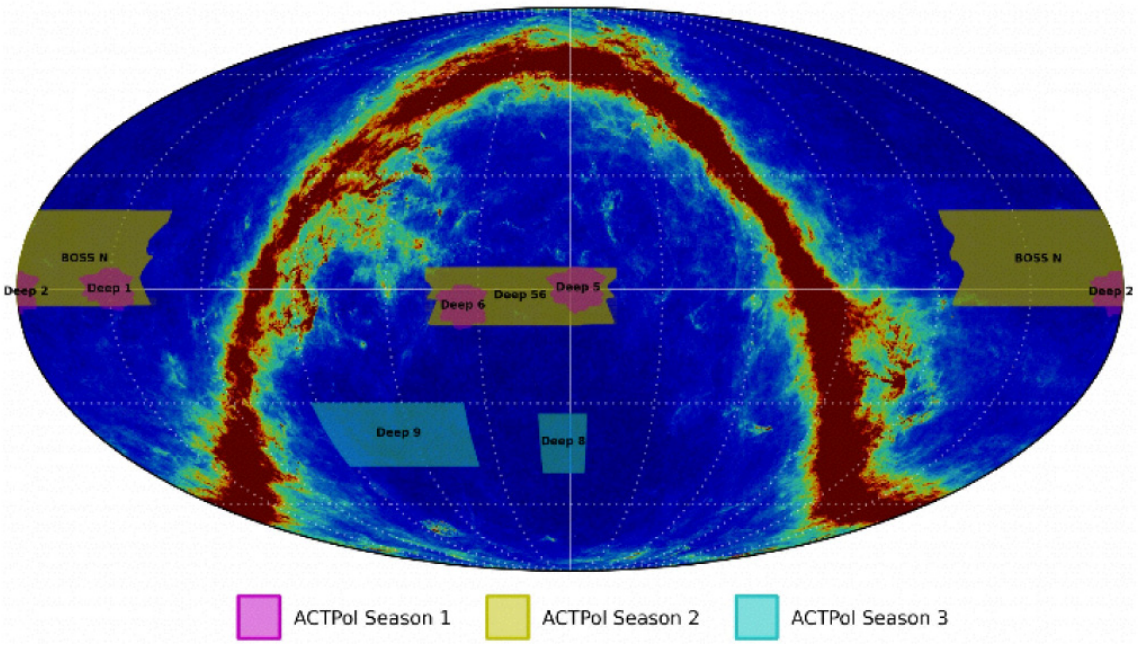

Figure 1.8: Map of the sky at 353 GHz. The deep and wide patches surveyed during the 2013 (S1), 2014 (S2), and 2015 (S3) seasons by ACTPol are indicated. More than half the sky is accessible to ACTPol. Overlapping surveys include SDSS, BOSS, CFHTLS, XMM-XXL, Herschel, HSC, DES, GAMA, and KiDS. Figure courtesy: ACTPol Collaboration

1.6.4 Optics

The design of the telescope mirrors was optimized to achieve diffraction limited performance across a $\sim 1^\circ$ field of view (FOV) at $\sim$arcminute resolution, best implemented with ellipsoidal primary and secondary mirrors of 6 and 2.5 meters diameters, respectively. The off-axis design of the telescope mirrors ensures that the primary mirror is unobstructed by the secondary, while the 5.2 m focal length of the telescope allows for a compact design. The angular resolution of ACT is approximately determined by the observing wavelength and the mirror diameter, according to the relation $\theta = 1.22\lambda/D$, which for the 6 m primary mirror corresponds to 1.4 arcminutes for 150 GHz and 2.3 arcminutes for 90 GHz. The major components of the telescope are shown in Figure 1.9. The primary and secondary mirrors are composed of 71 and 11 adjustable aluminum panels, respectively. In order to shield the optics of the telescope from warm radiation from the local environment, the mirrors are surrounded by an inner ground screen that moves with the telescope during scanning, and an outer, stationary ground screen. A climate-controlled receiver cabin is situated underneath the primary and secondary mirrors. A more thorough discussion of the telescope optical design can be found in [76, 77, 78].

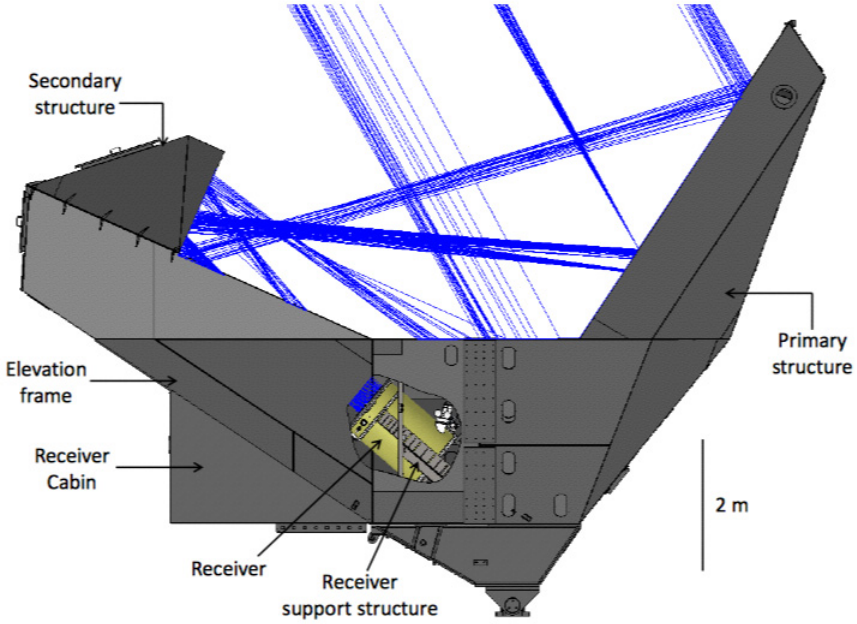

Figure 1.9: Ray trace of ACT primary and secondary mirrors up to the entrance of the receiver. The major components of the telescope upper structure are shown, except for the inner ground screen and part of the receiver cabin wall, which have been removed for clarity. The telescope is shown in its service position (where the receiver cabin floor is level), corresponding to a viewing elevation of 60°. Figure courtesy: R. J. Thornton [104]

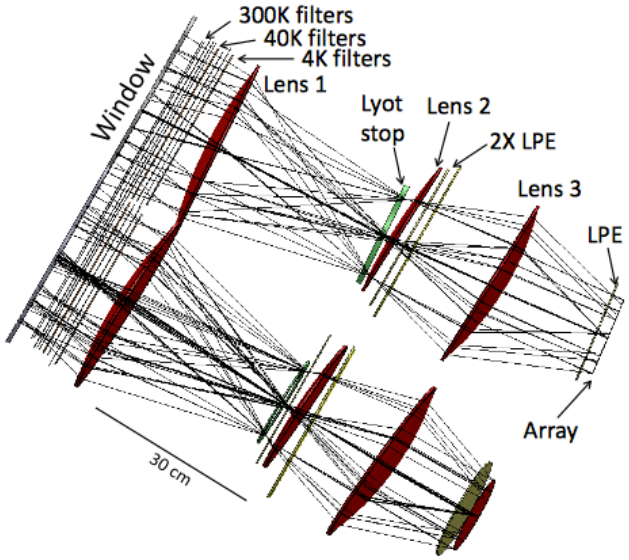

Figure 1.10: Ray trace of the cold optics. The upper trace shows the PA3 (multichroic) optical path and the lower trace shows the PA1 path. The PA2 optical path is a mirror image to that of PA1 and has been removed for clarity. The various filters, lenses, lyot stop and detector array are labelled. Figure courtesy: R. J. Thornton [104]

The ACTPol receiver contains three separate optical tubes with a $\sim$ kilo-TES array of Transition Edge Sensor (TES) bolometer detectors at the focal plane of each. Each of these tubes contains its own set of cryogenic, refractive optics comprising a set of three silicon lenses which re-image a portion of the Gregorian focus of the mirrors onto the corresponding detector array. To ensure high optical transmission, the lens surfaces have a simulated-dielectric anti-reflection coating [79] (see Chapter 2). The optical elements of the ACTPol receiver also include the vacuum window, the Lyot stop, and a set of thermal blocking and band-defining filters (see Figure 1.10). The first lens forms an image of the primary mirror on a 1 K cold aperture stop, or Lyot stop, which defines the mirror illumination and terminates the sidelobes of the detector beams. The second and third lenses refocus the image of the sky onto the detector arrays. The thermal radiation load on the cold stages of the receiver is reduced through the use of reflective IR blocking filters on the 300 K, 40 K, and 4 K stages, while the upper edge of the band pass in each optics tube is defined by a series of low pass metal mesh filters mounted on the 40 K, 4 K, 1 K, and 100 mK stages. Multiple such low pass filters are needed to attenuate harmonic leaks from the proceeding filters. Both the IR blocking filters and metal mesh filters are designed and manufactured at Cardiff University [80]. Each of the three vacuum windows of the cryostat is made from a 320 mm diameter disk of 6.4 mm thick Ultra High Molecular Weight Polyethylene (UHMWPE), which can sustain the vacuum pressure differential. A quarter wavelength thick layer of expanded teflon is applied on each window as an anti-reflection coating. A schematic of the optical path showing the optical components for each array type is shown in Figure 1.10.

1.6.5 Cryogenics

The cryostat which houses the cryogenic optics of the ACPol receiver is mounted in a climate controlled cabin below the primary and secondary mirrors. It contains the three independent optics tubes which house the three detector arrays. This modular design allows each array and its corresponding optical components to be deployed independently without requiring any disassembly of previously fielded optics tubes.

The ACTPol cryostat vacuum shell, which is shown in Figure 1.11, was constructed by Precision Cryogenics [81]. It is roughly 1.1 m in diameter and 1.5 m long. There are four temperature stages in the cryostat, 40 K, 4 K, 1 K, and 100 mK. The 40 K and 4 K stages are cooled using a Cryomech PT410 pulse tube cooler. The components operated at

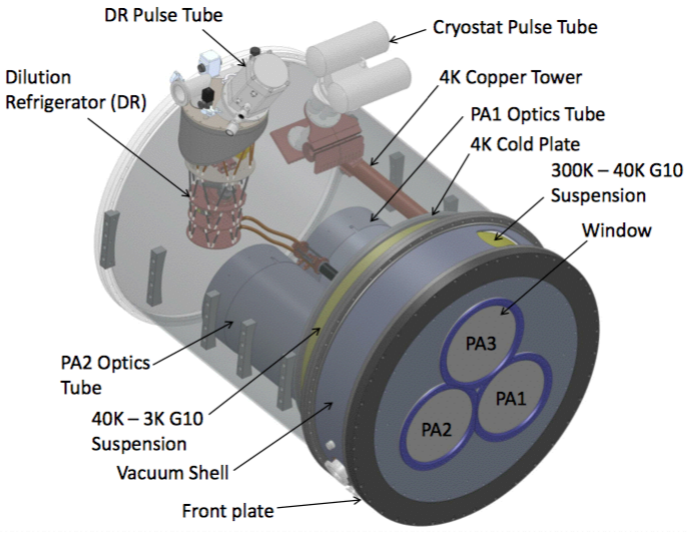

Figure 1.11: Model of the as-built cryostat. The length of the cryostat is 1.5 m. The PA3 optics tube and most of the radiation shields have been removed for clarity. A combination of flexible copper sheets and copper braid are used to reduce vibrational coupling between the pulse tubes and internal cryostat components. Figure courtesy: R. J. Thornton [104]

these temperatures include the first lens and the filter stacks which are mounted behind the window aperture. A dilution refrigerator, backed by its own pulse tube and manufactured by Janis Cryogenics [82], helps achieve the colder stages, at 1 K and 100 mK. The 1 K stage cools the Lyot stop, the remaining two lenses, two low pass filters, and the final stage of SQUID amplifiers for detector readout. The 100 mK stage, or mixing chamber plate of the dilution refrigerator, cools the detector arrays and a portion of their readout circuitry as well as the final low pass filter.

The total cooling time to reach the 100 mK base temperature with all three optics tubes installed is around 14 days. The majority of this time is needed to cool the significant thermal mass inside the cryostat to the base temperature of the pulse tube stages. The final cooling steps, in which the ^{3}He-^{4}He mixture is condensed by the dilution refrigerator, require around five hours to bring the arrays to their operating temperature. The dilution refrigerator also allows for 24-hour-a-day observations and is typically run through a thermal cycle once a month.

1.6.6 Detector Arrays

The ACTPol camera consists of three superconducting detector arrays, two with sensitivity to 148 GHz radiation (PA1 and PA2) and one dichroic array with simultaneous 90 and 150 GHz sensitivity (PA3). The 150 GHz arrays have a total of 512 pixels each while the dichroic array is populated with 255 pixels.

For each array, the incident radiation is coupled onto the detectors via a monolithic feedhorn array assembled by stacking twenty-five 500 μm thick etched and gold-plated silicon wafers of 150 mm diameter each. This approach enables precision corrugations, dense detector packing, and thermal matching to the silicon detector wafers [83]. The detectors are fabricated on monolithic three-inch silicon wafers at the National Institute of Standards and Technology (NIST), Boulder. Each pixel in an ACTPol array is composed of an Ortho-Mode Transducer (OMT) [84] coupled to a pair of transition edge sensor (TES) bolometers via superconducting microwave circuitry. The planar OMT is coupled to a waveguide input and a quarter-wave backshort. The two pairs of probes on the OMT separate the incident radiation into two perpendicular polarization signals [85]. These signals are then transmitted on niobium transmission lines through microwave circuit elements and the signals from the opposite OMT probes are combined and sent to a TES island where the power is deposited via a lossy gold meander termination [86]. As the island heats relative to the bath temperature, a molybdenum-gold bilayer, which has been biased onto its superconducting transition, responds with a change in resistance. The steep resistance versus temperature dependence of the superconductor enables very sensitive measurements of incident power. A very good review of the various detector architectures employed today for CMB measurements can be found in [88]. The design and operation of the ACTPol detectors will be discussed in further detail in Chapter 3.

1.6.7 Readout

The detectors are read out using three stages of Superconducting QUantum Interference Device (SQUID) amplification in a Time Division Multiplexing (TDM) scheme [89, 90, 91]. A SQUID is an extremely sensitive magnetometer composed of two superconductors separated by thin insulating layers which form a pair of Josephson junctions. The output of a SQUID amplifier is a voltage that is periodic in the magnetic flux through it. By coupling the SQUID magnetometer to an inductor in series with the TES, the SQUID can be operated as a sensitive ammeter. In order to operate the SQUID as a linear amplifier, such that

$V_{SQUID} \propto I_{TES}$, a Flux Locked Loop (FLL) readout technique is employed where current is applied to a feedback coil to maintain the SQUID in the linear regime. The required feedback current is then used as a measure of the fluctuations in TES current. Readout of a SQUID amplifier operated as a FLL without multiplexing requires a total of four wires for the bias and feedback lines. Therefore, an array of $\sim$ 1024 TES detectors would require $\sim$ 4096 wires to be heat sunk on the cold 100 mK cryostat stage, amounting to an unacceptable thermal load. The number of wires required for readout is dramatically reduced to a mere 64 in the TDM scheme which allows multiple SQUIDs to share bias and feedback lines.

1.7 The Advanced ACTPol (AdvACT) Experiment

AdvACT [69] is an ongoing upgrade of ACTPol's three existing detector arrays and their optics, staged over three years. It will reuse ACTPol's dilution refrigerator cryostat, while replacing the filters and lenses in the optics tubes with upgraded ones optimized for the AdvACT arrays. AdvACT will deploy four new multichroic arrays, one of which has recently been deployed (see Chapter 3). The plan is to map approximately half of the microwave sky in five frequency bands spanning from 25 GHz to 280 GHz. In addition to extended spectral coverage, AdvACT will have excellent angular resolution (expected: 1.4' at 150 GHz, 7.1' at 28 GHz), and increased polarization and temperature sensitivity as a result of roughly doubling the number of detectors per array in the mid- and high-frequency optical bands relative to ACTPol, enabled by advancements in detector and readout technology. Polarization systematics and low-frequency receiver noise will be controlled with the use of ambient temperature continuously rotating metamaterial silicon half-wave plates (HWPs), which will modulate the incoming polarized signals at $\sim$8 Hz, improving access to the large angular scale signals expected from inflation.

1.8 Outline of this Thesis

In Chapter 2 of this thesis, I present the design and development of large aperture wide bandwidth anti-reflection coatings for silicon optics. The increasing scale of cryogenic detector arrays for sub-millimeter and millimeter wavelength astrophysics has led to the need for large aperture, high index of refraction, low loss, cryogenic refracting optics. Silicon with a high index of refraction, low loss, and relatively high thermal conductivity is a nearly optimal material for these purposes, but requires an antireflection (AR) coating with broad

bandwidth, low loss, low reflectance, and a matched coefficient of thermal expansion. The coatings described reduces the reflection per optical surface from $\sim 30\%$ (for uncoated silicon) to $< 1\%$ across the detector bands and helps boost the sensitivity of the instrument. This represents the first large scale application of metamaterials for CMB research.

The development of a new polarization sensitive dichroic detector array designed to increase the sensitivity and enable high precision measurements of CMB polarization is presented in Chapter 3. The detector architecture for the ACTPol 90/150 GHz dichroic array deployed in 2015 is described and advancements in detector technology for the Advanced ACTPol (AdvACT) camera are discussed. AdvACT will be a staged upgrade to ACTPol over three years from 2016 to 2018 with new multichroic detector arrays, spanning from 25 GHz to 280 GHz in five frequency bands, replacing the existing ACTPol arrays. In Chapter 4, I describe a method to measure the passbands of deployed detectors and present the preliminary passbands of the deployed ACTPol dichroic polarimeter array. This receiver represents the first multichroic detector array deployed for a CMB experiment and is currently the most sensitive ACTPol array with a preliminary sensitivity of $< 10\ \mu K\sqrt{s}$.

In Chapter 5, I present a study of the diffractive far-sidelobes resulting from gaps between the panels that constitute the ACT primary mirror. Estimates of ground pick-up and contamination through these sidelobes are presented. The arcminute resolution of ACTPol means that many thousands of galaxies are detected as point sources in the ACTPol CMB temperature maps. The ACTPol flux measurements of these sources compared with data at radio frequencies can help distinguish between synchrotron and dusty sources. The astrophysically interesting sources can then be followed up by high resolution radio telescopes like ALMA. An investigation of such point sources and their polarization properties is presented in Chapter 6, and their impact on the estimation of the E-mode polarization power spectrum is discussed. This ongoing study will clarify the upper limit in terms of multipole l for obtaining reliable measurements of the E-mode power spectrum in the presence of unresolved point sources. E-mode polarization measured with high accuracy to fine angular scales (high l) could constrain the running of the spectral index of the density perturbations produced during inflation and the effective number of neutrino species.

The next few years will be really exciting for the CMB community with prospects of making tremendous progress towards answering many of the yet unanswered questions in cosmology. I conclude with a brief note on the early science results from ACTPol and

discuss the applicability of the technical developments presented in this thesis towards future CMB experiments.

CHAPTER 2

Large-aperture wide-bandwidth meta-material anti-reflection-coatings for millimeter wavelengths

In this chapter, I present a new method of antireflection (AR) coating silicon lenses that constitute the ACTPol cold refractive reimaging optics. Silicon with a high refractive index is a natural choice for the lens material, but requires an AR coating to mitigate the $\sim$30% reflection from a silicon surface. I describe in detail the approach adopted for designing these coatings, present the designs along with the manufacturing tolerances, describe the fabrication process, and show reflection measurements from the AR-coated lenses. Also presented are measurements of the optical properties of silicon at millimeter wavelengths at cryogenic and room temperatures. This coating and lens fabrication approach is applicable from centimeter to sub-millimeter wavelengths and can be used to fabricate coatings with greater than octave bandwidth.

2.1 Introduction

The development of large format superconducting detector arrays for millimeter and sub-millimeter astrophysics (e.g. [92, 93, 94]) has driven the need for high-throughput optical designs that maintain diffraction limited performance across the arrays (see [95] for a review). Silicon is an excellent material for these applications due to its high index of refraction ($n = 3.4$), low loss-tangent [1] ($\tan\delta < 7 \times 10^{-5}$), and a relatively high thermal conductivity. The essential development that was required to realize optical designs using silicon optics at millimeter wavelengths was an appropriate anti-reflection (AR) coating to

[1] loss-tangent ($\tan\delta$) is used to parametrize a dielectric material's inherent dissipation of electromagnetic energy. It is defined as the ratio of the resistive (lossy) component of an electromagnetic field to its reactive (lossless) counterpart

mitigate the 30% (-5 dB) reflective loss from each optical surface. In this chapter I describe the solution we developed to drastically reduce this reflection.

AR coatings [96] consist of one or more dielectric layers placed on the surface of refractive optical elements. The index of refraction and thickness of the AR layers are chosen such that the reflections from the vacuum-AR interface and from the AR-substrate interface interfere and cancel. If the optical path length through a single layer AR coating is one quarter wavelength, the refractive index of the coating is $\sqrt{n}$ (where n is the index of the substrate), and the coating is free from dielectric losses, the cancelation is perfect at one particular frequency. Applied to silicon, such quarter-wave coatings reduce reflections below 1% over 1.25:1 bandwidth at normal incidence. Lau et al. [97] demonstrated a quarter-wave coating for silicon using a polyimide (Cirlex) layer.

Wider bandwidths and larger ranges of angles of incidence can be accommodated by adding additional layers to the AR coating to form a multi-layer coating. These coatings require layers with a number of different refractive indices. Cryogenic applications require that the coefficient of thermal expansion of the AR layers also be sufficiently matched to that of the lens substrate to prevent damage upon cooling. The dielectric loss and birefringence of the AR coating material must also be carefully controlled. Locating materials with these properties poses a significant challenge to implementing cryogenic wide band AR coatings for silicon. One avenue to solve this problem is to engineer materials with the required dielectric constant by cutting sub-wavelength features into the lens surface [98, 99]. Engineered optical materials with properties determined by their detailed geometric shape, size and orientation are referred to as artificial dielectrics or metamaterials. This can be contrasted with random dielectric mixtures which achieve their desired properties through control over their detailed composition [100].

Simulated dielectric metamaterial AR coatings consist of layers of sub-wavelength holes [101, 32], posts, or grooves [102] cut into the substrate to be coated. This approach allows the index of the AR coating to be precisely tuned by adjusting the geometry of the machined features, naturally solves the thermal expansion problem, and has loss lower than that of the substrate. At cryogenic temperatures silicon has a dielectric loss tangent ~ 100 times lower than typical plastics like Cirlex, which have previously found use as antireflective coatings [97]. The advantages of silicon metamaterial AR coatings include precisely controlled indices of refraction, inherently matched thermal expansion, and significantly reduced dielectric losses.

This approach has been successfully applied to plastic millimeter wave optics through direct machining and silicon optics for visible wavelengths through patterning of geometric structures which perform as a AR coating similar to that found on a moth's eye[103, 104, 105]. At millimeter wavelengths Zhang et al. [106] fabricated an alternative class of simulated dielectric AR for silicon composed of metal resonant structures supported by a plastic substrate that had higher losses than the coating described here. Schuster et al. [107] fabricated single layer silicon micro-machined artificial dielectrics and Han et al. [108] have used silicon immersion grating technology to fabricate planar artificial dielectrics for THz radiation. Our work is the first demonstration of a broad-bandwidth metamaterial AR coating on silicon optics with finite curvature for millimeter wavelengths.

The AR coated lenses presented here were developed for the ACTPol experiment, described briefly in the previous chapter. In Section 2.2 we present the design requirements for the ACTPol optics as they apply to this work. The design of the coating is described in Section 2.3. In Section 2.4 we describe the ACTPol lens design. Cryogenic measurements of the dielectric properties of silicon samples taken from 45 cm diameter ingots at millimeter wavelengths are presented in Section 2.5. In Section 2.6 we describe the fabrication process of the coating on the lenses and present reflection measurements of a finished lens. The tolerance of the design to various possible manufacturing errors are discussed in Section **??**. As an aside, we discuss the AR coating being used for the plastic vacuum windows in the ACTPol cryostat in Section **??** and possible approaches to come up with a better coating over wider bandwidths. We conclude with a brief discussion of the range of applicability of this coating technique.

2.2 Requirements

The performance requirements for the AR coated silicon lenses described in this work are dictated by the scientific goals of the ACTPol project [68]. This instrument is designed to detect the faint polarized signals from the cosmic microwave background using three detector arrays fed by independent re-imaging optics [77]. Two of the arrays are horn coupled polarimeters for the 150 GHz band (passband from 125 to 165 GHz), while the third array will be a multichroic array including both 150 GHz and 90 GHz bands ('90 GHz' passband from 75 to 110 GHz) [85]. Extensive design studies demonstrated high index of refraction ($n \gtrsim 3$) lenses were needed to achieve high optical quality across the required field of view.

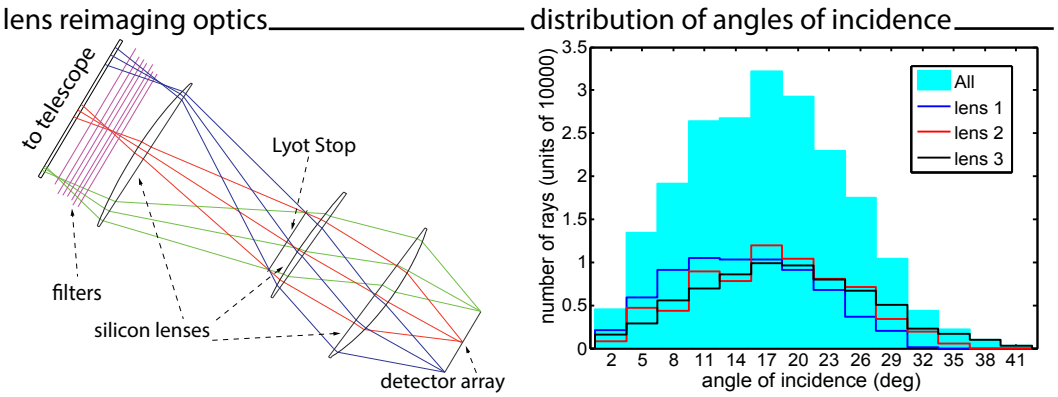

Figure 2.1: *Left:* A ray diagram of one set of ACTPol re-imaging optics, which includes three silicon lenses feeding a detector array. The AR coating developed here is optimized for this lens design but could be applied to a variety of similar problems in millimeter wave optics. *Right:* A histogram of the angles of incidence of rays at the surfaces of these three silicon lenses.

The left panel of Figure 2.1 shows the re-imaging optics for a 150 GHz array. The optics include three plano-convex silicon lenses with diameters up to 33.4 cm. The figure shows that rays passing through the optical system refract over a wide range of angles of incidence. This is quantified in the right hand panel of Figure 2.1 which shows that the distribution of angles of incidence is centered near 17° and that more than 96% of the rays have angles of incidence $< 30°$. This sets the requirement that the coatings must be optimized to minimize reflections for angles of incidence between 0° and 30°.

Since ACTPol is a polarization sensitive experiment, low cross-polarization is another requirement. Studies of polarization systematics (e.g., [109]) suggest that the CMB temperature to polarization leakage must be controlled to better than 1% which corresponds to a requirement that differences in the transmission for the two polarizations be 0.5%.

To reduce the thermal emission, all optics are cooled to 4K or below. Thus the AR coating must be able to withstand cryogenic cycling. As described in Section 2.5 high resistivity silicon which is available in boules up to 45 cm in diameter, offers a cryogenic loss tangent $\tan\delta < 7\times10^{-5}$, an index of refraction of $n = 3.4$, and a relatively high thermal conductivity making it an ideal material for this optical design. Our approach of directly machining metamaterial AR coatings into the lens surfaces guarantees that the coatings have low dielectric losses and coefficients of thermal expansion that are inherently matched to that of the silicon lenses.

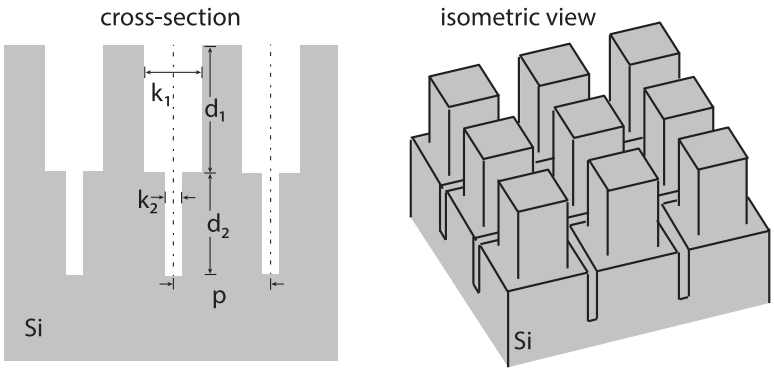

Figure 2.2: The geometry of the two layer metamaterial AR coating. The left side shows a cross section through the center of the pillars indicating the design parameters discussed in the text. The right side shows an isometric view of the structure resulting from making cuts along two perpendicular directions. In both drawings grey represents silicon and white represents vacuum.

We next describe the steps involved in the design of the coatings for the 150 GHz band lenses. These coatings are conceptually similar to those for the broader-band multichroic lenses, and I will comment on these later.

2.3 AR Coating Design

The AR coating for the ACTPol 150 GHz PA1/PA2 lenses is comprised of two metamaterial layers. Each layer consists of an array of square pillars on a square grid cut using silicon dicing saw blades by making two sets of parallel trenches rotated 90° relative to each other. It has been shown that any electromagnetic structure with an axis of n-fold (n>2) rotational symmetry must have polarization independent reflectance and zero cross-polarization when light is incident along this axis [110]. Hence the 90° rotational symmetry of this coating leads to zero cross-polarization at normal incidence and low birefringence for oblique incident angles. Figure 2.2 shows a cross-section and top view of this geometry which is parameterized by the depths d_1, d_2, and kerf widths k_1, k_2 of the outer and inner layer respectively and a pitch p. The outer layer is cut by using a blade of width k_1 and the inner layer is cut by making a second set of cuts to greater depth with a thinner blade of width k_2. We introduce the volume fill factor $v_f = (1 - k/p)^2$ to facilitate comparison to published analytic calculations based on the second order effective medium theory developed by Rytov [111] for the effective dielectric constant in the quasi-static limit ($p << \lambda$) [105, 112, 113, 114].

The metamaterial layers can be treated as a volume distribution of small electromagnetic scatterers characterized by electric and magnetic polarizability densities [98]. When the pitch is small compared to shortest wavelength of interest, the fields in the layer are homogenous [99] and one can define an effective dielectric constant which can be used to parameterize the propagation properties of the media. This effective dielectric function for the layer, ε_r^{eff}, is a function of the density of scatterers in the layer [115, 116], parametrized by the volume fill factor. As the feature size of a composite media approaches a significant fraction of the radiation wavelength the effective dielectric function becomes frequency dependent [117]. As the wavelength is further reduced the artificial dielectric structure no longer appears homogenous and these simple quasi-static considerations must be augmented to adequately model its behavior. In going beyond the quasi-static limit resonant effects, diffraction and scattering can occur in the artificial dielectric structure [101, 118, 119, 120]. The coatings described here, which operate between the quasi-static and diffractive regimes, rely on numerical simulations to estimate the relation between the volume fill factor and the effective refractive index of the metamaterial layer.

The values of d_1, d_2, k_1, k_2, and p were chosen using a three step design process. A preliminary design was carried out using a classical analytic model consisting of sheets of dielectric material each with a constant thickness and index of refraction [121]. These were varied to minimize the reflectance across the band yielding targets for the electrical thickness and index of refraction of our two layer coating.

The second step was to translate the index and thickness from the simple model into the pitch, kerfs and depths for our coating geometry. This step required knowledge of the relation between the effective index of refraction of an array of square pillars and the pitch and kerf of that layer. These relations were determined by fitting analytic models to HFSS (High Frequency Structure Simulator, [122]) simulations of single layer coatings with a wide range of volume fill factors for a few different choices of pitch. The HFSS simulations were carried out using master-slave boundary conditions [2] and Floquet ports [3] to

[2] to enforce a periodicity in the fields that would exist from an infinitely periodic structure while only physically solving a single unit cell. It can significantly reduce memory requirements and solve time. However, it does not account for any edge effects resulting from the finite nature of an array [123]

[3] radiated waves from the unit cell will be terminated in the Floquet Modes defined by the Floquet Port Setup. Each Floquet Mode is a plane wave supported by the periodic structure. They come in two polarizations; Transverse Electric (TE) and Transverse Magnetic (TM). Assuming the Floquet Port is parallel to the XY plane, TE modes are +/- Phi polarized waves and TM modes are Theta polarized wave. The dominant modes are the TE_{00} and TM_{00} modes which correspond to the phi and theta polarized components of the array's main beam [123]

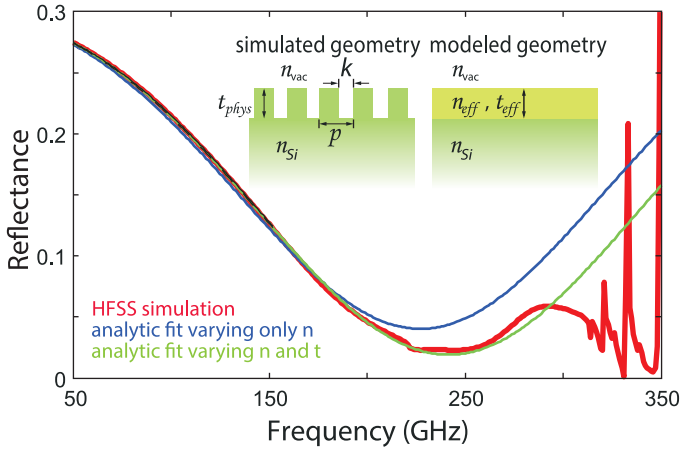

Figure 2.3: A comparison of the reflectance calculated from HFSS numerical simulation of a pillar geometry to fits based on a model of a simple dielectric layer. The geometry is specified in the inset in the top. In the simulated geometry, p = 400 µm, t_{phys} = 220 µm, k = 180 µm and n_{Si} = 3.38. A comparison between fits where only the index n is free and where both the index n and thickness t are varied is shown. The HFFS simulation and the best fit curve differ by 5% normalized root-mean-square deviation at 220 GHz ($\sim$ 1.36 mm). This corresponds to the minimum wavelength, $\lambda_{5\%}$ (and a corresponding maximum frequency $f_{5\%}$) for the specified pitch, p below (above) which the coating no longer behaves as a simple dielectric layer.

model a box containing a single post of the AR coating as an infinite periodic two dimensional array of features [122].

Figure 2.3 shows a representative simulation of a single layer pillar geometry with insets showing the simulated geometry and the simple dielectric layer modeled in the fit. The fit constrained the effective index n_{eff}, the effective electrical thickness t_{eff} and the maximum frequency to which our metamaterial coating behaves as a simple dielectric. For the purposes of our fit we define this maximum frequency as the point where the simulated reflectance and the analytic fit disagree at more than 5% in terms of normalized root-mean-square deviation of absolute reflectance. We refer to this frequency as $f_{5\%}$ and the corresponding wavelength $\lambda_{5\%}$. This indicates the transition between specular and diffractive behavior of the coating.

A second fit which fixed the electrical thickness to the physical thickness of the pillars is also shown in Figure 2.3. This fit implies a lower $f_{5\%}$. The discrepancy between the best fit thickness t_{eff} and the physical thickness t_{phys} of the metamaterial layer arises since the geometric structure of the pillars results in fringing of fields at the junction between layers causing a perturbative shift between the position of the physical interface and the effective location of the junction's electrical reference plane. An analogous effect is encountered in

the design of metallic waveguide structures [119].

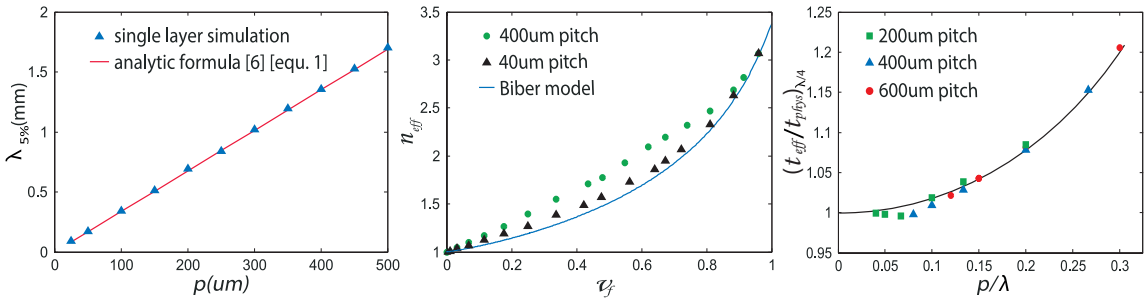

Figure 2.4: A summary of results from HFSS simulations of single layers of pillars with varying geometry. *Left:* The minimum wavelength $\lambda_{5\%}$ for which the single pillar layer is fit by an analytic model to 5% accuracy as a function of pitch p at normal incidence. *Center:* The effective index of refraction n_{eff} as a function of the volume fill factor v_f obtained by fitting the simulated reflectances upto the minimum wavelength $\lambda_{5\%}$ = 1360 µm for a pitch, p = 400 µm, 40 µm. The line labeled "Biber" is a prediction from the analytic Biber model [112], which corresponds to the quasi-static circuit approximation for the media. In the quasi static limit, the relation between v_f and n_{eff} extracted from simulation approaches the Biber approximation. *Right:* The thickness t_{eff} for a slab dielectric quarter-wave coating divided by the thickness t_{phys} of pillars forming an effective quarter wave coating at the same frequency (equivalent to the ratio of n_{eff} over $\sqrt{n_{Si}}$) as a function of p/λ. The simulated pillar geometries have pitch p = 200 µm, 400 µm, and 600 µm. A parabolic line (with offset of unity) is drawn through the points just to guide the eye. In the quasi-static limit, $p/\lambda << 1$, the metamaterial approximates a constant index material whereas for larger values of p/λ, the dielectric function becomes dispersive.

Figure 2.4 shows the results from fitting a number of HFSS simulations with different pitch and fill factor to the analytic model. Plots include the breakdown wavelength $\lambda_{5\%}$, the effective index n_{eff}, and the electrical thickness of a layer with index $\sqrt{n_{Si}}$ expressed as a ratio of the thickness of a quarter wave homogenous dielectric layer and a quarter wave metamaterial layer.

The recovered $\lambda_{5\%}$ is in good agreement with the analytic condition derived for a silicon optic in vacuum [101, 120] to prevent diffraction from a grating array,

$$p < \frac{\lambda}{(n_{Si} + \sin\theta_i)}, \tag{2.1}$$

where p is the pitch, λ is the wavelength, n_{Si} is the index of silicon, and θ_i is the angle of incidence. This analytic expression shows that the pitch must be smaller than implied by the $\lambda_{5\%}$ calculated at normal incidence to minimize diffraction at oblique angles of incidence. Figure 2.5 shows a plot of this breakdown frequency threshold above which diffraction starts dominating as a function of pitch for normal and 30° degrees oblique in-

cidence. Consideration of manufacturing cost and mechanical robustness of the two-layer AR coating design favors the largest possible pitch, as this choice minimizes the number of cuts required to cover a given area and makes the pillars larger and therefore stronger. A 435 μm pitch leads to acceptable performance up to $\sim$ 175 GHz ($\sim$ 1.7 mm) which is the upper edge of our band.

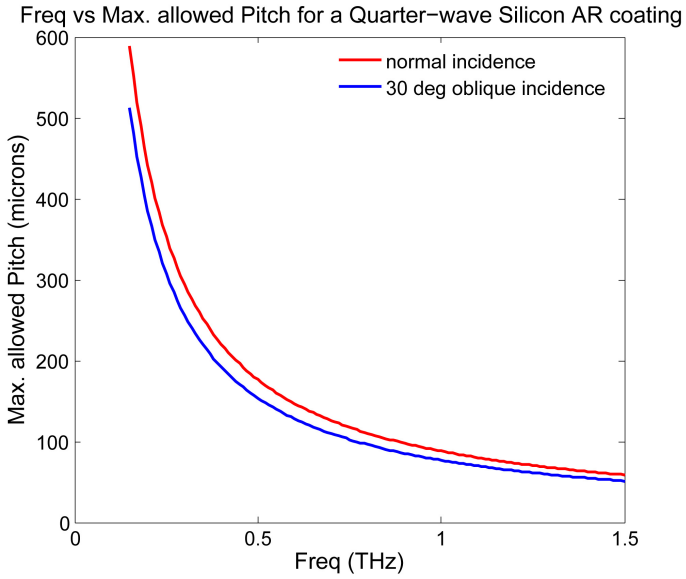

Figure 2.5: Maximum allowable pitch for diffraction-free operation at a given frequency given by Equation 2.1. The plotted curves are for normal and 30° oblique incidence.

Comparing this relation between v_f and n_{eff} to analytic models [112, 105] for the case where the electric field of the incident wave is perpendicular to the grooves, we found discrepancies that are reduced as the pitch decreases and we approach the quasi-static limit $p/\lambda << 0.1$. Given that our coating design does not operate in this limit we find the analytic models insufficiently accurate for our purposes. Thus we resort to numerical simulation to optimize the geometry of our coating.

The variation in the electrical thickness compared to the physical thickness (Figure 2.4, right) is shown for the case of a single quarter wave AR coating. Additional simulations show that this factor depends on the index of refraction of the material on either side of the metamaterial dielectric layer. This complicates the application of these single layer simulations to the design of multiple layer coatings and motivates the final numerical optimization step described later.

Table 2.1: The parameters for the 150 GHz ACTPol two-layer AR coating design.

parameter	symbol	dimension (μm)	dimension (units of p)
pitch	p	435	1.0
kerf*	k_1	190	0.437
	k_2	41	0.094
depth	d_1	349	0.802
	d_2	217	0.499
volume fill factor*	v_{f1}	0.317	
	v_{f2}	0.820	

* nominal average values

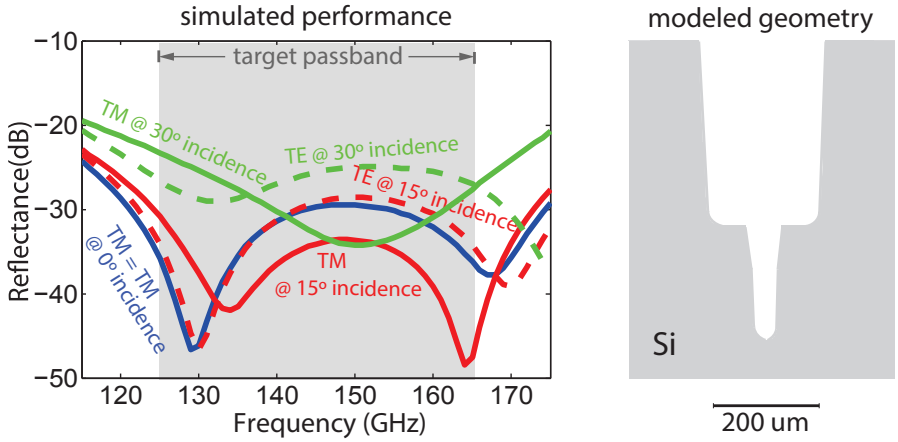

Figure 2.6: *Left:* A simulation of the performance of the AR coating designed for the 150 GHz ACTPol lenses at a range of angles of incidence. *Right:* The unit cell geometry modeled using HFSS.

With these relations (Figure 2.4) in hand one could convert the analytic design of our two layer coating (from step one) into parameters for the pillar geometry. In the final step we performed a numerical optimization of the coating at 15° angle of incidence using HFSS, with the constraint that the cut geometry must match the kerf geometry of commercially available dicing saw (See Section 2.6). This step enables manufacturability, accounts for any discrepancies between the electrical and physical thickness implied by our numerical simulations, and improves the performance at larger angles of incidence. Table 2.1 gives the parameters for the resultant design and the right panel of Figure 2.6 shows a cross-section of the final design geometry after optimization based on measurements carried out on prototype cut profiles of the blades. The left panel shows the simulated performance for a single-sided coating on a thick (>> wavelength of 150 GHz light) silicon sample as a

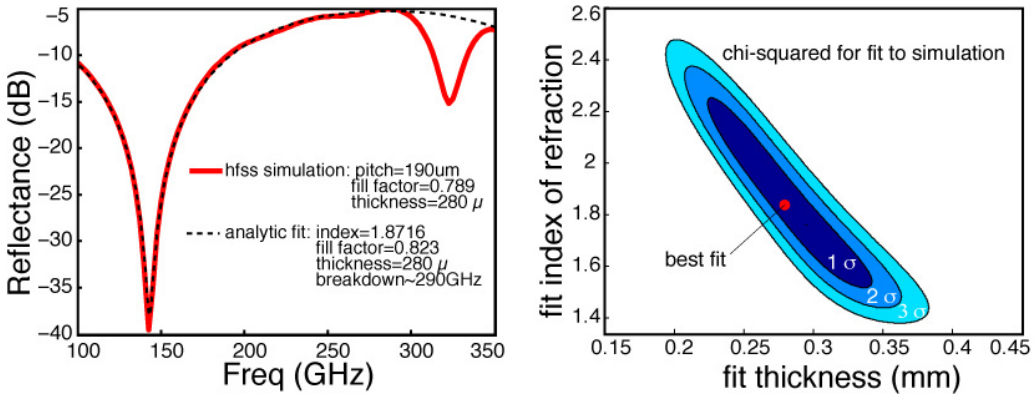

Figure 2.7: *left:* HFSS simulation of a single-layer quarter-wave coating and analytic fit curve obtained by varying the layer thickness and index. *right:* 2-D plot of the chi-square for the fit.

function of frequency for several ($0°, 15°$, and $30°$) angles of incidence. Even at $30°$ incidence the band averaged reflections are at -26 dB ($\sim 0.25\%$) and differences between the two linear polarization states (TE and TM, see [121] for definition) are below 0.5% for all frequencies and angles. At $15°$ incidence, average reflections are below -31 dB ($< 0.1\%$).

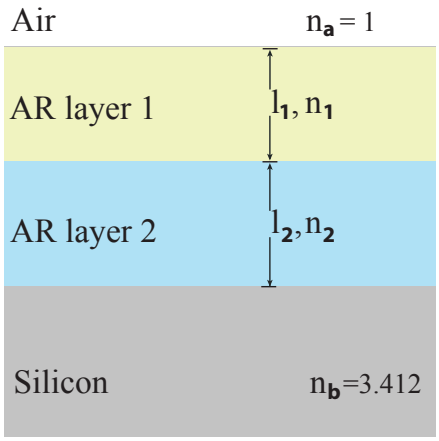

Figure 2.8: Two-layer AR coating modeled as two dielectric layers between air and silicon with thickness and index given by l_1, n_1, l_2, n_2.

Figure 2.7 shows the results of constraining the thickness and index of a single layer quarter-wavelength AR coating by fitting the analytical reflection to the HFSS simulated reflection. Extending this approach, the effective indices and thicknesses of the layers of the two-layer AR coating were determined by fitting the simulated reflection as a function of frequency to the analytical expression for overall reflection Γ_1 from a two-layer AR-coated silicon sample, obtained by recursive application of the Fresnel-derived equation

[124], with free parameters n_1, n_2, l_1, and l_2 (see Figure 2.8), as shown below:

$$\begin{gathered}\Gamma_1(\nu) = \frac{\rho_1 + \Gamma_2 e^{-2jk_1 l_1}}{1 + \rho_1 \Gamma_2 e^{-2jk_1 l_1}}, \;\; \Gamma_2(\nu) = \frac{\rho_2 + \rho_3 e^{-2jk_2 l_2}}{1 + \rho_2 \rho_3 e^{-2jk_2 l_2}} \\ \text{where, } k_i = \frac{2\pi n_i}{\lambda_o} = \frac{2\pi n_i \nu}{c}, \;\; i = 1,2 \\ \rho_1 = \frac{n_a - n_1}{n_a + n_1}, \;\; \rho_2 = \frac{n_1 - n_2}{n_1 + n_2}, \;\; \rho_2 = \frac{n_2 - n_b}{n_2 + n_b},\end{gathered} \tag{2.2}$$

where c = speed of light in free space, ν = frequency, n_a = 1 (air), and n_b = 3.412 (for silicon). The effective indices and thicknesses for the layers of the two-layer coating are listed in Table 2.2.

Table 2.2: Effective layer indices and thicknesses for the 150 GHz ACTPol two-layer AR coating.

parameter	symbol	best-fit value
effective index	n_1	1.38
	n_2	2.48
effective depth (μm)	l_1	360
	l_2	210

The ACTPol PA3 dichroic (90/150 GHz) array is coupled to the telescope via three cryogenic silicon lenses similar to those used for ACTPol [76, 77]. Implementing multi-chroic arrays requires optical designs with wide bandwidth. Two-layer AR coatings like the one developed for the 150 GHz ACTPol array would not meet the wide bandwidth requirement. So, we extended the approach to develop a three-layer AR coating optimized for 75 to 170 GHz frequency band. Figure 2.9 shows a cross-sectional schematic of the geometry which is parameterized by the depths d_1, d_2, and d_3, and kerf widths k_1, k_2, k_3 of the outer, middle, and inner layers respectively and a pitch p. Similar to the two-layer design, the outermost layer is cut by using a blade of width k_1 and the inner layers are cut by making a second and third set of cuts to increasing depths with successively thinner blades of width k_2 and k_3. Figure 2.9 also shows a photo of a mechanical prototype and a schematic (not to scale) of the final design geometry after optimization based on measurements carried out on the prototype, of the cut profiles of the blades. Table 2.3 gives the parameters for the resultant design and Figure 2.10 shows the simulated performance for a single-sided coating on a thick ($>>$ wavelength of 150 GHz light) silicon wafer as a function of frequency for

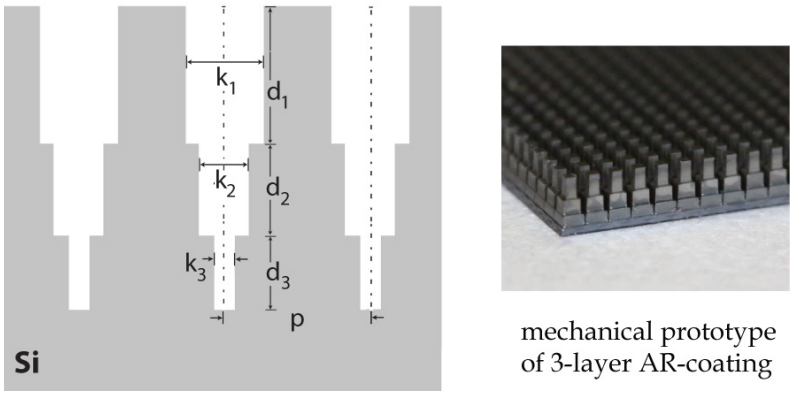

Figure 2.9: The geometry of the three layer metamaterial AR coating. The left side shows a cross section through the center of the pillars indicating the design parameters shown in Table 2.3. Grey represents silicon and white represents vacuum. The right side shows a photo of a mechanical prototype.

several ($0^\circ, 15^\circ$, and 30°) angles of incidence. This coating reduced reflections to less than 0.5% averaged over each of the two desired bands. The effective indices and thicknesses for the layers of the three-layer coating, determined in the same way as for the two-layer coatings earlier, are listed in Table 2.4. The tolerance of the design to various possible manufacturing errors are described in detail in Appendix A.

Table 2.3: The parameters for the 90/150 GHz ACTPol three-layer AR coating design.

parameter	symbol	dimension (μm)	dimension (units of p)
pitch	p	450	1.0
kerf*	k_1	248	0.551
	k_2	120	0.267
	k_3	35	0.078
depth	d_1	464	1.031
	d_2	330	0.289
	d_3	247	0.549
volume fill factor*	v_{f1}	0.202	
	v_{f2}	0.537	
	v_{f3}	0.850	

* nominal average values

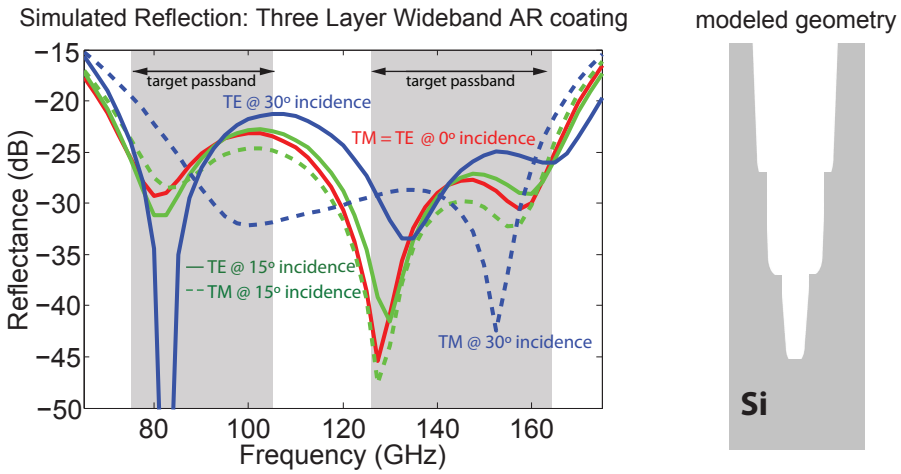

Figure 2.10: *Left:* A simulation of the performance of the AR coating designed for the 90/150 GHz ACTPol lenses at a range of angles of incidence. *Right:* The unit cell geometry modeled using HFSS.

Table 2.4: Effective layer indices and thicknesses for the 90/150 GHz ACTPol three-layer AR coating.

parameter	symbol	best-fit value
effective index	n_1	1.28
	n_2	1.95
	n_3	2.84
effective depth (μm)	l_1	470
	l_2	315
	l_3	245

* nominal average values

2.4 ACTPol Lenses

The ACTPol lenses are cylindrically symmetric plano-convex designs in which the convex surface is aspheric - a conic section with four perturbing terms proportional to the fourth, sixth, eighth, and tenth order of the distance from the axis. The design optimization procedure for the re-imaging optics is similar to that described in [77]; the primary difference being that the ACTPol optics are required to be image-space telecentric [4] to optimize the coupling to the flat feedhorn arrays. This was accomplished by constraining the chief rays at each field point to be near normal incidence at the focal plane and by allowing the tilts

[4]Image-space telecentricity is a special property of certain multi-element lens designs in which the chief rays for all points across the image are collimated. Such a design is good for systems that do not tolerate a wide range of angles of incidence

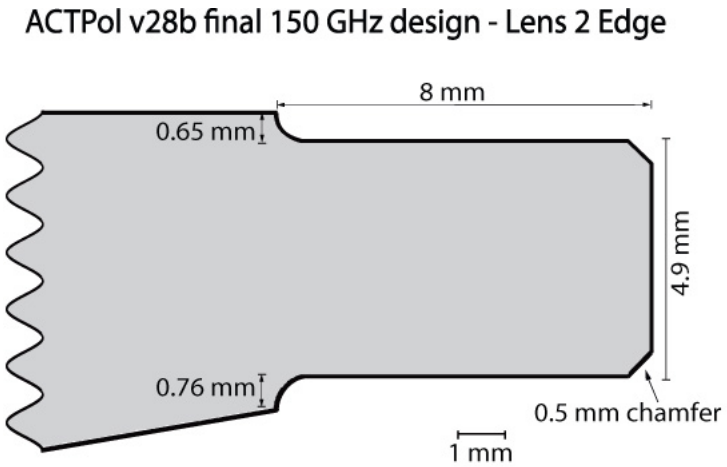

Figure 2.11: Cross-section of the perimeter of the ACTPol lens 2, which is designed to enable machining of the AR coating and clamping the lens without damaging the AR coating. Figure courtesy: Michael Niemack

of lens 2, lens 3, and the focal plane to vary during the optimization. The resulting design achieves Strehl ratios greater than 0.93 across the 150 GHz focal planes without accounting for the Gaussian illumination of the feedhorns, which effectively improves the image quality. All three of the ACTPol optics tubes use the same three silicon lens designs with the positions and tilts adjusted to optimize the coupling to the ACT Gregorian telescope [77].

The AR coating approach we have developed constrains the perimeter of the lens designs to enable accurate clamping during both machining of the AR coatings and cryogenic cycling of the lenses. Figure 2.11 shows a cross-section of the perimeter of the ACTPol lens 2 design with labels showing some of the critical design features. The lenses are designed to have handling rings around the perimeter that are not AR coated and can be used for precision alignment as well as clamping to cool the lens in the cryogenic receiver. The outer corners of the perimeter are chamfered to minimize chipping. There are steps that begin rising from the perimeter to provide clearance between the perimeter clamping region and the AR coating. The lens blanks were machined by Nu-Tek Precision Optical Corporation [125] and achieved 5 μm tolerances.

2.5 Properties of Silicon

Silicon manufacturing can produce different grades of material, such as ultra high purity silicon produced by the float zone process [126] that has a negligible density of impurities and silicon produced by the Czochralski process [126] that has a higher level of impurities. As charge carriers and associated states introduced by impurities are the cause of dielectric loss, use of the highest available purity (as inferred from the room temperature resistivity) silicon minimizes the dielectric losses. Measurements of the refractive index, dielectric permittivity and loss tangent of various high purity and high resistivity silicon specimen over a range of frequencies and temperature have been reported [127, 128, 129]. For example, ultra high purity silicon has been measured to have a loss tangent of $\sim 1 \times 10^{-5}$ at room temperature which would correspond to $< 1\%$ loss in the ACTPol optical system. Unfortunately, surface tension limits the zone-melt purification technique used to produce ultra high purity silicon to diameters below about 200 mm. Therefore, the substrates available for large diameter lenses considered in this work must be fabricated from Czochralski silicon. For our low temperature application we expect the bulk conductivity of silicon to freeze out dramatically reducing the dielectric losses, however, other loss mechanisms can persist in the desired design band. We validate this general picture of the dielectric loss in silicon by optically characterizing the influence of the bulk resistivity as a function of frequency and sample temperature.

Samples produced by the Czochralski process and readily available in 450 mm diameter stock with bulk resistivities specified to be in the range of 1 to > 500 Ω-cm were characterized both at room temperature and 4K using a Bruker 125 high-resolution Fourier Transform Spectrometer (FTS) with a Oxford Cryostat CF continuous liquid helium flow sample chamber. The cryostat is equipped with pair of 75 μm thick polypropylene windows that enable spectral measurement while allowing the sample to be held at a regulated temperature. The samples were cut to have a typical thickness of 180 μm, double side polished, and placed in a 25 mm diameter optical test fixture at the focus of an $f/6$ beam. The reflections from the two surfaces of the sample form a Fabry-Perot resonator for which the modeling is relatively simple permitting measurement of dielectric properties. The silicon samples are boron doped (p-type) to adjust the resistivity, we note that the highest resistivity silicon used in the ACTPol lenses has the minimum dopant level.

Each sample's transmission was measured between 240 GHz (8 icm) and 18 THz (600 icm) using different combinations of sources, beam splitters, and detectors for three fre-

quency bands between 240-450 GHz (8-15 icm), 450-2850 GHz (15-95 icm), and 2.85-18 THz (95-600 icm). The spectral resolution employed, 7.5 GHz (0.25 icm), fully resolves the sample's spectral features. Sliding stages permit the sample or a reference clear aperture to be moved into the FTS beam while in the cryostat for *in situ* calibration.

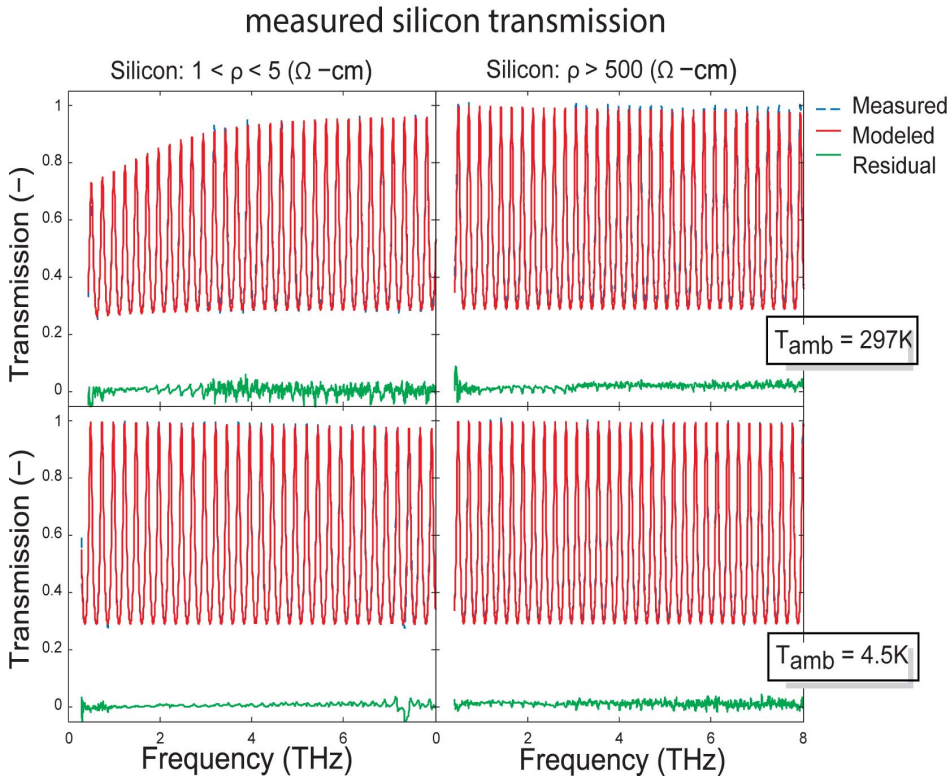

Figure 2.12: Measured silicon transmission at room-temperature (upper panels) and 4.5 K (lower panels). The left and right columns in the panel are for samples specified as $1 < \rho < 5$ Ω-cm and $\rho > 500$ Ω-cm respectively, the sample thickness is ∼180 µm thick. The figure contains the measured FTS data (red), model (dashed blue), and residual (green). Figure courtesy: Edward Wollack

The transmission spectrum was modeled as a series of homogeneous plane parallel dielectric layers [130]. The dielectric function for the silicon was approximated by a classical Drude dispersion model [131]:

$$\varepsilon_r^*(\omega) = \varepsilon_\infty^* - \frac{\omega_p^2}{\omega \cdot (\omega + i\Gamma)} \tag{2.3}$$

where $\varepsilon_r^* = \varepsilon_r' + i\varepsilon_r''$ is a complex function of frequency ω, the damping rate Γ, and the contribution to the relative permittivity ε_∞^* of higher energy transitions. The plasma frequency and the damping rates are related by, $\omega_p^2 = \Gamma/\varepsilon_o\rho$, where ε_o is the permittivity of free space and ρ is the sample's bulk resistivity [132]. In this approximation, the material's free car-

riers are treated as classical point charges undergoing random collisions and the resulting damping is assumed to be independent of the carrier energy. We find this representation suitable to represent the sample's properties over the spectral and temperature ranges of interest.

The sample thickness is known to ± 0.5 μm at room temperature and corrected for thermal contraction as a function of temperature [133]. Since the fringe rate is proportional to the product of the refractive index and sample thickness,uncertainties in the sample thickness directly limit the precision of the determination of $\Re\left(\varepsilon_{\infty}^{*}\right)$. Measurements of an optically polished crystalline quartz sample with accurately known thickness were used to measure a 1% amplitude uncertainty across the entire FTS band. This calibration uncertainty leads to a corresponding reduction in the measurement's sensitivity to $\Im\left(\varepsilon_{\infty}^{*}\right)$. These uncertainties were accounted for in fitting the FTS data. These fits produced root-mean-square deviations in the range of $\sim$0.005-to-0.016 between the model and the observation spectra. Representative data for the $\rho > 500$ and $1 < \rho < 5$ Ω-cm samples are shown in Figure 2.12 for sample physical temperatures of T_{phys}=297 and 4.5 K.

The results of these fits are shown in Table 2.5. As anticipated the finite plasma frequency and damping rate contribute significantly to the room temperature losses, however, the $\rho > 500$ Ω-cm sample could be approximated by a dielectric constant over the spectral range of interest (e.g., Γ and ω_p are consistent with zero). The influence of free carrier collisions at room temperature on the optical response becomes more pronounced in the $1 < \rho < 5$ Ω-cm sample, manifesting as a reduction in transmission at low frequencies. However, as the $1 < \rho < 5$ Ω-cm sample is cooled, bulk conduction is suppressed and this effect shifts to lower frequencies than of interest for millimeter wave applications. The observed dielectric parameters are a weak function of temperature below ~ 30 K as anticipated given exponential thermal dependance of the bulk resistivity [134].

Both samples show $\sim 1\%$ shifts in the magnitude of the index of refraction ($n \approx \sqrt{\varepsilon_{\infty}'}$) upon cooling. This shift is accounted for in our optical design. At low temperature both the high and low resistivity sample give an upper limit for the loss tangent of $\tan\delta \sim \varepsilon_{\infty}''/\varepsilon_{\infty}' < 7\times10^{-5}$. For the ACTPol optics at 150 GHz, this corresponds to an absorptive loss of $< 5\%$ for our optical system comprising three lenses. The ACTPol lenses were fabricated from $\rho > 500$ Ω-cm silicon as it may reduce loss and facilitates room temperature testing. Both high and low resistivity silicon would provide acceptable performance in 4 K cryogenic applications, but given the small cost differential high resistivity silicon is the natural choice.

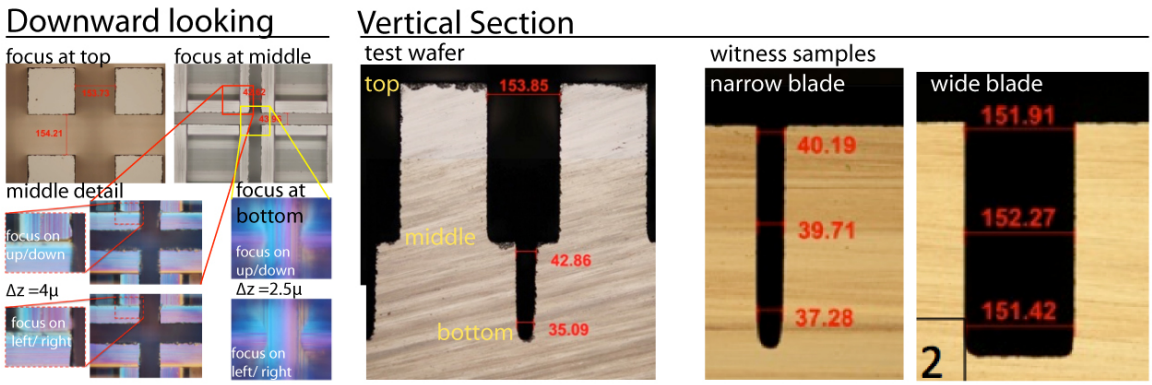

Figure 2.13: Summary of findings from metrology performed on a two-layer coating cut on a silicon test wafer at NIST, Boulder. Figure courtesy: John Nibarger

Although we have used high-resistivity silicon, our models and observations suggest that the carriers will be frozen out at 4K for the range of bulk resistivities considered here. We note that the conductivity of silicon at room temperature, and therefore the loss, is a strong function of UV irradiance. We have not investigated this dependence cryogenically.

Table 2.5: Silicon Drude Model Fit Parameters.

$\rho(T_{phys})$ [Ω-cm]	T_{phys} [K]	ε'_∞ [−]	ε''_∞ [−]	$\Gamma/2\pi$ [THz]	$\omega_p/2\pi$ [THz]
>500	297	11.7(1)	0.0015	–	–
	4.5	11.5(5)	<0.0008	–	–
1-to-5	297	11.6(55)	0.0046	0.571	1.60
	200	11.5(52)	0.0049	0.572	0.80
	100	11.4(78)	0.0028	0.459	0.26
	70	11.4(66)	0.0011	0.162	0.20
	30	11.4(64)	<0.0008	–	–
	10	11.4(62)	<0.0008	–	–
	4.5	11.4(62)	<0.0008	–	–

2.6 Coating Fabrication

The coatings were fabricated using silicon dicing saw blades which are available in widths ranging from ten to hundreds of microns. Mounted on a commercial silicon dicing saw machine these blades repeatedly cut with micron level precision and cutting speeds up to several centimeters per second. Unfortunately, commercial silicon dicing machines are not

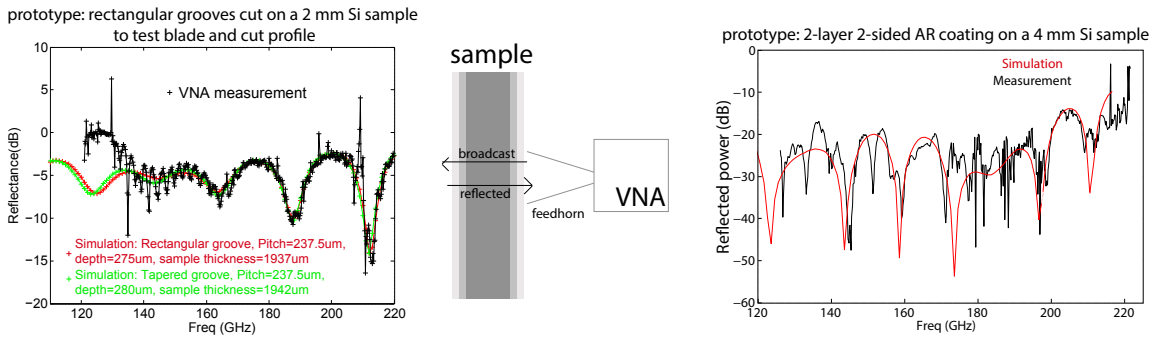

Figure 2.14: *left:* VNA measurements of reflection from a 2 mm thick silicon test wafer, on which a single layer of rectangular grooves were cut in perpendicular directions with a commercially available dicing saw blade, compared to HFSS simulations. *right:* VNA measurements of reflection from a 4 mm thick silicon test wafer, two-layer AR-coated on both sides, compared to HFSS simulations. The measurements were carried out by Michael Niemack and Joseph Fowler at NIST, Boulder.

designed for curved surfaces and cannot accommodate the large diameter lenses required for this project. Therefore, a custom three axis silicon dicing system was constructed in our lab by Charles Munson to fabricate these coatings. Before cutting the ACTPol lenses, several small test wafers were cut and careful metrology and reflection measurements were performed as a proof of concept. Both single layer quarter wave coatings and two layer coatings were cut on test wafers. The groove shapes were measured and compared with the dicing saw blade specifications. Figure 2.13 summarizes the metrology performed by John Nibarger at NIST, Boulder on sample grooves cut on a test wafer with blades of specified widths 40 µm and 150 µm. After confirming that the cut profiles matched the blade specifications to an acceptable level, a two-layer test coating was cut on both sides of a 4 mm thick, 2 inch diameter sample wafer. The reflection from this silicon sample was measured using a Vector Network Analyzer (VNA) at NIST, Boulder. Figure 2.14 shows a comparison between measurement and HFSS simulation at 15° angle of incidence. The measured reflections were in good agreement with predictions for both the test wafers, which gave us the confidence to move forward with the fabrication of the coatings on the ACTPol lenses.

The fabrication system is shown in Figure 2.15. It consists of a micron accurate three axis stage on which we mount an air bearing dicing spindle and a micron accurate depth gauge. The spindle and retractable depth gauge are attached to the vertical stage (Z-axis) which rides on the horizontal (Y-axis) stage. A lens is mounted on an aluminum mounting plate on a horizontal stage (X-axis) below the spindle. This plate permits the lens to be rotated by 0°, 90°, 180°, and 270° and carries a reference wafer that is used in setting up the blades prior to cuts. A side looking microscope is mounted parallel to the Y-axis to

characterize test cuts on the reference wafer. Flood cooling water is sprayed on the dicing blade while cuts are made to carry away debris. A temperature controlled water bath is used to regulate the temperature of the spindle and maintain the flood coolant and air surrounding the dicing system within 1° C.

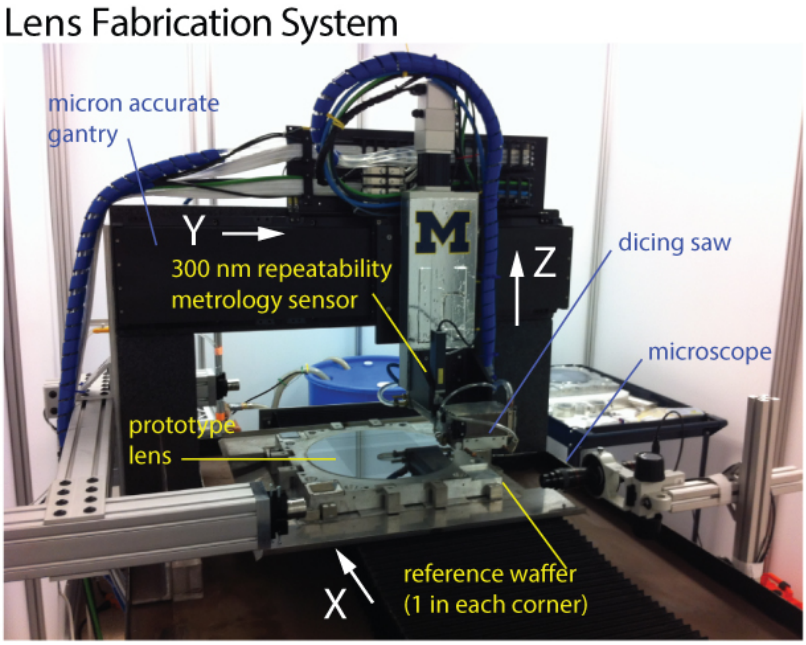

Figure 2.15: The custom, micron accurate, three axis silicon dicing system used to fabricate coatings on the lenses. The labels identify the key components and axes described in the Section 2.6. Figure courtesy: Charles Munson

The AR coatings on the ACTPol lenses were fabricated by Charles Munson and Kevin Coughlin using the custom-built silicon dicing saw in the McMahon Lab. The procedure for fabricating an AR coating on a lens is as follows.

1. Mount lens on X-axis and mount the wider blade to be used in the first set of cuts.
2. Raster the depth gauge across the lens surface. Fit these data to locate the lens in metrology coordinates.
3. Make a series of "plunge" test cuts on the reference wafer. These are made by moving the blade down along the Z axis, retracting, stepping along the X-axis by half a blade width, and repeating until a 2 mm wide arc is cut into the surface. Metrology is performed to measure the blade center and radius in metrology coordinates.
4. Make a test cut on the reference wafer. This cut is made by (i) locating the test wafter with metrology, and (ii) cutting while moving the spindle along the Y-axis.

This sample is characterized in two ways. First, the depth gauge is rastered across it in the X direction and the data are used to locate the X-position of the blade in metrology coordinates. Second, the side looking microscope is used to measure the shape and depth of the cut. This is used to verify the blade model from the previous step and to verify that the blade is cutting to specification.

5. Based on the measured lens and blade positions, cut a series of grooves into the lens by moving the saw in the Y-Z plane and stepping the lens along the X-axis between cuts.

6. Mount the narrow blade. Repeat steps 3 and 4 to locate this new blade and to locate its position. Then proceed with step 5 with a deeper depth.

7. Rotate the lens by 90° and repeat steps 1-6. Step 2 is modified as follows: we sample the lens surface at 20 locations spread across the surface, but at each location we densely sample the lens perpendicular to the cuts from the first direction. We then take the maximum of this dens sampling and take that as the top of the lens. We found that the partially coated lens was undamaged by contact with our touch probe.

For the flat sides of lenses this is the complete procedure. We flip the lens over in the mounting plate (which has a cutout in the middle) to cut the second side. For curved sides of the lenses there is an interference issue between the body of the dicing spindle and the highest point on the lens. Therefore for curved sides we only cut half the lens in each setup and we add steps similar to step 7, but rotated by 180° and 270°.

Our system does not show any appreciable change in cut shape or surface damage when cutting at the maximum travel speed of 50 mm/s. We conservatively operate at 25 mm/s for which it takes a total of 12 hours of machining per lens side. Factoring in setup time it takes six 8-hour days to fabricate a single lens.

Figure 2.16 shows photographs of one of the ACTPol AR coated silicon lenses. The fabricated coating is sufficiently robust to permit handling the lenses by touching the AR coatings. The manufacture resulted in less than 10 out of 500,000 posts with damage visible by eye. The shape of the cut profiles was evaluated by making cuts on a reference silicon wafer before cutting (pre-cut) and after cutting (post-cut) the lens and measuring them using the side looking microscope. Comparison of the pre-cut and post-cut measurements (see Figure 2.16) show that the wide blade cuts repeatably with negligible evolution to cut profile while the the narrow blade shows some evolution in width in the upper third

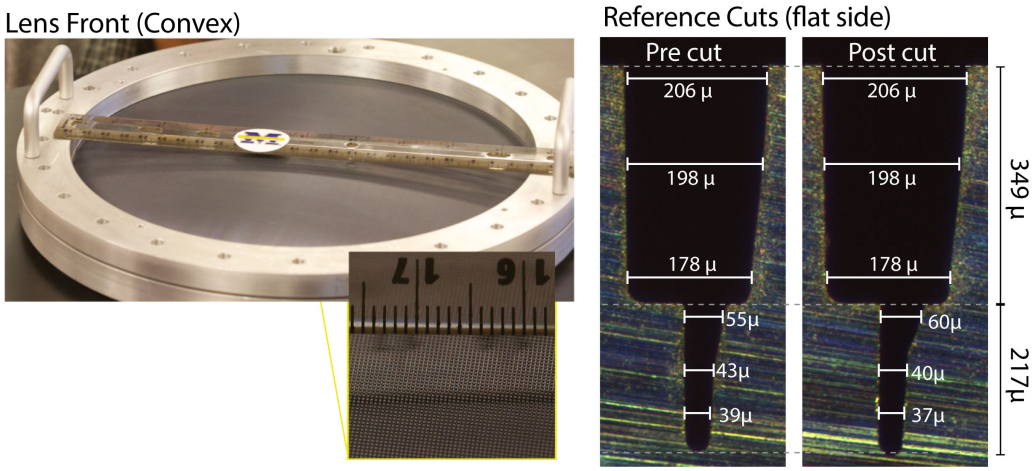

Figure 2.16: *Left:* Photograph of the curved front surface of a two-layer AR coated 150 GHz (PA1/PA2) ACTPol silicon lens (lens 2) with zoomed view of a small patch. *Right:* Photographs taken with side looking metrology microscope. By focusing on the top, middle, and bottom of the pillars it is possible to determine the depth of the grooves including measuring asymmetries between left/right and up/down grooves, which in this case are less than 4 µm. Measurement of the profile of the grooves requires cutting a vertical section from the silicon substrate. Since creating these sections damages the substrate, the vertical section measurements were only performed on cuts made on a reference wafer before (pre-cut) and after (post-cut) cutting the lens. The measurements were made by Charles Munson.

of the cut. Simulations show that this evolution, leads to a few tenths of a percent increase in the reflectance. The accuracy of the depths of the cuts is limited by a 3 µm uncertainty in the zero point for the blade depth and a ± 7 µm quadruple warp in the lens. This warp is due to imperfections in the lens mounting plate that stress the lens.

2.7 Reflectometer Measurements

The reflectance of the completed ACTPol lenses were measured using a scalar reflectometer. This reflectometer consisted of a tunable narrow band continuous wave source which illuminated the flat side of a lens through a 20° full width half power horn, from a distance of 5 cm, and tilted at an angle of 15° relative to the lens surface normal. A receiver consisting of an identical horn coupled to a detector diode was placed at the mirror image of the source horn relative to the plane defined by the point of maximum illumination of the lens and perpendicular to a line joining the source and receiver. The reflectometer could be set up for both linear polarizations (TE and TM modes [5]) by using a 90° microwave

[5] in a waveguide where boundary conditions are imposed by a physical structure, a wave of a particular frequency can be described in terms of a transverse mode. In rectangular waveguides, there can be (i)

waveguide twister. This system was calibrated by (1) placing an aluminum reflector at the same position as the lens to calibrate gain, and (2) by removing the lens and calibration reflector to measure the stray reflections which were found to be negligible. The reflectometer setup evolved over time as we learned more and more about the systematics of the reflection measurements by trying different configurations.

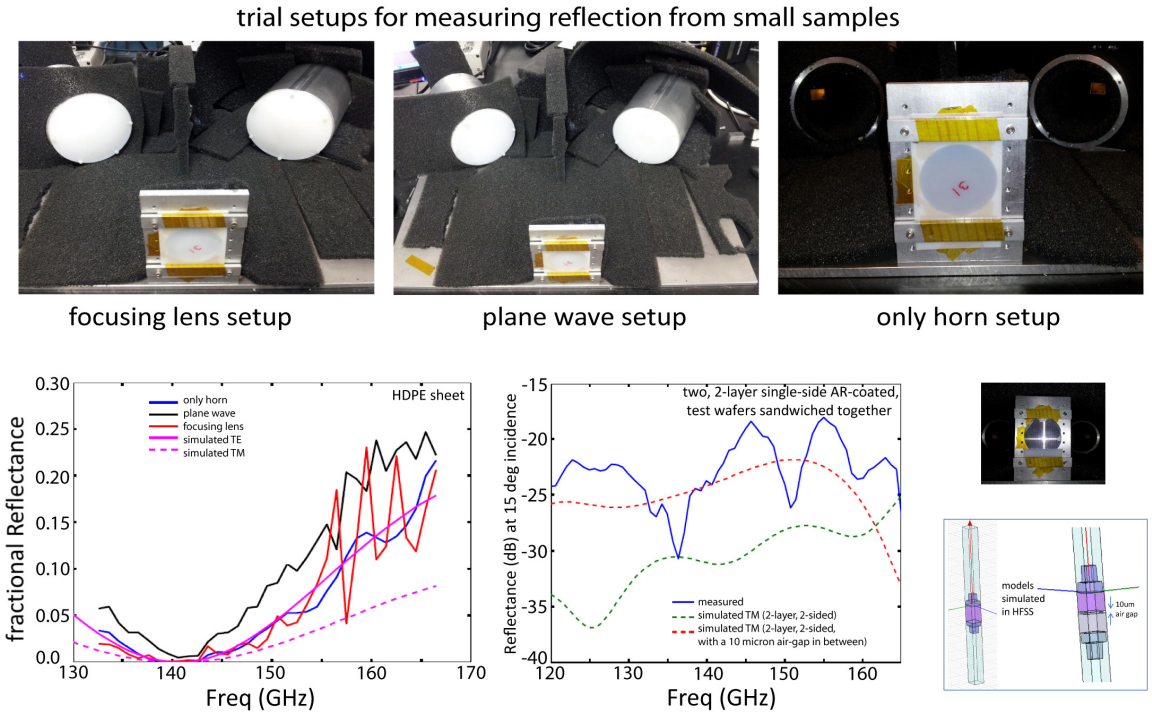

Figure 2.17: *top:* Photos of different reflectometer setups used for measuring reflections from the small AR coated silicon test wafers. A white sheet of HDPE (for setup verification) is shown being measured in the photos. *bottom left:* The left panel shows a comparison between simulation and measurements of reflection from the HDPE sheet with the three setups shown above. *bottom right:* Two test wafers were two-layer AR-coated on one side of each and stuck back-to-back. The reflection was measured and compared to simulations of an equivalent two-layer two-sided AR coating with and without a hypothetical 10 µm air gap between the two test wafers sandwiched together.

Figure 2.17 shows a picture of some of the first configurations of the reflectometer. We measured reflections from the small AR-coated test wafers using this setup. Applying the principles of Gaussian beam quasioptics [135], we tried using a plastic lens to focus the microwave signal from the transmit horn on to a small spot on the sample being measured,

Transverse Electric (TE) modes: no electric field in the direction of propagation, only a magnetic field along the direction of propagation and (ii) Transverse Magnetic (TM) modes: no magnetic field in the direction of propagation, only an electric field along the direction of propagation. The mode numbers are designated as TE_{mn} or TM_{mn}, where m is the number of half-wave patterns across the width of the waveguide and n is the number of half-wave patterns across the height of the waveguide

shown in the top left panel of Figure 2.17. We also tried a configuration (top middle panel) where we used a plano-convex lens to make a plane wave illuminate the sample uniformly. The design of the plastic lens is described in Appendix B. In the simplest setup, we had no lens in front of the horns, shown in the top right panel. We measured HDPE sheets of known thicknesses to validate our setup and found that the no-lens configuration gave the most accurate measurements, probably because the non AR-coated lenses caused extra reflections. Some measurements are shown in the bottom panels of Figure 2.17.

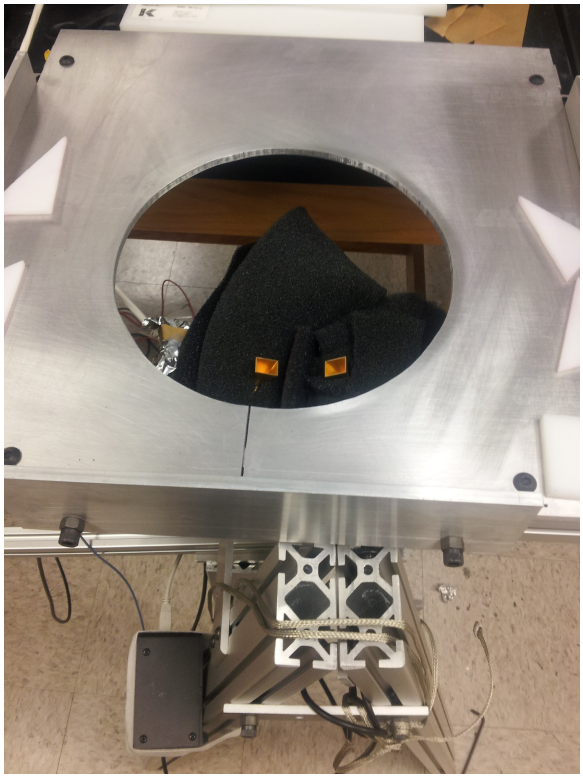

Figure 2.18: A photo of the reflectometer setup used for measuring reflections from the ACTPol lenses. The lens being measured sits on the plate with the circular hole cut out. The two feedhorns are the transmit and receive horns, and the angle and distance of each feedhorn from the lens under test are adjustable. The black material is Eccosorb HR-10, which is a very good absorber of microwave radiation, and is used to mitigate stray reflections in the setup.

For measuring the reflections from the AR-coated ACTPol lenses, we switched to a slightly different configuration shown in Figure 2.18 that let us set down the large lenses being measured conveniently on a plate, thus mitigating the risk of damage. The results of this reflectance measurement performed on a two-layer AR-coated lens are shown in Figure 2.19 for both the TE and TM polarization space. Precise modeling of this measurement configuration requires accounting for the interference between reflections from the flat and

curved lens surface, which is beyond the scope of this work. However, the results are expected to be intermediate between the reflectance from a single AR coated surface (single sided) and the easily simulated result for two surfaces separated by the central thickness of the lens (two sided). These two cases are presented in Figure 2.19 for both linear polarization states. These simulations incorporate the measured surface profiles shown in Figure 2.16. We empirically find that moving the lens so that it is well centered on the beam increases the interference effects (TM case) while moving the lens off center reduces these effects (TE case). The measured reflection from a three-layer AR-coated lens is shown in Figure 2.20 along with a photo of an AR-coated lens. The measured performance differs from our predictions at the sub-percent level. This is due to imperfections of the machining process we identified after fabricating the first batch of the wider bandwidth lenses. Based on the reasonable agreement between these simplistic simulations and the measurement we are confident we are reducing reflections to a few tenths of a percent over the range of angles of incidence required for ACTPol.

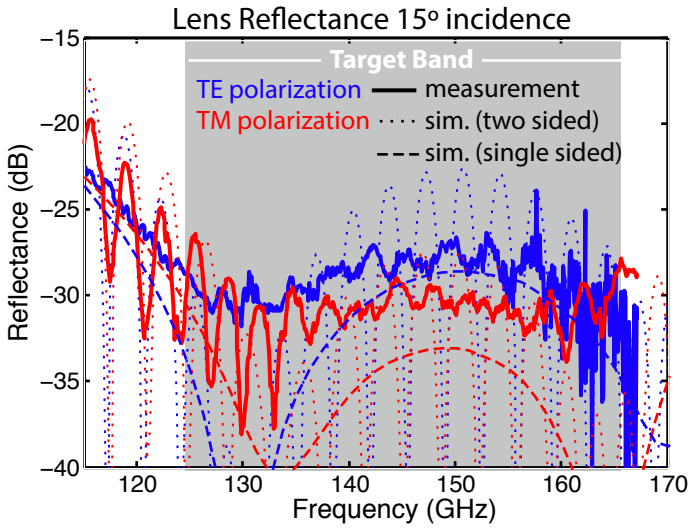

Figure 2.19: Comparison between simulations and measurements of the fabricated lens. The two sided simulations include the AR coating on both sides of a flat silicon sample of thickness equal to that of the lens at its center. The single sided simulations are for AR coating on only one side of a flat silicon sample.

We explore several possible options for AR coating of the plastic receiver dewar window in Appendix C.

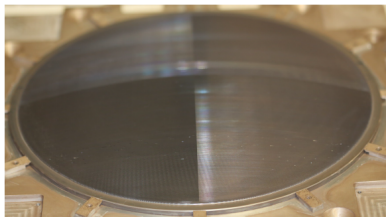

broadband 3-layer AR-coated Si Lens

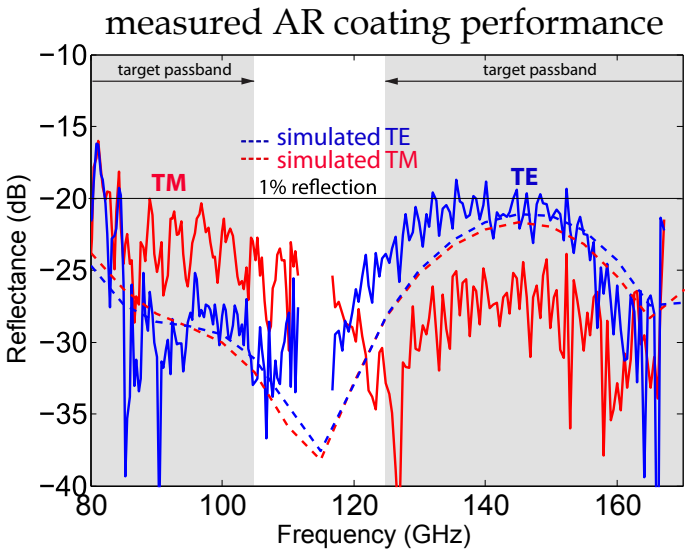

Figure 2.20: *Left:* Photo of a three-layer AR-coated lens. *Right:* Comparison between simulations and measurements of the fabricated lens. The simulations are for a single-sided AR coating on a flat silicon sample of thickness equal to that of the lens at its center, illuminated at 15° angle of incidence. The two-sided simulations are not shown for preserving clarity.

2.8 Conclusion and Future work

We have described a new approach for AR coating silicon lenses over broad bandwidths and a range of angles of incidence. Simulations, backed up by measurements of an AR coated lens, show that the fabricated coating of the lenses presented here can reduce reflections below few tenths of a percent between 125 and 165 GHz for angles of incidence between 0 and 30° for cryogenic applications. We have developed a micron-accurate 3-axis silicon dicing saw facility and are using it to manufacture these coatings on lenses for ACTPol. We have also shown that a range of p-type silicon doping levels can achieve low loss at cryogenic temperatures using silicon samples from boules as large as 45 cm diameter. This approach for implementing wide-bandwidth AR coated silicon lenses is applicable for millimeter and sub-millimeter wavelength ranges and can be expanded to wider bandwidth by adding additional layers to the AR coating. In recent years, some other interesting approaches have been developed for AR coating [136, 137, 138] of optics operating over microwave to terahertz frequencies. The design procedure described in this chapter can be trivially expanded and applied to multilayer antireflection coatings beyond two layers to cover even wider bandwidths. Figure 2.21 shows some representative designs for multilayer AR coatings.

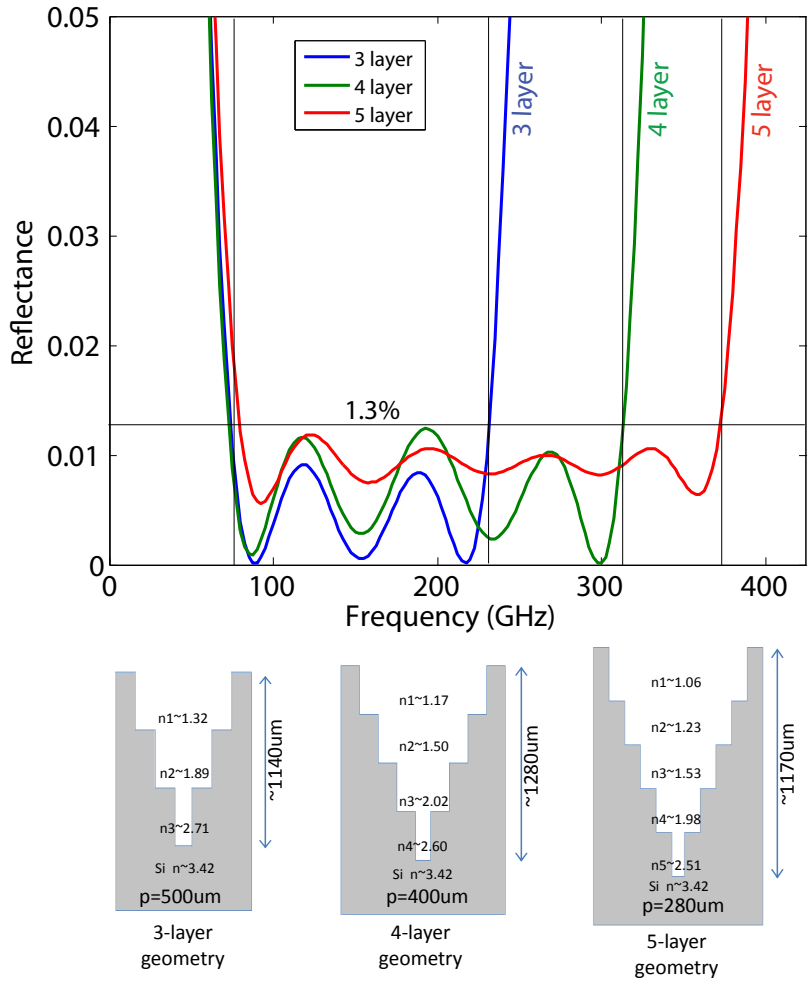

Figure 2.21: *bottom*: Practically feasible (manufacturable) multiple-layer AR coatings, assuming a kerf width of 20 µm for the thinnest blade. n_i's refer to the effective indices of the layers, p refers to the pitch and an approximate total coating thickness is shown. *top*: Simulated reflections for the corresponding geometries, showing maximum achievable bandwidths.

CHAPTER 3

Multichroic Pixel Design and Array Optimization

In this chapter, I present the development of dichroic pixels for the ACTPol and AdvACT multichroic detector arrays. I describe the motivation behind the choice of multichroic pixels over pixels sensitive to a single frequency band. The constituent microwave components of these feedhorn-coupled multichroic polarimeters are described in detail. The optimization of the ACTPol 90/150 GHz multichroic array parameters as well as the design of the array along with wiring layout is presented. I also describe optical efficiency measurements of prototype pixels fabricated at NIST, Boulder.

3.1 Introduction

CMB polarization provides a unique window into the physics of inflation [31], an alternative means to measure the neutrino mass sum [139], and a rich assortment of other astrophysical and cosmological results. Detections of the small angular scale B-mode polarization from gravitational lensing [140] have been reported [141, 142, 143, 144] in the last two years. Recent results from Planck and BICEP [60] show that measurements of the inflationary B-mode signal at larger angular scales requires instruments capable of mapping the CMB at multiple frequency bands with unprecedented sensitivity and excellent control over systematics. Feedhorn-coupled detectors with sensitivity to multiple spectral bands within a single focal plane element offer an avenue to achieve these goals.

A linearly polarized electromagnetic wave $\vec{E}$ propagating in the z-direction can be de-

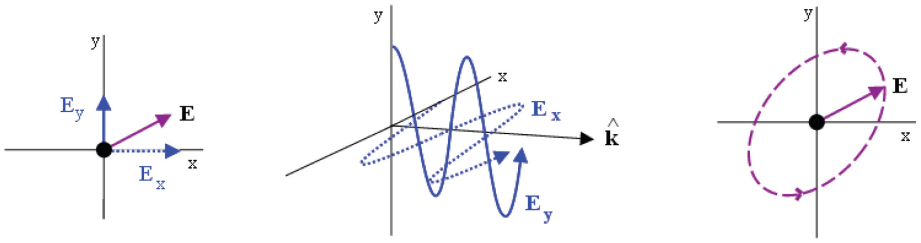

Figure 3.1: A linearly polarized electromagnetic wave with an electric field vector $\vec{E}$ (*left*) traveling in the z-direction can be decomposed into two orthogonal linearly polarized components along the x- and y-direction (*middle*). *right*: the locus of the points of the tip of $\vec{E}$.

composed into two orthogonal linearly polarized components (see Figure 3.1) as:

$$\begin{aligned} \vec{E} &= \vec{E}_x + \vec{E}_y, \\ \vec{E}_x &= E_{x,o} cos(kz - \omega t)\hat{i} \\ \vec{E}_y &= E_{y,o} cos(kz - \omega t - \delta)\hat{j} \end{aligned} \tag{3.1}$$

where k is the wavenumber, ω is the frequency, t is the time, and δ is the phase difference between the two orthogonal linearly polarized components, E_x and E_y. The Stokes parameters are a set of values that describe the polarization state of electromgnetic radiation:

$$\begin{aligned} I &= E_{x,o}^2 + E_{y,o}^2 \\ Q &= E_{x,o}^2 - E_{y,o}^2 \\ U &= 2E_{x,o}E_{y,o} cos\delta \\ V &= 2E_{x,o}E_{y,o} sin\delta \end{aligned} \tag{3.2}$$

Measuring the CMB polarization requires mapping the Stokes parameters I, Q, and U on the sky. One way to achieve this is through the use of polarimeters (see Figure 3.2). Since circular polarization cannot be generated through Thomson scattering, the mechanism which imparts polarization to the CMB photons, the Stokes parameter V is expected to be 0. Our collaboration has been developing feed-horn coupled polarimeter arrays for the Atacama Cosmology Telescope (ACT) [83]. ACTPol is the second generation receiver deployed on ACT. The ACTPol instrument [68] is optimized to make arcminute resolution measurements of CMB polarization, CMB lensing, and other secondary anisotropies. It consists of three independent optical paths with a kilo-pixel detector array at the focal plane of each tube, housed in a custom-built cryostat [82]. Two of these optics tubes are identical with 148 GHz detectors [145]. The first detector array (PA1) was installed in 2013 and the second array (PA2) in 2014. The original plan for ACTPol was to field two 148

GHz arrays and a third 90 GHz array (PA3) using the readout system from the original ACT receiver (MBAC) [76] that could read 1024 channels per array. However, the collaboration later decided to switch to a dual-frequency (dichroic) detector array which could potentially provide a gain in terms of sensitivity over a single-frequency array. In the previous chapter, we described the broadband refractive optics (silicon lenses) required for focusing light on to the focal plane. In this chapter, we motivate our decision to switch to a dichroic array by describing the gains; and present the design of our horn coupled multichroic polarimeters encompassing the 90/150 GHz CMB bands along with some measurements of the prototype detectors and feed-horns. We fielded this PA3 array on the Atacama Cosmology Telescope (ACT) as part of the ACTPol project [68] in June 2015. We will also touch upon some of the multichroic detector development that our collaboration has been working on for the third generation Advanced ACTPol (AdvACT) receiver.

3.2 Detector Architecture

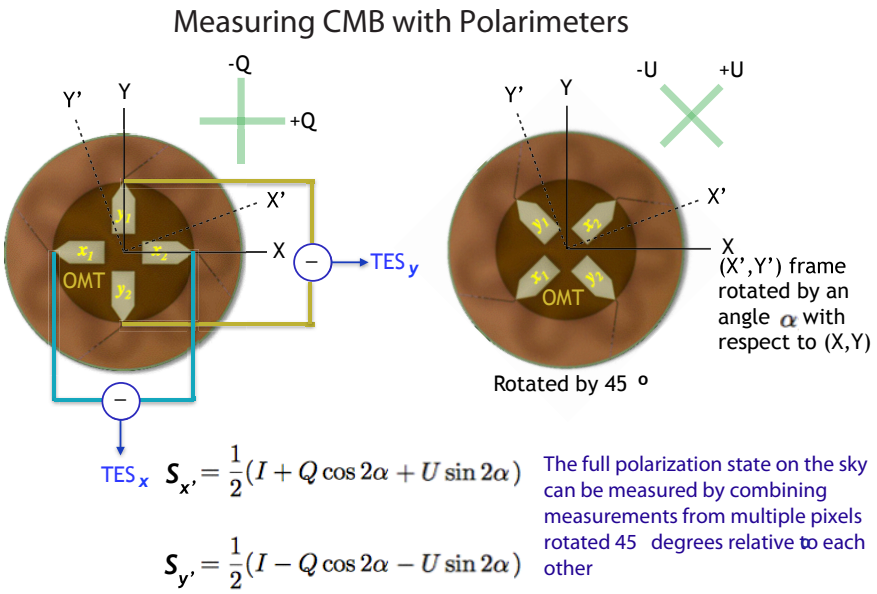

Figure 3.2: The Stokes parameters I, Q, and U on the sky can be fully mapped by combining measurements from multiple polarimeters rotated 45° relative to each other. Schematics of two polarimeters rotated 45° with respect to each other are shown here. Incident radiation couples to the planar detector wafer through the OMT (Ortho-Mode Transducer described in detail in Section 3.3.3) fins. The mutually perpendicular pair of fins pick up the two orthogonal components of linear polarization.

3.3 Multichroic Array Optimization

A detector array design is optimized to maximize the sensitivity of the instrument. The multichroic focal plane area was limited by the ACTPol optics design to 150 mm diameter, while the total number of detectors was limited by the read-out capacity of the previous generation squid-based 32 rows x 32 columns time-division multiplexing scheme. Thus for the ACTPol multichroic array optimization we were restricted by the number of available channels which limited us to 256 feed horns with 4 detectors per pixel. We know that sensitivity of an array increases as the square-root of number of pixels. However, the width of the Gaussian beam from a diffraction-limited feed-horn coupled pixel is inversely proportional to the sky-facing aperture size of the feed-horn. As the beam widens, a larger fraction of the beam terminates on the cold Lyot stop and a smaller fraction of it receives a signal from the sky, in effect reducing the sensitivity per pixel. Hence, determining the most efficient way to populate the available real estate on the focal plane involved careful optimization of array parameters like pixel size, spacing between pixels, and packing scheme, subject to the read-out limit. Multichroic feed-horn coupled detectors bring an additional challenge to the pixel size optimization process because different frequency bands share the same feed-horn.

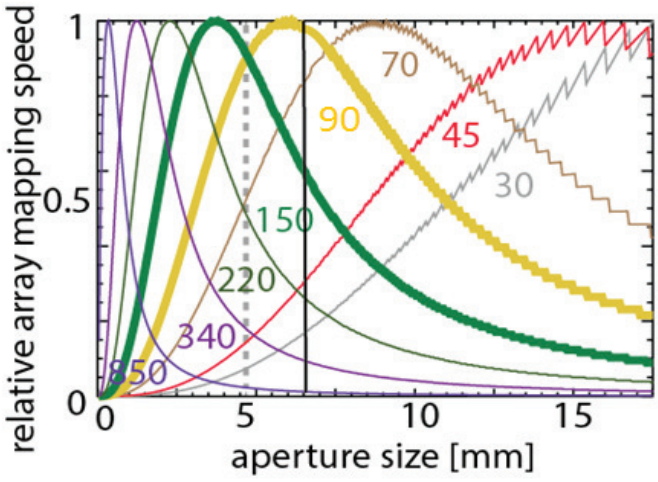

Figure 3.3: A simulation of the mapping speed as a function of horn aperture for a six inch detector array with 1.4:1 ratio bandwidth detectors with the band centers as labeled. For a multichroic array with two wide bands (centered at 90 and 150 GHz for example) it is possible to achieve sensitivity equivalent to 1.7 single frequency arrays with a 5 mm horn aperture diameter. Adding additional frequency bands leads to diminishing returns in sensitivity as these are sub-optimally coupled to the telescope. Figure courtesy: Suzanne Staggs

Thus, the first step towards maximizing the sensitivity of our fixed diameter detector array for the given optical system required choosing the optimal horn aperture size. This optimization takes into account a detailed optical model including transmission efficiency and emission from the lyot stop, filters, optics, and atmosphere. The calculation for mapping speed [146] as a function of horn skyward aperture size is performed (by Suzanne Staggs) for a variety of CMB bands each with 1.4:1 ratio bandwidth and plotted in Figure 3.3. The peak of a single curve corresponds to the optimal horn aperture for a single frequency array. For a multichroic array one must choose a horn aperture that maximizes the sensitivity of two or more channels simultaneously. For the case of two neighboring bands (e.g. 90 and 150) it is possible to achieve 85% of sensitivity of an optimized 90 GHz and an optimized 150 GHz single frequency array with one multichroic array with a feed-horn skyward aperture of $\sim$5 mm. However, the read-out constraint drove us to a larger aperture of 7.05 mm with a hexagonal close-packing scheme to maximally fill the focal plane. We chose a 7.09 mm pixel-to-pixel spacing and a 6.5 mm diameter pixel, leaving enough space for the readout wiring traces. This leads to nearly optimal mapping speed at 90 GHz, but reduced sensitivity at 150 GHz.

Lyot stop is an optical aperture stop that is cryogenically cooled to truncate the beam of a detector in order to mitigate stray reflections. Assuming a feed-horn to be a transmitting antenna (using symmetry between transmitting and receiving antenna), the fraction of the beam that would make through a Lyot stop with a radius r is referred to as the spill-over efficiency given by :

$$\eta_{spillover} \;=\; 1 - e^{-\frac{2r^2}{w(z)^2}} \tag{3.3}$$

where, w(z) is the beam-waist at a distance z from the feed-horn phase center.

Repeating the mapping speed calculations, including the detector losses described in the next section and with calculated spill-over efficiency of 75% and 95% at 90 and 150 GHz respectively, we find that this array will achieve 85% the mapping speed of a 90 GHz array and 50% the mapping speed of a 150 GHz single frequency array. This comparison assumes lower losses for the single frequency array owing to the shorter lengths of transmission lines and detector efficiencies of 72% and 64% at 90 and 150 GHz, respectively (based on simulations to be discussed in later sections of this chapter) for the dichroic array. With this array we gain a factor of 1.35 in sensitivity, which motivates the decision to switch from the baseline plan for the 220 GHz only array. Moreover, this will only inflate the noise in the 90 GHz maps by 8%. In more recent applications of this technology, for e.g.

AdvACT, we increased the number of readout channels and optimized the optical design to optimally field multichroic arrays. With perfect optimization a single multichoric array would be equivalent to 1.7 times a single frequency detector array in terms of sensitivity while also boosting spectral coverage.

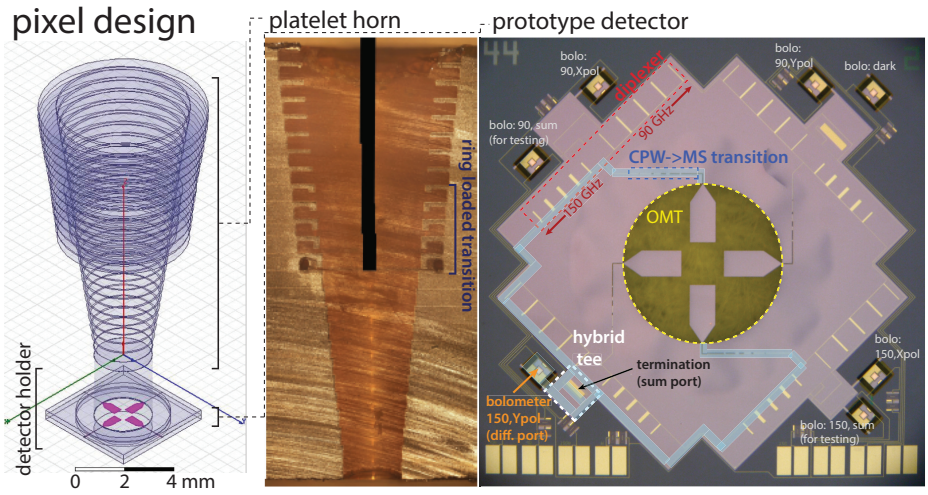

Figure 3.4: *Left:* design of a single horn coupled multichroic polarimeter with labels on the major components. *Center:* A photograph of a cross-section of a broad-band ring-loaded corrugated feed horn fabricated by gold plating a stack of etched silicon platelets. *Right:* A photograph of a prototype 90/150 multichroic detector with the major components labeled. A description of these components is in the text. For clarity, the path light follows to reach the bolometer corresponding to Y polarization in the 150 GHz band has been highlighted.

Figure 3.4 shows a design of a single multichroic polarimeter with sensitivity to the 90 and 150 GHz CMB bands, a photograph of a cross-section of a prototype feed (courtesy: Jim Beal), and a photograph of a prototype detector chip. The beam pattern is defined by a broad-band ring-loaded corrugated feedhorn [147] which couples light onto a planar detector chip that sits above a waveguide back short to prevent leakage of electromagnetic fields from the waveguide. A broad-band Ortho-Mode Transducer (OMT) [84] separates the incoming radiation according to linear polarization and couples it to high impedance Co-Planar Waveguide (CPW) lines. The Y-polarized light is split onto the two vertically oriented OMT probes and propagate through identical electrical paths that have been highlighted in the figure. The signal then transitions onto low impedance Micro-Strip (MS) lines via a broad-band CPW to MS transition. Next, diplexers comprised of two separate five pole resonant stub band-pass filters split each signal into two frequency channels with 75-110 and 125-170 GHz pass-bands. The signals from opposite OMT probes within a single frequency band are then combined onto a single MS line using the difference output

of a hybrid tee [149]. Two microstrip lines are required to cross over on the way to the hybrid tee. These signals are detected using Transition Edge Sensor (TES) bolometers and read out using SQUIDs. Signals appearing at the sum output of the hybrid are routed to a termination resistor and discarded. The circuit is symmetric and the signal path length on the microstrip lines is identical for both frequency bands and both polarizations. These detectors operate over a 2.25:1 ratio bandwidth over which round waveguide is multimoded. However, the TE11 mode (which has desirable polarization properties) couples to opposite fins of the OMT with a 180° phase shift while the higher order modes which couple efficiently to the OMT probes have a 0° phase shift. This fact allows the hybrid tee to isolate the TE11 signal at the difference port and reject the unwanted modes at the sum port. This ensures single moded performance over our 2.25:1 bandwidth. For testing purposes, the prototype pixel (shown in Figure 3.4) included additional bolometers connected to the hybrid tee sum port. The architecture described above offers excellent control over beam systematics provided by corrugated feeds, a frequency independent polarization axis defined by the orientation of the planar OMT, and a metal skyward aperture to minimize electrostatic buildup that is useful for future space applications [150]. Next, we describe each component on the pixel in further detail. Each post-OMT component was separately simulated and optimized using the AWR Microwave Office [151] simulation environment or the SONNET full-wave EM simulation software or a combination of the two. The feedhorn was designed by Harrison Smith. The OMT was designed by Prof. Jeff McMahon.

3.3.1 Ring-loaded Corrugated Feedhorns

Electromagnetic radiation is coupled to the planar detector wafer using a ring-loaded corrugated feed-horn [147], whose design is similar to a standard corrugated feed but with the addition of five ring-loaded sections that form a broad-band impedance matching transition between the round input waveguide and the corrugated output guide that defines the beam pattern. It essentially acts like an adiabatic transmission line changing the impedance gradually along the horn's length from the wave impedance in the waveguide to the impedance of free space, ($\sim$377 Ω), or an optical medium with a smoothly varying refractive index. In addition, this widens the aperture (7.05 mm) to a few times of the wavelength from the narrow aperture of the waveguide (2.4 mm), thus preventing diffraction of the waves issuing from it, resulting in a narrow well directed radiation pattern. The corrugation along the surface of the taper imparts the desirable characteristics of low cross-polarization and symmetric beam. This horn was optimized by Harrison Smith using the HFSS software

package to produce a round beam with low cross-polarization over a band from 70 to 175 GHz, but has excellent performance up to 225 GHz. Prototypes (including the one that has been cut in half and photographed in Figure 3.4) have been fabricated by gold-plating stacks of micro-machined silicon wafers. This fabrication method is nearly identical to what was done for the previous generation of single frequency NIST horn coupled polarimeters [152] and is the most cost effective way to produce thermal coefficient of expansion matched ring loaded feeds for the millimeter band. The simulated properties of the feed-horn cross-pol [1], insertion loss [2], return loss [3], and beam ellipticity [4] are shown in Figure 3.5.

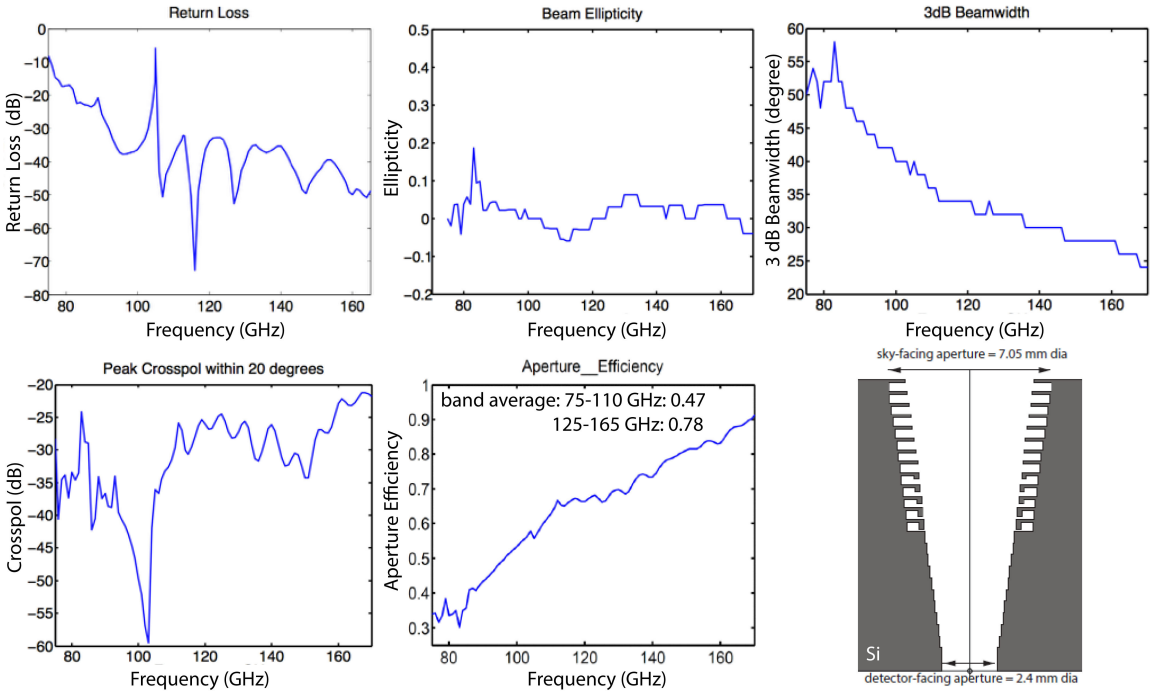

Figure 3.5: Simulated properties of the ring-loaded corrugated feedhorn. The bottom right panel shows a schematic of the cross-section of the feed.

The beam pattern of a single prototype feed was measured at a number of frequencies using a warm beam mapping facility in the McMahon lab. The measurements (see Figure 3.6) show better than 1% agreement with theoretical predictions based on HFSS[122]

[1] Cross-Polarization Isolation measures how much leakage there is between the two polarizations in a given antenna

[2] it is the ratio between output power and input power and tells us how much power is lost in the signal passing through the component

[3] it is the ratio between the reflected power and input power and tells us how much of the input signal is reflected

[4] it is a measure of how circular a beam is

simulations, and demonstrate round beams with low cross-polarization. Calculations of the temperature to polarization leakage induced by these beams demonstrate that these pixels achieve temperature to polarization leakage subdominant to the CMB B-modes for $r = 0.01$. The array was fabricated at NIST, Boulder by stacking together twenty-five 500 μm thick etched silicon wafers and gold-plated thereafter. A photo and some measurements performed on the feedhorn array are shown in Figure 3.7. The measured return loss was well below 1% across the band except at a couple of points. We have checked to make sure that these would not be a problem. The measured insertion loss was consistent with expectations

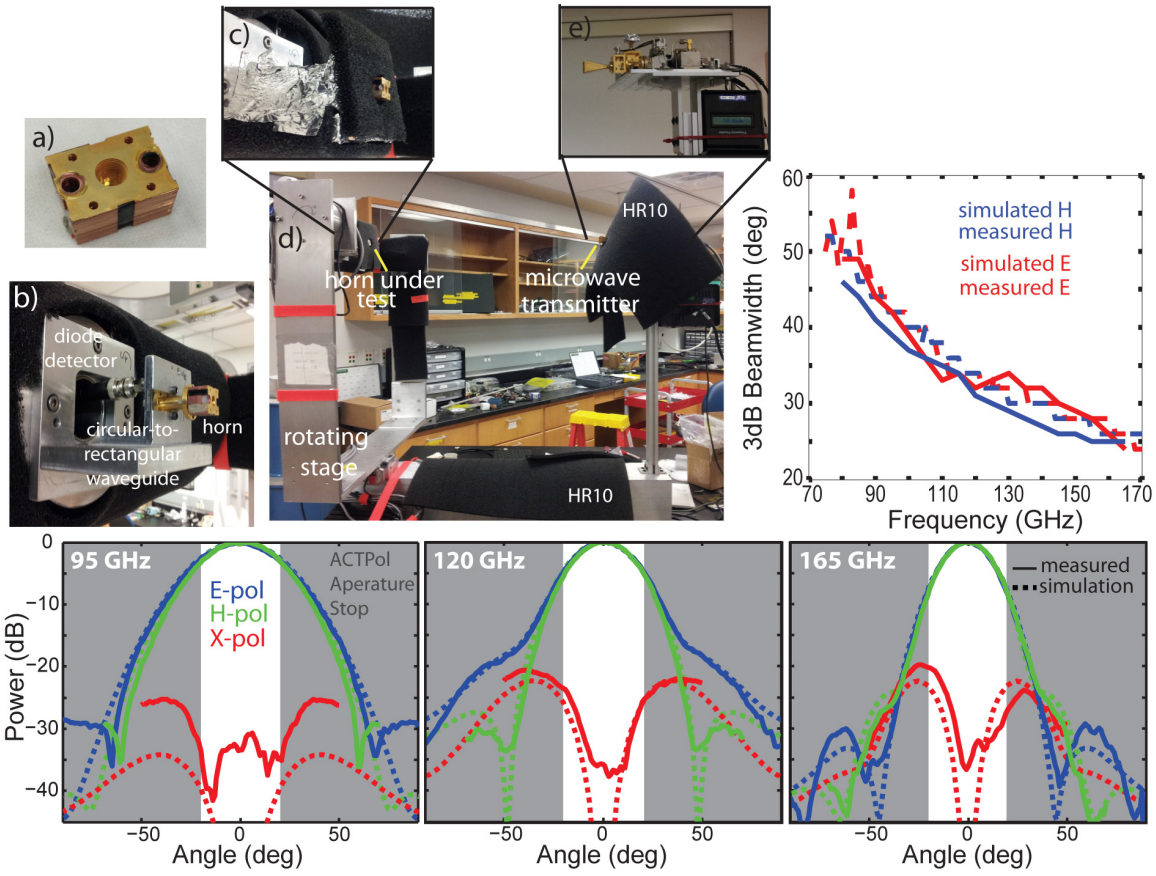

Figure 3.6: *a:* A photo of a single prototype gold-plated stacked silicon feed fabricated at NIST, Boulder, *d:* a photo of the warm beam-mapping setup in our lab to measure the beam pattern of the prototype feed, *b, c and e:* zoomed in sections of the beam-mapper set-up showing the horn under test and the transmit horn, *top right:* comparison between measurements and simulations of the half power beamwidth over a range of frequencies. *bottom:* Measurements and simulations of the beam pattern of the ring loaded corrugated feed horn. These measurements of the E-, H-, and X-pol beams were made using a room temperature beam mapping system. The angles at which the beams hit the ACTPol aperture stop are greyed out.

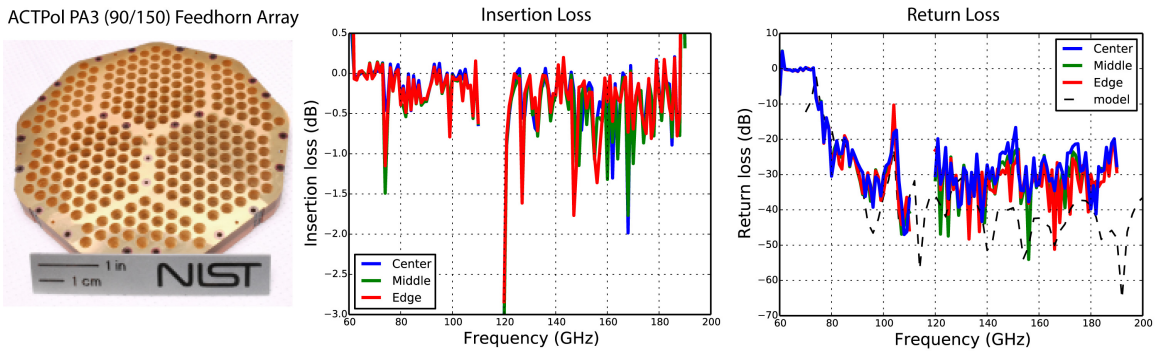

Figure 3.7: A photograph of the ACTPol PA3 feed-horn array fabricated at NIST, Boulder along with measurements of return loss and insertion loss performed at different locations on the array using a Vector Network Analyzer (VNA). Plot Courtesy: Justus Brevik

3.3.2 Co-Planar Waveguide (CPW) and Microstrip (MS) Transmission Lines

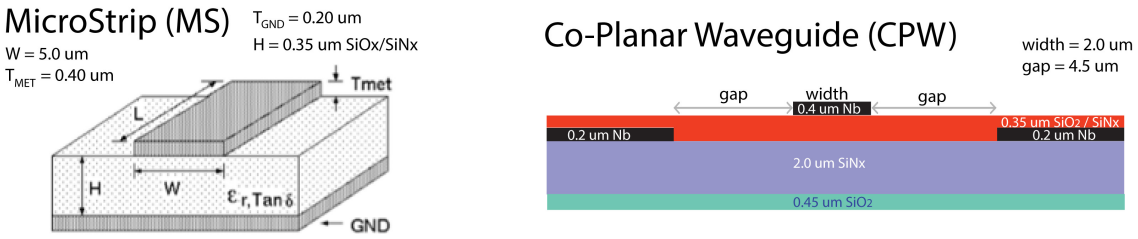

Figure 3.8: Schematics of the CPW and MS lines implemented in our pixel design. The dielectric layers along with the thicknesses are noted.

The properties of the transmission lines on which the signal is routed from the OMT to the bolometric detectors are presented here. A MS transmission line consists of a center conductor trace and a ground plane conductor separated by a dielectric layer as shown in the left panel of Figure 3.8. The characteristic impedance of the MS can be adjusted by varying the width of the center trace. A CPW transmission line in its basic form comprises a center conductor trace on an underlying dielectric substrate with ground plane conductors on either side (on the same plane as the center conductor) separated by a fixed gap. In our pixel, we would need a transition between CPW and MS which would then require an electrical contact or via between two layers. We would like to avoid vias for fabrication related reasons. To circumvent the vias, we use a pseudo-CPW (not really co-planar) geometry as shown in the right panel of Figure 3.8, where the ground plane is below the dielectric layer. This geometry approximately behaves as a CPW because the thickness of the dielectric layer is much less than the gap between the pseudo-CPW center trace and the

ground plane. This figure also shows our full dielectric stack, which consists of a thicker SiN_x dielectric layer under the ground plane as well as an SiO_2 layer. The propagation wavelength is a useful parameter while designing circuit components using transmission lines. For waves propagating in a dielectric medium, the propagation (guide) wavelength is given by

$$\lambda_g = \frac{c}{f\sqrt{\varepsilon_{eff}}} \tag{3.4}$$

where ε_{eff} is the effective dielectric constant. We simulated the CPW and MS geometries using SONNET and obtained the characteristic line impedances Z_o and effective dielectric constants ε_{eff} as listed in Table 3.1. We switched from a SiO_x dielectric layer for ACTPol to a SiN_x dielectric layer for AdvACT because the latter has a lower dielectric loss tangent. In addition to increased efficiency, this also naturally leads to a smaller pixel size because the dimensions of each circuit component is reduced by a factor roughly equal to $\sim Z_{o,SiO_x}/Z_{o,SiN_x}$.

The center conductor is implemented on a 0.4 μm thick Niobium (Nb) layer while the ground plane is implemented on a 0.2 μm thick Nb layer, separated by a 0.35 μm thick SiO_x/SiN_x dielectric layer. The superconducting Nb layers are modeled in the full-wave EM simulator SONNET using the "general metal model". In the simulation, the conductor layers of finite thickness were approximated by infinitesimally thin sheets with appropriate surface inductance. When the thickness t of the superconductor is not too large compared to the London penetration depth λ_L, the surface inductance L_s is given by:

$$L_s = \mu_o \lambda_L coth\left(\frac{t}{\lambda_L}\right) \tag{3.5}$$

where μ_o is the permeability of free space, and λ_L = 0.085 μm superconducting London penetration depth for Nb [153]. This takes care of the kinetic inductance effect in superconducting niobium.

The MS was fabricated by placing a 0.35 μm thick layer of SiO_x on top of a Niobium ground plane with a 5 μm wide center trace placed on top of the oxide layer. The CPW sections were fabricated by removing the ground plane in boxes that were 11 μm wide to approximate CPW with a 2 μm wide center trace placed on top of the oxide layer and 4.5 μm gap on each side. It may be required to bend the CPW and MS lines at several locations on the way from the OMT to the TES. This introduces a discontinuity which changes the line characteristic impedance, and could lead to unwanted reflections of the signal ul-

Table 3.1: Co-Planar Waveguide and Microstrip Transmission Line Properties

	CPW		*MS*	
Dielectric	Z_o	ε_{eff}	Z_o	ε_{eff}
SiO_x	114.4Ω	3.17-0.01j	14.1Ω	3.32-0.022j
SiN_x	110.2Ω	3.59-0.01j	10.8Ω	9.40-0.018j
Properties of:	SiO_x	SiN_x		
ε_r	4.318	6.8		
Tan δ	2e-3	7.8e-4		

timately resulting in lower efficiency. In addition, the effective length of the transmission line containing bends becomes shorter than the centerline length as electromagnetic waves like to take shortcuts. The effects of such bends can be minimized by mitering or curving the transmission lines. I studied the effects of various mitering schemes and the effective transmission line lengths using SONNET simulations in order to determine the best way to bend the CPW and MS lines. The findings are summarized in Appendix D.

3.3.3 Broadband OMT

Radiation at the throat of the horn is coupled onto a microwave transmission line using a planar ortho-mode transducer (OMT), whose design is based on the OMT described in Kogut et al. [148]. This OMT (see Figure 3.9) consists of four probes suspended on a silicon-nitride membrane inside a waveguide. The waveguide is terminated in a back-short approximately one quarter wavelength behind the probes. Each probe couples radiation from the circular input waveguide onto Co-Planar Waveguide (CPW) transmission lines that have an impedance of $\sim$140 Ω. Pairs of probes on opposite sides of the guide couple to a single incoming linear polarization. This OMT is operated over a bandwidth which includes the TE11, TM01 and many other higher order modes in circular waveguide. The TM01 mode will be rejected with a corrugated horn or a section of narrow wave guide in front of the OMT.

The shape of the probes, and backshort were chosen using HFSS simulations to optimize the total co-polar coupling. During these simulations the wave guide diameter, CPW geometry, and choke geometry were fixed. The diameter of the choke was chosen to be one quarter free-space wave-length at the center of the OMT. The width of the gap above and between the choke was chosen to accommodate machining tolerances in the holder and

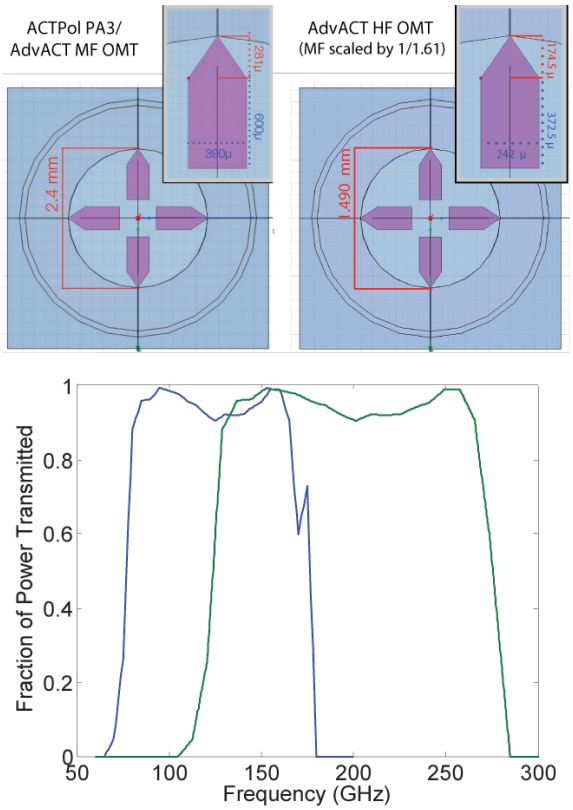

Figure 3.9: *top left:* A schematic of the ACTPol PA3 OMT with the fin dimensions shown in the inset. The AdvACT MF (90/150 GHz) OMT is identical to this one. *top right:* Scaling down the PA3 OMT dimensions by a factor of 1.61 gives the OMT used for the AdvACT HF (150/230 GHz) array. *bottom:* The OMT Coupling for ACTPol 90/150 pixel (blue) and AdvACT 150/230 pixel (green).

possible wrinkling in the SiN_X membrane layer. Simulations showed that a 100 gap gives less than 1.5% radiative loss. The CPW is defined by a 2 wide center trace with two 4.5 gaps separating it from a niobium ground, all of which are suspended on a SiN_x membrane. There is 50 of vacuum gap above and below the CPW with metal boundaries which are defined by the choke structure. Simulations show that provided the vacuum gap is larger than 10 there is no effect on the impedance of the CPW. A simulation of the coupling from this OMT is shown in Figure 3.9. The TE11 co-polar coupling, averaged over our bands 70-110 and 125-175 GHz is 96.3% and 94.3% respectively. The loss comes from a combination of reflections and radiation into the gap in the wave guide. The cross polarization is less than -40 dB ($\sim$0.01%) across the entire frequency range. Detailed tolerances of the OMT design for the first two 148 GHz ACTPol arrays are presented in McMahon et al [85].

3.3.4 CPW to MS Transition

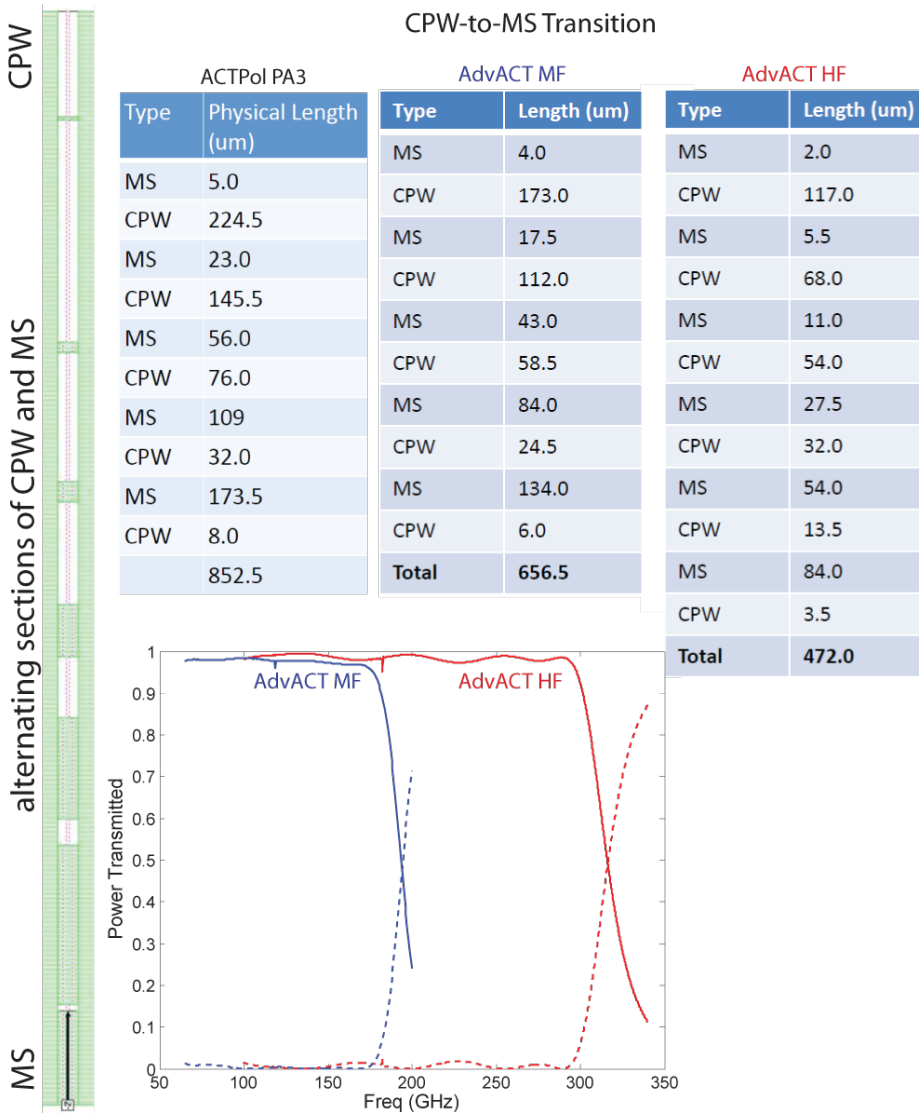

Type	Physical Length (um)
MS	5.0
CPW	224.5
MS	23.0
CPW	145.5
MS	56.0
CPW	76.0
MS	109
CPW	32.0
MS	173.5
CPW	8.0
	852.5

Type	Length (um)
MS	4.0
CPW	173.0
MS	17.5
CPW	112.0
MS	43.0
CPW	58.5
MS	84.0
CPW	24.5
MS	134.0
CPW	6.0
Total	**656.5**

Type	Length (um)
MS	2.0
CPW	117.0
MS	5.5
CPW	68.0
MS	11.0
CPW	54.0
MS	27.5
CPW	32.0
MS	54.0
CPW	13.5
MS	84.0
CPW	3.5
Total	**472.0**

Figure 3.10: CPW-to-MS transition design for ACTPol PA3, AdvACT MF, and AdvACT HF pixels, consisting of alternating sections of CPW and MS (length of each section shown in the tables). It behaves as a low pass filter as shown in the plot.

The wave impedance at the throat of the horn waveguide is too large to match to a MS transmission line with a practical geometry, so we use a CPW transmission line to receive the electrical signal from the OMT. High impedances are difficult to realize on a MS line because the width of the center trace would have to be made so small that it would be highly susceptible to fabrication tolerances but can be easily achieved on a CPW by simply increasing the gap between the center trace and the ground plane. However, we ultimately want to transmit the power further via a MS transmission line on which it is much simpler

to implement the circuit elements down the line both theoretically and from a fabrication point of view. Therefore, a CPW-to-MS transition is required, which we implement using alternating sections of CPW and MS lines of carefully chosen lengths, behaving as a stepped impedance transformer. This also acts like a low-pass filter. The characteristic impedances of the CPW and MS are input to a transmission line model then used to optimize the electrical length, θ of each section so as to minimize reflections over the desired band from 70 to 175 GHz. This optimization is carried out using the AWR Microwave Office circuit simulation software. The electrical lengths are converted to physical lengths by using the equation $l = \theta\lambda_g/2\pi$, where λ_g is the guide wavelength given by Equation 3.4. The full design is then validated using SONNET. Over the desired band the reflections are well below 1% corresponding to a negligible loss in efficiency. Figure 3.10 presents the ACTPol PA3 (90/150) and AdvACT MF (90/150) and HF (150/230) designs. The design goals for ACTPol PA3 and the AdvACT MF pixels were similar so only PA3 is plotted in the figure.

3.3.5 Diplexer

Once on the microstrip line, the signal is fed into a diplexer that splits the signal path into two. The diplexer consists of two bandpass filters with 3 dB (half-power) bandwidths 68-108 GHz and 128-168 GHz. Bandpass filters can be designed to be comprised of shunt short-circuited stubs that are $\lambda_g/4$ long with connecting lines that are also $\lambda_g/4$ long, where λ_g is the guided wavelength in the medium of propagation at the midband frequency f_0. The short-circuit is realized by using vias running from the end of the MS stub center trace to the ground plane. These vias are tricky to implement on the 4 mm diameter membrane and hence the diplexer is placed outside the membrane. For a five-pole stub filter, the bandpass characteristics will then depend on the characteristic admittances of the stub lines denoted by Y_i (i = 1 to 5) and the characteristic admittances of the connecting lines denoted by $Y_{i,i+1}$ (i = 1 to 4). The design equations for determining these characteristic admittances

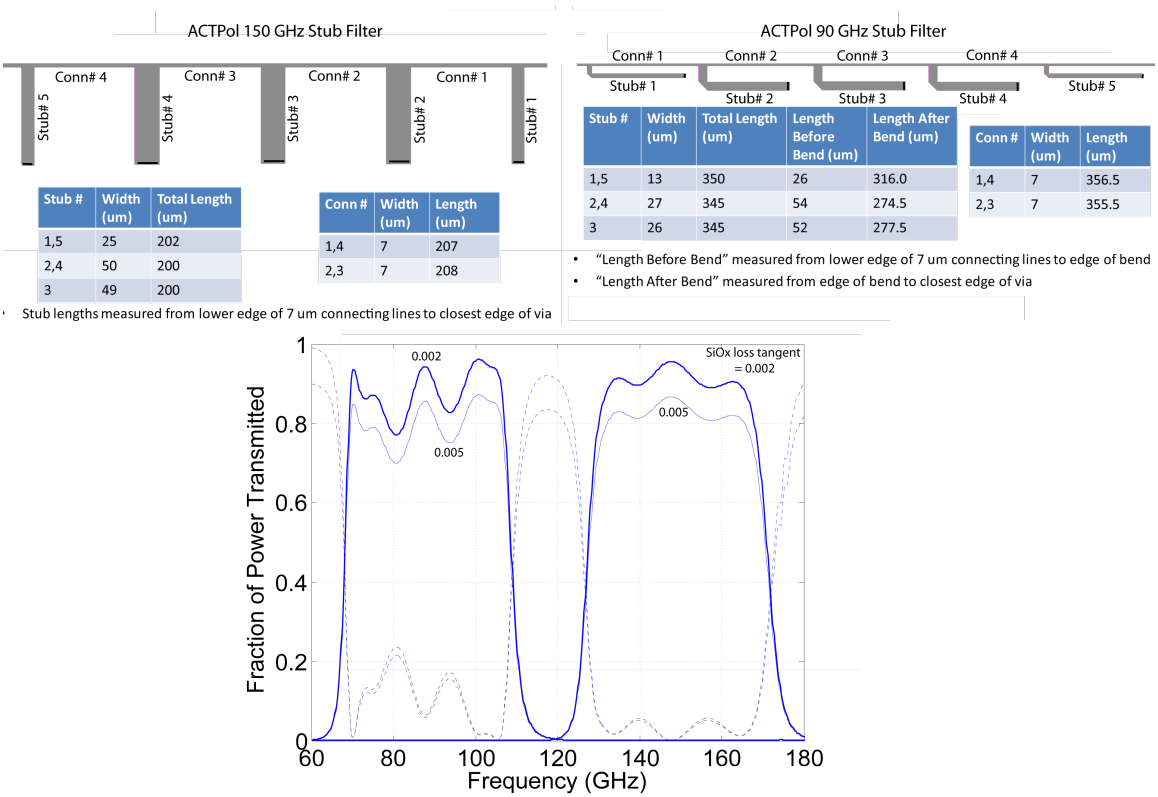

Figure 3.11: Designs of the PA3 five-pole resonant stub filters. The combined diplexer response is simulated for two different values of SiO_x loss tangent, 0.002 and 0.005.

described in [154] are presented below.

$$\begin{aligned}
\frac{J_{1,2}}{Y_0} &= g_0\sqrt{\frac{2g_1}{g_2}} \\
\frac{J_{4,5}}{Y_0} &= g_0\sqrt{\frac{2g_1g_6}{g_0g_4}} \\
\frac{J_{i,i+1}}{Y_0} &= \frac{2g_0g_1}{\sqrt{g_ig_{i+1}}}\ for\ i\ =\ 2\ to\ 3 \\
\theta &= \frac{\pi}{2}\left(1-\frac{FBW}{2}\right)
\end{aligned} \tag{3.6}$$

where, $Y_o = 1/Z_o$ is the characteristic admittance of the MS line, and g_i are the element values of a ladder-type lowpass prototype filter such as a Chebyshev, given for a normalized cutoff Ω_c = 1.0 as: $g_0 = g_6 = 1.0, g_1 = g_5 = 1.1468, g_2 = g_4 = 1.3712, g_3 = 1.9750$ [154, 155]. Z_o is the characteristic impedance of the terminal microstrip line with a 5 µm wide center conductor, i.e., 10.8 Ω. $\omega_o = \sqrt{\omega_{c1}\omega_{c2}}$ is the desired center frequency,

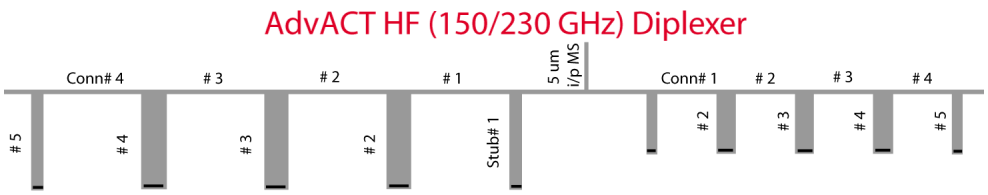

*150 GHz filter dimensions

Stub #	Width (um)	Total Length (um)
1,5	18.5	155.0
2,4	38.5	153.0
3	37.5	154.0

Conn #	Width (um)	Length (um)
1,4	5.5	159.0
2,3	5.5	160.0

Diplexer

150 GHz Distance	220 GHz Distance
103 um*	94.5 um*

*5 um wide microstrip Distances are from edge of T-junction to first stub in filter

*220 GHz filter dimensions

Stub #	Width (um)	Total Length (um)
1,5	15.0	97.5
2,4	29.5	96.5
3	29.0	96.5

Conn #	Width (um)	Length (um)
1,4	5.5	97.0
2,3	5.5	97.0

Stub lengths measured from lower edge of 5.5 um connecting lines to closest edge of via

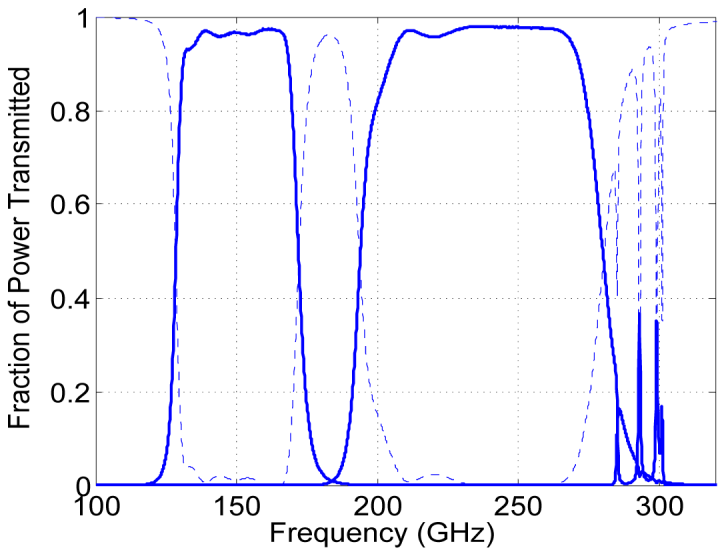

Figure 3.12: Design of the AdvACT HF diplexer along with the simulated passbands.

and $\Delta = \omega_{c2} - \omega_{c1}$ is the desired bandwidth when ω_{c1} and ω_{c2} are the lower and upper 3 dB cut-off frequencies of the filter. The Fractional Bandwidth, FBW = Δ/ω_o. Using the

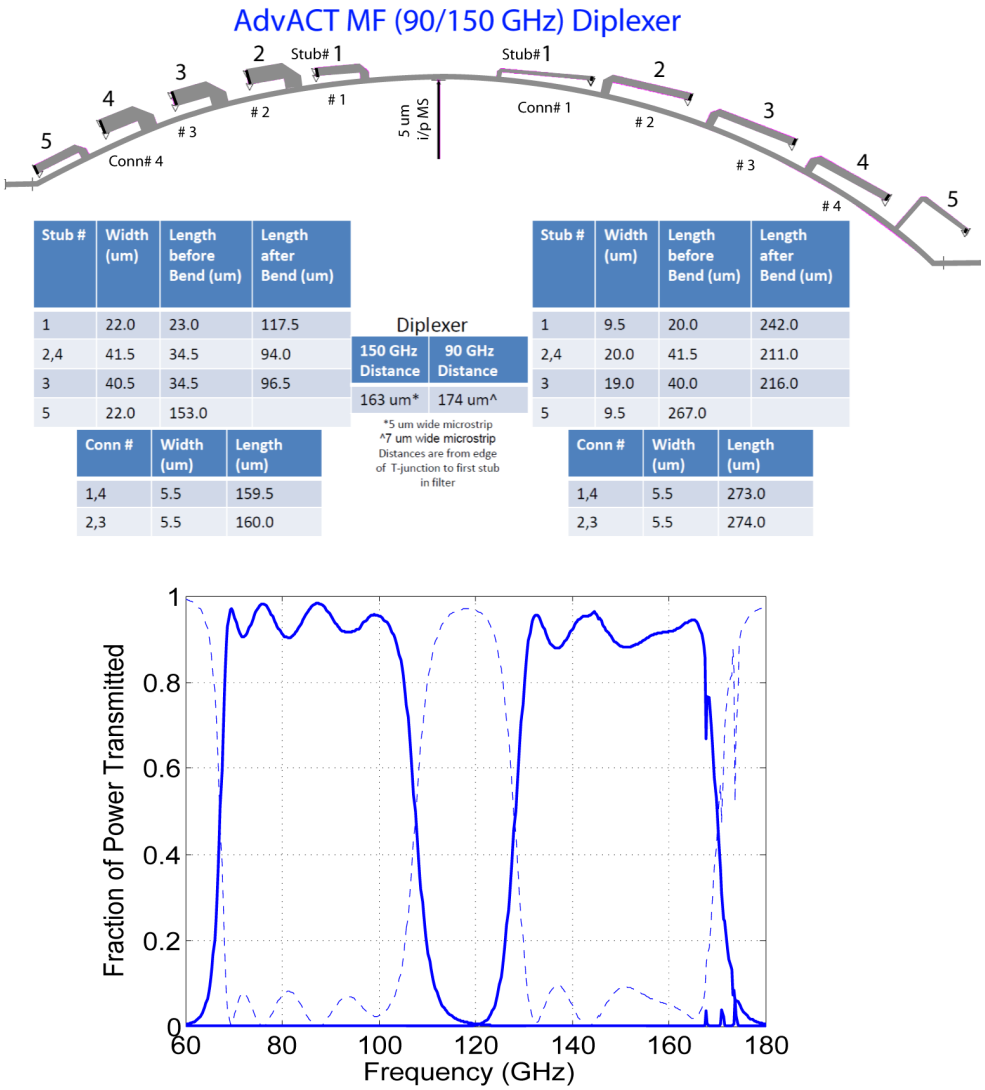

Stub #	Width (um)	Length before Bend (um)	Length after Bend (um)
1	22.0	23.0	117.5
2,4	41.5	34.5	94.0
3	40.5	34.5	96.5
5	22.0	153.0	

Conn #	Width (um)	Length (um)
1,4	5.5	159.5
2,3	5.5	160.0

Stub #	Width (um)	Length before Bend (um)	Length after Bend (um)
1	9.5	20.0	242.0
2,4	20.0	41.5	211.0
3	19.0	40.0	216.0
5	9.5	267.0	

Conn #	Width (um)	Length (um)
1,4	5.5	273.0
2,3	5.5	274.0

Figure 3.13: Design of the AdvACT HF diplexer along with the simulated passbands.

calculated J_i's and θ, we can now compute the characteristic admittances as below:

$$
\begin{aligned}
N_{i,i+1} &= \sqrt{\left(\frac{J_{i,i+1}}{Y_0}\right)^2 + \left(\frac{g_0}{g1} tan\theta\right)^2} \quad for\ i\ =\ 1\ to\ 4 \\
Y_1 &= Y_0\left(N_{1,2} - \frac{J_{1,2}}{Y_0}\right) \\
Y_5 &= Y_0\left(g_5 g_6 - g_0 g_1\right) tan\theta + Y_0\left(N_{n-1,n} - \frac{J_{n-1,n}}{Y_0}\right) \\
Y_i &= Y_0\left(N_{i-1,i} + N_{i,i+1} - \frac{J_{i,i+1}}{Y_0} - \frac{J_{i,i+1}}{Y_0}\right) \quad for\ i\ =\ 2\ to\ 4 \\
Y_{i,i+1} &= Y_0\left(\frac{J_{i,i+1}}{76}\right) \quad for\ i\ =\ 1\ to\ 4
\end{aligned}
\tag{3.7}
$$

We first design the two stub filters individually and optimize them in SONNET, before combining the two via a microwave T-junction [155], which is again optimized in SONNET to minimize reflections.

Figure 3.11 shows the design of the 90 and 150 GHz stub filters for the ACTPol PA3 pixel along with the passbands. We scaled the stubs to get the AdvACT HF diplexer presented in Figure 3.12. For AdvACT MF, we bent all the stubs and curved the diplexer as shown in Figure 3.13 in order to save space on the chip and fit all the components on a more compact pixel compared to ACTPol PA3.

The stub filters presented above are distributed element filters, with good (though not perfect) suppression of even-order harmonics, i.e., spurious responses at $2\omega_o$, $4\omega_o$, and so on, ω_o being the center frequency of the passband. The odd-order harmonics, i.e., spurious responses at $3\omega_o$, $5\omega_o$, and so on, are mostly cut-off by the OMT as well as free-space filters in our optics chain. The spurious response of the 90 GHz bandpass stub filter, of the order of $\sim$5% centered at $\sim$180 GHz, lies partially within our frequency range of interest. In order to ensure that this spurious is completely rejected, we employ a stepped-impedance low-pass filter after the stub filter in the 90 GHz signal path. This low-pass filter is designed in Microwave Office and optimized in SONNET. The designs for the AdvACT MF and HF low-pass filters are presented in Figure **??**. The design approach for the ACTPol PA3 low-pass filter was similar, but

3.3.6 Hybrid Tee

$$\begin{aligned} P_{sum,\ even} &= \frac{1}{2}(|S_{41}+S_{42}|)^2 \\ P_{sum,\ odd} &= \frac{1}{2}(|S_{41}-S_{42}|)^2 \\ P_{diff,\ even} &= \frac{1}{2}(|S_{31}+S_{32}|)^2 \\ P_{diff,\ odd} &= \frac{1}{2}(|S_{31}-S_{32}|)^2 \ \text{(desired signal)} \end{aligned} \tag{3.8}$$

The hybrid tee implemented on microstrip is a 4-port network with two inputs and two outputs (see Figure 3.14) and is based on the design by Knoechel and Mayer [149]. The signals from opposite OMT probes within a single frequency band constitute the two inputs. This requires two microstrip lines crossing over on the way from the diplexer to the

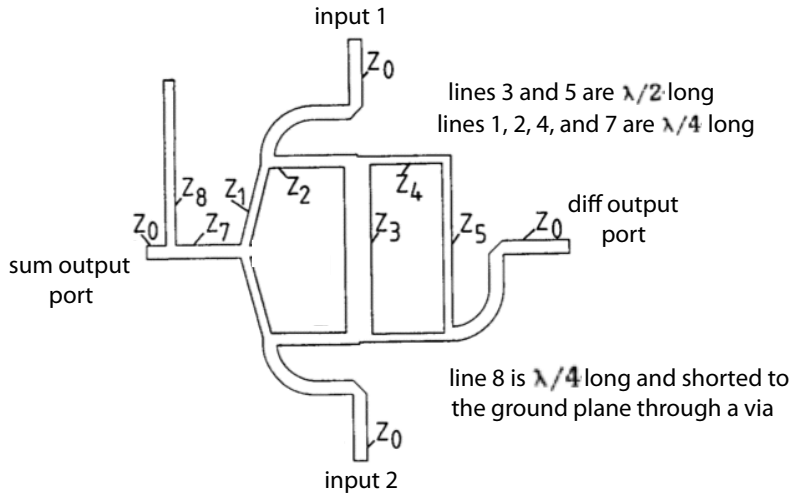

Figure 3.14: A schematic of the hybrid tee consisting of sections of microstrip lines of given lengths as shown and carefully optimized widths [149].

hybrid tee. The two outputs are essentially the sum and the difference of the signals at the two input ports given by Equation 3.8. The odd and even modes at each output port refer to the various modes of electromagnetic radiation that propagate through a round waveguide, which is multimoded over 2.25:1 bandwidth. The TE11 mode (which has desirable polarization properties) couples to opposite fins of the OMT with a 180° phase shift while the higher order modes which couple efficiently to the OMT probes have a 0° phase shift. This fact allows the hybrid tee to isolate the TE11 signal at the difference port and reject the unwanted modes at the sum port. Signals appearing at the sum output of the hybrid are routed to a termination resistor and discarded. This ensures single-moded performance over our 2.25:1 bandwidth. Figure 3.15 shows the simulated s-parameters of the hybrid response.

3.3.7 Nb-Au Transition

The signal appearing at the sum output port of the hybrid is discarded by routing to a gold (Au) termination resistor, where the signal gets absorbed. The signal is transitioned from Nb to Au through a stepped-impedance transformer consisting of alternating Nb and Au sections, designed the same way as the CPW-to-MS transition. This reduces unwanted reflections back to the hybrid tee. The design is shown in Figure 3.16 and the reflections are plotted assuming different values for conductivity of Au.

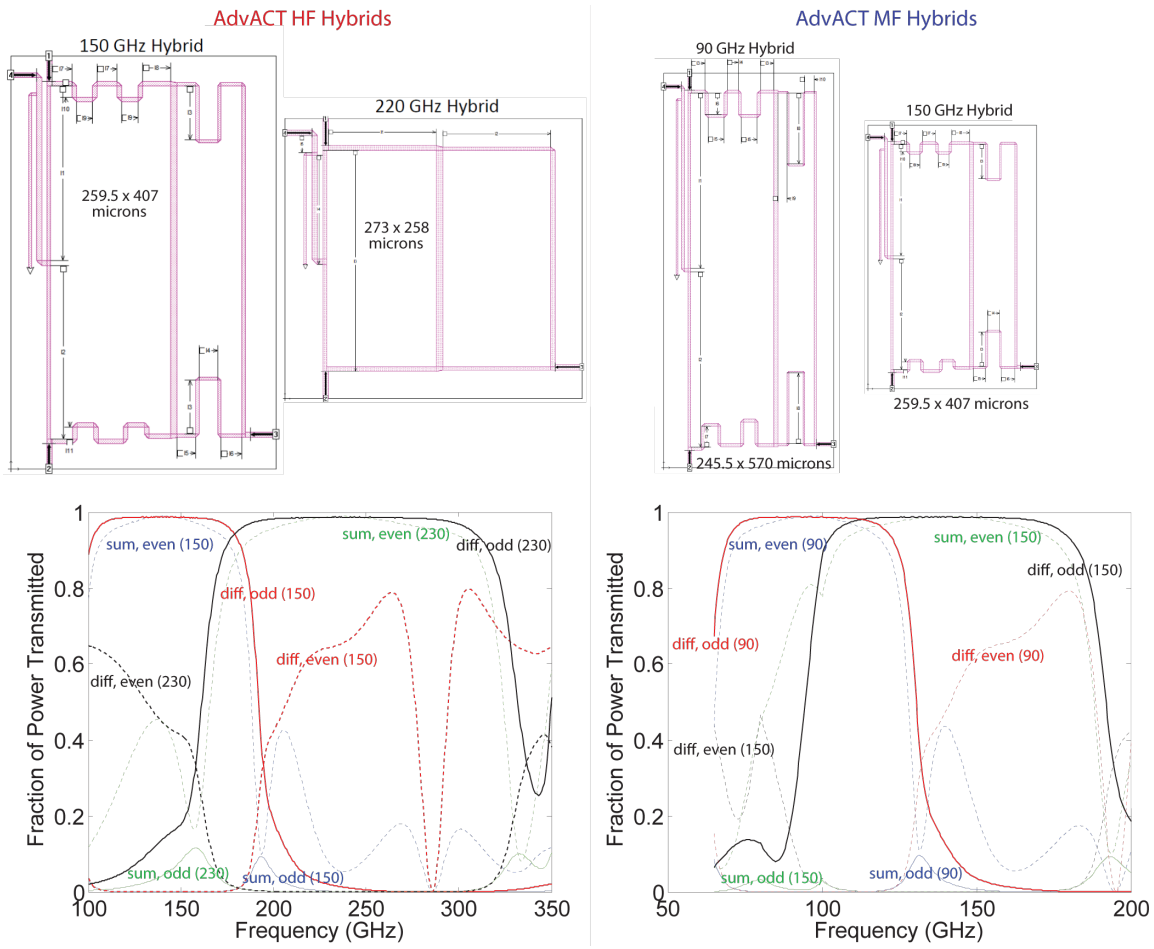

Figure 3.15: Designs of the Hybrids for AdvACT MF and HF pixels. The detailed dimensions are excluded for clarity. The sum port output is terminated while the difference port output (red and black lines) of each hybrid is routed to a TES. The difference port, odd-mode output (solid lines) represent our desired signal while the power in the difference port, even-mode output (dashed red and black lines) is suppressed by the on-chip bandpass filters before the hybrid.

3.3.8 TES bolometers

The desired TE11 signal at the difference output port of the hybrid tee is routed to a bolometric transition edge superconductor detector. Designing the TES involved careful optimization of several detector parameters through tuning of the TES geometry described in Ho et al. [158].

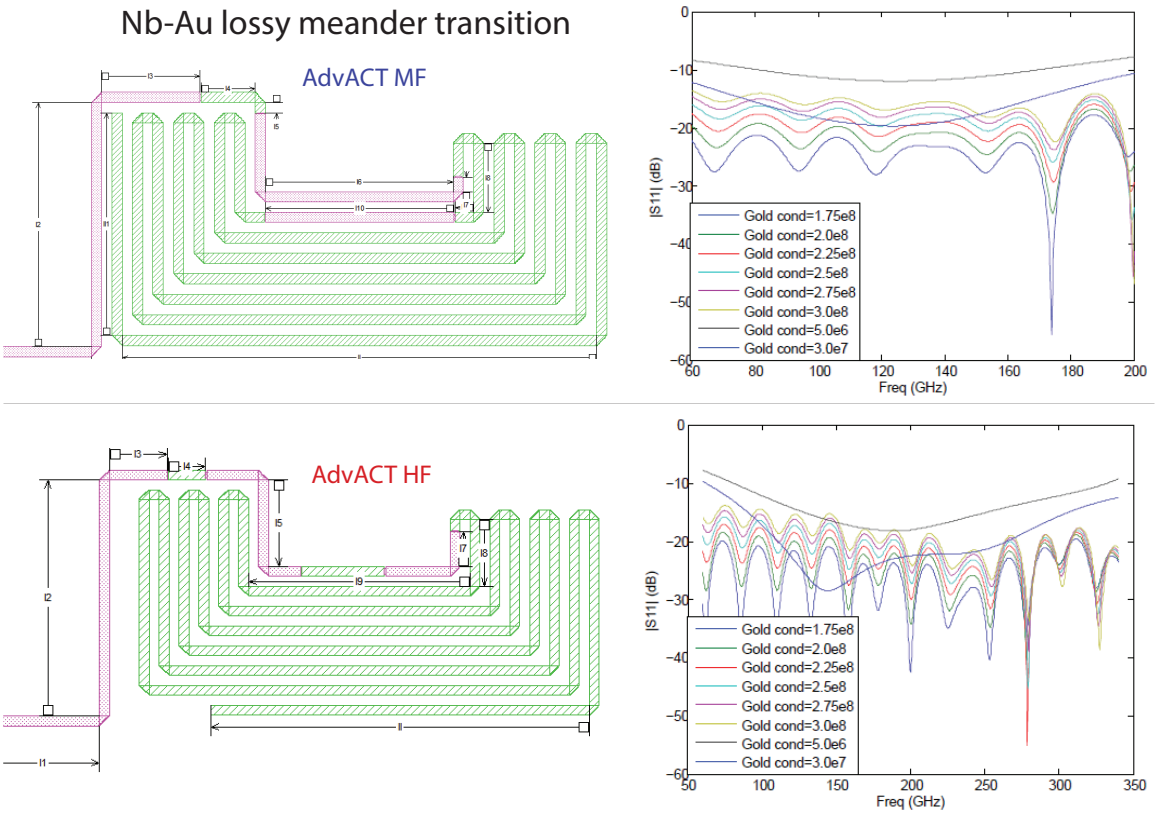

Figure 3.16: Designs of the stepped-impedance Nb-Au transition for AdvACT MF and HF pixels consisting of alternating sections of Nb and Au. The detailed dimensions are excluded for clarity. The simulated reflections for different values of conductivity of Au (our best estimate lies within the range of simulated values) are shown.

3.3.9 Efficiency

Once we have designed the individual circuit components and simulated them in SONNET, we take the frequency response of all the components in the form of s-parameters and combine them in Microwave Office to get the full end-to-end frequency response. We can use this to estimate the detector optical efficiency, defined as the fraction of the power entering the feed-horn that reaches the TES bolometers. Optical efficiency loss occurs due to signal absorption by the SiO_x/SiN_x dielectric on which the signal lines are fabricated and some reflections in the signal lines and in the circuit components like the diplexer. Starting at the output of the OMT, we combine the post-OMT components: (1) CPW-to-MS transition, (2) Diplexer, (3) Low-pass filter, and (4) Hybrid-tee in Microwave Office. Among these, the diplexer is by far the dominant source of loss. In addition to these, the other major sources of loss are the OMT and the dielectric loss as the signal propagates through the long microstrip transmission lines. The contribution of the feed-horn and the

Nb-Au transition to loss in efficiency are negligible (<1%). We predict the loss in the various circuit components that are listed in Table 3.2 based on $\tan\delta = 0.005$ for the SiO_2 and $\tan\delta = 0.060$ for the SiN_x [156] dielectric layers. The optical efficiency averaged over the 70-110 GHz and 125-170 GHz bands are ∼72% and ∼64%, respectively. Recent NIST resonator measurements at ∼7 GHz suggest $\tan\delta \sim 0.002$ for SiO_x and $\tan\delta \sim 0.0008$ for SiN_x at our frequencies which would lead to higher efficiency. The combined frequency response (passband) is plotted in Figure 3.17 for the ACTPol PA3 and AdvACT pixels.

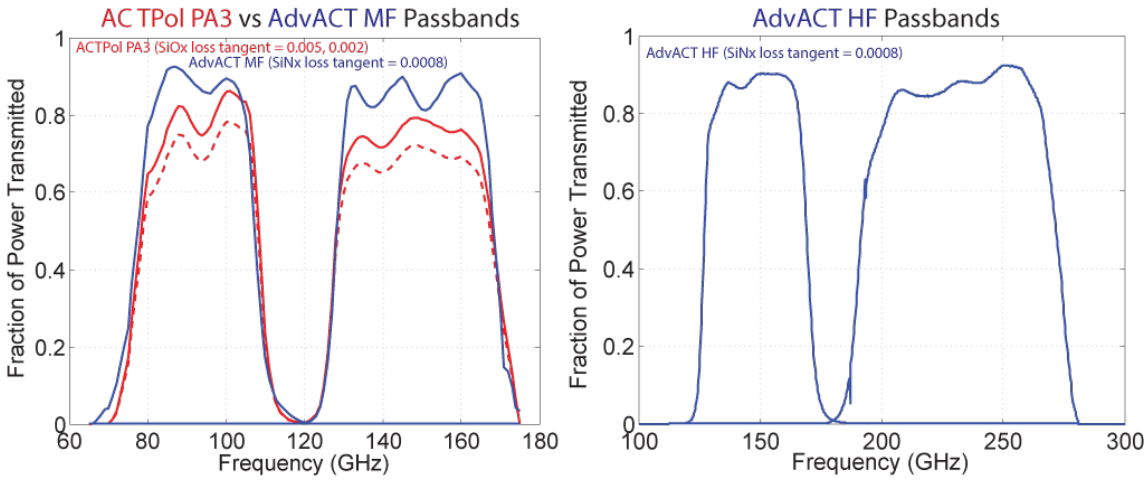

Figure 3.17: *left:* Simulated passbands for ACTPol PA3 and AdvACT MF pixels. The ACTPol PA3 passband is plotted for two different values of SiO_x loss tangent. *right:* Simulated passbands for the AdvACT HF pixel.

Table 3.2: Total Losses in post-OMT microwave components assuming SiO_x loss tangent = 0.005

Item	90 GHz loss	150 GHz loss
CPW→MS transition	5.3%	8.7%
bandpass filter	10 %	13.5%
hybrid tee	3.5%	3.3%
microstrip line	8.6%	14.5%
total efficiency†	72%	64%

† The losses in OMT and other components, for e.g., the Nb-Au transition and feed-horn amount to ∼4% and ∼6% in the 90 and 150 bands, respectively.

Figure 3.18 shows measurements and simulations of the detector pass-bands. These results show excellent agreement with simulations for the 90 and 150 GHz passbands both

for the nominal polarization sensitive bolometers and the extra test bolometers connected to the sum ports of the hybrid tee. This agreement verifies the function of the diplexer and confirms that unwanted modes are being correctly rejected by the hybrid tee.

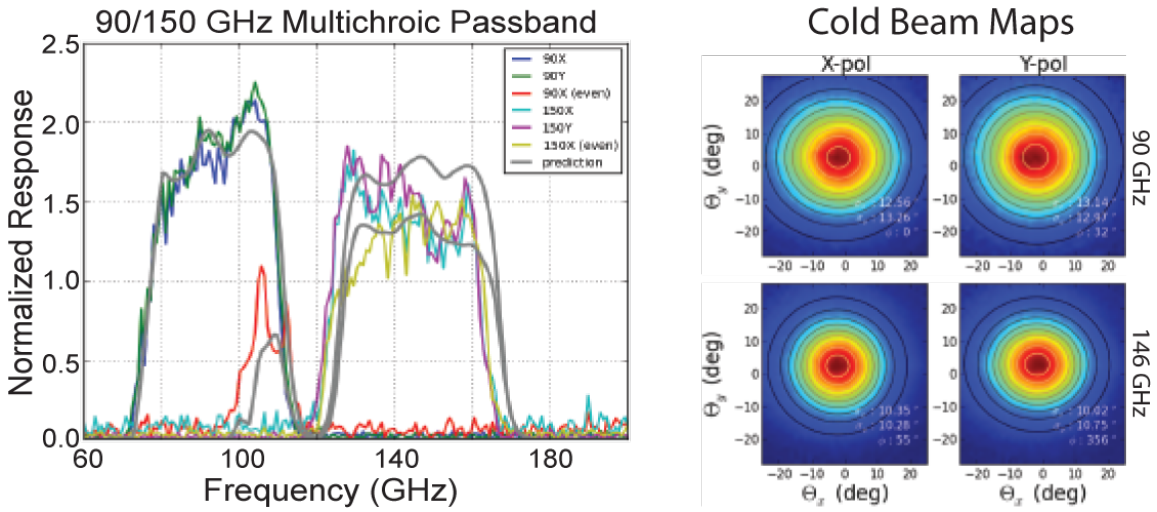

Figure 3.18: *left:* FTS measurements and simulations of the ACTPol prototype Multichroic (90/150 GHz) detector pass-bands. For the 90 and 150 GHz channels, measurements of both linear polarizations as well as the terminated sum port were carried out. The agreement between the sum port measurements and simulations show that these detectors are properly rejecting unwanted waveguide modes. The agreement between the measured and simulated pass-band for the nominal X and Y polarized pixels is good, but has a 2% shift in the band edges. *right:* The prototype detector beams as measured by raster scanning with a hot thermal source in the lab at NIST.

Figure 3.19 shows a picture of the AdvACT HF multichroic (150/230 GHz) pixel. Measurements of the AdvACT HF pixel are presented in Duff et al. [159]. The predicted lowering of loss in the various circuit components achievable by switching to a SiN_x dielectric are listed in Table 3.3. These were calculated based on assumptions for loss-tangent of SiO_x ($\tan\,\delta = 2\times10^{-3}$) and of SiN_x ($\tan\,\delta = 8\times10^{-4}$). The corresponding dielectric losses are shown in Figure 3.20.

3.4 Design tolerances

Repeatability in achieving the fiducial passband has been a concern as we have observed shifts of $\sim 4\%$ in the bands between different fabrication runs. We believe this could be attributed to changes in material properties and wafer uniformity. The passbands of the filters are sensitive to the properties of the dielectric layer, namely, relative dielectric

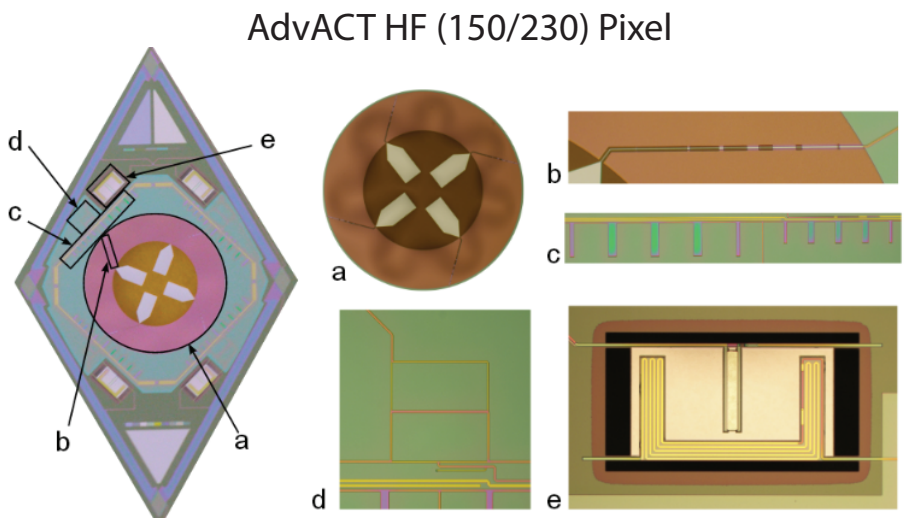

Figure 3.19: *left:* Optical microscope image of one high frequency 150/230 GHz multichroic AdvACT HF single pixel. *right:* Zoomed images of the major pixel components: a) the planar OMT, b) the CPW-to-MS transition, c) the in-line diplexer composed of two five-pole resonant stub filters, d) the 180° hybrid tee, and e) one of the AlMn TESs, which is thermally isolated on a SiN_x membrane suspended with four narrow legs. Figure courtesy: Shannon Duff

Table 3.3: Dielectric Losses in post-OMT microwave components in the AdvACT HF Pixel

Item	150 GHz loss		230 GHz loss	
Dielectric	SiO_2	SiN_x	SiO_2	SiN_x
CPW→MS transition	1.3%	0.5%	2.4%	0.9%
Diplexer	7.6%	2.8%	6.5%	2.3%
Hybrid tee	1.8%	0.7%	1.4%	0.7%
MicroStrip line	4.5%	2.2%	7.0%	3.5%
Total dielectric loss	15%	6%	17%	7%
Gain in efficiency†		∼9%		∼10%

† The losses in OMT and other components do not effect this.

constant (ε_r) and layer thickness (t). The designs of the other circuit components are robust to such variations. In the worst case scenario, we expect a variation of $\sim 2\%$ in the dielectric constant and $\sim$10% in the thickness of the dielectric layer based on studies of uniformity across the 150 mm wafer. We studied the impact of these variations on our diplexer using SONNET simulations and plotted the resulting passbands in Figure 3.21. In our multichroic pixel design, the highest band edge is defined by a combination of the on-chip filter and the OMT cut-off while the lowest band edge is defined by a combination of the on-chip filter and the waveguide cut-off. The inner band edges are defined completely by the on-chip

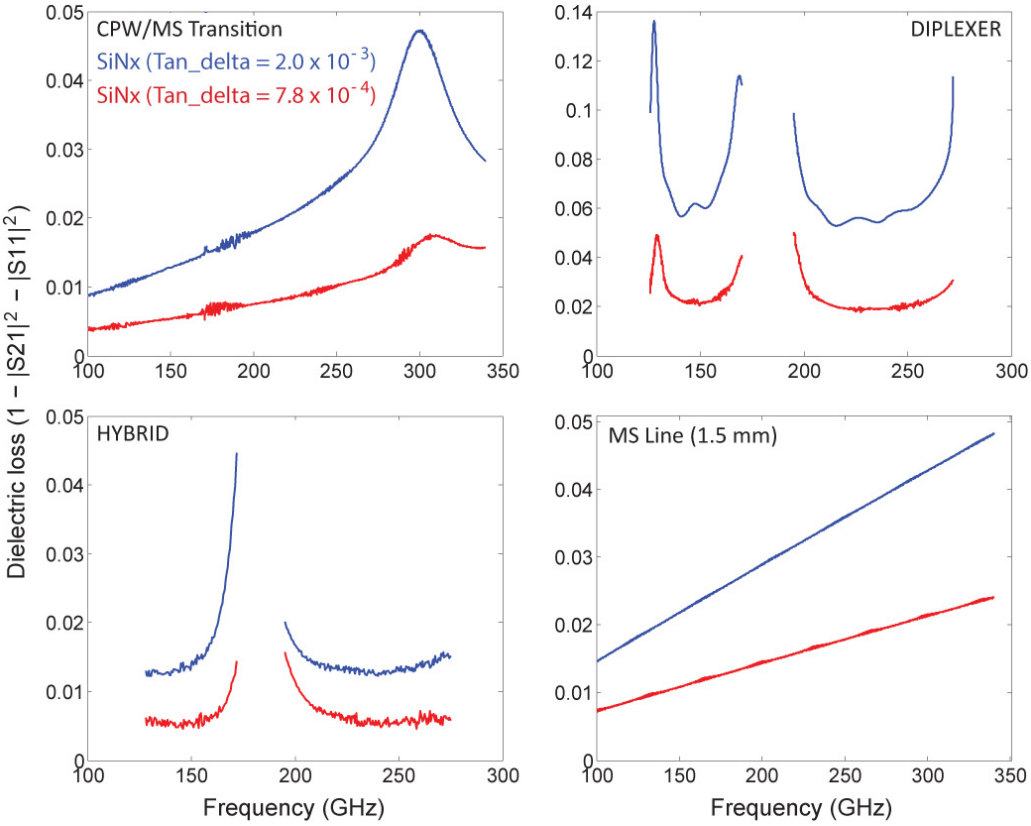

Figure 3.20: Comparison between dielectric losses using SiO_2 and SiN_x dielectrics.

diplexer and our goal is to keep the passbands away from the atmospheric lines.

Magnetic impurities or stress in the niobium superconducting traces can also lead to shifts in the passbands by changing the London penetration depth and thus the kinetic inductance. We have examined the impact of changes in the penetration depth on the diplexer bands using SONNET simulations (see Figure 3.22). Table 3.4 summarizes the tolerances.

Table 3.4: Stub Filter Design Tolerances

Parameter	% change	% shift in passband
ε_r	-2%	+1%
t	-5%	-1%
$\lambda_{l,Nb}$	+5%	-1%

The thickness of the dielectric can be measured after fabrication, however, there is some

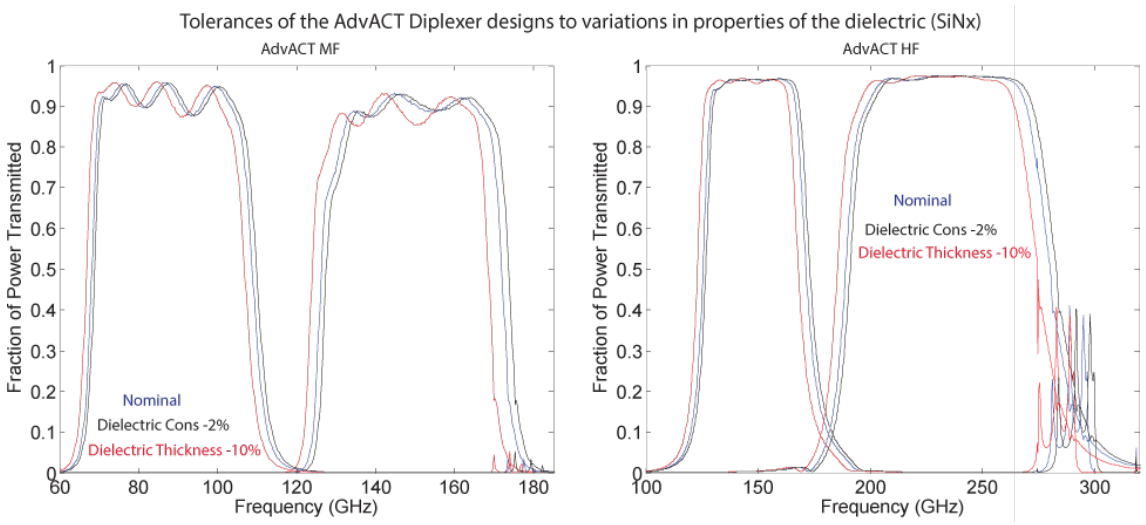

Figure 3.21: AdvACT MF (left) and HF (right) diplexer passbands for fiducial and worst case shifted values of dielectric constant and thickness.

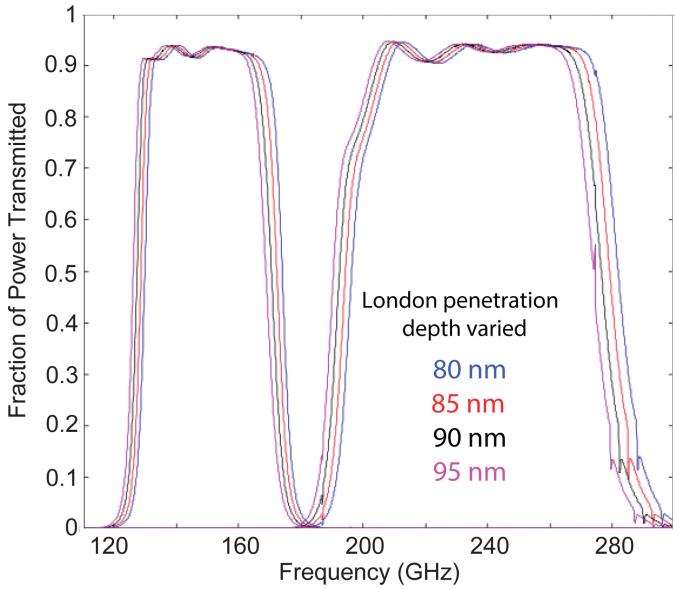

Figure 3.22: Frequency response of the post-OMT microwave components in the AdvACT HF pixel for different values of Nb London penetration depth.

uncertainty on the fiducial value of the relative dielectric constant (ε_r) itself, let alone its variation. The phase velocity or the wave speed of the electromagnetic waves in the dielectric medium is dependent on this parameter as well as the kinetic inductance of Nb. Resonator measurements have been carried out at NIST to determine ε_r, though at a lower frequency of $\sim$7 GHz. We expect the extrapolation to our frequencies to be straight forward [156], however, it will still be useful to have a method to determine the value of ε_r

directly at millimeter wavelengths. We are working on single-stub filter designs with sharp peaks (high Q-values) whose locations would depend on ε_r to constrain this parameter.

3.5 Study of alternative Filter types

The increase in the number of detectors from the ACTPol multichroic 90/150 array to the AdvACT 90/150 multichroic array by a factor of $\sim$2 was enabled partly by a reduced pixel size. The diplexer is one pixel component that occupies a large area on the chip. We ended up using the same type of diplexer comprised of stub filters, but bent in a way to occupy minimum space. However, in our quest for new filters with compact size and low loss for the AdvACT pixels, we did explore a few alternative filter designs. I will describe two such designs here: (1) CPW stub filters and (2) Lumped element filters, and compare these with the MS stub filters that we use.

3.5.1 CPW Stub Filter

CPW filters comprising open-circuit quarter-wavelength long stubs connected in series have the advantage of lower loss over MS stub filters with laterally extended stubs. Further, these do not require vias which means that these could be put entirely on the membrane where there is plenty of available space (provided it is small enough to fit). Series open-circuit terminated stubs within the center conductor leads to greater field confinement and thus lower radiation loss than that of straight gap-coupled resonators or stubs with lateral extension. Each unit cell consists of two open-circuit stubs within the center conductor connected in series. A unit cell along with its equivalent circuit model is shown in Figure 3.23.

Cascading more than one unit cell in series helps suppress the spurious signals as well as achieves sharper roll-off at the band edges. The length and characteristic impedance of the transmission line between the cascaded unit cells is carefully chosen so as to minimize in-band reflection (insertion and return losses). If the length of the center open stub is equal to $\lambda_g/4$, then the stub has a bandpass filter characteristic. Since the length of the stub is a significant fraction of λ_g, the inductors behave as distributed elements rather than lumped elements and hence, there are leaks at integral multiples of the desired frequency band. Figure 3.24 shows the frequency response of two cascaded unit cells optimized for

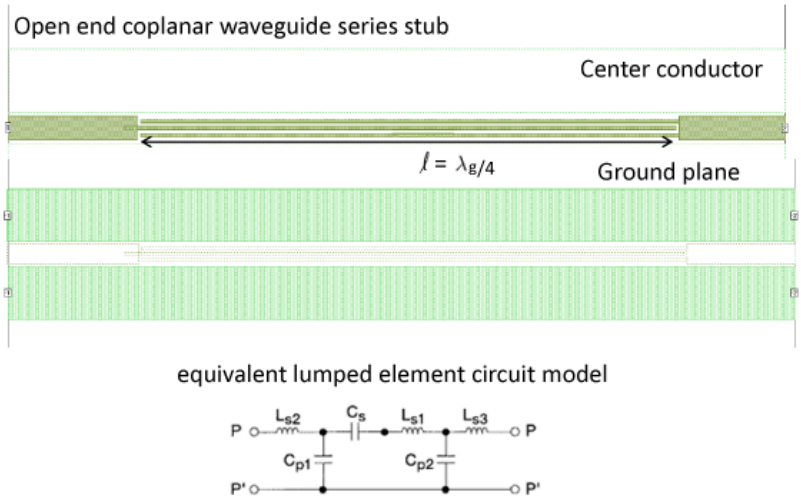

Figure 3.23: Unit cell of the CPW stub filter consisting of open-circuit quarter-wavelength long stubs. The top layer conductor traces and the ground plane are shown. The equivalent lumped element circuit model is shown.

the 90 GHz band connected in series. In order to achieve a sharper roll-off similar to the MS stub filters, we would need to cascade more than two unit cells, defeating our goal of compactification. We could bend and twist the quarter-wave long stubs, which would reduce the overall length of the filter, but would still take up a significant area on the pixel. With a low loss tangent material for the dielectric like SiN_x, the disadvantage associated with a larger footprint on the chip would offset the gain derived from lower CPW loss. Hence, we rejected this option.

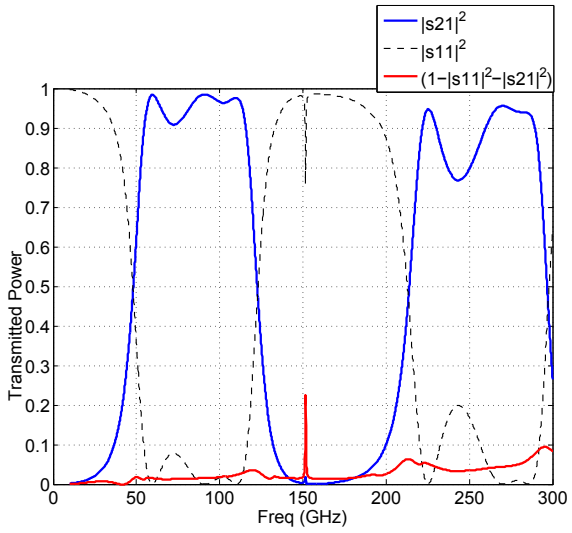

Figure 3.24: The response of the bandpass CPW stub filter comprising two series-connected unit cells optimized for the 90 GHz band. The first odd-order harmonic is shown.

3.5.2 Lumped Element Filter

For designing the lumped element filter, we started with the ladder circuit for a low pass filter prototype consisting of three elements and beginning with a series element [155], and extended it to a fifth-order low-pass maximally flat filter circuit. This normalized filter has a cut-off at $\omega_c = 1$ with a 1Ω load termination, and has element values $L_{1o} = 0.618 = L_{5o}$, $C_{2o} = 1.618 = C_{4o}$, and $L_{3o} = 2$. It is transformed to a fifth-order lumped element band-pass maximally flat filter by: replacing the series inductor L_{ko} by a series combination of inductor $L_{k,ser}$ and capacitor $C_{k,ser}$,

$$C_{k,ser} = \frac{\Delta}{\omega_o L_{ko} Z_o},\ L_{k,ser} = \frac{L_{ko} Z_o}{\Delta \omega_o}, \tag{3.9}$$

and shunt capacitor $C_{k,sh}$ by a parallel combination of inductor $L_{k,sh}$ and capacitor $C_{k,sh}$,

$$L_{k,sh} = \frac{\Delta Z_o}{\omega_o C_{ko}},\ C_{k,sh} = \frac{C_{ko}}{\Delta \omega_o Z_o}, \tag{3.10}$$

where, $\omega_o = \sqrt{\omega_{c1}\omega_{c2}}$ is the desired center frequency, and $\Delta = \omega_{c2} - \omega_{c1}$ is the desired bandwidth. ω_{c1} and ω_{c2} are the lower and upper 3 dB cut-off frequencies of the filter, Z_o is the characteristic impedance of the terminating MS line with a 4 μm wide center conductor, i.e., 12 Ω. Impedance inverter networks can be used to replace a parallel shunt admittance. Since shunt inductors are hard to implement, the parallel LC sections are replaced by impedance inverter blocks. The steps in the transformation are shown in Figure 3.25.

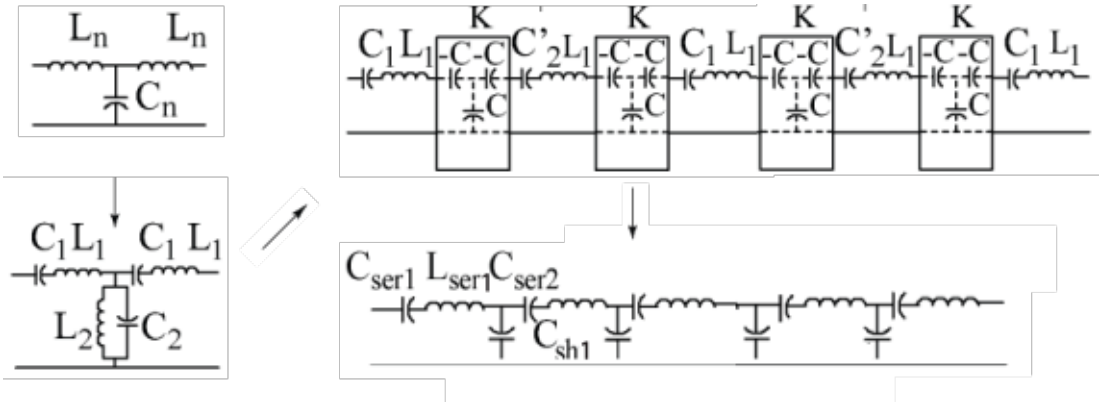

Figure 3.25: Lumped element bandpass filter design. *top left:* ladder circuit for a low pass filter prototype consisting of three normalized elements. *bottom left:* transformation to a bandpass filter with series LC and shunt parallel LC. *top right:* five-pole bandpass filter with impedance inverter blocks replacing the shunt inductors. *bottom right:* Final five-pole lumped-element bandpass filter circuit.

The next step was the on-chip implementation of these capacitors and inductors. Inductors were realized with short high impedance sections of CPW lines entirely on the ground plane and parallel plate capacitors were formed between the ground plane and top conductor layer of MS line as shown in Figure 3.26. In order to keep sensitivity to fabrication tolerances within acceptable limits, we were required to keep the CPW (width + 2 $\times$ gap) dimension significantly smaller than 25 µm (which is the space between the planar detector wafer and the top/bottom metal box). These, along with a minimum width of 2 µm for the conductor traces and a minimum spacing of 2 µm between the traces, were our main design constraints.

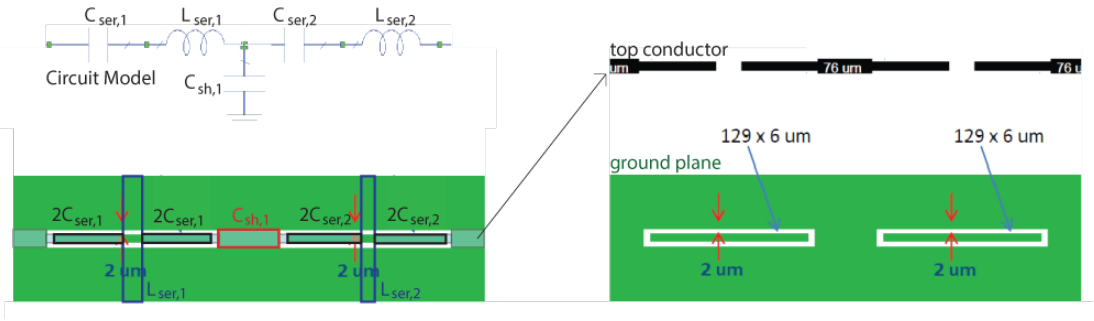

Figure 3.26: Implementation of a section of the lumped element bandpass filter using CPW and MS transmission lines.

The dimensions of the capacitor were estimated using the formula:

$$C = \frac{\varepsilon_o \varepsilon_d A}{d} \tag{3.11}$$

where ε_d = dielectric constant of SiN_x, A = area of the parallel plates, and d = thickness of SiN_x

The inductance per unit length of a CPW line is given by:

$$l = \frac{\beta Z_c}{\omega} = \frac{\sqrt{\varepsilon_{eff}} Z_c}{c} \tag{3.12}$$

The bottom plates of the series capacitors were isolated whereas the bottom plate of the shunt capacitors were continuous (shorted) with the larger ground plane. The two five-pole filters were simulated and optimized in SONNET. Then they were combined via a T-junction optimized using SONNET. The input and output to the diplexer was a 4 µm wide MS line with a low characteristic impedance, Z_o = 12 Ω, which brings the broadband power from the OMT output through a broadband CPW-to-Microstrip transition. These

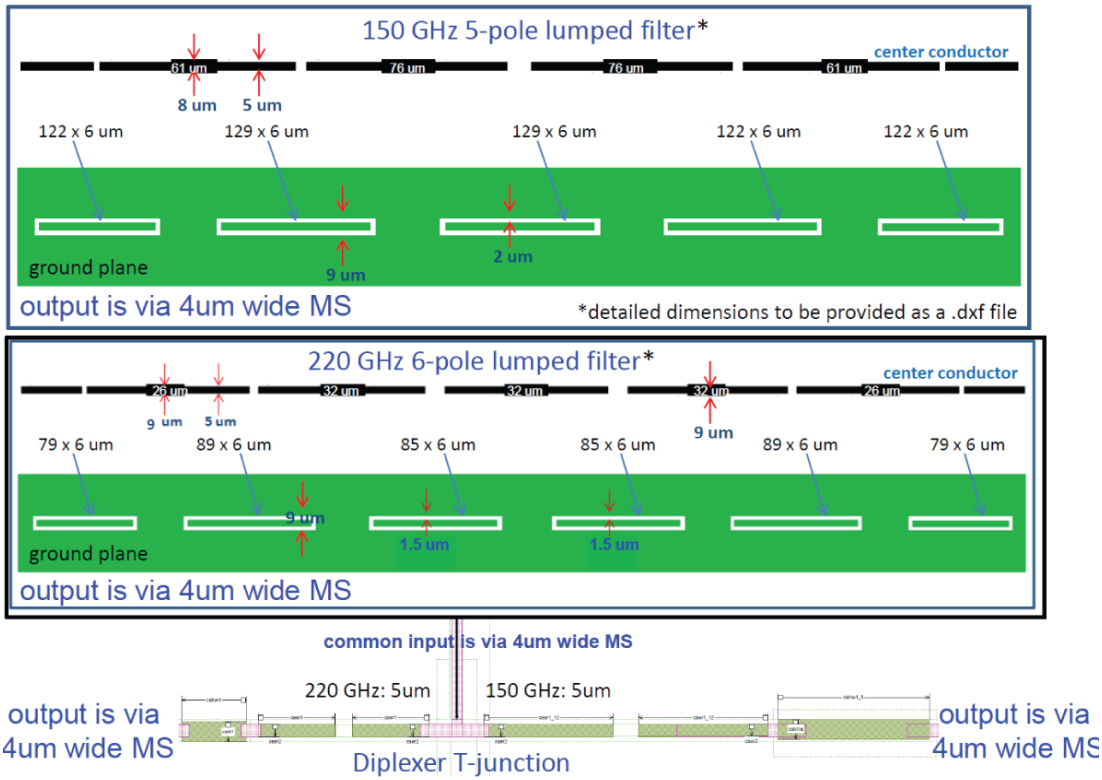

Figure 3.27: Lumped element filter designs for the 150/230 GHz multichroic pixel. The 150 GHz filter is a five-pole design whereas the 230 GHz filter is a six-pole design. The two filters are connected to the two ends of a microstrip T-junction via a 5 µm long microstrip which is 5 µm wide. The input microstrip line to the T-junction is 4 µm wide and the output of the filters are also 4 µm wide microstrip lines.

filters use both CPW and MS transmission lines; do not require vias (means they could be safely placed on the membrane) nor do they have harmonics. In the final diplexer design shown in Figure 3.27, we checked for radiation loss using SONNET and found it to be negligible. We checked that the fabrication tolerances in the relative alignment between the top conductor trace and the ground plane features were acceptable. We also checked the design tolerances and found that the lumped element filter was more sensitive to variations in the dielectric thickness compared to the MS stub filter, which was expected since it uses CPW lines. However, it was less sensitive to variations in the London penetration depth of superconducting niobium compared to the MS stub filter.

Two types of pixels, one employing the MS stub filters and the other employing the lumped element filters were prototyped together for the AdvACT HF pixel. A comparison between the measured and predicted passbands is shown in Figure 3.28. We do not understand the large shift in measured passbands with respect to the design in the case of the lumped filter. Hence, we decided to use the MS stub filters with already demonstrated per-

Table 3.5: Lumped Element Filter Design Tolerances

Parameter	% change	% shift in passband
ε_r	-2%	+1%
t	-5%	-2.3%
$\lambda_{l,Nb}$	+5%	<-0.5%

formance. The lumped element filters could be an interesting option in the future, but need to be understood better through more rounds of design, prototyping, and measurement.

3.6 Lab measurement of Optical Efficiency using a Cold-load

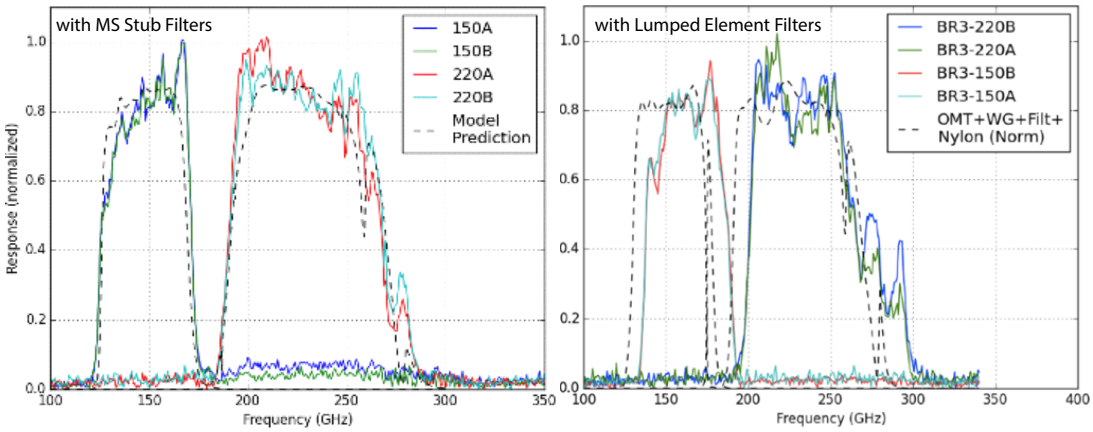

Figure 3.28: Measured passbands of AdvACT HF prototype pixels (using MS stub filters (left) and lumped element filters (right)) compared to predictions. The measured passbands match predictions quite well for the pixel containing stub filters. The pixel with lumped element filters have passbands shifted by ∼5%.

The multichroic pixels were fabricated by our collaborators at NIST, Boulder. We measured the optical efficiency of several single pixels both from the prototyping fabrication runs and from the same batch as the final multichroic array fabrication. We used a cold load blackbody radiation source made of a cubical block of aluminum with a pyramid geometry cut into one surface to act as an anti-reflection coating, then coated with the commercially available microwave absorber Eccosorb 110. It is put inside a copper box made of high purity OFHC Copper. The entire setup is then placed inside the cryostat, thermally coupled to the ∼4 K pulse tube stage via a tube made of G10 fiberglass. A thermometer for reading

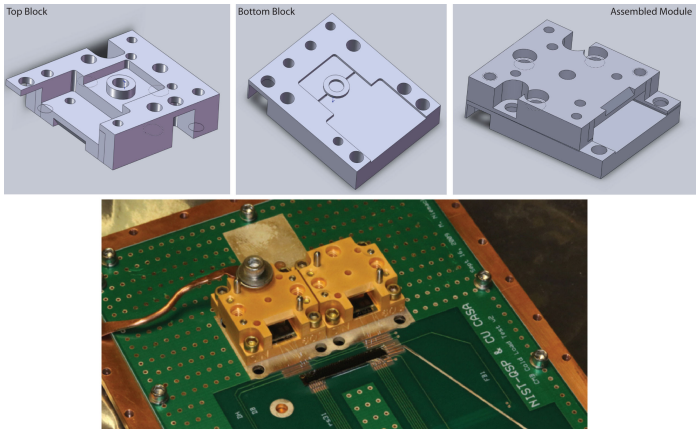

Figure 3.29: The split-block brass module on which the detectors are mounted. *top*: Schematics showing the top and bottom parts of the module. *bottom*: A photo of 2 single pixels mounted on two such modules on a PCB.

out the cold load temperature and a resistor for dissipative heating of the aluminum cold load by passing a current are screwed to the back of the aluminum block. A good thermal connection is made by applying Apiezon N Grease. The pyramidal surface of the cold load shines power on the detectors through a 25 x 50 mm rectangular hole cut in the enclosing copper box. A free-space low pass filter is placed between it and the detector to minimize heating of the colder dilution refrigerator stages and the PCB on which the detector is mounted by high frequency, out-of-band radiation. Our lab setup can read two pixels (8 TES detectors + 4 test TESs) simultaneously in a single cool-down. We used a two-pixel board (PCB) made by NIST on which we mount the pixels and the auxiliary interface and multiplexing chips. The two pixels are mounted in a brass split-block module (see Figure 3.29) and a prototype ring-loaded corrugated feed-horn is used to capture the light for each detector. The PCB is mounted on a board made of OFHC Copper, which is then mounted on the cryostat cold stage, again applying adequate amounts of Apiezon N Grease. The transmission function of the filter is assumed to be $\sim$1 in our bands. We are able to heat the cold load to temperatures between 3 K and 12 K without overloading our cooling system. The cold load is an almost perfectly emissive black-body, according to room temperature Vector Network Analyzer (VNA) measurements, so we assume that it has an emissivity $\sim$1. The measurement setup is shown in Figure 3.30.

We define the optical efficiency in two ways: (1) assuming the simulated 90 GHz and 150 GHz passbands shown in Figure 3.32, and (2) assuming top-hat passbands with transmission equal to 0.95 between 70-110 GHz and 128-170 GHz. So, if the fabricated pixels have the exact simulated 90 GHz and 150 GHz passbands, we would measure the optical

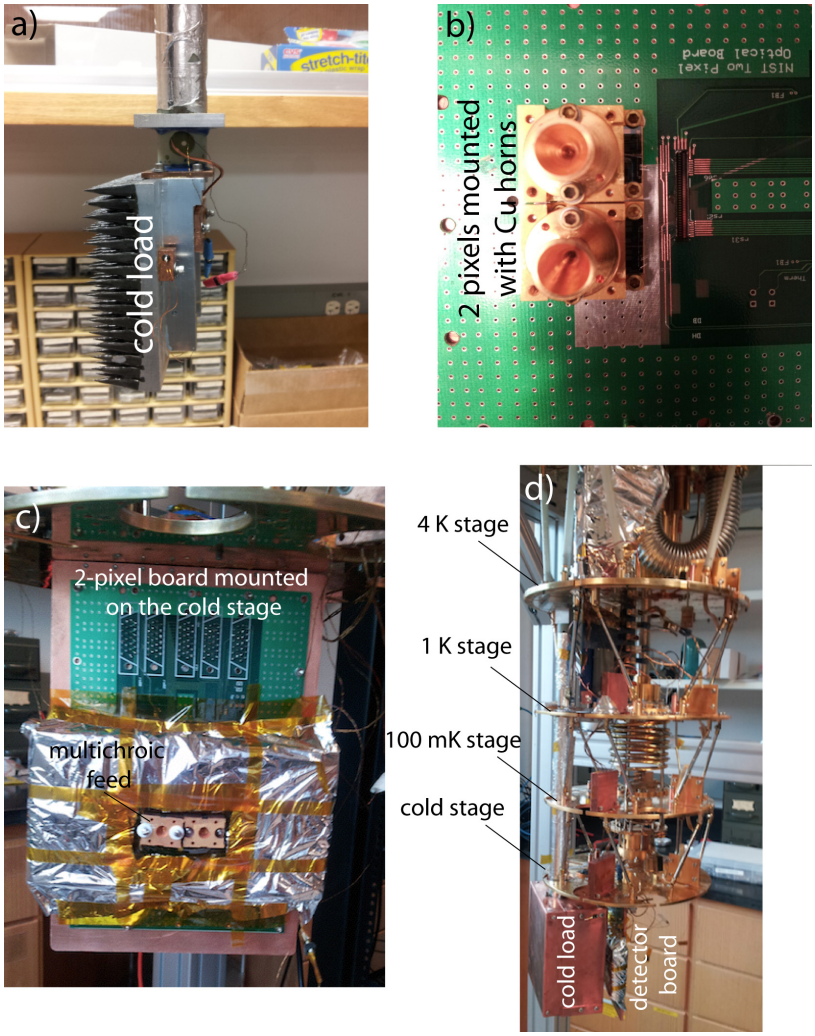

Figure 3.30: *a*: A photo of the cold load. *b*: 2 single pixels mounted on a PCB with 2 copper horns. *c*: The PCB on which the pixels are mounted are screwed on to a copper board that is heat sunk to the cryostat cold stage. The two prototype ring-loaded corrugated silicon platelet single feeds are visible. Super-insulating mylar is used to prevent radiative heating of the PCB and the pixels. *d*: A photo showing the different cryostat stages and the aluminum cold load, enclosed in a copper box heat sunk to the 4 K stage via a G-10 tube, facing the detector board. A free-space low-pass filter (not visible here) is taped to the copper board in between the cold load and the feeds.

efficiency as 100% calculated by the first method. To measure the optical efficiency, we set the cold load to a series of temperatures between 3 K and 12 K, acquire TES IV curves and measure the TES bias power P_{TES} averaged over the linear region of the $\%R_n$ vs V curve, where $\%R_n$ refers to the percentage of the TES normal resistance. The optical efficiency is then calculated as:

$$\eta_{eff} = \frac{\Delta P_{TES}}{\Delta P_L} = \frac{P_{TES}(T_1) - P_{TES}(T_2)}{P_L(T_2) - P_L(T_1)} \tag{3.13}$$

where T_1 = 3 K, and T_2 = various temperatures. $P_L(T_L)$ is the total load power or the

expected amount of radiation from the cold-load and is given by:

$$P_L(T_L) = \int_{\nu_0}^{\nu_1} \varepsilon f(\nu) \frac{h\nu}{e^{h\nu} kT_L - 1} d\nu \tag{3.14}$$

where f(ν) is either the simulated passband of the pixel (method 1) or a top-hat function (method 2).

Each text pixel being measured has so-called dark TES(s) that is located at an available space at the corner of the pixel, but not electrically wired to the circuit. We read out these pixels to check for thermal heating of the pixel probably caused by one or more of the following: (1) high frequency, out-of-band leakage, (2) the free-space filter absorbing power from the cold-load and re-radiating, (3) heating of the PCB directly or through the copper board to which it is heat sunk, as the cold-load temperature is raised in effect raising the detector bath-temperature; we try to keep this temperature constant with a PID servo loop, however the T_{bath} still increases slightly with increasing cold load temperature. In order to minimize these effects, we take extra care while heat sinking the copper board to the cryostat cold stage, wrap the exposed areas of the PCB (other than the feed-horns) with super-insulating mylar and acquire IV curves at a T_{bath} as high as possible (keeping it just sufficiently below the transition temperature of the TES). Also, I attempt a rough calculation of the emissive loading from the free-space filter below.

The frequency dependent emissivity of the filter is calculated as:

$$\varepsilon(\nu) = 1 - e^{-\frac{2\pi n\nu}{c}\delta z} \tag{3.15}$$

where n is the index of polypropylene $\sim$1.5, ν is the frequency, z is the thickness of the filter $\sim$1.35 mm, δ is the loss tangent of polypropylene assumed to be 6 x 10^{-4}.

The emitted power for a given filter temperature T is then calculated as:

$$P(\nu) = \varepsilon(\nu) \frac{h\nu}{e^{h\nu} kT_L - 1} d\nu \tag{3.16}$$

and plotted in Figure 3.31 for different temperatures along with the loading obtained by integrating the power between 300 GHz and 3 THz. The results suggest that the emissive loading from the free-space filter should not be a concern in our setup.

If the system was perfect, we would not expect to see any difference in the P_{TES} of the dark detector with increasing cold-load power. However, we do see an excess power that,

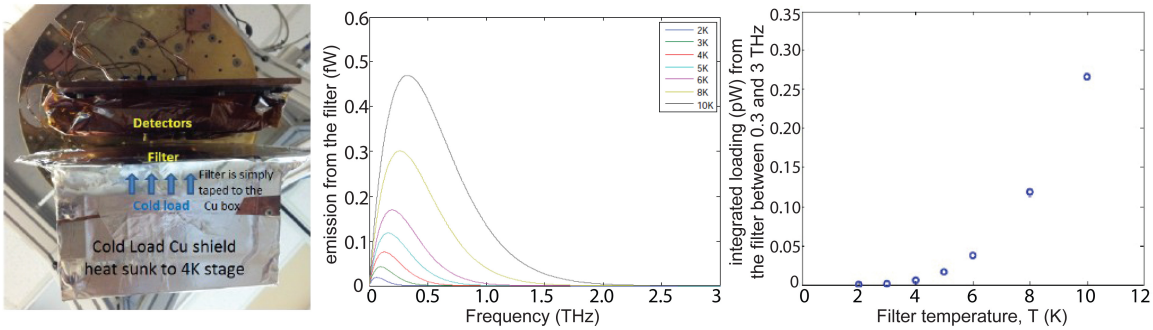

Figure 3.31: Emissive loading expected from heating of the free-space low-pass filter between the cold load and the detectors.

unless subtracted off, would systematically bias the measured efficiency higher.

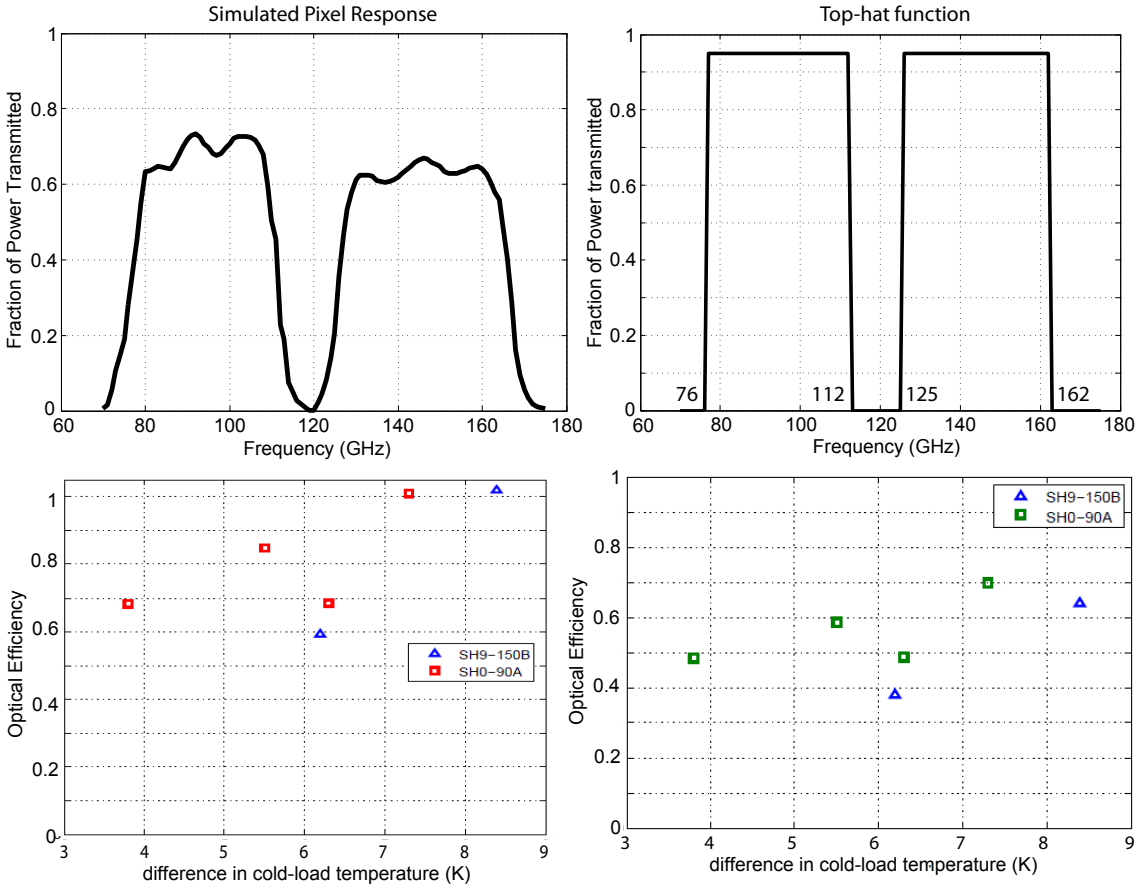

Figure 3.32: *top:* Assumed passbands for computing the optical efficiency. *bottom:* The respective measured dark-subtracted optical efficiencies. When assuming the simulated passband (left), we would ideally expect the optical efficiency to be equal to 1.

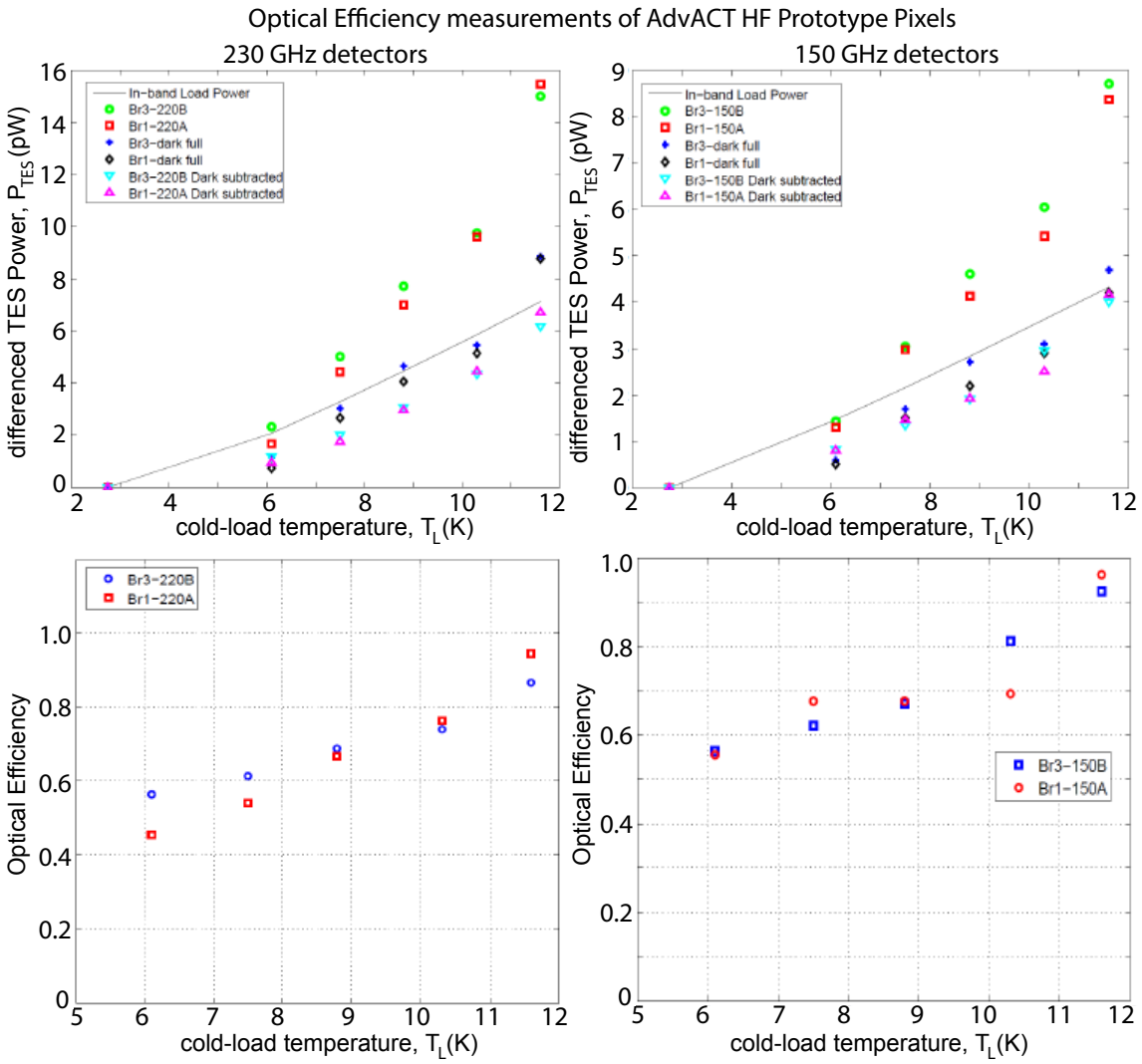

Figure 3.33: *top:* The differential Incident load power and detector powers for the 230 (left) and 150 (right) GHz prototype AdvACT HF pixels assuming top-hat passbands. *bottom:* The respective measured dark-subtracted optical efficiencies. The gradual rise in measured efficiency with cold load temperature indicates that some unwanted systematic is affecting our measurement. We are investigating this.

The measurements of end-to-end optical efficiencies for the 90 and the 150 GHz bands for the ACTPol PA3 prototype pixel are shown in Figure 3.32. Based on these measurements and limited by systematic effects in our set-up, our best estimates for optical efficiencies are 58% and 51% respectively for the 90 and the 150 GHz bands. These efficiencies are roughly 10% lower than that expected from the predicted losses for the various detector components that are listed in Table 3.2. The reasonable agreement between simulations and measurements of the beam, pass-band, and optical efficiency demonstrated the function of the prototype detectors. We next incorporated this pixel design into the ACTPol multichroic (PA3) detector array. The array layout and wiring is described in the next sec-

tion.

3.7 ACTPol 90/150 GHz Multichroic Array Wiring Layout

The ACTPol PA3 multichroic array consists of 255 pixels with a total of 1020 polarization sensitive bolometric detectors fed by a 140 mm diameter silicon platelet monolithic feedhorn array [152]. It was deployed in January 2015, as the third and final ACTPol array, along with the two existing 150 GHz single frequency arrays. The full array was composed of three 75 mm diameter hexagonal wafers (hex) and three semi-hexagonal wafers (semihex). The full linear polarization state of a given location on the sky can be measured by combining measurements of multiple pixels (polarimeters) rotated 45° relative to each other. These two types of pixels (rotated versions of each other) were approximately uniformly distributed across the array (see left panels of Figures 3.34 and 3.35. Each hex had 61 pixels and each semihex had 24 pixels.

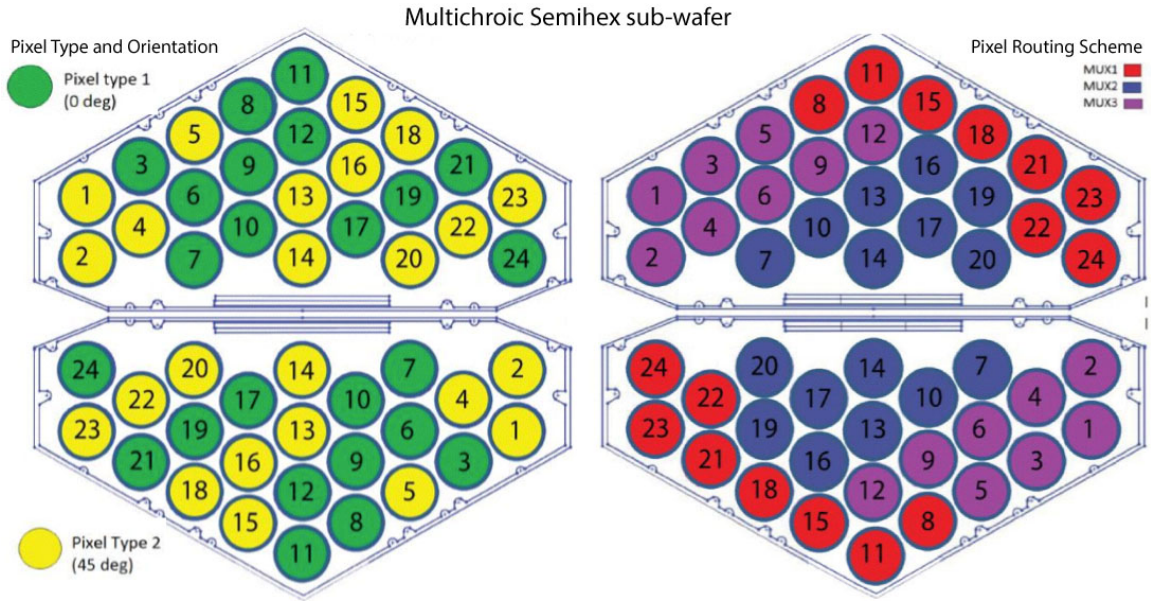

Figure 3.34: Each semihex sub-array consists of 24 pixels. *left*: The distribution of the two pixel types within the sub-array is indicated by the yellow and green filled circles. *right*: A group of upto 8 pixels (32 detectors) can be read-out via one multiplexing (mux) chip, the pixel routing scheme based on this is indicated by the three different types of colored circles. All read-out traces are routed to two groups of bond-pads along two edges of the hex.

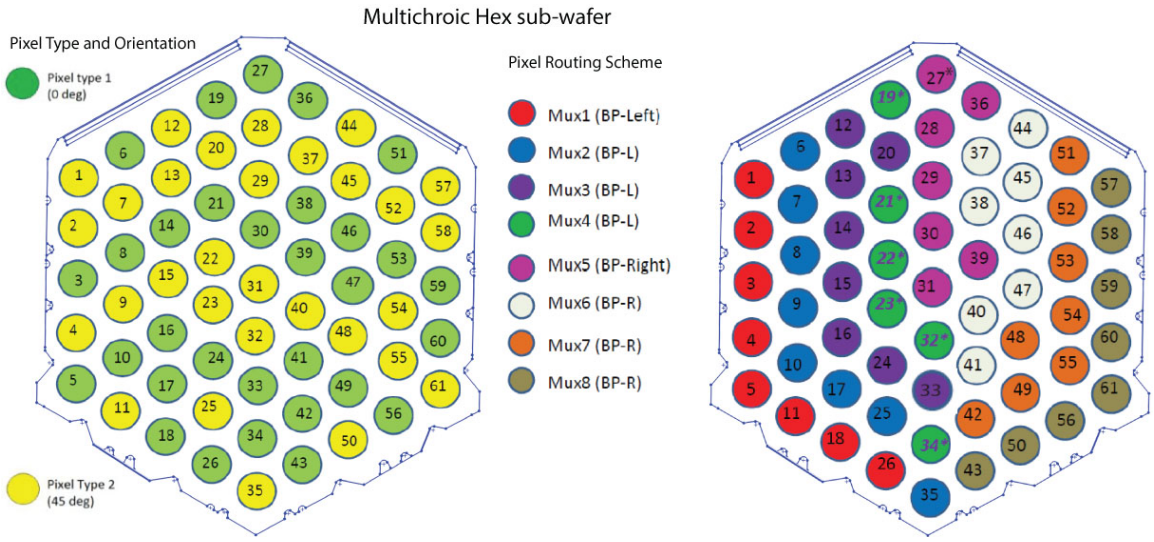

Figure 3.35: Each hex sub-array consists of 61 pixels. *left*: The distribution of the two pixel types within the sub-array is indicated by the yellow and green filled circles. *right*: A group of upto 8 pixels (32 detectors) can be read-out via one multiplexing (mux) chip, the pixel routing scheme based on this is indicated by the eight different types of colored circles. All read-out traces are routed to a group of bond-pads along an edge of the semi-hex.

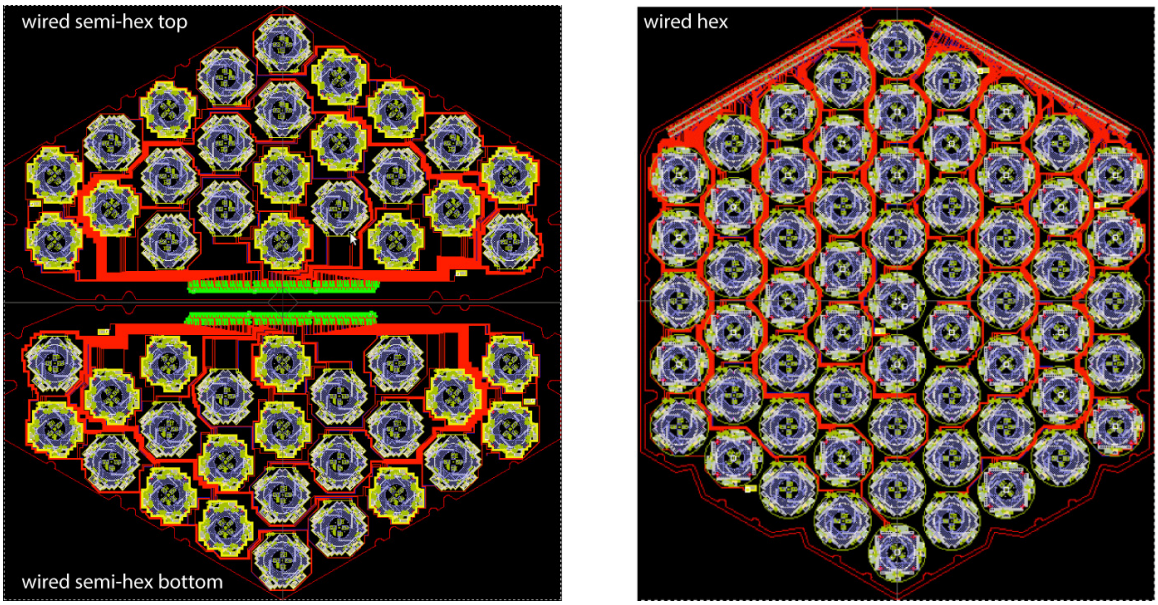

Figure 3.36: The ACTPol multichroic array comprises three 3″ diameter hex sub-arrays (61 pixels each) and three 3″ diameter semi-hex sub-arrays (24 pixels each). *Left:* Schematic of two semihex sub-array layouts. *right:* Schematic of a hex sub-array layout.

The four TESs in each pixel were routed to bondpads at the edge of each sub-array via niobium wiring traces (see Figures 3.36 and **??**). In the TDM multiplexing scheme, a group of 32 detectors (4 pixels) are connected to a single mux chip (see right panels of Figures

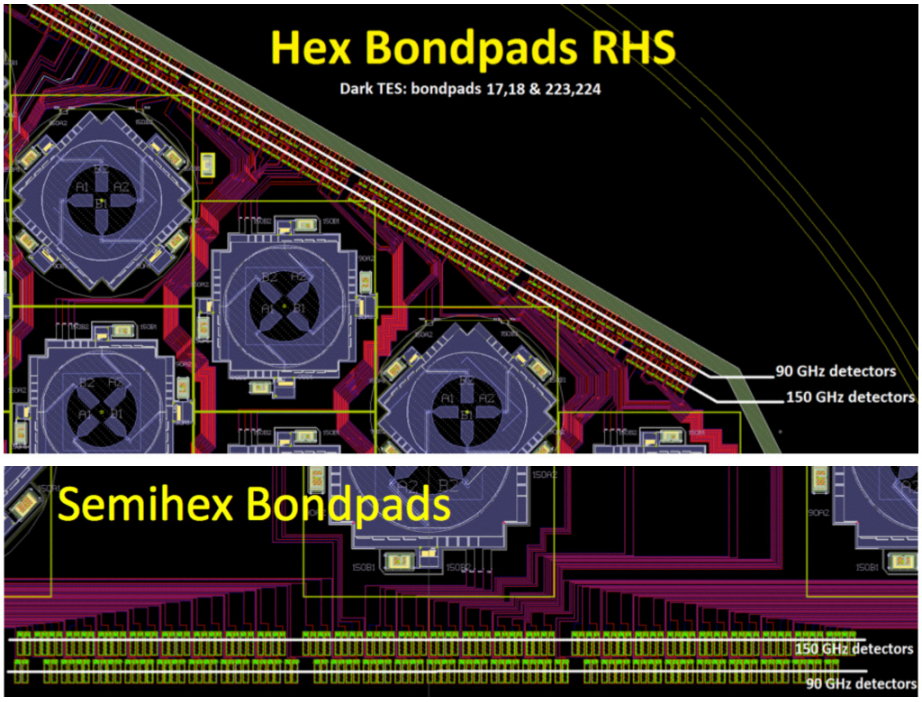

Figure 3.37: Separate rows of bondpads for the 90 and 150 detectors enable differential TES biasing.

3.34 and 3.35. Each wiring trace was 8 µm wide with a 5 µm gap between the traces in each pair. For the first two ACTPol arrays, we had twisted the traces in each pair to mitigate any crosstalk. For the PA3 array, I did a rough calculation to check if this twisting was required. If we could get away with straight/un-twisted pairs, it would ease the fabrication process significantly as it would make it much easier to check for and correct wiring discontinuities in the masks. In Appendix E, I have described the calculation which suggested that we would not have significant cross-talk if we used straight pairs, which we eventually used. Figure 3.38 shows a schematic of the full PA3 array.

3.8 Summary

We developed and deployed (in June 2015) a polarization sensitive multichroic array with 255 feedhorns and 1020 bolometers on ACT in Chile as part of the ACTPol experiment. The preliminary sensitivity of the array is $<10\ \mu\mathrm{K}\sqrt{s}$, with the exact value changing with the atmospheric loading, which makes it the most sensitive ACTPol array. The so-called PA3 array has completed one season of observation. The data are currently being analyzed. This receiver represents the first multichroic detector array deployed for a CMB experiment

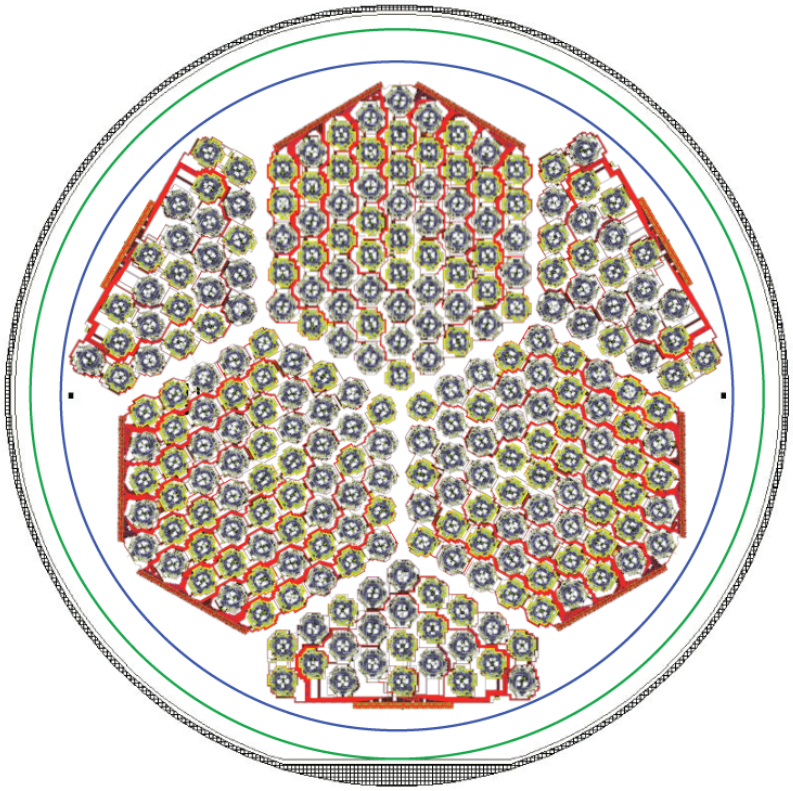

Figure 3.38: The PA3 full array consists of 255 pixels distributed between hex and semihex sub-arrays.

and paves the way for the extensive use of multichroic detectors and broadband optical systems in the next generation of CMB experiments, such as AdvACT [69], which will be a staged upgrade over three years of ACTPol's three existing detector arrays and their optics. The new detector arrays [159, 160] being developed are more densely packed multichroic arrays spanning from 25 GHz to 280 GHz with an upgraded read-out system. The AdvACT multichroic arrays with fully optimized instruments can achieve performance equivalent to 1.7 single frequency arrays. The first of the AdvACT arrays, the HF (150/230 GHz) array was deployed in June 2016.

CHAPTER 4

In-situ Passband Characterization of Deployed Detector Arrays

In this chapter, I present a novel system for in-situ characterization of the passbands of millimeter-wave polarimeters using a Fourier Transform Spectrometer (FTS). The design of optics for coupling the output of the FTS to the feedhorn-coupled detectors without saturating them is described. I present passband measurements performed at the ACT site on the deployed ACTPol arrays and use these to compute the effective central frequencies of the ACTPol arrays with respect to diffuse and compact sources with different types of spectra.

4.1 Introduction

Precision calibration of frequency bands is critical for interpreting data. We present a method for in-situ calibration of detector passbands using a Fourier Transform Spectrometer (FTS). In the field of CMB, the COBE satellite even used a FTS to make a precise measurement of the CMB spectrum in the 90's, demonstrating its near perfect blackbody characteristics. Today, in the era of precision cosmology, the importance of foreground characterization and subtraction in order to unambiguously recover the faint CMB polarization signals, is widely recognized. The different sources of foreground contamination have unique spectral signatures. To this end, precise knowledge of the instrument's bandwidth and effective central frequency to these sources goes a long way in ensuring accurate characterization of the foregrounds. In addition to measuring the passband of the detectors in the fully integrated on-sky configuration, for the ACTPol receiver, we also checked for unexpected out-of-band leakages and shifts in the passband with respect to the targeted design.

4.2 Fourier Transform Spectrometer

The FTS that was used here is a variant of the compact Martin-Puplett type [161, 162] FTS, which has also been proposed for a new satellite mission called PIXIE [163]. This FTS achieves high performance relative to its volume and mass and produces a polarization symmetric output. These attributes are attractive not only for space missions, but also for use in lab and in characterizing fielded instruments since low mass and volume means the unit is easy to transport and align. The polarization symmetry simplifies the calibration of polarization sensitive detectors. The FTS consists of two sets of six mirrors (mirror totems) located at the edges of a base plate that defines the alignment of the system. A grid totem is mounted on the base plate half way between and parallel to the mirror totems. The grid totem is comprised of a machined mount that carries four wire grids and has a central opening allowing for the passage of an assembly of two back-to back dihedral mirrors. The dihedral mirror was mounted on a 5 µm accurate linear stage with a travel of 150 mm manufactured by Aerotech [164] Corporation. The base plate has a grid of alignment pin holes and taped holes to facilitate the attachment of the appropriate coupling optics for in situ calibration of the ACTPol receivers.

4.3 Design of the FTS Coupling Optics

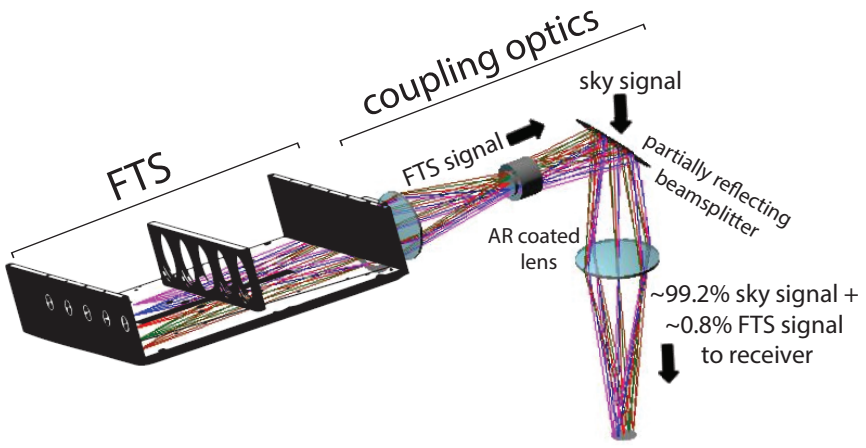

Figure 4.1: A schematic of the optics which couple the FTS output port to the ACTPol receiver.

The FTS has a full tendue [1] of 100 mm-Sr[2]. The output of the FTS needs to be matched

[1] it is the product of the area A of the light beam and the solid angle Ω contained within the beam. It is a

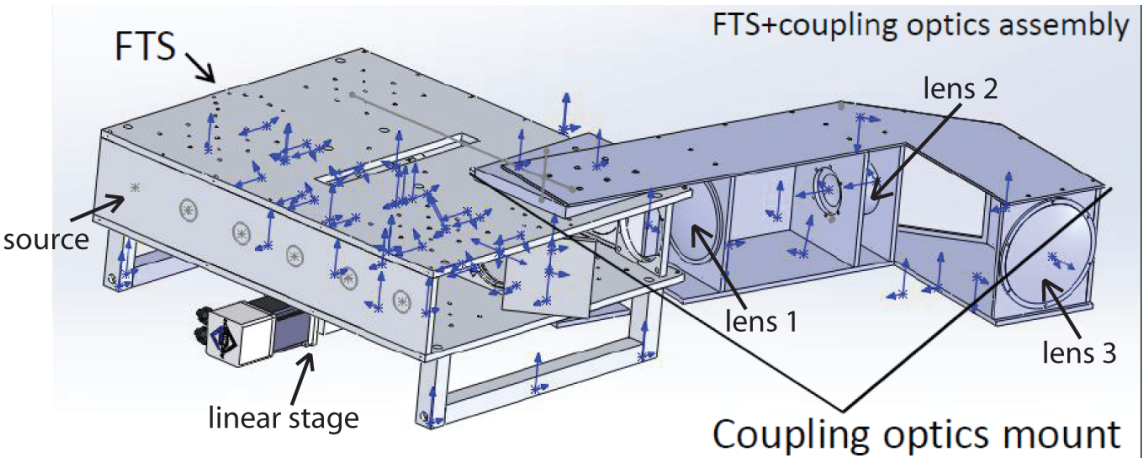

Figure 4.2: A schematic of the L-shaped mount (made of aluminum) for the coupling optics attached to the FTS.

to the f-number of the telescope to perform in-situ passband characterization of the instrument deployed on the telescope. The coupling optics designed (using the CodeV software package [166]) to achieve this consisted of three thick polyethylene (HDPE) lenses and a thin polyethylene (LDPE) beam splitter (see Figure 4.1). The Strehl ratio [2] for this design was > 0.997 for all field points. The requirements and constraints that drove the design of the coupling scheme include: (1) minimization of the emissive loading on the receiver from the lenses, thus preventing the detectors from saturating during the measurement, (2) distance of the focal plane from the vacuum window of the cryostat, (3) accounting for the non-telecentric nature of the ACTPol focal plane.

The lenses were mounted on a L-shaped base plate attached to the FTS, thus locating the coupling system relative to the FTS and the lenses relative to each other (see Figure 4.2). A semi-transparent window mounted at the corner of the L-shaped base plate at an angle of 45° to the light path partially reflects the light changing its path by 90° along the L-shaped plate. This semi-transparent window is a partially reflective folding mirror, created by sandwiching a one micron thick layer of LDPE between two aluminum frames with 4-40 bolts spaced every inch around the perimeter, acts as a beam splitter and reflects $<1\%$ of the incident light which is focused on to the detectors. This provides a crucial reduction in the intensity of the FTS signal to prevent saturation of the sensitive CMB detectors. The

FTS design parameter and is one of the major factors in controlling the signal-to-noise ratio. The product of tendue and overall system transmittance gives the throughput of an optical system [165]

[2] it indicates the level of image quality in an optical system may be defined as the ratio of the peak aberrated image intensity from a point source compared to the maximum attainable intensity using an ideal optical system limited only by diffraction over the system's aperture [167]

remaining >99% of the light passes through the beam splitter and reflects off the telescope structure onto the sky. The HDPE lenses were each fabricated with six tapped holes on flanges around their perimeters to bolt to the aluminum mounting plates. Only the lens facing the receiver window (and the only lens after the folding mirror in the optical chain) was AR coated by cutting concentric circular grooves on both surfaces (see Figure 4.3), which behaves as a metamaterial quarter-wavelength anti-reflection coating, optimized for 120 GHz, between the 90 and 150 GHz bands that were calibrated in the ACTPol instrument, and mitigates loading from reflected light. The focus on the ACT telescope is f/2. The coupling optics focal ratio of 1.6 ensures that the output can fill the beam of any of the feedhorns on the non-telecentric focal plane without having to point the FTS at an angle. Finally, a distance of $12''$ between the last lens and the focus enables us to mount the FTS such that the last lens is safely a few inches away from the vacuum window of the receiver. With this setup, approximately 20 detectors are illuminated simultaneously at the focus.

To estimate the optical loading from the coupling optics, we calculate the emission from the HDPE lens facing the cryostat. HDPE was chosen because it has a low loss tangent (tan $\delta < 3 \times 10^{-4}$ below 300 GHz and tan $\delta < 6 \times 10^{-4}$ up to 1.2 THz) which would help keep the emissive loading low. The fraction of incident power absorbed in the dielectric medium of the lens is given by:

$$\Delta P_{abs} = (1 - \frac{P}{P_o}) = 1 - e^{-\delta k_n z} \sim 1 - e^{-tan\delta \frac{2\pi n}{\lambda} z} \tag{4.1}$$

Assuming $n = 1.517$ and tan $\delta < 3 \times 10^{-4}$ for HDPE, λ = 2 mm (corresponding to 150 GHz), and z = 29.64 mm (center thickness of the lens), ΔP_{abs} = 4.15%. The loading would then be $\sim$ 12 K assuming a 280 K atmosphere.

The six surfaces of the three HDPE lenses included spheric and aspheric surfaces. An aspheric surface is defined as [168]:

$$Z = \frac{cr^2}{1 + \sqrt{1 - (1 + K)c^2r^2}} + A_4r^4 + A_6r^6 \tag{4.2}$$

where, Z = Depth or Sag of the curve, r = Distance from the centre, c = Curvature (=1/Radius), K = Conic constant, and A_x = Higher order terms. Figure 4.4 and Table 4.1 show the lens surface profiles in detail.

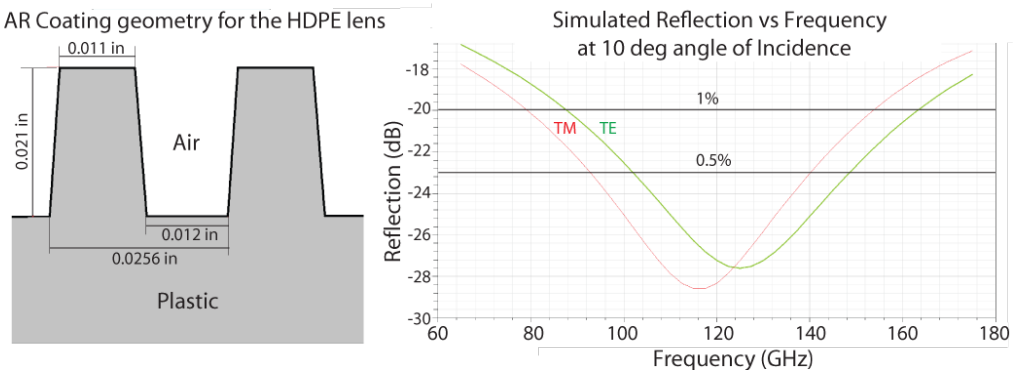

Figure 4.3: *left:* A schematic of the cross-section of the AR coating geometry. *right:* Simulated (HFSS [122]) reflection from a single-sided AR-coating on HDPE.

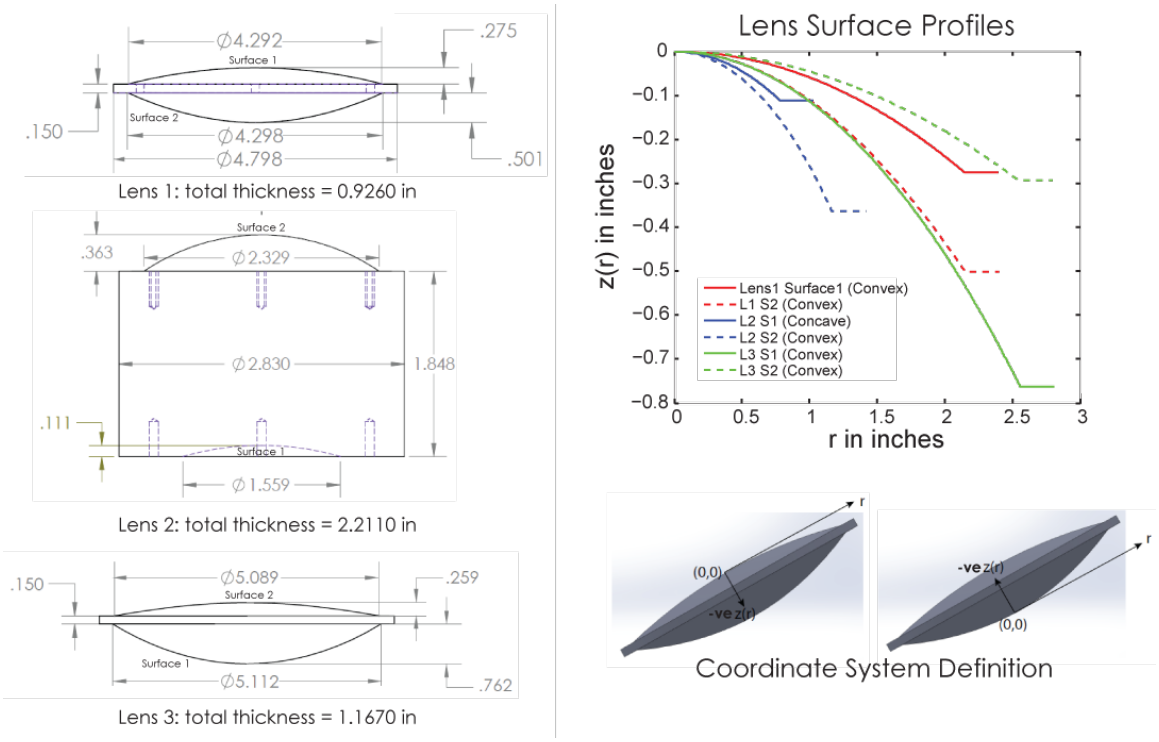

Figure 4.4: *left:* Side-view drawings of the three HDPE lenses. *right:* Surface profiles of the 6 lens surfaces. Three of these surfaces are spheric and three are aspheric. The lenses were cut in the Princeton Physics machine shop.

4.4 Frequency Calibration and Verification of the FTS Operation

The FTS was first calibrated using a microwave transmitter in a frequency range between 80 and 170 GHz. For example, the microwave source, placed at the FTS input, was made

Table 4.1: Surface Profiles of Lenses for the Coupling Optics

	c	K	A_4
Spheric surfaces			
Lens 1 surface 1	0.1176		
Lens 2 surface 1	-0.3571		
Lens 2 surface 2	-0.4878		
Aspheric surfaces			
Lens 1 surface 2	-0.2222	-1.8567	0.0005
Lens 3 surface 1	-0.2260	-0.9603	0.0005
Lens 3 surface 2	-0.0913	-6.5390	-0.0004

to transmit at a known frequency ν = 150 GHz and an interferogram was recorded by operating the FTS in the step-and-integrate mode (described in the next section). The frequency ν_{FTS} (= 146.5 GHz) of the signal was recovered by Fourier transforming the recorded interferogram (see Figure 4.5). The frequency calibration factor ν_{fac} was thus determined to be $150/\nu_{FTS}$ = 1.024. Analytical calculation of this calibration factor from the geometry of the FTS gives ν_{fac} = 1.017. We will assume ν_{fac} = 1.02.

The performance of this system was further verified with lab measurements of passbands of known detectors before using the system at the site. For lab measurements of detectors, the LDPE partial reflector was replaced with an aluminum mirror. The FTS was pointed into a cryostat which was opened to light using a set of teflon, nylon, and a IR blocking filter to block external radiation and a CR-110 neutral density filter. Two prototype pixels, whose passbands were accurately known from previous measurements by our collaborators at NIST Boulder, were mounted on the cryostat cold stage. To minimize the radiative loading on the 100 mK stage, the aperture size was stopped down from $\sim$ 6 inches on the exterior vacuum shell of the cryostat to $\sim$ 3 inches on the interior-most 1 K shell of the cryostat. Figure 4.5 shows the lab setup.

Interferograms were acquired using the FTS operating in a step-and-integrate mode. In this mode, the optical path difference in the interferometer is incremented in discrete steps, and the detector signal is integrated when the interferometer mirrors are stationary. The programmable linear stage shifts the position of back-to-back dihedral mirrors in the optical path to introduce a phase delay. The FTS has two input and two output ports, each supporting both linear polarization states simultaneously. We used only a single output.

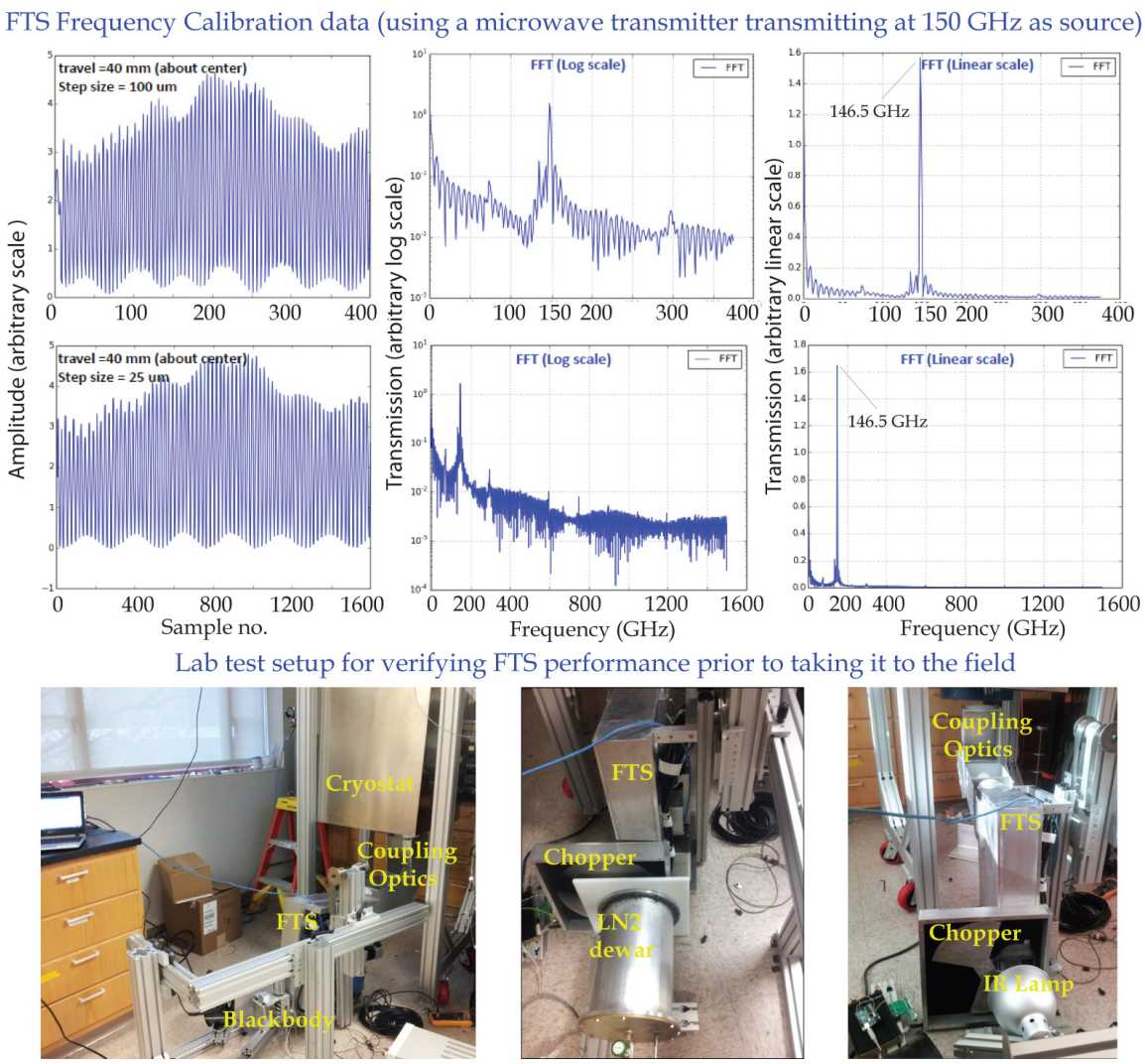

Figure 4.5: *top:* A 150 GHz microwave transmitter was used as a source for frequency calibration of the FTS. A diode detector was placed at the focus of the coupling optics. Resulting interferograms and Fourier transformed spectra obtained by operating the FTS in the step-and-integrate mode with two different step sizes. *bottom:* The lab setup for measuring prototype detector passbands. The FTS is pointing into a cryostat with a downward facing window. The three photos show different FTS sources (a blackbody emitter, a LN2 dewar, and an IR lamp) used for the measurement and testing/verification of the test setup.

The second output was terminated in Eccosorb HR-10 to help damp spurious reflections. HR-10 [169] has been shown to absorb $> 99\%$ of the incoming light below 300 GHz. One of the two inputs was also terminated in a 300 K piece of Ecccosorb HR-10 to provide a reference load. The second input was terminated in various sources including: (1) a dewar with a plastic (HDPE) window and filled with liquid nitrogen; and (2) a $\sim 600^{\circ}C$ IR lamp (type [171]). The step-and-integrate mode requires an additional modulation which was implemented by chopping the source at ~ 7 Hz so that the detector alternately views source

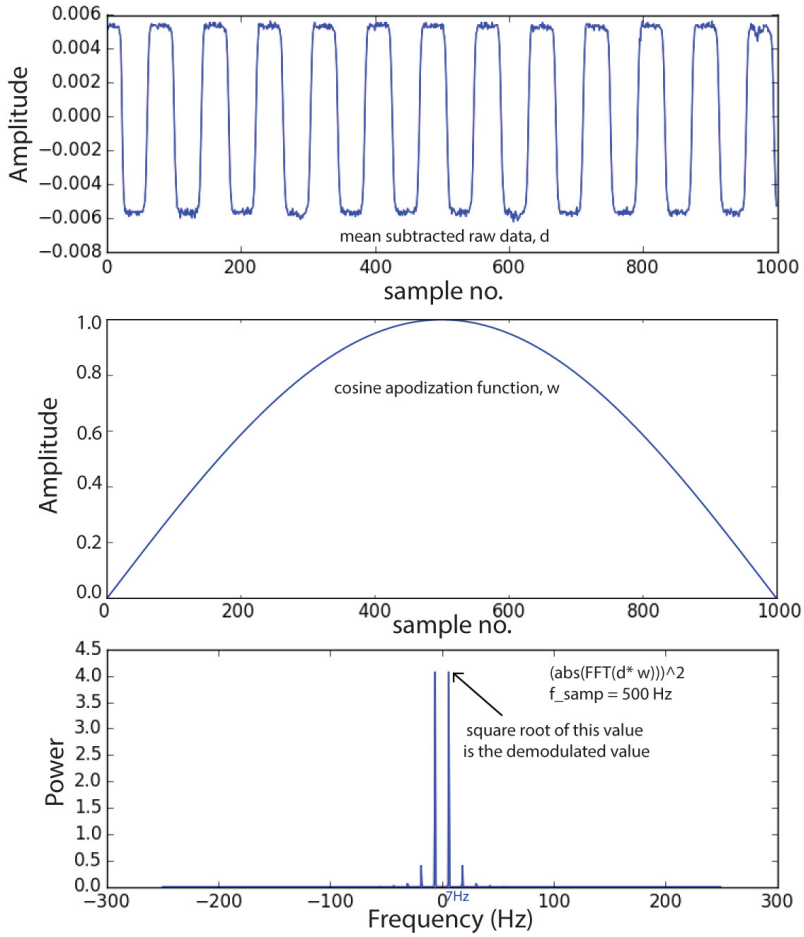

Figure 4.6: Lab testing of the FTS: measuring the spectrum of a prototype 150 GHz ACTPol pixel. *top:* Raw data acquired with the ADC (Labjack T7) at 500 samples/second at an arbitrary position of the FTS dihedral mirror. *middle:* A cosine apodization function. *bottom:* Software demodulated signal amplitude.

and ambient temperature. This chopper wheel, placed between the FTS and the blackbody source, consisted of a 14 inch diameter disc cut to have two blades covering 50% of the disc's area. The chopper wheel was covered with Eccosorb HR-10 and spun using a motor driven by an micro controller, programed to spin the chopper wheel at a frequency of ~ 7 Hz based on considerations about the chopper mass and motor power. The etandue of the FTS decides the lower operable frequency limit which happens to be ~ 50 GHz.

The modulated signal was detected with a phase-independent software lock-in technique, that does not require an external reference signal. Python commands were sent to the programmable linear stage on the FTS over ethernet to move the dihedral mirror to a certain location. While the mirror was stationary, data were acquired with a Labjack [172],

which is an ADC (analog-to-digital converter), with a sampling rate of 500 Hz over a 2 second integration time. The 1000-sample sized array of the mean subtracted raw data is then multiplied by a cosine apodization function (see Figure 4.6) and Fast Fourier Transformed (FFT). The amplitude of the signal in the bin(s) corresponding to 7 Hz (chopper frequency) is the value of the demodulated signal. The mirror moves on to the next step and the above steps are repeated until the specified travel of the mirror is completed. The set of demodulated data points at each step represent the interferogram. The spectrum was obtained after a Fourier transform of the measured interferogram. The maximum frequency ν_{UL} and resolution $\Delta\nu$ of the spectra are determined by the travel L and step size Δl of the movable FTS mirror according to the relations (for this FTS configuration): (1) $\nu_{UL} = c/(8 \times \Delta l)$, and (2) $\Delta\nu = c/(4 \times L)$, where c is the speed of light.

4.5 In-situ Passband Characterization

4.5.1 On-site Measurements

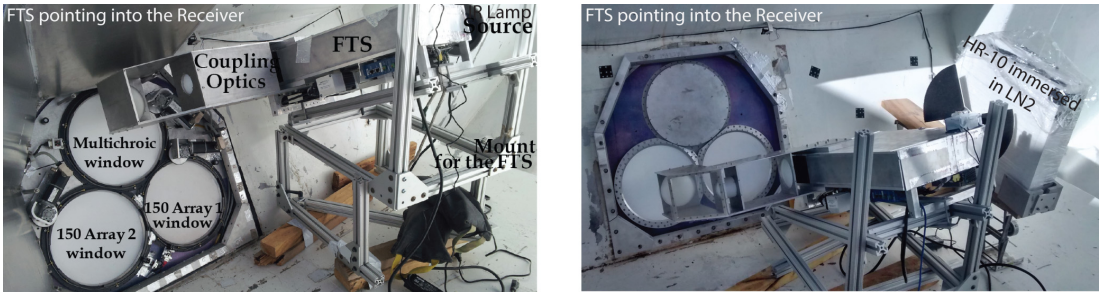

Figure 4.7: *Left:* A photograph of the FTS setup in front of the ACTPol receiver to measure the instrument passbands; using an IR lamp as the source and pointing into the PA3 array, and *Right:* using an Eccosorb HR-10 immersed in LN2 as the source and pointing into the PA1 array.

The FTS and the coupling optics were taken to the telescope site in Chile to characterize the passbands of the deployed receivers. The FTS was mounted between the receiver and the secondary mirror on a temporary T-slot mount [3] (see Figure 4.7). For these measurements, two full beam-filling sources were used at the FTS input: (1) a sheet of Eccosorb HR-10 immersed in a 77K liquid nitrogen bath contained within a transparent polystyrene bucket; and (2) a $\sim 600°C$ IR lamp (type [171]). Source (1) was expected to have a constant emissivity across microwave frequencies and be more thermally stable, provided one

[3] made of custom T-slotted aluminum extrusions [170]

watches for frost build up. However, it requires frequent refilling which is cumbersome in the field. The emissivity of source (2) was not well known and could potentially vary with frequency and must be empirically determined. We used a combination of these sources and found identical results for the passbands between both the sources (see Figure 4.8), justifying the use of source (2) in the field, which provided a higher signal-to-noise ratio. Based on consistency of results, we treat both sources to have a Rayleigh-Jeans spectrum. The coupling optics coupled the output of the FTS to the detectors, illuminating $\sim$5 pixels at a time. Its focal ratio of 1.6 ensures that the output can fill the beam of any of the feed-horns on the non-telecentric focal plane without having to point the FTS at an angle. This approach prevented the detectors from saturating and maintained $\sim$20 detectors, within the field of view of the FTS, in transition ($\sim$ 40% R_n). We measured the bandpasses of $\sim$ 5% of the $\sim$3000 ACTPol detectors with $\sim$7 re-pointings of the FTS in December 2014 and May 2015.

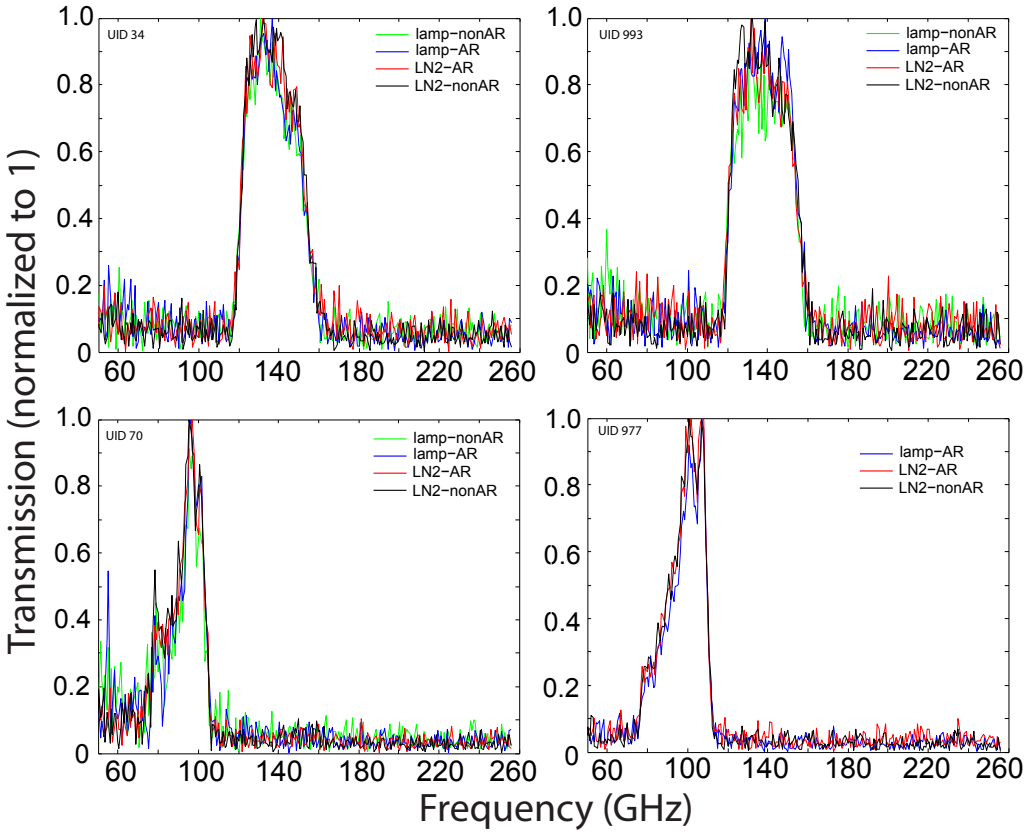

Figure 4.8: Comparison between the spectra measured using two different types of FTS sources (IR lamp and LN2) and AR coated/non-coated HDPE lens in the coupling optics. Apart from the higher signal-to-noise with the hot IR lamp source, no noticeable differences were observed between the various spectra.

We used two types of scans, one at high resolution (see Figure 4.9) across the nominal bands to measure their shapes, and another with low resolution (see Figure 4.10) to check for out-of-band leakage. The step size and throw combination of the dihedral mirrors was (Δl = 0.15 mm, L = 100 mm) for the high resolution ($\Delta\nu$ = 0.75 GHz, ν_{UL} = 250 GHz) scans, and (Δl = 0.03 mm, L = 20 mm) for the low resolution ($\Delta\nu$ = 3.75 GHz), high bandwidth (ν_{UL} = 1250 GHz) scans. Frames of data were drawn directly from the ACTPol MCE computers [67], which acquire detector data with a sampling rate of 400 Hz. The modulated signal was detected with the software lock-in technique described earlier. Using the ACTPol multiplexed readout scheme, multiple detectors could be simultaneously read out. The demodulated data for all detectors were saved as a single text file; each column corresponding to a single detector and each row corresponding to a position of the FTS moving mirror. The signal-to-noise ratio for each detector was also calculated and recorded. The few illuminated detectors were then chosen for further processing based on meeting an acceptable signal-to-noise ratio threshold.

4.5.2 From Interferograms to Spectra: Analysis and Results

The recorded interferograms were processed, phase corrected using the Mertz method [173, 174], and Fourier transformed to get the final spectra. For each recorded interferogram that passed the signal-to-noise ratio threshold criterion, the data processing involved the following steps. After removing obvious glitches/spikes in the data, the raw interferogram was first mean subtracted. A polynomial function, fit to an aggressively smoothed version of the raw interferogram, was then subtracted to remove any large scale spurious modulation of the data. Thereafter, the Mertz phase correction algorithm (described in detail here [175, 176]) was applied. This involved recovering the phase information using a near-symmetric subset of the interferogram centered about its peak (the zero path difference (ZPD) point), where the signal amplitude was high. The phase is given by:

$$\phi = tan^{-1}((Imag(\mathfrak{F}(dw))/Re(\mathfrak{F}(dw))) \tag{4.3}$$

where d denotes the interferogram data (after some processing, see [175, 176]), w is a ramp apodizing function, and $\mathfrak{F}$ denotes Fourier transform. The phase corrected spectra was obtained as:

$$Y_{pc} = Re((e^{-i\phi})\mathfrak{F}(dw)) \tag{4.4}$$

The frequency calibration factor (ν_{fac}) was applied and the final spectra was corrected

for the transmission of the lenses constituting the coupling optics, the reflection from the LDPE beam splitter, and the Rayleigh-Jeans (RJ) nature of the source blackbody spectrum, which amounts to dividing out the spectra by the two factors below:

$$RJ_{fac} = \frac{2h\nu^3}{c^2}\left(\frac{1}{e^{\frac{h\nu}{k_B T_A}}-1} - \frac{1}{e^{\frac{h\nu}{k_B T_S}}-1}\right) \qquad (4.5)$$
$$\eta = R_{mirror}R_{Lens1}R_{Lens2}R_{Lens3}$$

where, h, k_B, c are the well known constants; T_A is the ambient temperature ($\sim$280 K), and T_S is the blackbody source temperature ($\sim$873 K for the IR lamp and $\sim$77 K for LN2). Figures 4.9 and 4.10 show some sample interferograms and the corresponding corrected spectra.

Figure 4.11 shows the spectra for all the measured detectors, grouped by array and frequency, plotted over each other. Figure 4.12 shows the spectra averaged over measured detectors per array and frequency. For the single frequency band PA1 and PA2 pixels, the OMT coupled over a much wider than required bandwidth, and free space low-pass filters were responsible for defining the higher band edge. For the dichroic PA3 pixels, the OMT and the waveguide cutoff, together with the on-chip stub filters help define the bands, with the inner band edges being defined entirely by the stub filters. The OMT, together with the high edge of the 150 GHz stub filter define the highest band edge. The lowest band edge is defined by the cut-off associated with the waveguide section of the feedhorn, together with the low edge of the 90 GHz stub filter. We found that the detectors from one of the hex wafers (FH4) in PA3 and one semihex wafer in PA1 had shifted passbands that could be explained by changes in dielectric and/or material properties. The constituent hex and semihex sub-wafers of each array were fabricated in different runs and at different times. We think that the properties of the materials might have changed between the runs causing these unwanted shifts in the bands, though we note that the extent of the shifts observed would require almost unbelievably large deviations in the dielectric properties and/or London penetration depth of the superconducting niobium. It is worth noting that we did not find significant differences between the passbands of PA1 and PA2 measured on the telescope in December 2014 and May 2015.

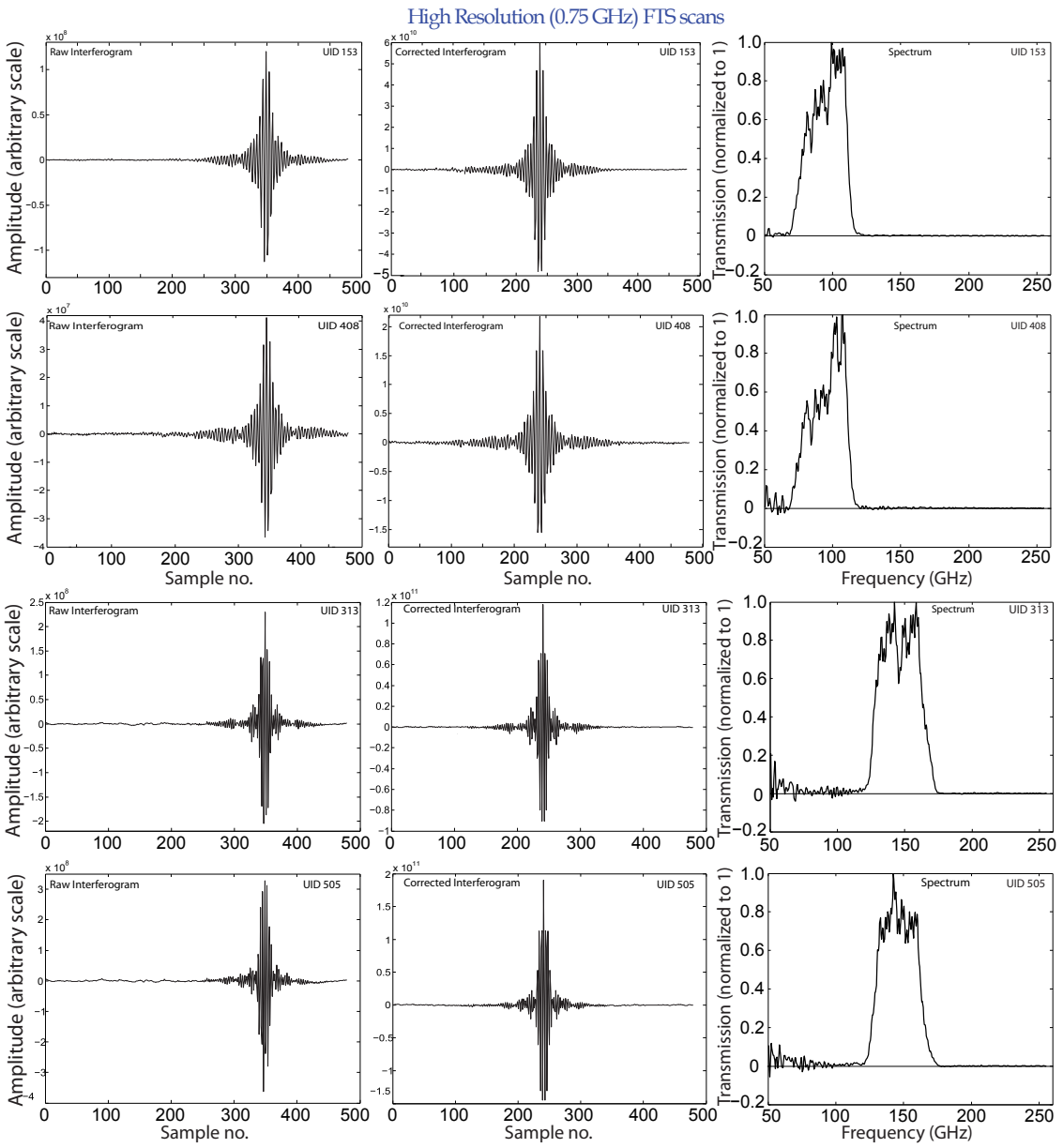

Figure 4.9: The left column shows some raw interferograms. The zero-path-difference (ZPD) point is not at the center because the throw of the movable mirror was not equal on either side of the center. The step size and throw combination of the dihedral mirrors was (Δl = 0.15mm, L = 100mm) for this higher resolution ($\Delta\nu$ = 0.75 GHz, ν_{UL} = 250 GHz) scanning. The middle column shows the same interferograms after phase correction. The right column shows the recovered spectra from the measured interferograms.

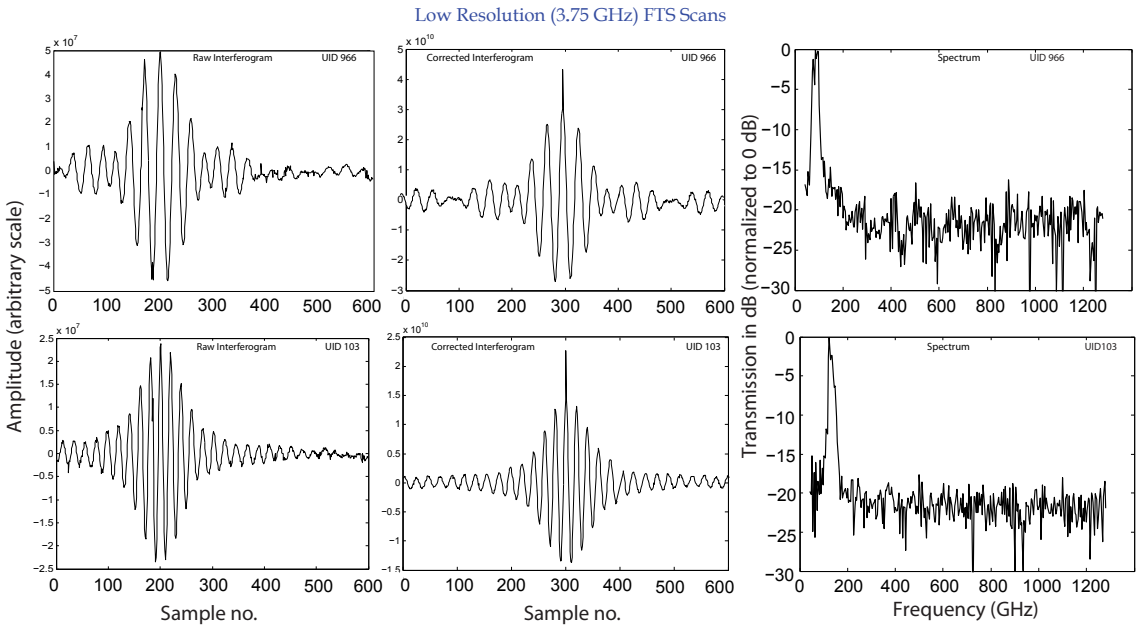

Figure 4.10: The left column shows some raw interferograms. The zero-path-difference (ZPD) point is not at the center because the throw of the movable mirror was not equal on either side of the center. The step size and throw combination of the dihedral mirrors was (Δl = 0.03mm, L = 20mm) for this lower resolution ($\Delta\nu$ = 3.75 GHz), high bandwidth (ν_{UL} = 1250 GHz) scanning. The middle column shows the same interferograms after phase correction. The right column shows the recovered spectra from the measured interferograms.

4.5.3 Effective Array Central Frequencies and Bandwidth

The wide bandwidth of the ACTPol receiver means that sources with different spectra have different effective central frequencies, which may be defined as [177, 178]:

$$\nu_e = \frac{\int \nu f(\nu)\eta(\nu)A_e(\nu)\sigma(\nu)d\nu}{\int f(\nu)\eta(\nu)A_e(\nu)\sigma(\nu)d\nu}, \tag{4.6}$$

where $f(\nu)$ is the passband response to an emitter whose power is flat in frequency, η is the loss which we take as unity across the band, A_e is the effective area, and $\sigma(\nu) \propto \nu^\alpha$ is the frequency dependence of the source, with α referring to the spectral index. We assume the following spectral indices for the different type of sources: α = -0.7 for synchrotron, α = -0.1 for free-free, α = 2.0 for Rayleigh-Jeans, and α = 3.7 for dusty sources, whereas for the CMB anisotropy and SZ sources, the $\sigma(\nu)$ is defined as:

$$\begin{aligned} \sigma(\nu) &\propto \frac{x^4 e^x}{(e^x-1)^2} \quad \text{(CMB anisotropy)} \\ \sigma(\nu) &= x\,coth(x/2) - 4 \quad \text{(SZ)} \end{aligned} \tag{4.7}$$

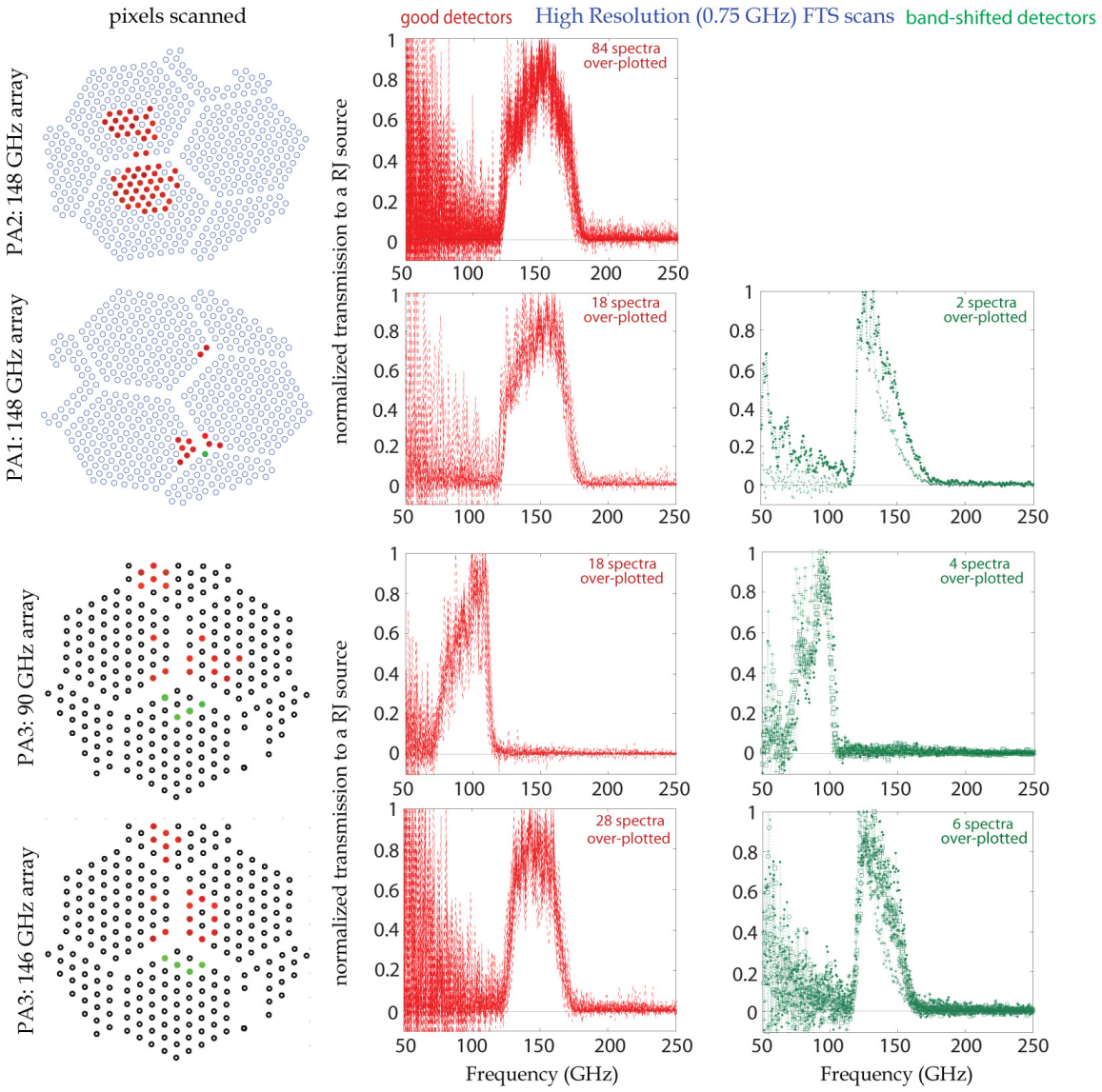

Figure 4.11: The left column shows schematics of the ACTPol arrays, with each circle representing a pixel and the filled circles representing the detectors whose measured passbands are over-plotted in each row. The 'good' detectors (red) refer to ones whose measured passband approximately matches the design, whereas the 'band-shifted' detectors refer to those which have a shifted passband with respect to design. Dividing by the RJ source spectrum blows up the noise at low frequencies.

where, $x = h\nu/k_B T_{CMB}$. In the case of observing a point source with a scalar feed, $A_e(\nu)$ would be constant across the band and Equation 4.6 reduces to:

$$\nu_e = \frac{\int \nu f(\nu)\sigma(\nu)d\nu}{\int f(\nu)\sigma(\nu)d\nu} \tag{4.8}$$

On the other hand, if the beam from the feed reflects off an ellipsoid mirror, as for ACT,

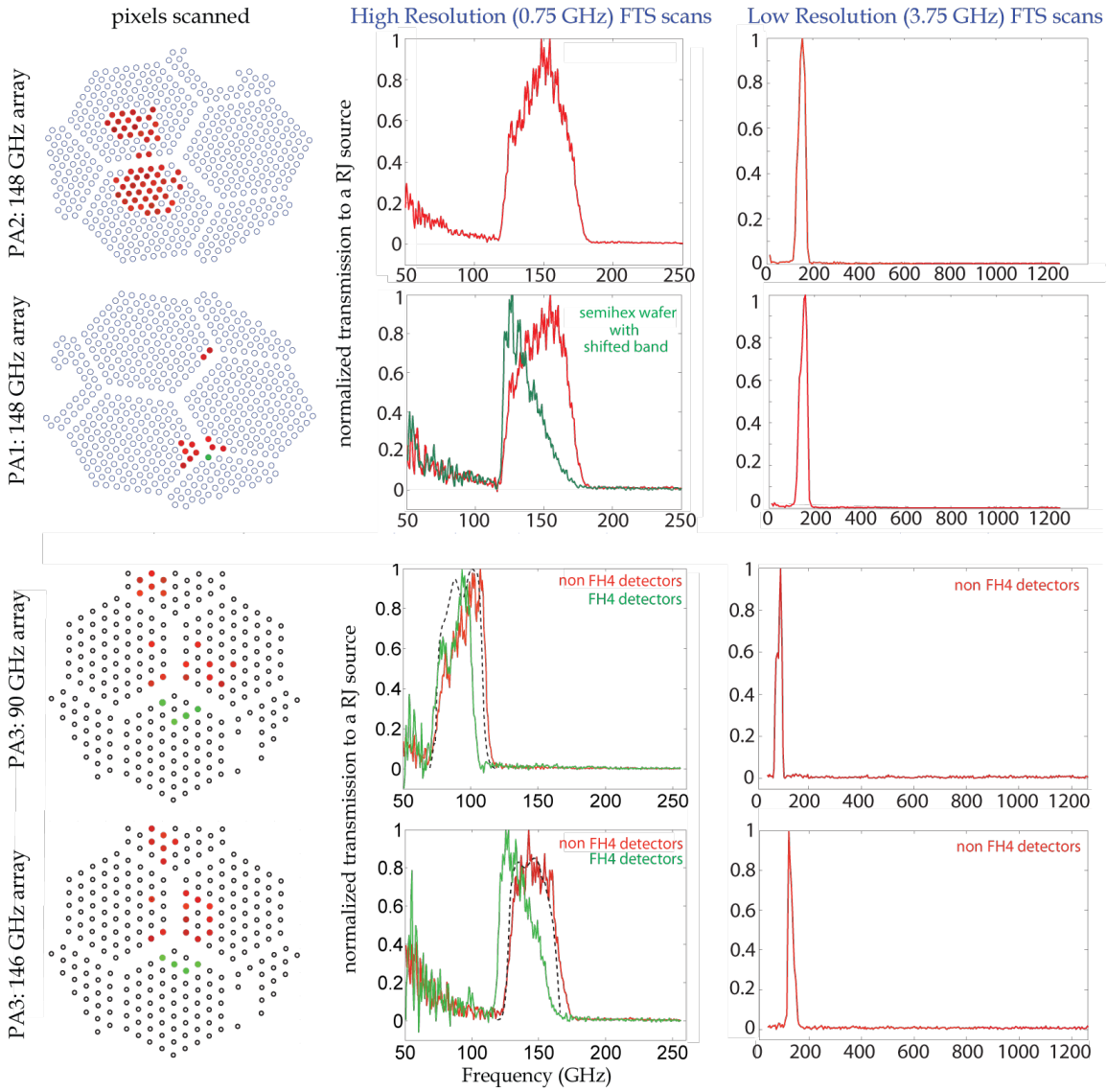

Figure 4.12: The left column shows schematics of the ACTPol arrays, with each circle representing a pixel and the filled circles representing the detectors whose measured passbands are averaged and plotted in each row. The subsequent columns show averaged high resolution and low resolution spectra. The detectors, represented by the green filled circles, have passbands shifted down in frequency (for the PA3 array, these are detectors on the FH4 hex wafer). The lowest band edge, defined by the feedhorn waveguide section, is not affected by this. The dotted lines (over-plotted with the PA3 spectra) are from simulations of the multichroic pixel, including the feedhorn and the OMT. However, the simulations do not include the filters in the optical path. The sharper roll-off (than design) in the lowest PA3 90 GHz band edge is a result of a design flaw in PA3 that the waveguide section of the feedhorn was much shorter than required, which has been rectified for the subsequent dichroic arrays. Dividing by the RJ source spectrum blows up the noise at low frequencies. No evidence for out-of-band leakage was found.

then the effective area $A_e(\nu)$ would be inversely proportional to frequency squared, and

Equation 4.6 reduces to:

$$\nu_e = \frac{\int \nu f(\nu)\sigma(\nu)\nu^{-2}d\nu}{\int f(\nu)\sigma(\nu)\nu^{-2}d\nu} \tag{4.9}$$

Using the measured spectral response of the detectors, we follow the method described in [177] to calculate the effective central frequency of broadband sources, including the CMB and the Sunyaev-Zeldovich (SZ) effect [179] and the effective bandwidth of the detectors. Both limits (Equations 4.8 and 4.9), differing by a ν^2 weighting, are calculated for all types of sources considered here. The average of the central frequencies computed using Equations 4.8 and 4.9 provides the best estimate of the effective central frequency for point-like sources. However, for a diffuse beam filling source, we approximate $A_e(\nu) = 1$ and recover an effective central frequency using Equation 4.8. The effective central frequencies to various types of sources and detector bandwidths, averaged over the measured detectors for each array, are listed in Table 4.2. The effective central frequencies to compact and diffuse sources as well as the effective bandwidths per measured detector are plotted in Figure 4.13.

In order to compute the effective bandwidth, we use the following definition due to Dicke [180]:

$$\Delta\nu = \frac{\left[\int f(\nu)d\nu\right]^2}{\int f(\nu)^2 d\nu} \tag{4.10}$$

Figure 4.14 shows the distribution of the efficiencies of the 90 and 150 GHz detectors in the deployed ACTPol PA3 multichroic (dichroic) array, with respect to the expected passbands from simulation of the pixel and the feedhorn. These were computed by Christine Pappas [234] using the relative response of the detectors to the atmosphere. The low optical efficiency of the FH4 detectors can be explained by their shifted bands relative to the simulated design. More details about the on-sky performance of the multichroic array are presented in [158], including detector sensitivities, time constants and NEP figure of the pixels.

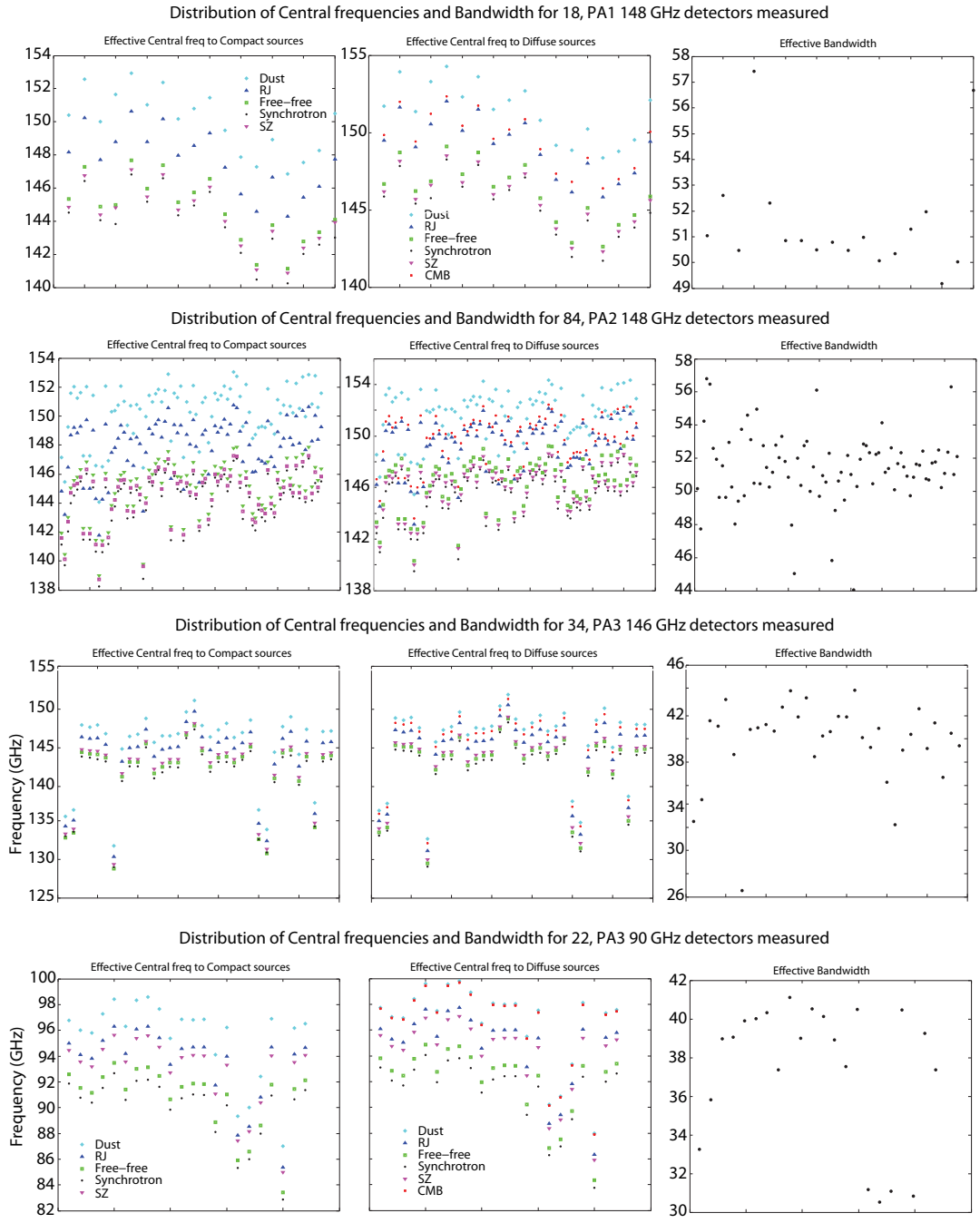

Figure 4.13: Plotted along each row are the per measured detector effective central frequencies to compact sources (left column), diffuse sources (middle column), and effective bandwidths (right column). The four rows correspond to the PA1 148 GHz array, PA2 148 GHz array, PA3 150 GHz array, and PA3 90 GHz array, respectively. All measured detectors (including the ones with shifted passbands are plotted here). Error bars are excluded to preserve readability.

The conversion factors listed in Table 4.2 are defined as:

$$\begin{aligned} \delta T_{CMB}/\delta T_{RJ} &= \frac{(e^x-1)^2}{x^2 e^x}, \text{ where } x = \frac{hf}{kT_{CMB}} \\ \delta W/\delta T_{RJ} &= 2k\Delta\nu, \text{ where the factor 2 comes from 2 polarization states} \\ \Gamma_{RJ} &= \frac{c^2}{2k_B\Omega\nu^2} \\ \Gamma_{CMB} &= \Gamma_{RJ}(\delta T_{CMB}/\delta T_{RJ}) \end{aligned} \tag{4.11}$$

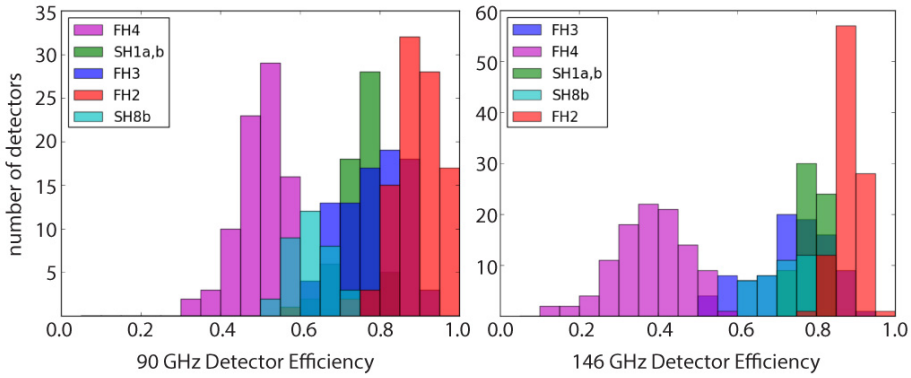

Figure 4.14: A histogram plot of the 90 and 150 GHz PA3 (dichroic array) detector efficiencies, relative to the simulated passband shown in dotted lines in Figure 4.12. FH4, FH3 and FH2 represent the three hex sub-arrays and SH1a, SH1b and SH8b represent the three semi-hex sub-arrays. Figure courtesy: Christine Pappas

4.6 Conclusion

We have demonstrated a method to measure the on-sky instrument passband and calculate the effective central frequencies of the detectors to various broadband sources. The detector arrays are individually characterized in the lab prior to deployment, but the on-sky characterization of the deployed instrument provides a way to test the entire receiver chain end-to-end in its final observing configuration. Knowing well the detector central frequency is becoming more and more critical as CMB receivers attain ever-increasing sensitivities. Our goal for the future is to further reduce the uncertainty in the passband by carrying out measurements with finer frequency resolution.

Table 4.2: ACTPol effective central frequencies and bandwidth
(from Dec 2014 and May 2015 on-site FTS measurements)

Array	*PA1 150 (GHz)*	*PA2 150 (GHz)*	*PA3 90 (GHz)*	*PA3 150 (GHz)*
Effective bandwidth[a,†]	51.2±2.1	51.1±1.9	38.4±1.9	41.1±1.6
Effective band centers[b]	*compact sources*			
Synchrotron	143.9±1.9	144.2±1.9	91.0±1.1	143.1±1.6
Free-free	144.7±1.9	145.0±1.9	91.8±1.1	143.7±1.6
Rayleigh-Jeans	147.7±1.9	148.0±1.9	94.6±1.1	145.6±1.6
Dusty source	150.0±1.9	150.3±1.9	96.7±1.1	147.2±1.6
Effective band centers[b]*:*		*diffuse sources*		
Synchrotron	145.3±1.9	145.6±1.9	92.4±1.1	144.1±1.6
Free-free	146.1±1.9	146.4±1.9	93.2±1.1	144.6±1.6
Rayleigh-Jeans	149.1±1.9	149.4±1.9	95.9±1.1	146.6±1.6
Dusty source	151.4±1.9	151.7±1.9	97.9±1.1	148.1±1.6
CMB	148.9±1.9	149.1±1.9	97.1±1.1	146.6±1.6
SZ effect	145.0±1.9	145.3±1.9	94.1±1.1	143.7±1.6
Conversion factors				
$\delta T_{CMB}/\delta T_{RJ}$[c]	1.72±0.03	1.72±0.03	1.27±0.01	1.69±0.02
$\delta W/\delta T_{RJ}(pW/K)$[d]	1.41±0.06	1.41±0.06	1.05±0.06	1.13±0.04
$\Gamma_{RJ}(\mu K/Jy)$[e]	7640±260	8160±240	6160±250	5740±270
$\Gamma_{CMB}(\mu K/Jy)$[f]	13160±440	14070±410	7820±310	9720±450
Beam solid angles (nsr)	192±4	179±3	560±19	264±11

[a,b] These values are obtained by averaging over individual detectors (excluding the ones with the shifted passbands). The uncertainties quoted in the table are equal to the standard deviation representative of the dispersion between the measured detectors. The measurement resolution of the FTS was ∼0.8 GHz and has not been deconvolved.

[b] Spectral index assumed: Synchrotron emission ($\alpha = -0.7$), Free-free emission ($\alpha = -0.1$), Rayleigh-Jeans emission ($\alpha = 2.0$), Dusty source emission ($\alpha = 3.7$).

[c] This gives the conversion factor from T_{RJ} to T_{CMB}.

[d] This gives the power in a single mode of radiation or the conversion factor from T_{RJ} to pW.

[e] This gives the conversion factor from T_{RJ} to Jy.

[f] This gives the conversion factor from T_{CMB} to Jy.

† The bandwidth uncertainty for PA1 and PA3 (90) is higher than the central frequency uncertainty because a couple of detectors in each of these arrays were measured to have significantly wider (in the case of PA1) and narrower (in the case of PA3 90) bandwidths than the mean. We are trying to understand what caused this.

CHAPTER 5

Simulation of Diffractive Far-sidelobes resulting from Panel Gaps in the ACT Primary Mirror

5.1 Introduction

The diffractive far-sidelobes of the telescope beam, that result from diffraction from the gaps between the 71 panels that make up the 6 m ACT primary mirror, will couple radiation from undesirable sources on the ground and in the sky, that can contaminate scientific measurements. Simulations of these far-sidelobes are presented in this chapter. Using these simulations we can make rough order of magnitude estimates of the systematic contamination due to pickup from ground structures, terrestrial features, and astronomical sources like the Sun through these lobes during CMB observations. Modulation of the pickup due to telescope scanning or time-variation can introduce contaminating signals with unique signatures into the data. The simulated sidelobe models are convolved with various expected sources of pickup to predict levels of expected contamination. The simplified approach adopted for this work makes several approximations and only provides an order of magnitude estimate of the level of contamination in μK units. The results help assess the need for a more accurate analysis using powerful software tools and extensive ray tracing. Results from such an analysis could then feed into the algorithm that selects the data to be used for science, throwing out the chunks of the time-ordered-data (TOD) with unacceptable levels of contamination. We also estimate the reduction in contamination that is achieved by covering the panel gaps with aluminum tapes.

Here, I treat the ACT telescope as a transmitting antenna and simulate the diffractive far-sidelobes to understand the spatial structure of these lobes. The reciprocity theorem states that the characteristics of a transmitting and receiving antenna are essentially equivalent, therefore these simulations can be used to understand how radiation from various sources couple to the telescope through the sidelobes.

5.2 Simulations

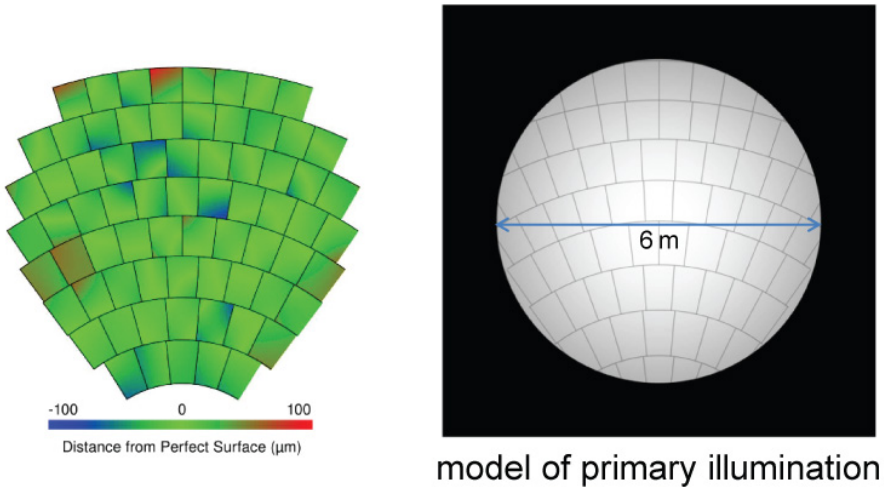

Figure 5.1: *left:* A schematic of the ACT primary mirror showing the 71 panels (courtesy: Swetz et. al. [76]). *right:* Model of the primary illumination pattern with the panel gaps, which is also the aperture field for our simulation.

Simulations of the side lobes due to diffraction from the gaps between the panels that make up the primary mirror were generated using the Scalar theory of Diffraction which follows directly from Maxwell's equations [181]. This relates the radiation pattern B at a distance $r(x,y,z)$ from the telescope to the distribution of fields on the aperture plane $F((\zeta,\eta,0)$ [182] by:

Far field approximation (Fraunhofer region):

$$B(u,v) = \frac{i}{\lambda}\frac{e^{-ikr}}{r}\int_A F(\zeta,\eta)exp[-ik(\zeta u+\eta v)]d\zeta d\eta, \tag{5.1}$$

Near field approximation (Fresnel region):

$$B(u,v) = \frac{i}{\lambda}\frac{e^{ikr}}{r}\int F(\zeta,\eta)exp(i[-k(u\zeta+v\eta)+\delta\phi])d\zeta d\eta, \tag{5.2}$$

where $\delta\phi$ is a defocus term given by:

$$\delta\phi = kr(\sqrt{1-\frac{\zeta^2+\eta^2}{r^2}}-\sqrt{1-\frac{R^2}{r^2}}) \tag{5.3}$$

where, $u=\frac{x}{r}$, $v=\frac{y}{r}$, $k=2\pi/\lambda$ is the wave number and the wavelength λ is taken to be 2 mm for our calculations, corresponding to a frequency of 150 GHz. The coordinates

(ζ, η) parameterize the position on the aperture and (u, v) are the direction cosines which are used to parameterize the angular position on the beam. In the limit that $R >> D$ (far-field) this equation is essentially a 2D Fourier transform of the aperture illumination pattern F over the area of the aperture plane. In the near-field region, where $R < D$, this is a Fourier transform modified by a phase term (see Equation 5.2) corresponding to a spherical defocus. The defocus term is defined over the aperture of the telescope which we will assume has a radius R = 3 m.

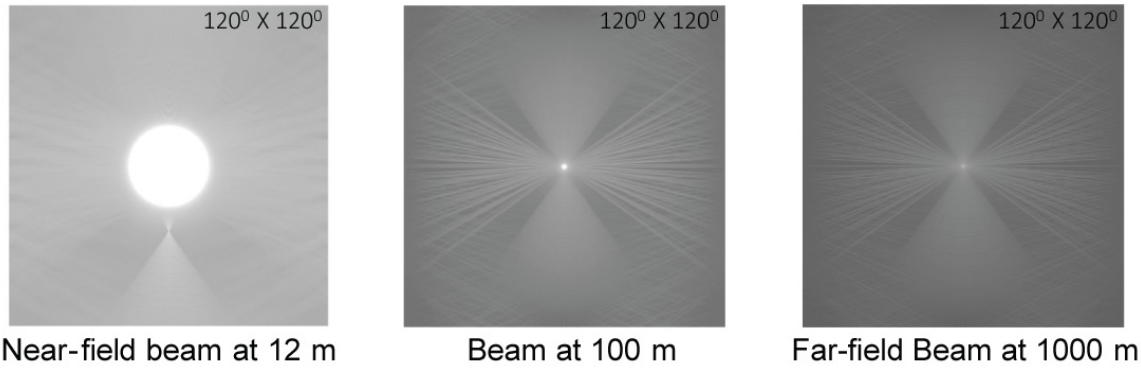

Figure 5.2: Grayscale images of the simulated near and far field beams plotted in log scale. The square patches represent a 120° x 120° region on the sky. The panel gaps were assumed to be not covered for these simulations.

We modeled the ACT primary mirror as having a Gaussian illumination on the panels and zero field within the 2 mm wide gaps and outside the mirror edges. The fields F were calculated by assuming a Gaussian with a -3 dB width of 6 m, equal to the diameter of the primary mirror. Rays which hit the mirror panels are reflected to the aperture plane, while those that hit the gaps are terminated. The aperture field was gridded with ∼0.5 mm (= $8/2^{14}$ m) resolution corresponding to one quarter wave length at 150 GHz. The resulting illumination pattern F on the aperture plane is shown in Figure 5.1. The simulated beam or the radiation pattern was calculated using Equations 5.1 and 5.2 and shown in Figures 5.2 and 5.3. Assuming a flat sky, the anglular extent of the simulated beams when projected on the sky is calculated using the relation: $d\theta$ (radians) = λ / (N dx), where N is the number of pixels on a side of the map, λ = wavelength (in mm), and dx is the spacing (in mm) between pixels on the aperture.

The gaps in the primary mirror of the ACT are covered by $l \sim 1$ inch wide aluminum tapes that are $t \sim 6$ mils thick. The effect of these aluminum tapes is modeled by removing the gaps from the simulation and introducing a phase term $\phi_{tape} = e^{i\frac{2\pi}{\lambda}(2t)}$, where t is the

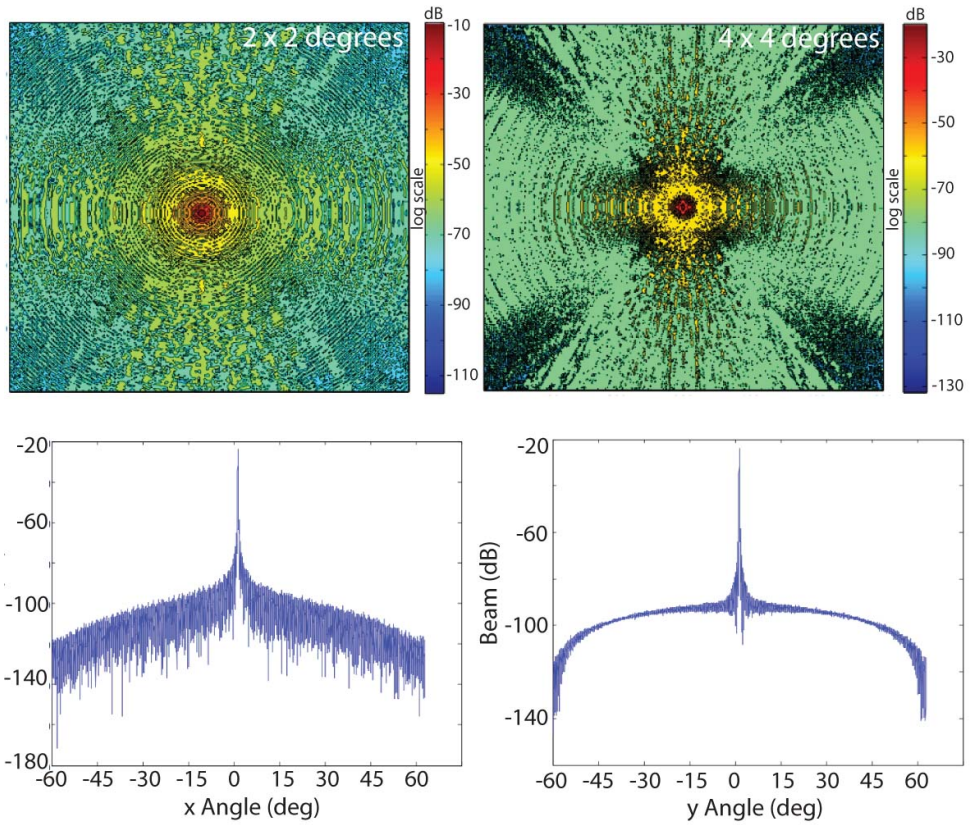

Figure 5.3: *top:* Filled contour plots of the simulated far-field beam zoomed in to 2° x 2° and 4° x 4° patches. *bottom:* 1D cuts across the center of the beam plotted in logarithmic dB scale.

thickness of the tape. The simulated beams are shown in Figure 5.4. Comparison between the simulated beams with and without the tapes clearly shows that the sidelobes are reduced by the use of the tapes, though not entirely eliminated.

5.3 Estimates of Systematic Contamination

To estimate the amplitudes of the spurious signals picked up through these sidelobes, we convolve the simulated beam maps with models of possible sources of contamination in Fourier space. We carry out these convolutions in the flat sky approximation. The convolved map is given by:

$$\text{Convolved Map} = \mathfrak{F}^{-1}[\mathfrak{F}(B)\mathfrak{F}(Model)], \tag{5.4}$$

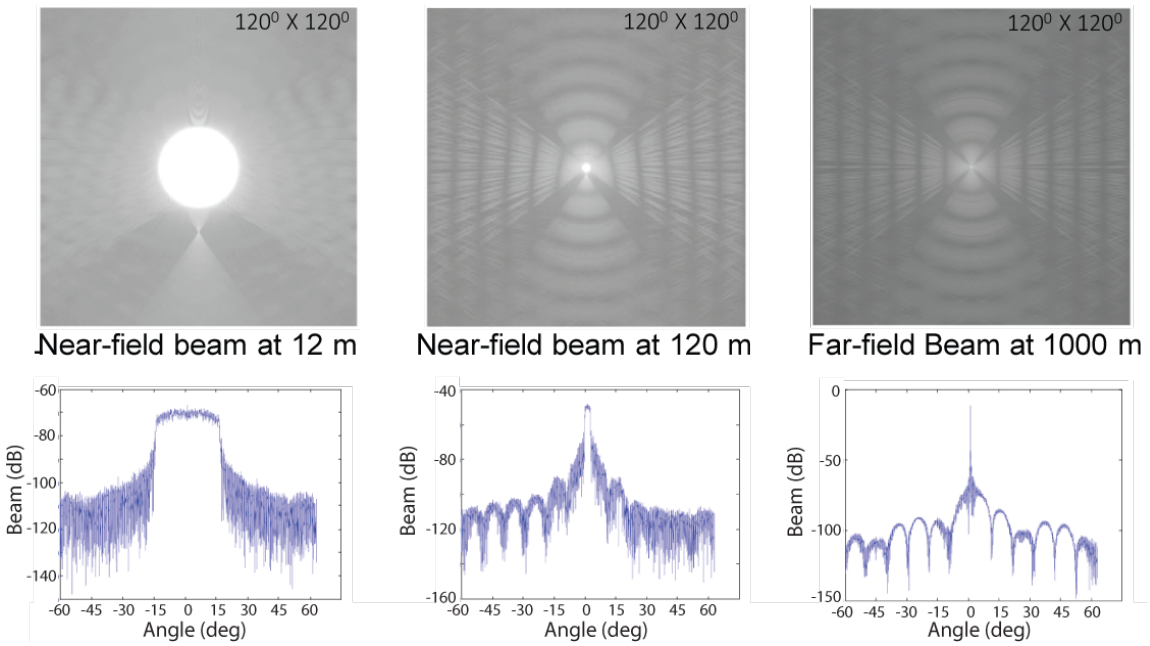

Figure 5.4: Grayscale images of the simulated near and far field beams plotted in log scale along with 1-D cuts (x-, y-, y-) across the center plotted below. The square patches represent a 120° x 120° region on the sky. The panel gaps were assumed to be covered with aluminum tapes for these simulations.

Figure 5.5: A panoramic view of the landscape surrounding the telescope.

where, $\mathfrak{F}$ refers to the Fast Fourier Transform algorithm and $\mathfrak{F}^{-1}$ is the Inverse Fast Fourier Transform implemented using commercially available Matlab/Python FFT2 routine. Figure 5.5 shows a panoramic view of the landscape around the telescope. Couple of mountain peaks seen to the left of the telescope in the figure are worth investigating from the point of view of ground pick-up. Figures 5.6 shows the major sources of ground pick-up. Figures 5.6 shows the major sources of ground pick-up We considered the following sources: (1) Fixed ground shield. The ACT telescope structure is surrounded by a stationary ground shield made of 12 flat reflecting panels shielding the telescope from potential sources of contamination on the ground, like mountains. The radiation from these panels is assumed to have a 20 K peak-to-peak sinusoidal variation of temperature in azimuth across the surface of the panel with a mean of 10 K. The temperature peaks at the center and is zero at the edges of the panel with no dependence on elevation as shown in Figure 5.7. By convolving the simulated near-field beam at a distance of 12 m with this model of the flat ground

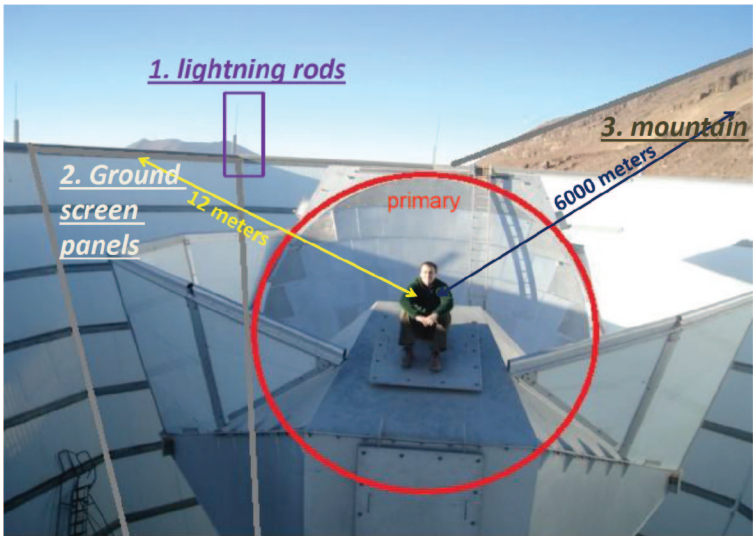

Figure 5.6: A photo of the telescope showing the major sources of ground pick-up.

shield panels, we estimate the contamination signal picked up through the sidelobes. The amplitude of the pick up is plotted at four different elevations in Figure 5.7.

(2) Lightning rods. The ground shield also had a lightning rod attached to the top of each panel. We assumed these to be radiating at 100 K and calculated the resulting pick up, shown in Figure 5.8.

(3) Mountains. Some of the mountain peaks surrounding the ACT site have a direct line of sight to the telescope over the fixed ground shield. To model this, we took a 360° panoramic image of the region as seen from the telescope. By convolving the simulated beam at a distance of 6 kilometers with a model of the mountains assumed to emit at 300 K, we calculated the pick up as shown in Figure 5.9.

The simulations of the ground pick-up that I have presented here assume that the primary mirror panel gaps were covered by tapes. Though these are at best order of magnitude estimates, we can get an idea of the dominant sources of contamination. Among the sources considered here, it appears that the lightning rods and mountain peaks are relevant sources of contamination, while the fixed ground screen is probably not a big concern.

(4) The Sun. The diffractive sidelobes in the far-field beam have significant power on the sky as well, so contamination from astrophysical sources must be considered. The Sun is the brightest among these sources and is carefully avoided during scans. However, the

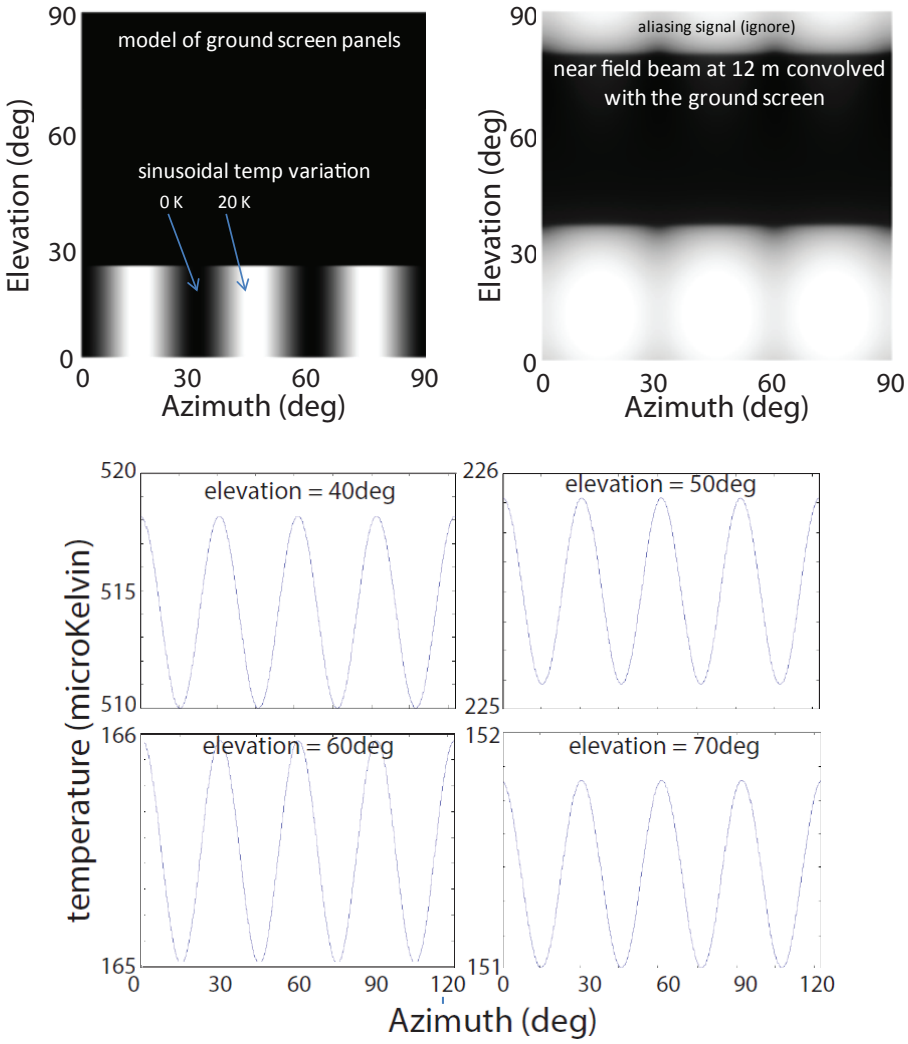

Figure 5.7: *top left:* Model of the emission from the stationary ground screen encompassing 90° in azimuth. *top right:* Convolved map with the simulated near-field beam at a distance of 12 m. *bottom:* 1-D constant-elevation cuts of the convolved map showing the amplitude of the contamination when the telescope is pointed to different elevations

.

far-sidelobes in the far-field beam still makes the Sun a potential source of contamination. The Sun is modeled as a 0.5° circular disc on the sky emitting at 6000 K. We convolved this model of the Sun with the far-field beam and compared the contamination with and without tapes covering the primary panel gaps in Figure 5.10. The radial stripes in the Sun map going away from the center are qualitatively similar to the simulation of Sun contamination for the case where panel gaps are assumed to be covered with aluminum tapes.

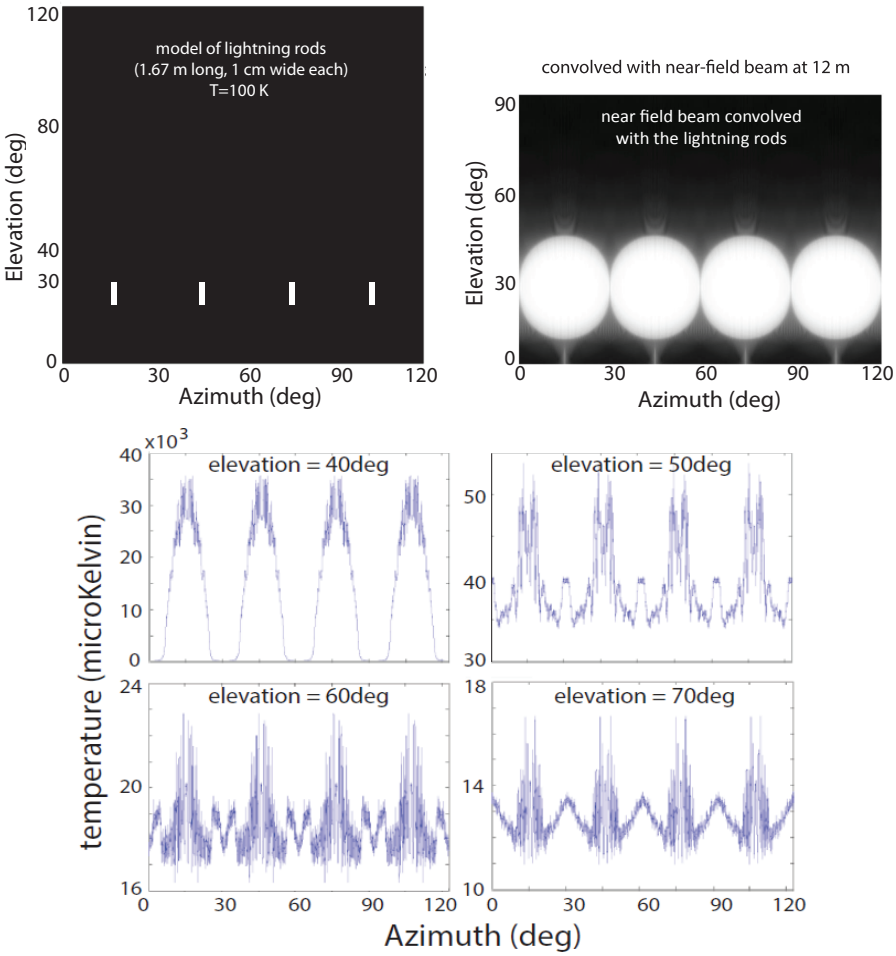

Figure 5.8: *top left:* Model of the emission from the lightning rods encompassing 90° in azimuth. *top right:* Convolved map with the simulated near-field beam at a distance of 12 m. *bottom:* 1-D constant-elevation cuts of the convolved map showing the amplitude of the contamination when the telescope is pointed to different elevations

.

5.4 Summary

We have found that the diffractive far-sidelobes in the beam caused by the gaps between the panels making up the ACT primary mirror pose a serious risk of contamination from the ground and from bright astrophysical sources like the Sun. These sidelobes are difficult to get rid of entirely as that would require changes to the structure of the primary mirror itself. However, the panel gaps have always been covered with aluminum tapes and the simulations confirmed that the tapes reduce the impact of the sidelobes significantly, especially in the case of pick-ups from contaminants in the far-field. The pick up from near-field contaminants in the ground is much larger in amplitude and steps are being continuously

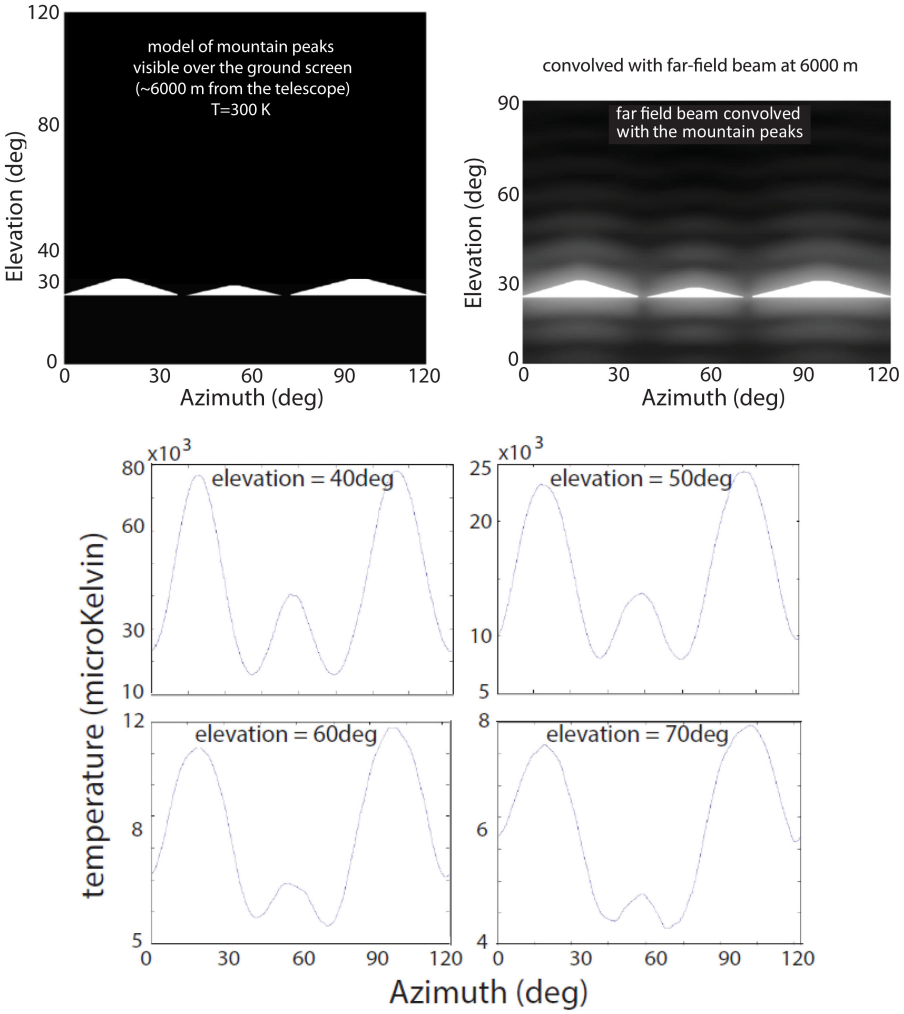

Figure 5.9: *top left:* Model of the emission from the mountain peaks encompassing 90° in azimuth. *top right:* Convolved map with the simulated beam at a distance of 6 km. *bottom:* 1-D constant-elevation cuts of the convolved map showing the amplitude of the contamination when the telescope is pointed to different elevations

.

taken to mitigate these. For example, maps from the TOD's made by S. K. Naess confirmed that there was significant contamination from the lightning rods, most of which have since been removed. Recent work by Rojas et al. [183], who modeled the full telescope structure and generated detailed simulations using powerful commercial software (GRASP), has significantly improved our understanding of the various pick-ups through the sidelobes. It has further shown that diffraction from the panel gaps in the secondary mirror also contribute significantly to the far-sidelobes. The collaboration is investigating this further. For contamination from astrophysical sources like the Sun and the moon, routines have been developed to throw out the contaminated TOD's based on some acceptable thresholds.

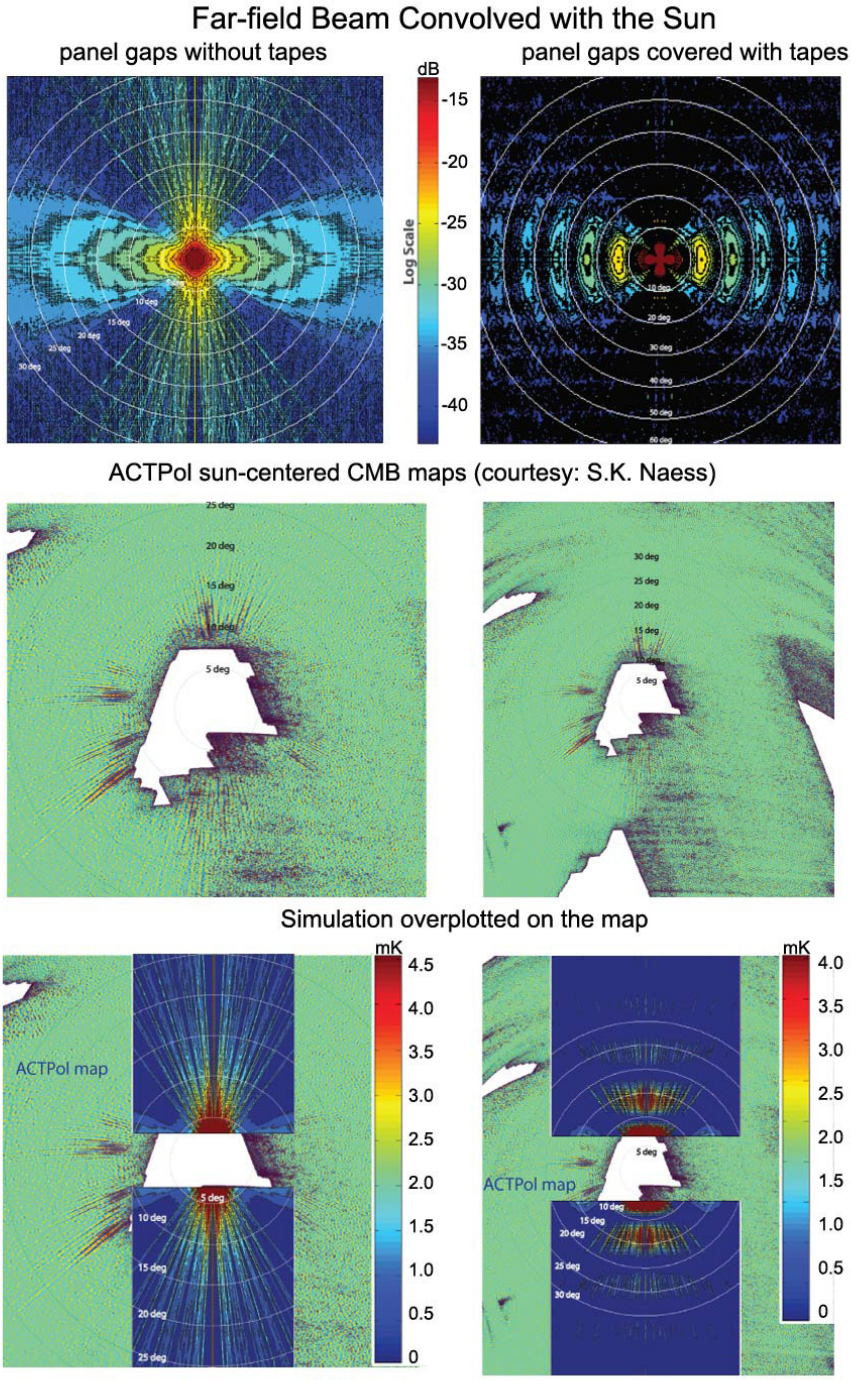

Figure 5.10: *top row:* Map of the Sun convolved with the simulated far-field beam, coordinate-transformed to polar coordinates with the Sun at the center and plotted in logarithmic dB scale. The white circles are spaced at 5° intervals away from the center. *middle row:* Sun-centered ACTPol maps made by S. K. Naess. The radial stripes are a result of Sun contamination. *bottom row:* Simulated contamination superimposed on the map. The left column plots are with uncovered panel gaps while the right column plots assume aluminum tapes covering the gaps.

.

CHAPTER 6

ACTPol: Polarized Point Sources at 148 GHz

6.1 Introduction

The increasing resolution of millimeter wavelength telescopes has enabled detections of a large number of extragalactic sources that emit brightly on small angular scales in the millimeter-wavelength sky. Based on the frequency dependence of the intensity of the emitted radiation, these sources can be broadly categorized into two populations: active galactic nuclei (AGN), which are compact regions at the centre of galaxies, and dust-obscured star forming galaxies (DSFG), which represent the most intense starbursts in the universe. The AGNs have been explored for decades through long-wavelength radio surveys. However, the characterization of the DSFG population has gathered momentum only in the last few years owing to significant recent advances in millimeter and submillimeter-wave observing capabilities. The ACTPol receiver deployed on the Atacama Cosmology Telescope (ACT) in Chile have been scanning large areas of the sky with the primary goal of measuring fluctuations in the CMB polarization signal over small angular scales. Together with SPTPol, the two experiments have the finest angular resolution ($\sim$arc-minute) among currently operating CMB observatories. Hundreds of extragalactic sources (galaxies) are being detected in CMB maps as high point-like fluctuations above the mean. These detections, combined with galaxy type confirmation from optical surveys, has opened up a major avenue for understanding the evolution of underlying galaxy populations over cosmic time, and over epochs of intense star formation. Results from observations with the original ACT receiver MBAC at 148 GHz revealed more than 150, mostly synchrotron, sources [184]. The South Pole Telescope SPT-SZ survey detected nearly 200 foreground sources [185, 186], again mostly synchrotron dominated. In both cases, virtually all the detected sources were identified with radio sources contained in catalogs constructed at lower radio frequencies, though there were evidences of a few dust dominated sources peaking at higher frequencies [187], which opens up an exciting new way of studying dusty star-forming galaxies by identi-

fying these sources and subsequently following them up with arc-second resolution radio telescopes like ALMA. The DSFGs, which play an important role in the assembly of stellar mass and the evolution of massive galaxies in the universe, are mostly hidden from the view of optical/UV observations due to the high dust obscuration. Millimeter and submillimeter observations can provide a more complete picture of star formation over a large range of look-back times and improve our understanding of the underlying astrophysics that govern the start and end of the dusty starburst phase, which is still in a nascent stage.

Compared to high resolution ($\sim$arc-second) radio telescopes with very high sensitivity, millimeter-wave survey telescopes have only recently achieved $\sim$arc-minute resolution and are also typically less sensitive. Further, the synchrotron type spectra of radio sources make them increasingly dim at higher frequencies. Hence, measurements of the spectral energy distributions (SEDs) of extragalactic sources at $\sim$ millimeter wavelengths [188] have improved only recently. Several astrophysical processes generate linearly polarized photons, such as synchrotron radiation. Quasars are one of the most powerful sources of synchrotron radiation, from radio to the visible and X-ray bands. The fractional polarization of a source, along with the spectral shape of the polarized emission, is a powerful tool to study the emission mechanisms [189]. Therefore, characterization of these extragalactic sources, including their polarization properties, across a wide range of frequencies, will be critical for validating models of the physics of accreting black holes and radio jet formation.The role of magnetic fields, for e.g., in accreting black holes in stellar mass systems and AGNs, and isolated neutron stars, can be efficiently studied. Polarization measurements can also provide valuable insight into physical processes occurring in high-redshift galaxies. Over the last few years, efforts to measure polarization of extragalactic sources at millimeter wavelengths have started picking up. These include 145 sources measured with the Institut de Radioastronomie Millimetrique (IRAM) 30m dish at 90GHz [190]; 22 objects [191] identified in the Wilkinson Microwave Anisotropy Probe (WMAP) polarization data [192]; VLA measurements at 8-43 GHz [193] of WMAP catalog sources [194] and AT20G selected sources [195]; extragalactic radio sources observed during the CMB polarization survey of the Q/U Imaging Experiment (QUIET), operating at 43GHz (Q-band) and 95GHz (W-band) [196]; search for transient point sources [197] using the 10-meter South Pole Telescope [198]; measurement of polarization properties of NVSS sources [199]; and sources identified in the Planck satellite polarization data [200, 201].

The measurement of CMB polarization anisotropies, particularly the E-mode anisotropies at small angular scales, can help break some of the degeneracies between cosmological pa-

rameters. One such parameter is the spectral index n_s of the primordial fluctuations which in turn constrains the form of the inflationary potential. Other parameters that could be constrained using the contribution of the SZ signal to the power spectrum include fluctuations in the matter density field σ_8 [202, 203], and dark energy [204, 205, 206]. However, it is at the small angular scales that the extragalactic point sources have the maximum contribution to the power spectrum, which is expected to be a significant fraction of the polarization power [193]. Hence, an extensive characterization of these sources in terms of their spectral and spatial distribution is essential in order to separate foregrounds from the CMB polarization anisotropies. This is becoming increasingly important as measurements of the small angular-scale fluctuations in the CMB are attaining higher sensitivity and finer resolution. Data already available suggest that the existing models [207, 208, 209] based on extrapolations from lower frequency radio observations overestimate the effect of radio sources at millimeter wavelengths [184].

We present measurements of the polarization fraction of $>$200 intensity selected sources in the ACTPol Deep56 region at 148 GHz using data from seasons 1 and 2 of ACTPol observations. We describe a method to correct for noise bias in the polarization fraction measurements through a Monte Carlo analysis and test it on simulated maps. We also match these sources with catalogs from other surveys at a number of frequencies and compare measurements of the flux and polarized flux. The spectral characteristics of the source emission is also discussed. We also attempt to model the distribution of source polarization fraction as a function of frequency extendable to lower flux limits. This could help estimate the contamination of the CMB polarization signal at small angular scales by unresolved polarized point sources [210].

6.2 Observations

6.3 Point Source Detection in Intensity maps

The Atacama Cosmology Telescope Polarimeter (ACTPol) receiver is a millimeter-wave camera which has surveyed thousands of square degrees of sky at arc-minute resolution with sensitivity to sources at the level of a few milli-Jansky (mJy). Achieving first light in 2013, ACTPol observed in a band centered at 148 GHz (2.0 mm) for the first two seasons, and simultaneously in bands roughly centered at 150 GHz (2.0mm), and 90 GHz (1.2 mm) in its third season. In its first two seasons from September 11, 2013 to December 14, 2013

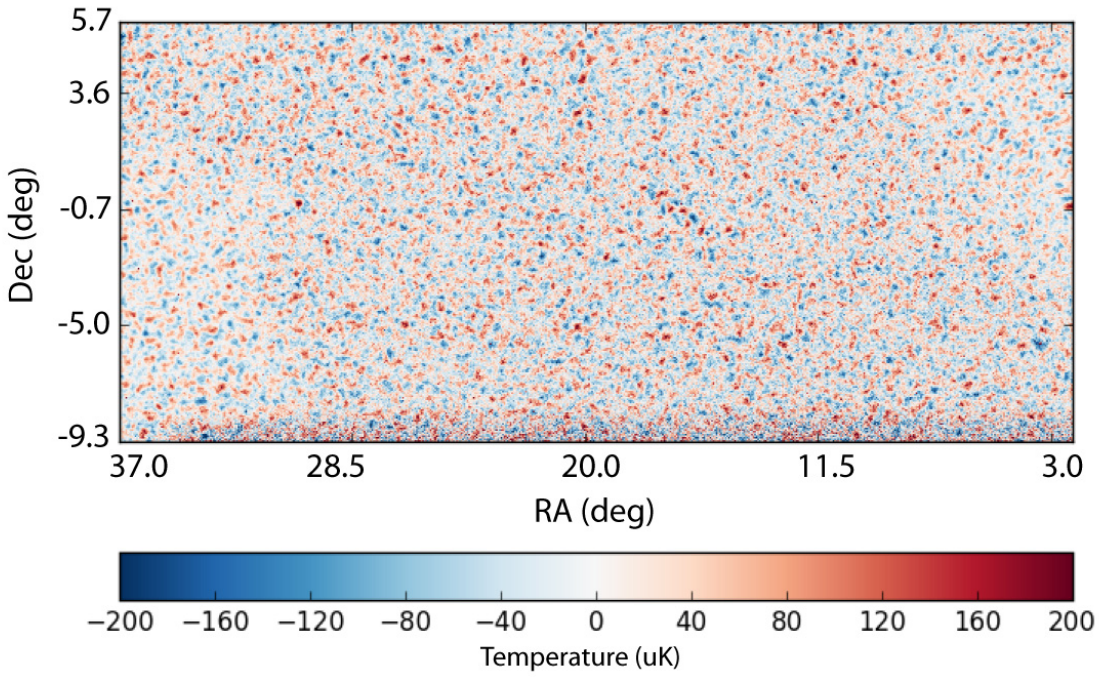

Figure 6.1: Intensity map of a selected region within the ACTPol Deep56 patch. The color scale is restricted to $\pm 200\ \mu K$.

(S1), and August 20 2014 to December 31 2014 (S2), ACTPol observed four deep regions and two wider regions. Here, we present the properties of extragalactic sources detected in the night-time data in one of the wider regions, namely D56 covering 540 deg^2 with coordinates $-7.2^\circ <$ dec $< 4^\circ$ and $352^\circ <$ RA $< 41^\circ$, including the deeper D5 and D6 sub-regions measured in both S1 and S2. The combined map and weight map of the two-season data is presented in [211]. The combination of S2 data from both the 148 GHz receiver arrays for D56, and S1 data for D5 and D6 from the first 148 GHz array results in a white noise map sensitivity of 20, 12, and 8μK arcmin^{-1} for D56, D5 and D6 respectively. The corresponding Stokes Q and U sensitivities are obtained by multiplying by $\sqrt{2}$. This white noise level, when match filtered with the ACTPol beam, results in typical sensitivities to point source flux densities from 3 to 5 mJy for a signal-to-noise ratio greater than 3.

Point sources in the maps for CMB studies are a source of foreground contamination, that need to be identified and removed from the maps prior to using them for computing properties of the CMB, in particular, power spectrum and lensing of CMB photons. We used the matched filtering method [212] developed by T. Marriage et al. [184] to find sources in the ACTPol intensity maps. Figure 6.1 shows a region of the ACTPol Deep56 intensity map and Figure 6.2 is the match-filtered version. Source flux density recovery is a

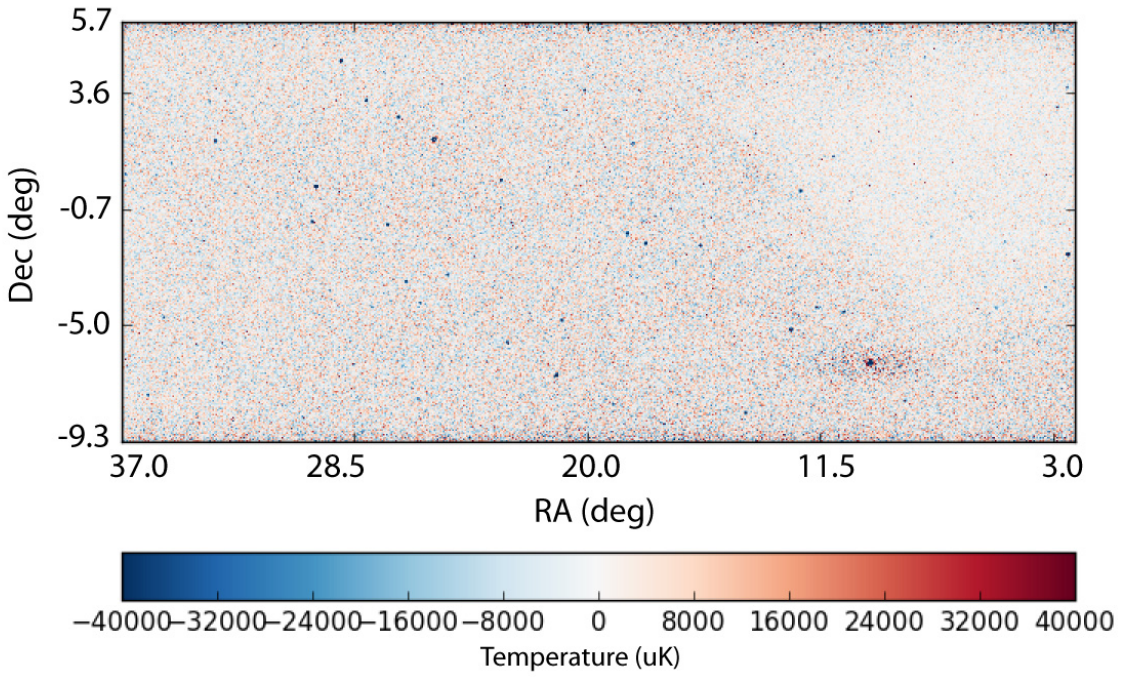

Figure 6.2: Match filtered map of the region shown in Figure 6.1. The bright spots in this map correspond to galaxies. The color scale is restricted to $\pm 40000\ \mu K$.

function of the form of the source profile assumed in the matched filter, for which we take the ACTPol 148 GHz beam. The profiles of some of the brightest sources in the ACTPol map were examined and fit with a background term plus a beam profile to arrive at the most accurate and refined representation of the beam. The spatial representation of this beam (courtesy: Marius Lungu) on the sky in the ACTPol pixelization (half arc-minute) is shown in Figure 6.3.

There are some irregular sources whose profiles do not match the beam profile, for e.g., spiral galaxies and extended galaxies. In the first pass, the matched-filter source-finding algorithm doesn't completely remove these sources. In order to remove such irregular sources completely, of which there are only a few ($\sim$10 in the Deep56 region), we visually look for residual bright spots (from the initial partial subtraction) in the maps after the first pass of source subtraction. After identifying these, we run the source-finding algorithm again on a $\sim 1^{\circ}$x1° patch of the template-subtracted map (obtained by making a template for the sources detected in the first pass and subtracting this template from the original map) centered around each of these sources and carry out a second round of source subtraction. A few examples, illustrating this, are in Figure 6.4. Figure 6.5 shows a histogram plot of the number of sources detected as a function of the detection signal-to-noise ratio.

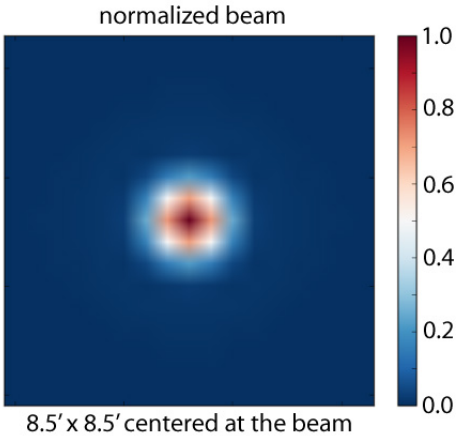

Figure 6.3: The ACTPol beam used in the point-source detection algorithm shown in the ACTPol pixelization of 0.5' (the non-circular appearance is a result of pixelization artifacts).

6.3.1 Purity and Completeness

Table 6.1: Completeness and Purity of the ACTPol sources

Completeness		*Purity*	
Flux (mJy)	%Completeness	SNR	%Purity
>500 mJy	100	>50	100
>200 mJy	99.0	>25	98.0
>100 mJy	98.6	>10	95.0
>50 mJy	98.6	>5	85.0
>30 mJy	98.2		
>15 mJy	97.8		
>10 mJy	95.4		
>5 mJy	92.4		
>4 mJy	91.6		

To estimate the completeness of the catalog, we check how well the source-finding algorithm detects a known sample of sources. For this purpose, we construct a template map from the catalog of the detected sources and subtract this from the original map to get a template-subtracted map. We then randomly draw a sample of sources from the catalog and add them back to the template-subtracted map at random locations. Running the source-finder on these maps, we find the number of input sources that are recovered as a function of

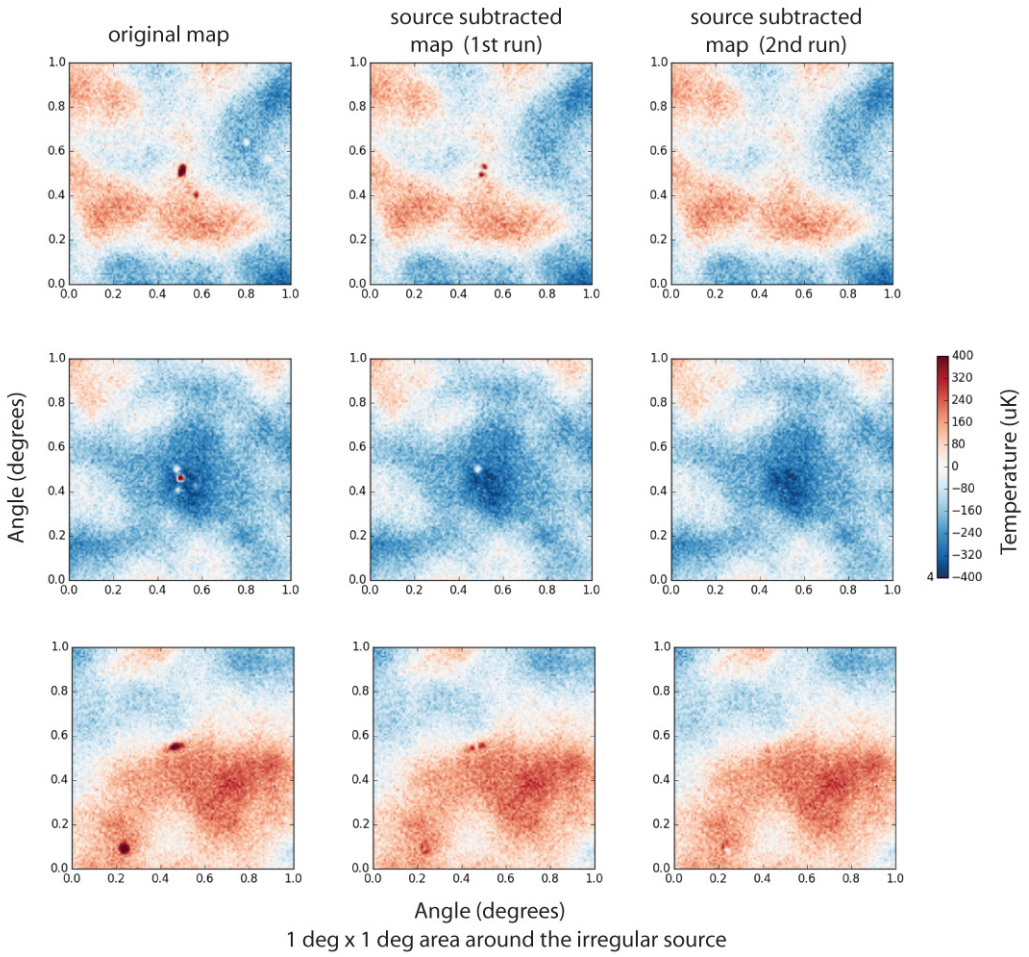

Figure 6.4: Example of three irregular or extended sources, removal of which require a two-step matched-filtering method. The left column shows thumbnails of the original sources, the middle column shows the residuals after the first run of the source removal algorithm, and the right column shows the residuals after applying the source removal algorithm the second time.

flux. The completeness expressed as a function of point source flux density is then given by $C(>Flux) = N_{recovered}/N_{input}$. The incompleteness is due primarily to the uneven depth of coverage within the D56 region. The purity of the source catalog is determined by estimating the number of false detections in our catalog of sources, $P(>SNR) = 1 - N_{false}/N_{total}$. This is estimated by counting the number of additional sources detected as a function of source flux density that do not have matches in the input catalog. Table 6.1 shows the completeness and purity of the source catalog for D56.

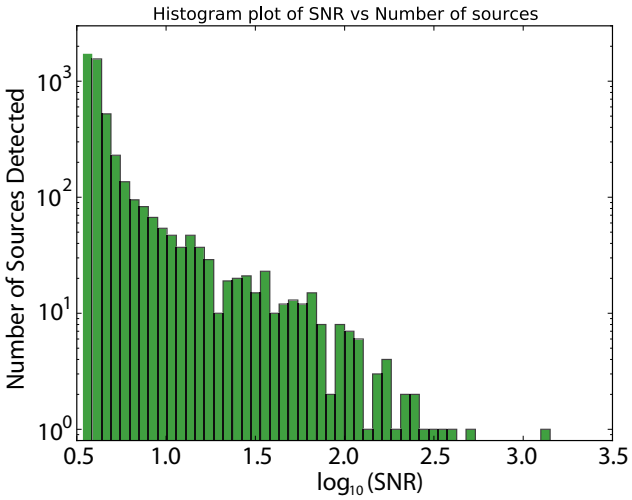

Figure 6.5: Histogram of the number of detected sources in the ACTPol Deep56 Intensity map plotted against the signal-to-noise ratio of the detections binned in log space.

6.4 Degree of Polarization

Measurements of linear polarization involve measuring the Stokes components I, Q = pIcos(2ψ), and U = pIcos(2ψ), from which the polarization fraction $p = \sqrt{Q^2 + U^2}$/I and angle ψ = 1/2 atan(U/Q) can be derived. The estimates of the Stokes parameters from the ACTPol Q and U maps are unbiased and approximately uncorrelated, but computing the polarized flux as $P = \sqrt{Q^2 + U^2}$ introduces a noise bias because of the squaring, which is significant when the signal-to-noise ratio is low. In this section, we work with the I, Q, and U maps of the ACTPol Deep56 region shown in Figure 6.6. Figure 6.7 shows thumbnails of some of the intensity-selected sources having the strongest polarization signal. The measured Stokes parameters Q and U are real, finite quantities. In the presence of measurement noise, a hypothetical source with a true polarization fraction $p_0 \sim 0$ can appear to have a $p > 0$, unless the noise bias is accurately subtracted. This bias was first discussed in [213] and has since been treated extensively in the literature: Simmons & Stewart [214] account for the biases when Stokes parameters are uncorrelated and have the same errors; an analytic, approximate distribution for the general case of correlated errors was developed by Plaszczynski et al. [215]; Quinn [216] and Maier et al. [217] adopt Bayesian approach based on the assumption of Gaussian error; Stil et al. [218] correct for polarization bias through a Monte Carlo analysis; and Montier et al. [219, 220] compare several estimation methods. We present a simple alternative approach based on numerical debiasing described in the next section.

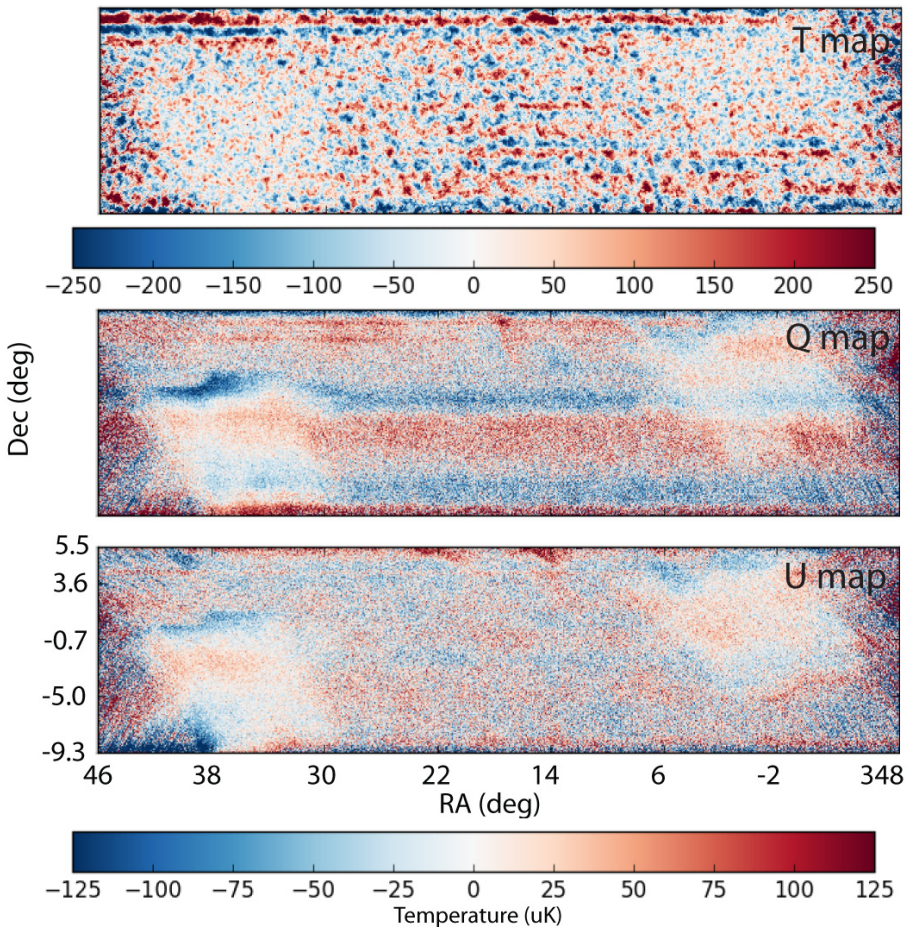

Figure 6.6: I, Q, and U maps of the ACTPol Deep56 patch. The color scale is restricted to $\pm 250\ \mu K$ in the T map and to $\pm 125\ \mu K$ in the Q and U maps.

$$N = \begin{bmatrix} \sigma_{QQ} & \sigma_{QU} \\ \sigma_{UQ} & \sigma_{UU} \end{bmatrix} \tag{6.1}$$

Our goal is to estimate the true values of the Stokes parameters I_o, Q_o, and U_o, given measured values I, Q, and U. The fundamental assumption we make is that the measurement of the Stokes parameters, I, Q, and U is described by a three-dimensional Gaussian with standard deviations, σ_I, σ_Q and σ_U, respectively. Figure 6.8 shows the inverse variance weighted maps which constitute our per-pixel covariance matrix. We will work with the intensity selected sources with flux density greater than 25 mJy. For these bright sources, the signal-to-noise ratio I/σ_I of the intensity measurement is so high that I can be assumed to be perfectly known, yielding $I = I_o$. Assuming $\sigma_{II} = \sigma_{IQ} = \sigma_{IU} = 0$, the noise covariance

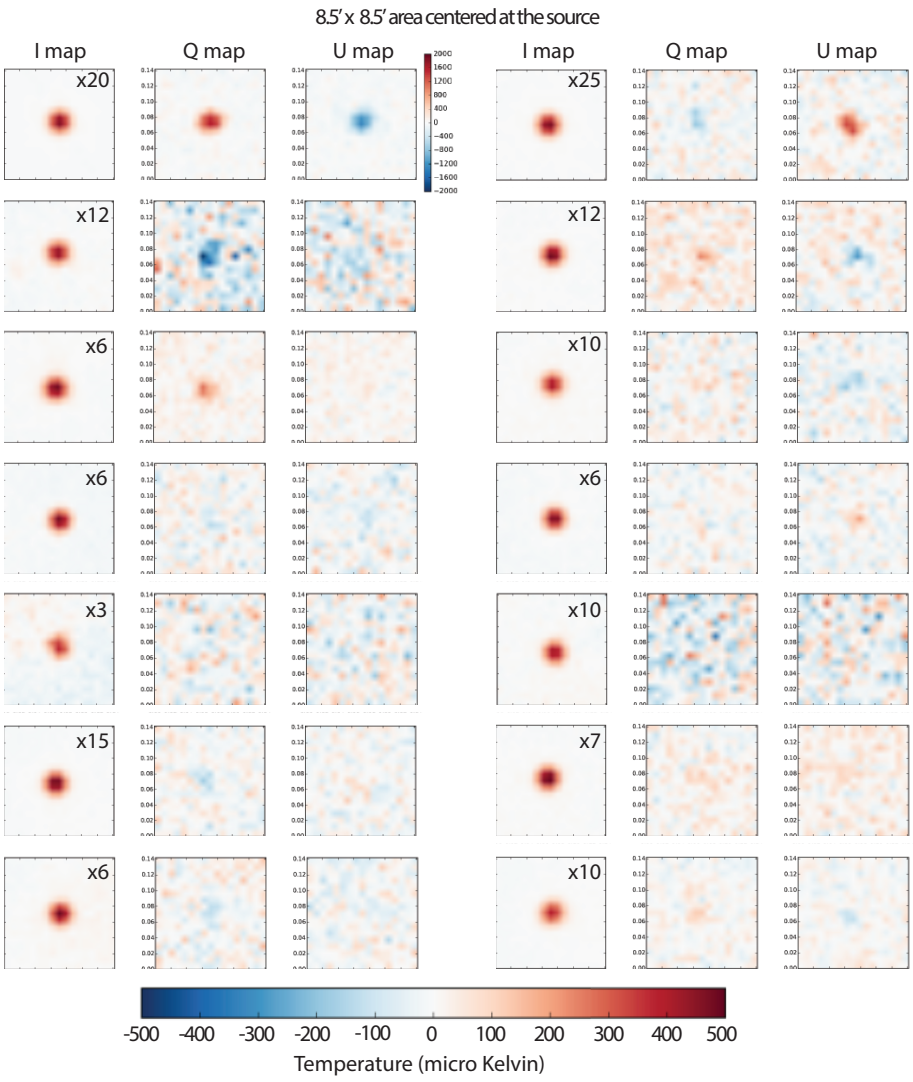

Figure 6.7: Thumbnails of some of the intensity detected sources that have the largest polarization signal in the corresponding Q and U maps.

matrix, N is given by Equation 6.1.

We then define a Chi-squared statistic given by:

$$\chi^2 = \sum_{i=1}^{17}\sum_{j=1}^{17} \begin{bmatrix} Q_{i,j} - Q_0 b_{i,j} \\ U_{i,j} - U_0 b_{i,j} \end{bmatrix}^T N_{i,j}^{-1} \begin{bmatrix} Q_{i,j} - Q_0 b_{i,j} \\ U_{i,j} - U_0 b_{i,j} \end{bmatrix} \tag{6.2}$$

over an area covering 17x17 pixels centered on the location of the source. This corresponds to a 8.5' square patch. This choice is well motivated because the amplitude of the beam is nearly negligible 8.5' away from the center. Here, $Q_{i,j}$ and $U_{i,j}$ refer to the values

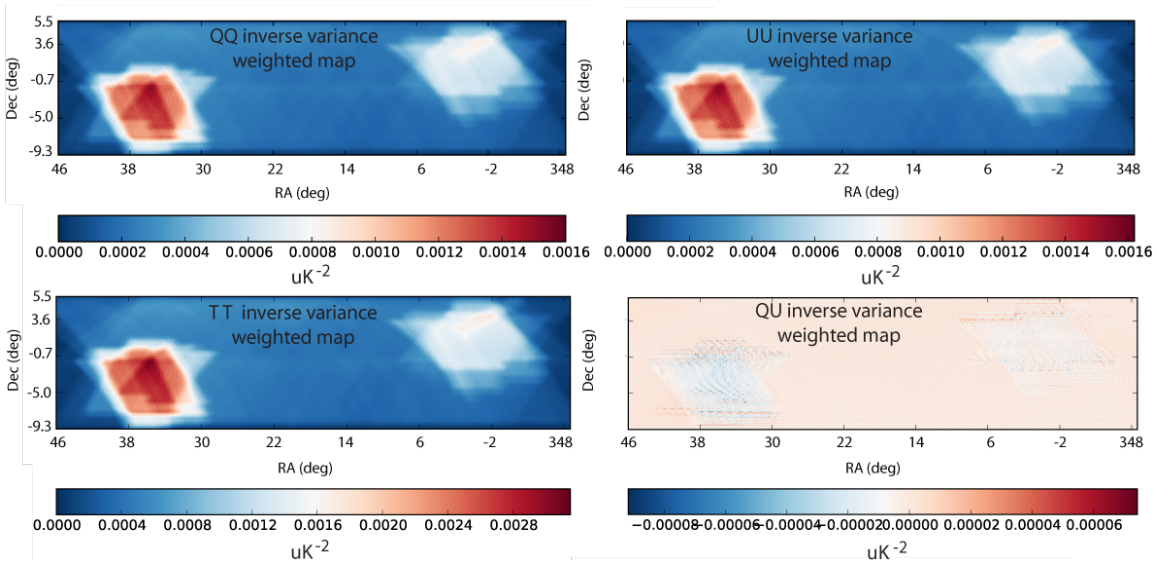

Figure 6.8: Inverse variance weighted maps of the region shown in Figure 6.6. These constitute the per pixel covariance matrix.

of the corresponding (ith,jth) pixel in the Q and U maps; Q_o and U_o are our estimates of the true vales, and $b_{i,j}$ refers to the value of the corresponding (ith,jth) pixel of the beam map as shown in Figure 6.3. Our model is chosen to be a 2D Gaussian which is nothing but the normalized instrument beam convolved with two free parameters (Q_f, U_f).

$$log\mathscr{L} \propto \exp(-\chi^2/2) \propto P_{2D}(Q_f, U_f) \tag{6.3}$$

The best-fit values of (Q_f, U_f) are the true values (Q_o, U_o) and are found by maximizing the log likelihood (equivalent to minimizing the chi-square) given by Equation 6.3.

$$P_{1D}(Q_f) = \frac{\sum_{U_f} P_{2D}(Q_f, U_f)}{\sum_{Q_f,U_f} P_{2D}(Q_f, U_f)},\ P_{1D}(U_f) = \frac{\sum_{Q_f} P_{2D}(Q_f, U_f)}{\sum_{Q_f,U_f} P_{2D}(Q_f, U_f)} \tag{6.4}$$

The joint error distribution of (Q_f, U_f) can be found by calculating the values of the Chi-squared over a grid of (Q_f, U_f), where the grid spans a parameter range much wider than the errors on (Q_f, U_f). Examples of this maximum likelihood estimation for two of the brightest sources are shown in Figure 6.9. Since we assumed Q and U to be Gaussian random variables, the log likelihood function is a 2D probability distribution. The marginalized 1D probability distributions for Q_f (U_f) is obtained by integrating over all possible values of the other parameter U_f (Q_f), as in 6.4. Since the probability distribution

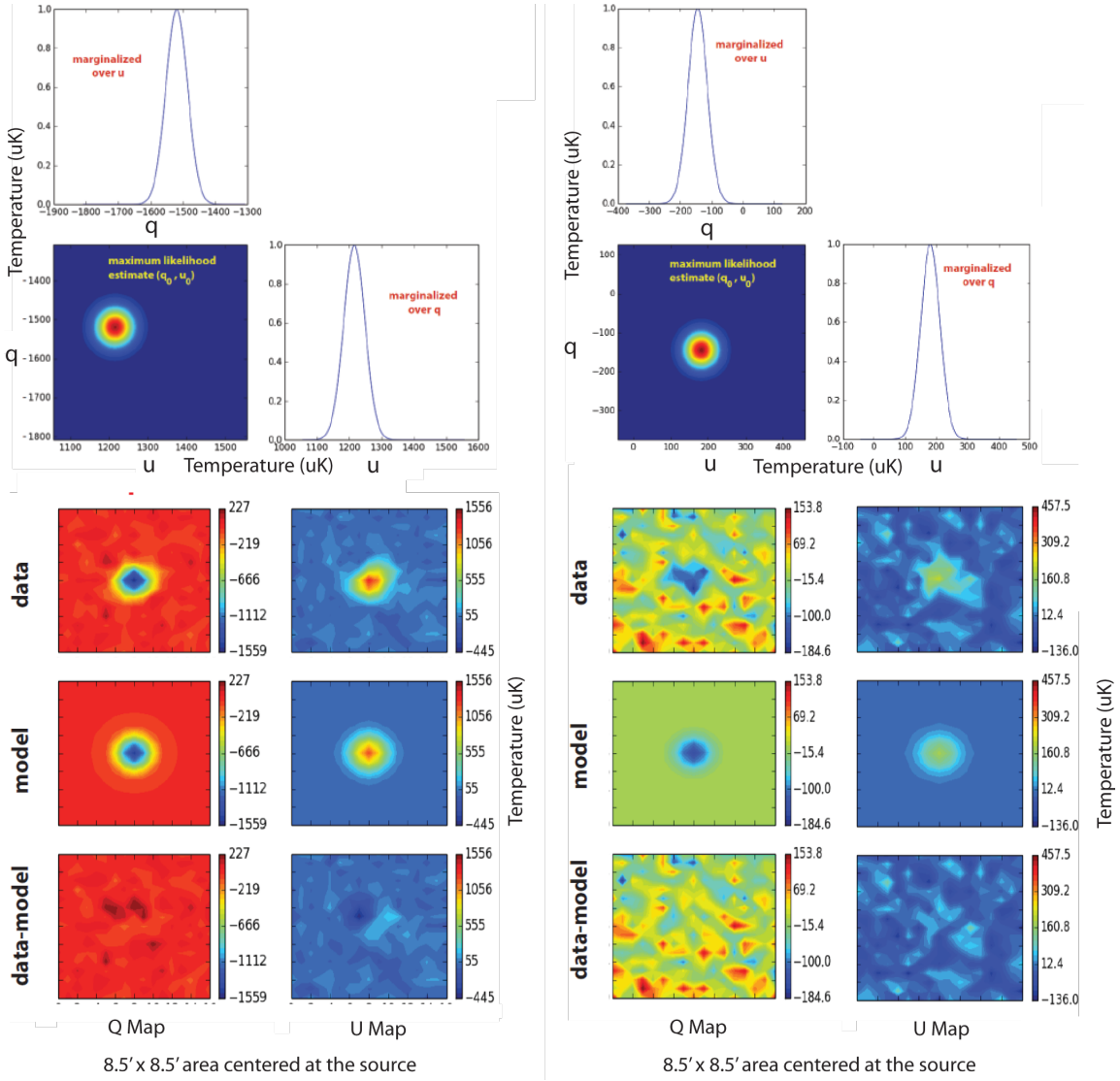

Figure 6.9: Examples of the maximum likelihood estimation of the true values of Q and U in the presence of correlated noise for two of the brightest sources. *top:* 2D maximum likelihood contour and Gaussian estimates of the true value of Q/U obtained by marginalizing over the other variable. *bottom:* Data, model and residuals showing that the maximum likelihood estimation works.

is Gaussian, the mean is equal to the best-fit value $(Q_o,\ U_o)$ and the standard deviation $(\sigma_{Qo},\ \sigma_{Uo})$ is equal to the 68% confidence limit.

$$\begin{aligned} &\text{Fit } Q_i \text{ to } Q + \alpha_{(T-Q)} T_i \text{ and } U_i \text{ to } U + \alpha_{(T-U)} T_i \\ &\text{where } Q = \frac{\sum_i \frac{Q_i}{\sigma_{QQi}}}{\sum_i \frac{1}{\sigma_{QQi}}} \text{ and } U = \frac{\sum_i \frac{U_i}{\sigma_{UUi}}}{\sum_i \frac{1}{\sigma_{UUi}}} \end{aligned} \tag{6.5}$$

An approximate estimate of the instrument-induced systematic, T-to-P (temperature-to-polarization) leakage is obtained by fitting the values of the Q (U) pixels to the sum of the mean of the inverse variance weighted Q (U) values and a variable temperature term $\alpha_{T-Q(T-U)}T_i$ at the locations of the sources detected in the intensity (temperature) map according to Equation 6.5. The percentage leakages are found to $\alpha_{(T-Q)}$ = -0.01% and $\alpha_{(T-U)}$ = -0.5% and are corrected for in the calculation of the polarization flux. The brightest source (three times brighter than the next brightest) was excluded from this fitting. Figure 6.10 shows the result of stacking patches of Q and U maps on sources detected in the intensity maps for two different signal-to-noise ratio ranges. This further confirms that the temperature-to-polarization leakage is less than a percent.

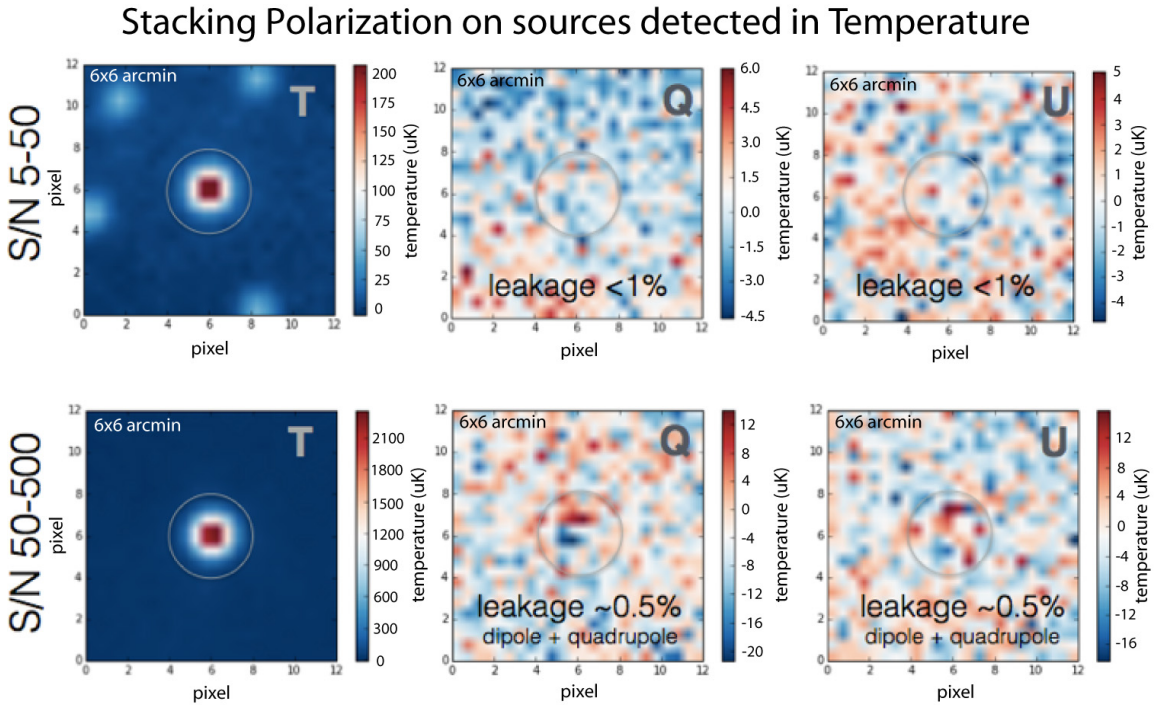

Figure 6.10: Stacking polarization signal (from Q and U maps) on sources detected in temperature with signal-to-noise ratio between 5 and 50 (top), 50 and 500 (bottom).

$$
\begin{aligned}
p_o &= \frac{\sqrt{Q_o^2+U_o^2}}{I}, \\
\sigma_{p_o} &= \frac{1}{\sqrt{\left(\frac{Q_o}{I}\right)^2+\left(\frac{U_o}{I}\right)^2}}\sqrt{\left(\frac{Q_o}{I}\right)^2\sigma_{q_o}^2+\left(\frac{U_o}{I}\right)^2\sigma_{u_o}^2}, \\
\textit{where } \sigma_{q_o} &= \frac{Q_o}{I}\sqrt{\left(\frac{\sigma_{Q_o}}{Q_o}\right)^2+\left(\frac{\sigma_I}{I}\right)^2} \text{ and } \sigma_{u_o} = \frac{U_o}{I}\sqrt{\left(\frac{\sigma_{U_o}}{U_o}\right)^2+\left(\frac{\sigma_I}{I}\right)^2}
\end{aligned}
\tag{6.6}
$$

The measured polarization fraction p_o and the standard deviation σ_{po} are then given by Equation 6.6.

6.4.1 Numerical Debiasing based on Simulations

We adopt a numerical de-biasing scheme for correcting the noise bias in the polarization fraction estimates. Starting with simulated CMB temperature and polarization maps (CAMB Online), we add noise to these maps. The noise model is constructed so as to replicate the combined effect of instrumental white noise, atmospheric noise and detector $1/f$ noise in the ACTPol maps. We first compute noise power spectra from maps obtained by differencing 4-way data splits of the ACTPol Deep56 region. Then, we construct noise maps given by some combination of the three types of noise and fit the corresponding power spectra to that from the difference maps and find the best fit combination. The resulting noise maps are added to the simulated CMB T, Q, and U maps. A 2-D Fourier transform of the noise map is shown in Figure 6.11 along with the T, Q, and U noise spectra. We acknowledge that the uneven map depth across the region makes it impossible to come up with a uniform noise model closely approximating the ACTPol noise. In the future, we will do a more thorough modeling of noise by dividing the Deep56 region into patches based on map depth and modeling the noise separately for each patch.

We then inject sources into the T+Noise map drawn from a source count distribution that is an extrapolation of the ACTPol intensity selected sources down to flux levels of $\sim 10^{-4} Jy$ (see Figure 6.12). These sources are imparted a constant $p_{sim,c} = 0\%$ polariza-

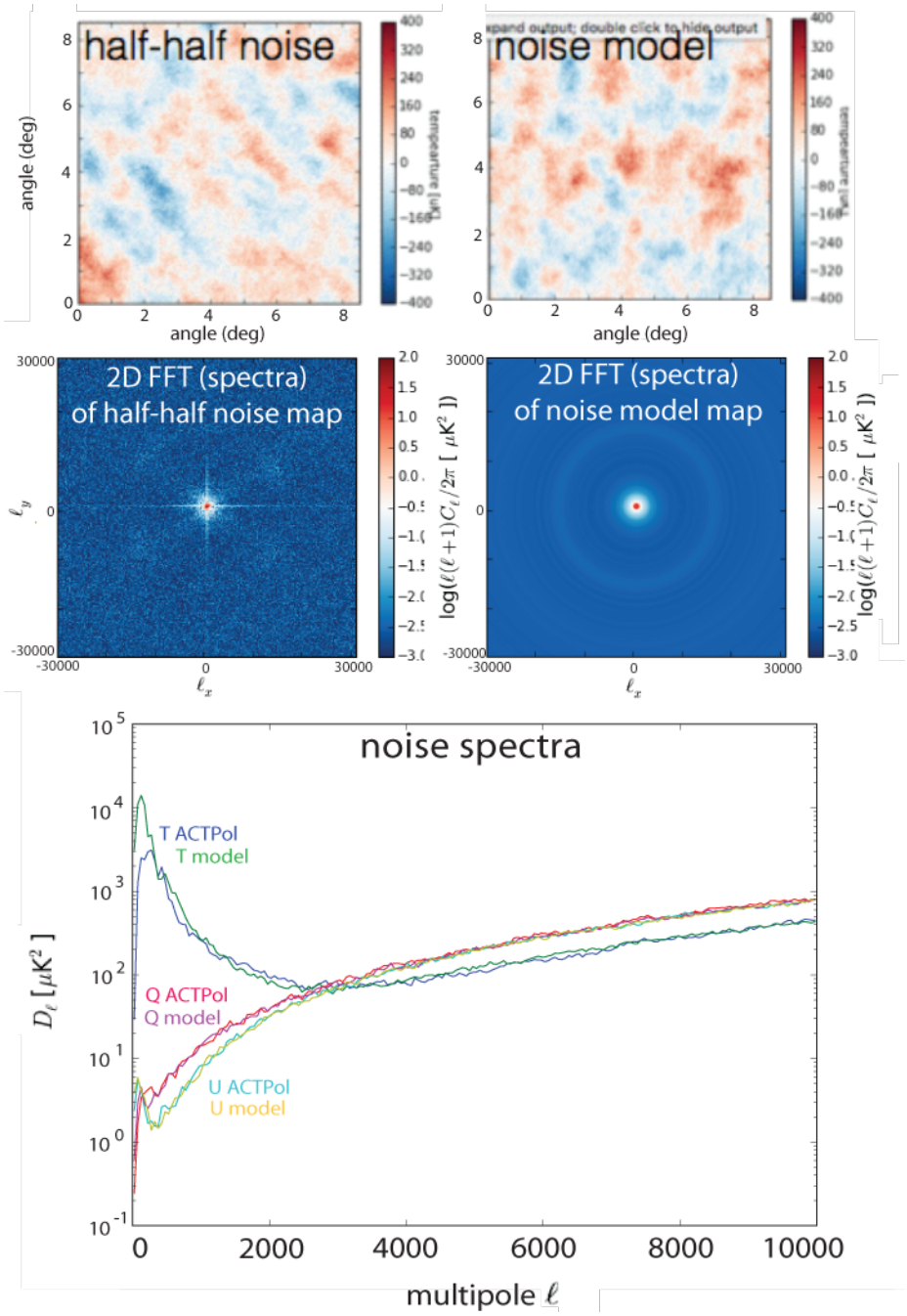

Figure 6.11: *top left:* ACTPol intensity (T) noise map obtained by differencing one half of a 2-way data split from the other. *top right:* Map of the constructed noise model. *middle left:* 2D spectrum of the ACTPol noise map in *l* space. *middle right:* 2D spectrum of the noise model in *l* space. *bottom:* Comparison between ACTPol and modeled T, Q, U noise power spectra.

tion fraction. We then calculate the polarization fractions for these sources by running our polarization fraction estimation algorithm on a 2^{10} x 2^{10} pixel patch of the simulated maps. For the per pixel noise covariance matrix, we use a 2^{10} x 2^{10} pixel patch from the actual

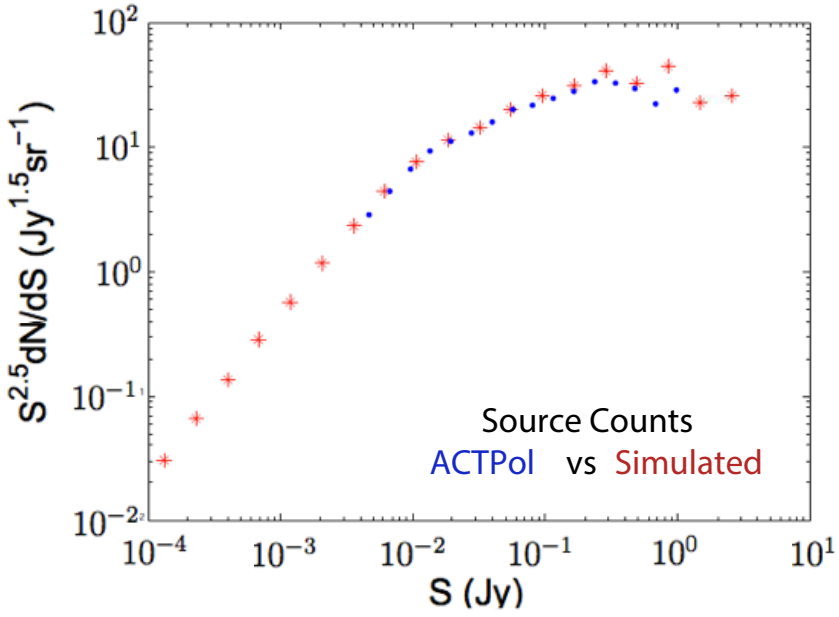

Figure 6.12: Comparison between ACTPol Deep56 detected source counts and simulated source counts.

ACTPol TT, QQ, UU and QU maps. The recovered polarization fraction as a function of intensity is our noise bias. We run multiple realizations of this and the result is plotted in the bottom right panel Figure 6.13. The polarization fraction of the intensity selected ACTPol sources brighter than 25 mJy is calculated using the method described above and our de-biased estimate of polarization fraction is obtained by subtracting this noise bias (by interpolating the simulation) from the biased estimate p_o and plotted in Figure 6.15 along with error bars that encompass the 95% confidence interval. For sources detected with the highest signal-to-noise ratios (> 100), the maximum likelihood estimate of polarized flux lies far away from zero and approaches the true value. When the signal-to-noise ratio for a given source is low in the Q and U maps, the likelihood peaks are associated with much broader 95% confidence regions that are consistent with zero polarized flux after the numerical debiasing. We consider sources for which the lower limit of the 95% confidence region of polarization fraction is greater than zero, to be a detection in polarization. We found $\sim$50 such sources in the ACTPol Deep56 patch. In addition to learning about the polarization properties of these sources, the other equally important goal of this study is to make a prediction for the distribution of polarization flux of extragalactic sources in the ACTPol patches that is valid not only across the range of sensitivity to point sources but also extendable to lower flux limits to understand the contribution of unresolved point sources to the E-mode polarization power spectrum at high l's. An attempt to model this is described in the next section.

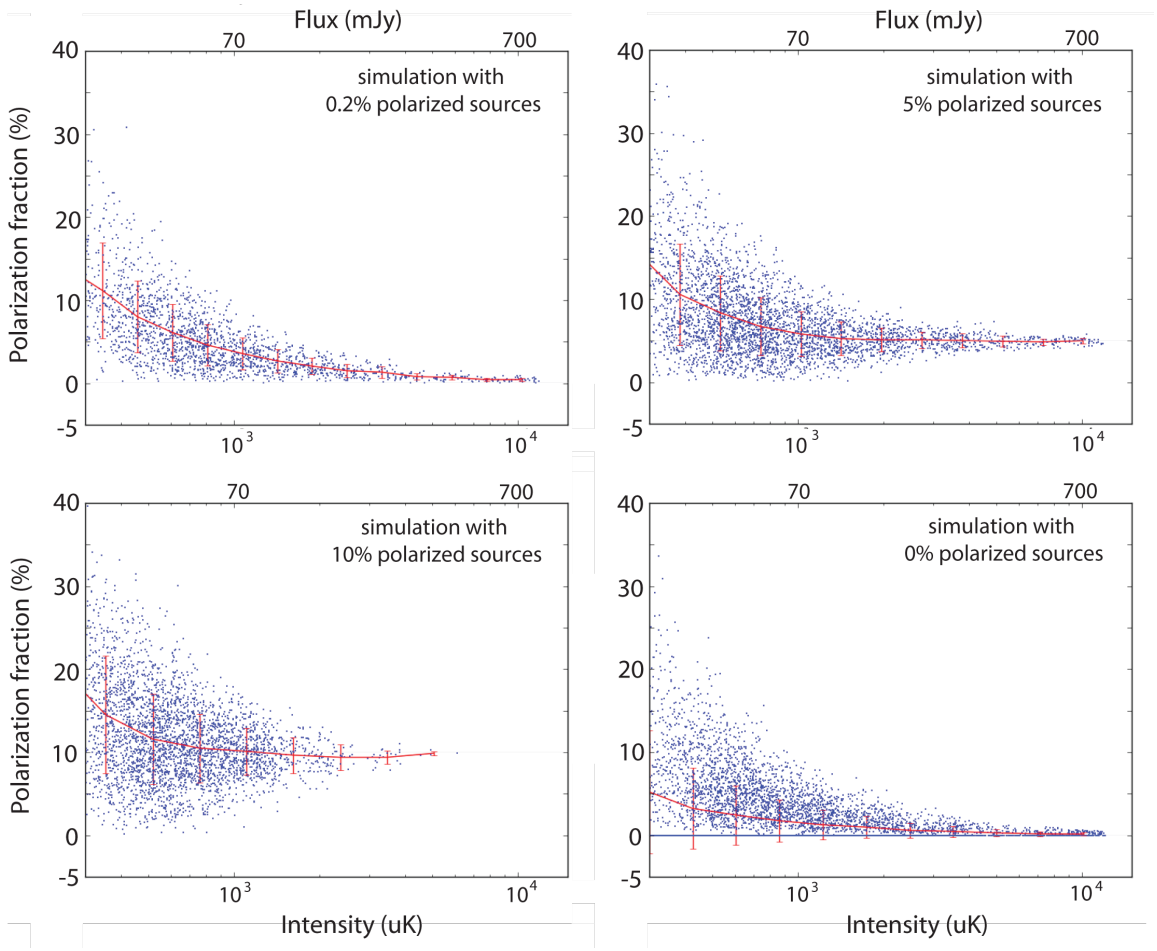

Figure 6.13: Polarization fraction simulations. The blue dots represent the polarization fraction of the simulated sources and the red curve is the polarization fraction binned in intensity.

6.4.2 Distribution of Fractional Polarization

Earlier work by Mesa et al. [221] and Tucci et al. [222] presented fractional polarization distributions for NVSS sources, exhibiting a log-normal form with approximately equal dispersion. A separate component with a peak at a much lower value was also present, representing sources with polarization dominated by instrumental leakage. They also concluded that NVSS sources exhibited an anti-correlation between fractional linear polarization and total intensity flux density as did recent 1.4 GHz polarimetric studies of the ELAIS-N1 field [223, 224] and ATLBS fields [225]. However, Hales et al. [226] argued that a general observational consequence of the rising distribution of fractional polarization upper limits with decreasing total flux density is that the mean or median fractional

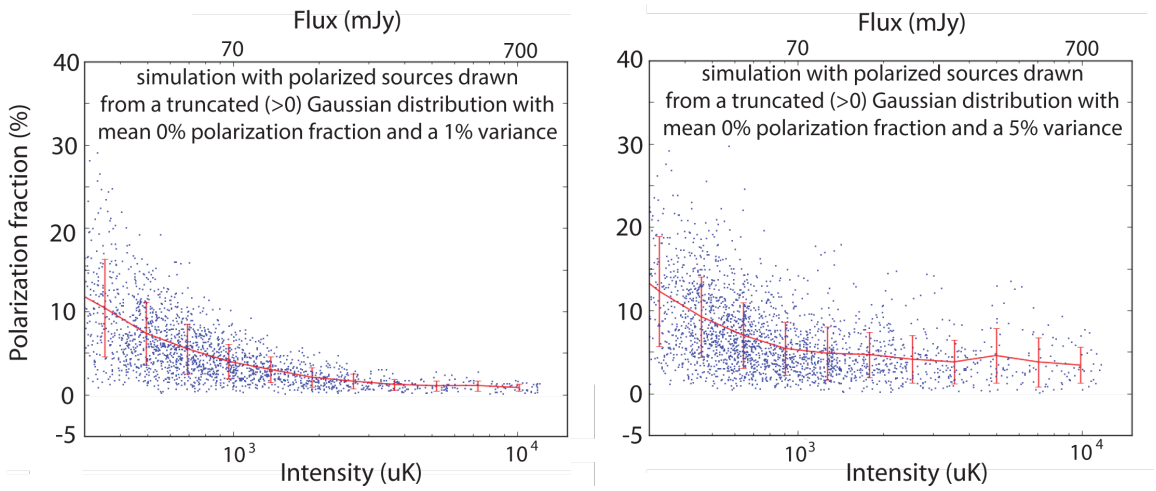

Figure 6.14: Polarization fraction simulations. The blue dots represent the polarization fraction of the simulated sources and the red curve is the polarization fraction binned in intensity.

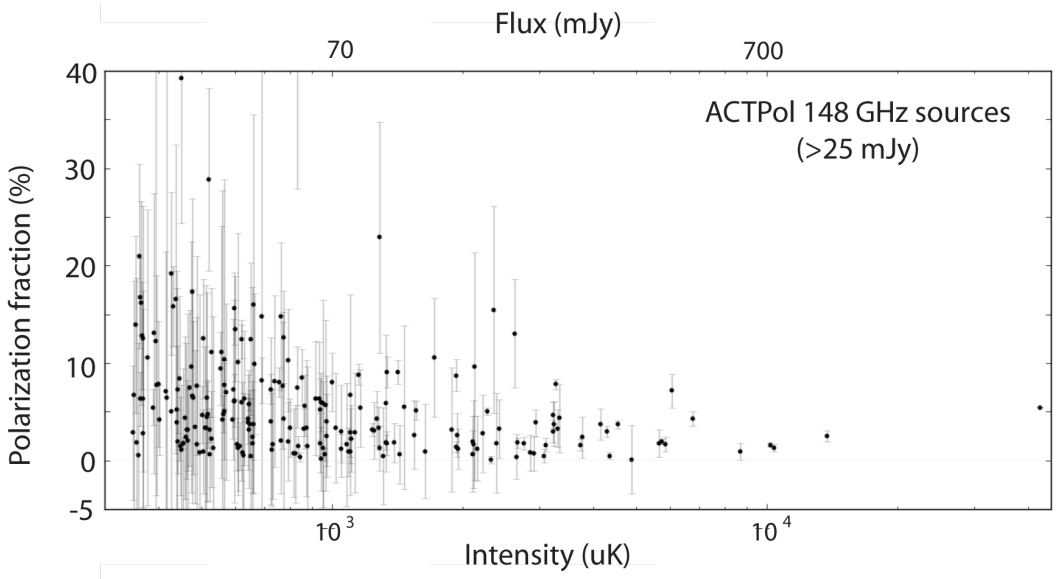

Figure 6.15: Polarization fraction plotted against intensity (total flux) for the ACTPol sources brighter than 25 mJy in the Deep56 region. The error bars encompass the 95% confidence interval.

polarization of detected polarized sources will always appear to increase with decreasing flux density. This increase represents a selection bias; it is not possible to detect low levels of fractional polarization for the faintest total intensity sources. They also found the distribution to be log-normal and that the maximum level of fractional polarization exhibited by ATLAS [226] sources were not correlated with total intensity flux density.

$$\chi^2 = \frac{1}{n}\sum_{i=1}^{n}\left(\frac{p_{meas,i} - p_{sim,i}}{\sigma_{p_{sim,i}}}\right)^2$$
$$\text{where} \;\; p_{sim,i} = p_{sim,c,i} \tag{6.7}$$
$$\text{and} \;\; \sigma_{p_{sim,i}} = \sqrt{\sigma^2_{p_{sim,tG,i}} + \sigma^2_{p_{sim,c,i}}}$$

We make an attempt to come up with a model of a polarized source population that would describe the distribution of the measured source polarization fractions as a function of intensity. For this, we run our polarization fraction calculation algorithm on simulated maps which contain (i) sources with a constant polarization fraction and random polarization angles, for e.g., $p_{sim,c}$ = 0 (0%), 0.05 (5%), and 0.1 (10%) and (ii) sources that are imparted a polarization fraction drawn from a Gaussian distribution with mean $p_{sim,tG}$ = 0 (0%) and variance $\sigma_{p_{sim,tG}}$ = 0.01 (1%) and 0.05 (5%), truncated at $p_{sim,tG}$ = 0. The results are shown in Figures 6.13 and 6.14. The polarization fractions calculated from constant $p > 0$ simulations are then numerically debiased by subtracting out the $p_{sim,c}$ = 0 simulation shown in the bottom right panel of Figure 6.13. These simulations are then interpolated between $p_{sim,c}$ = 0 and 10% and $\sigma_{p_{sim,tG}}$ = 1 and 5% and a model is constructed consisting of a constant polarization fraction component, $p_{sim,c}$ with a variance equal to the uncertainties in the two types simulations added in quadrature, $\sigma_{p_{sim}}$. The best fit to the debiased ACTPol source polarization distribution is determined by computing a Chi-square per degree of freedom as in Equation 6.7. The two brightest ACTPol sources (intensity $>$ 1 Jy) are excluded from this fitting exercise. The best fit model along with the 1σ standard deviation band is shown in Figure 6.16. About 10% of the sources have a Chi-square $>$ 1. The error bars in the fractional polarization of the individual sources are a result of instrumental effects. Here, we are essentially fitting for the intrinsic scatter in the source population for which we calculate the polarization fraction. This is a work in progress and we are developing methods to model the distribution better and studying additional ways to confirm whether our model is a realistic one.

With the above model, we try to determine how the sources will effect the measurements of EE power spectrum at high multipoles. Figure 6.17 shows preliminary plots from simulations of TT and EE power spectra in the presence of extragalactic sources with different flux thresholds and in the absence of any sources. This is just to show that the level of source removal from the CMB maps determine how high in multipole we can measure the EE power spectrum. These simulations were run for only a small patch with unrealistic

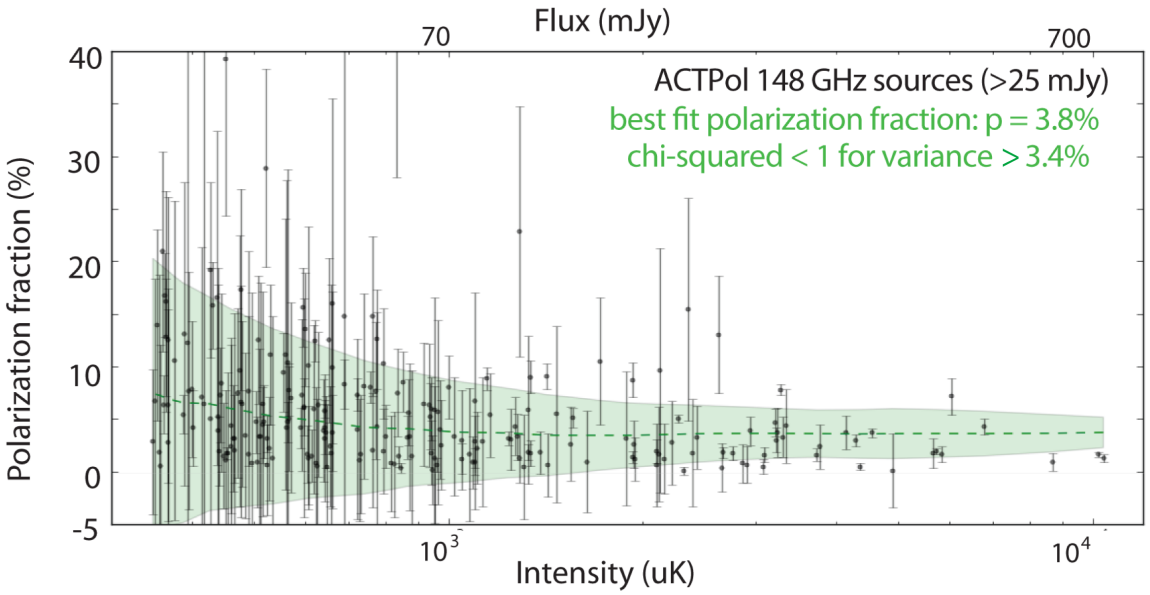

Figure 6.16: Best fit model for distribution of source polarization fraction with the green band representing the $\pm 1\sigma$ standard deviation.

noise levels and much more work needs to be done.

6.5 Source Variability

$$V_{rms} = \frac{100}{S}\sqrt{\frac{\sum [S_i - S]^2 - \sum \sigma_i^2}{N}} \tag{6.8}$$

We present a comparison of flux densities of the ACTPol sources observed at 148 GHz over the first two seasons, S1 and S2, derived from 11-day maps. Figure 6.18 shows a comparison of the 148 GHz fluxes for 12 sources with >100 mJy flux, that were observed both in S1 (Sept. 11, 2013 to Dec. 14, 2013) and S2 (Aug. 20 2014 to Dec. 31 2014). The S2 measurements were made with higher sensitivity. Based on maps made from 11-day observation periods during S1 and S2, and following the prescription in [227], we estimate the variability index of each source using Equation 6.8. Figure 6.19 shows a histogram of the variability indices for our sources, where available. Given that the typical source flux density uncertainty is $\sim 1\%$, it would be reasonable to assume that the sources with $V_{rms} > 5\%$ are clearly variable.

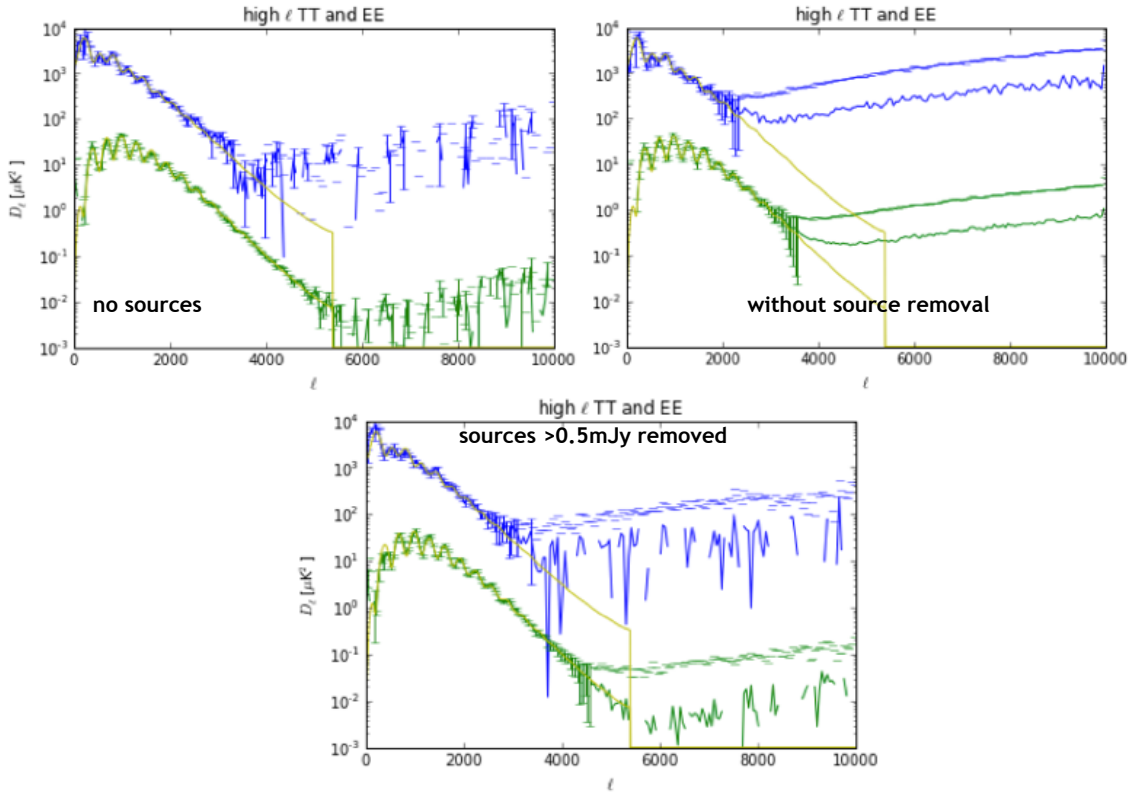

Figure 6.17: Simulations of TT (blue) and EE (green) power spectra with *top left:* no extragalactic sources, *top right:* without source removal, and *bottom:* sources with flux greater than 0.5 mJy removed. The dashed line shows the upper limit of the error bars.

6.6 Comparison to Other Source Catalogs

As a first step in ACT source characterization we consider cross-identifications with other catalogs. With respect to cross-identifications of the ACTPol sources with other catalogs, matches are established within a given radius about an ACTPol 148 GHz source. The values for the radius were chosen based on the positional errors of the different catalogs of sources, the beam size of the instruments, and by looking at the distribution of offsets between ACTPol sources and their closest counterpart in each catalog. For e.g., the positional offsets between the brightest ACTPol sources and their nearest counterparts in the VLA First catalog are plotted in Figure 6.20. For this work, we consider the following catalogs from surveys that overlap with the ACTPol Deep56 region: NVSS 1.4 GHz, AT20G 20 GHz, IRAS PSC, VLA FIRST. The AT20G catalog is incomplete below 100 mJy (Murphy et al. 2010), the PCCS is incomplete below 400 mJy. The measurements of source polarized flux are also compared between ACTPol, AT20G, and NVSS.

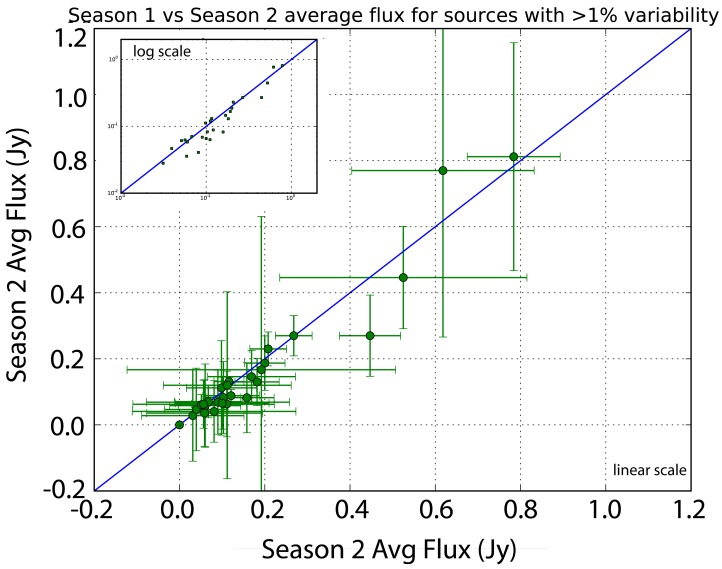

Figure 6.18: A comparison of the average Season 1 and Season 2 flux for sources with >10% variability. The length of the bars along each axis are equal to the $\pm 1\sigma$ deviation in measured flux between the 11-day maps within the respective season. The inset shows the plot in log scale.

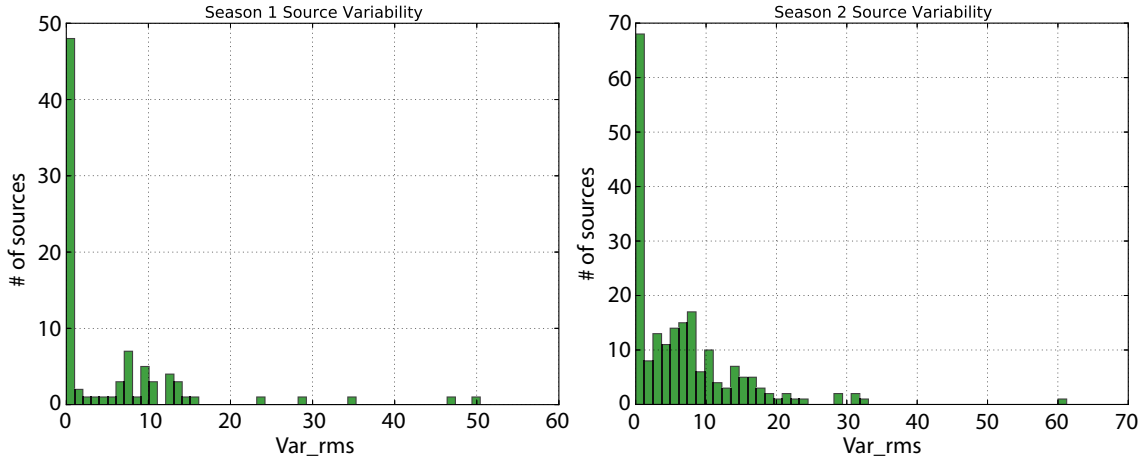

Figure 6.19: Histogram plot of the number of sources as a function of source variability index computed as per Equation 6.8 based on ten, 11-day maps made from Season 1 data (left panel) and twelve, 11-day maps made from Season 2 data (right panel).

AT20G: The Australia Telescope 20-GHz Survey (AT20G) is a blind radio survey carried out at 20 GHz with the Australia Telescope Compact Array (ATCA) from 2004 to 2008, and covers the whole sky south of declination 0°. The AT20G source catalogue [228] includes 5890 sources above a 20-GHz flux-density limit of 40 mJy. All AT20G sources have total intensity and polarization measured at 20 GHz. North of -15° Dec, between 14 and 20 hours in RA, the catalog completeness is lower than 91% above 100 mJy/beam and

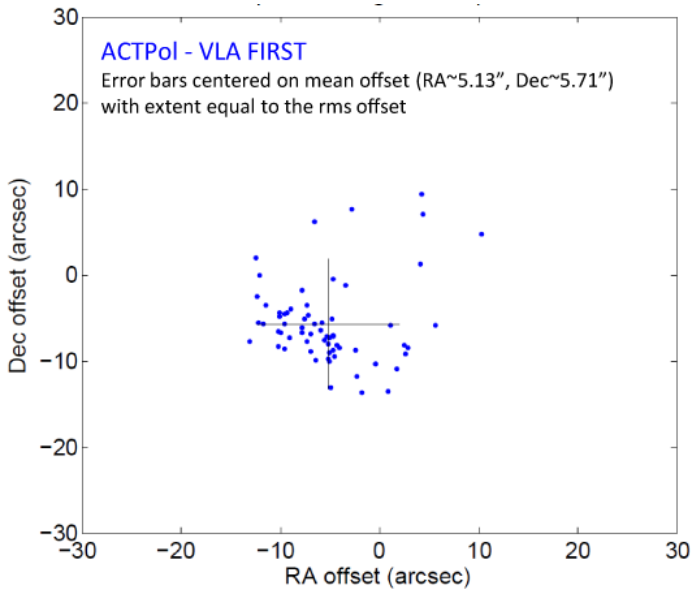

Figure 6.20: Positional offsets between ACTPol catalog and VLA First catalog obtained by comparing the positions of ACTPol sources detected with flux greater than 100 mJy and their VLA First counterparts. The cross is centered on the mean offset with lengths along either axis indicating the rms offset.

79% above 50 mJy/beam. Among the 153 sources detected with a flux cut of 25mJy in the ACTPol Deep56 region with Dec below 0°, 129 matches were found in the AT20G catalog within 30". The number of non-existing counterparts is consistent with that expected from ACTPol and AT20G catalog completeness and purity.

NVSS: The National Radio Astronomy Observatory (NRAO) Very Large Array (VLA) Sky Survey, the so-called NVSS, covers the sky north of the declination of -40° at 1.4 GHz. The NVSS catalog consists of almost 2 million discrete sources stronger than a flux density of about 2.5 mJy. The rms uncertainties in right ascension and declination vary from $<$ $\sim$1" for the 400,000 sources stronger than 15 mJy to 7" at the survey limit. Among the 241 sources detected with a flux cut of 25mJy in the ACTPol Deep56 region, 230 matches were found in the NVSS catalog within 15".

VLA FIRST: Faint Images of the Radio Sky at Twenty-cm is a survey covering 10,575 square degrees of the North and South Galactic Caps at 1.4 GHz. The astrometric reference frame of the maps is accurate to 0.05", and individual sources have 90% confidence error circles of radius $<$ 0.5" at the 3 mJy level and 1" at the survey threshold. The VLA FIRST catalog [229] contains $\sim$946,000 sources. Among the 241 sources detected with a flux cut of 25 mJy in the ACTPol Deep56 region, 234 matches were found in the VLA FIRST cat-

alog within 15".

IRAS PSC: The Infrared Astronomical Satellite Point Source Catalog [230], Version 2.0, is a catalog of some 250,000 well-confirmed infrared point sources observed by the Infrared Astronomical Satellite (IRAS), i.e., sources with angular extents less than approximately 2' in the in-scan direction at 3 to 25 THz. Away from confused regions of the sky, the survey is complete to about 0.4 and 1.0 Jy at 25 and 3 THz, respectively. Typical position uncertainties are about 2" to 6" in the in-scan direction and about 8" to 16" in the cross-scan direction. Among the 241 sources detected with a flux cut of 25mJy in the ACTPol Deep56 region, 7 matches were found in the IRAS PSC catalog within 60". These are potentially dust dominated sources. In future, we will look for counterparts in X-ray and Gamma-ray catalogs, for e.g., Master XRAY database and FLAT catalog.

6.6.1 Source Spectra

Spectral energy distributions (SEDs) can be used to differentiate source types by their dominant emission mechanisms. Assuming the commonly used simple power law model $S_\nu \propto \nu^\alpha$, a negative α is indicative of sources dominated by synchrotron emission, such as radio galaxies. Sources with free-free emission dominating will have an index close to 0. The high-redshift population will have spectra dominated by re-emission of their flux by the surrounding dust resulting in a greybody spectrum, with indices expected to be greater than 2 and more typically 3-4.

$$\alpha_{\nu_b-\nu_a} = \frac{log(S_{\nu_a}) - log(S_{\nu_b})}{log(\nu_a) - log(\nu_b)} \tag{6.9}$$

However, it has been shown that the spectra of radio sources are not well characterized by a simple power law [188]. A color-color comparison of spectral indices α [228] has been widely used to decompose a source population based on spectra. In Figure 6.21, we construct a color-color comparison of 1.4-20 GHz, 20-148 GHz measurements for the ACTPol sources detected with a flux threshold of 25 mJy and cross-identified with NVSS and AT20G catalogs, where the 1.4 GHz and 20 GHz flux densities are from NVSS and AT20G, respectively. The spectral indices are defined as in Equation 6.9. Similar color-color comparison of polarized flux densities are also presented. These sources are predominantly

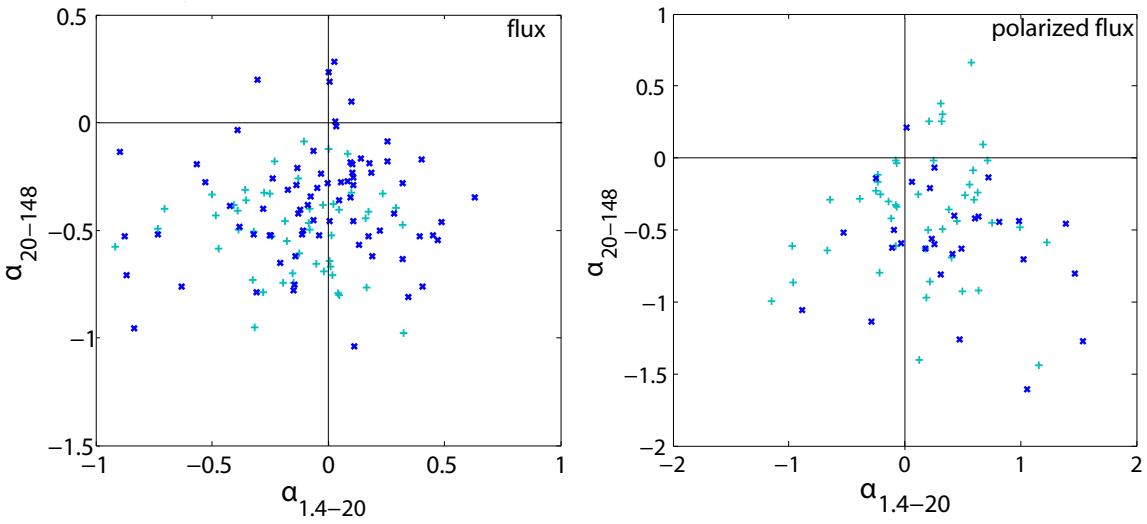

Figure 6.21: Source spectral indices. In this color-color diagram, 1.4-20 GHz and 20-148 GHz spectral indices are shown for ACTPol-AT20G-NVSS cross-identified sources with 148GHz flux density greater than 25 mJy (the darker blue dots represent sources with 148 GHz flux greater than 50 mJy). The population is dominated by sources which are peaked (lower right quadrant) or falling (lower left quadrant). The low flux sample is incomplete and suffers from selection bias that favors sources with more negative spectral indices. The left panel shows the color-color diagram for source flux estimated from the intensity map, while the right panel is for polarized flux.

synchrotron/free-free dominated characterized by a falling (steepening) spectra. There are also a significant number of sources with peaked (emission peaking within the 1.4-148 GHz frequency range) and flat spectra. The sample is biased towards steepened spectra at low flux density ($S_{148} < 50mJy$) due to incompleteness in AT20G. The polarized flux has a predominantly peaked spectra, which is worth investigating as part of future work. It must be noted that we do not expect to see spectral characteristics of any dusty sources in the ACTPol-AT20G-NVSS cross-identified sample since such sources would most likely be very dim and undetectable at 1.4 GHz.

The ACTPol source flux (and polarized flux) densities are plotted against cross-identified NVSS and AT20G source flux densities in Figure 6.22 . From this figure, we again infer that the sources are dominated by synchrotron or free-free emission. However, the same cannot be said for the polarized flux densities. Figure 6.23 shows a plot of the 1.4-148 GHz spectral index as a function of 148 GHz flux (and polarized flux) density. As part of future work, we will characterize the ACTPol-IRAS PSC cross-identified sources which are expected to be dusty in nature. Though Planck had a much larger beam than ACTPol, it would be interesting to look for counterparts of the brightest ACTPol sources in the Planck high frequency maps, which could potentially be dusty star-forming galaxies.

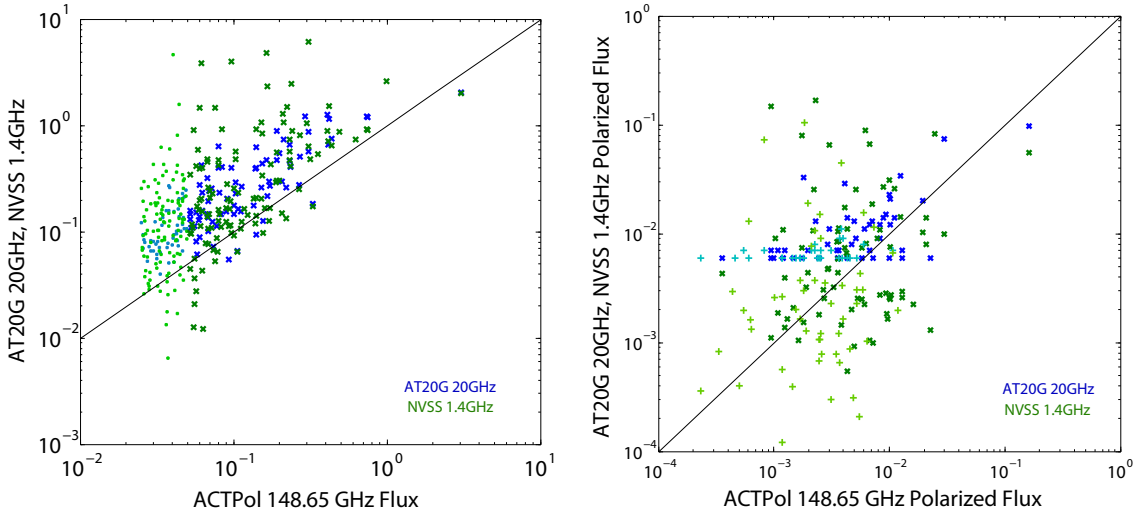

Figure 6.22: 1.4 GHz NVSS flux (green dots) and 20 GHz AT20G flux (blue dots) are plotted against 148 GHz flux for ACTPol-AT20G-NVSS cross-identified sources with 148GHz flux density greater than 25 mJy. The left panel shows the source flux estimated from the Intensity map, while the right panel is for polarized flux. The darker dots are sources with 148 GHz flux greater than 50 mJy.

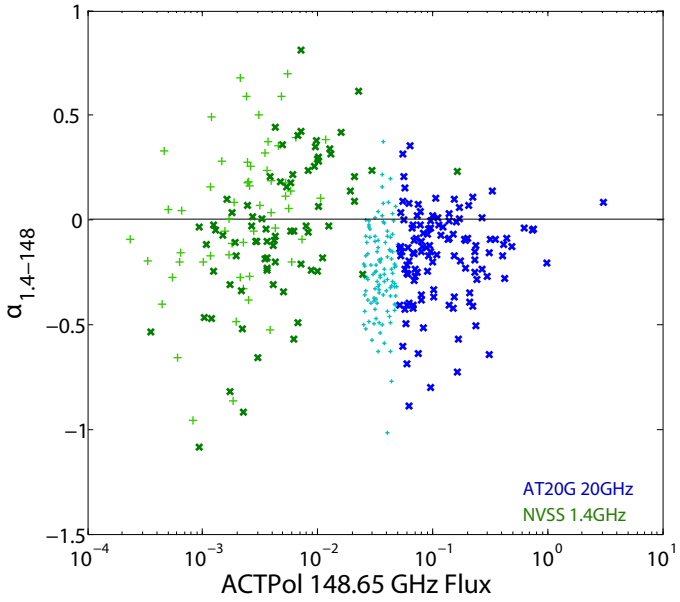

Figure 6.23: 1.4-148 GHz spectral indices are plotted against 148 GHz flux for ACTPol-NVSS cross-identified sources with 148 GHz flux density greater than 25 mJy. The blue dots are source flux derived from the intensity map while the green dots represent polarized flux (the darker blue and green dots are sources with 148 GHz flux greater than 50 mJy).

6.7 Discussion and Future Work

We have presented measurements of fractional linear polarization of >200 extragalactic sources at 148 GHz from data taken by the ACTPol during the 2013 and 2014 observing seasons covering ∼650 deg^2. Using a Monte Carlo method for correcting noise bias, we found the distribution of the fractional polarization to be consistent with a mean 3.8% polarized source population with a 3.4% variance, independent of the total source flux. We also compared the ACTPol measured total and polarized source flux with measurements at other frequencies and found that ∼98% of the sources detected with a total flux threshold of 25 mJy have counterparts at lower radio frequencies, while ∼2-3% have counterparts at IR wavelengths. A color-color comparison of the sources cross-identified with surveys at lower frequencies indicated that most of these are synchrotron or free-free dominated (as expected) with steepening or peaked spectra. While we did not find evidence of any correlation between the spectral indices derived from total flux and polarized flux, both cases were consistent with synchrotron/free-free type emission. We also presented flux variability measurements for sources detected in 11-day maps both during 2013 and 2014. Some of these sources are found to be significantly variable, which means that we should be careful while computing spectral indices from measurements at different epochs. The brightest source, detected at 1.5° RA and -6.5° Dec, was three times brighter than the next brightest one. This is an AGN/ Blazar that has been widely studied in literature.

As the ACTPol data increases and maps become more deep, we will repeat our analysis to characterize many times more number of sources. With that, we will also calculate the ACTPol differential source counts (based on total flux and polarized flux) at 148 GHz and compare with ACT, SPT measurements and predictions in literature, for e.g., Toffolatti et al. [207], de Zotti et al. [231], Sehgal et al. [205], Tucci et al. [222]. Past comparisons between ACT, SPT, WMAP measurements and predictions have concluded that the predictions are an overestimate. From the differential source counts, we will be able to estimate the polarization power spectra of extragalactic radio sources and their contamination of CMB polarization maps [232, 233].

For sources with detected polarized flux, we will look for trends in the variation of degree of linear polarization with frequency, within source populations classified by spectral indices derived from total flux, for e.g., steep- and flat-spectrum. Past studies have found that: (1) fractional polarization increases with frequency and the trend is stronger for steeper spectrum sources as well as for the lower flux density sources, and (2) degree

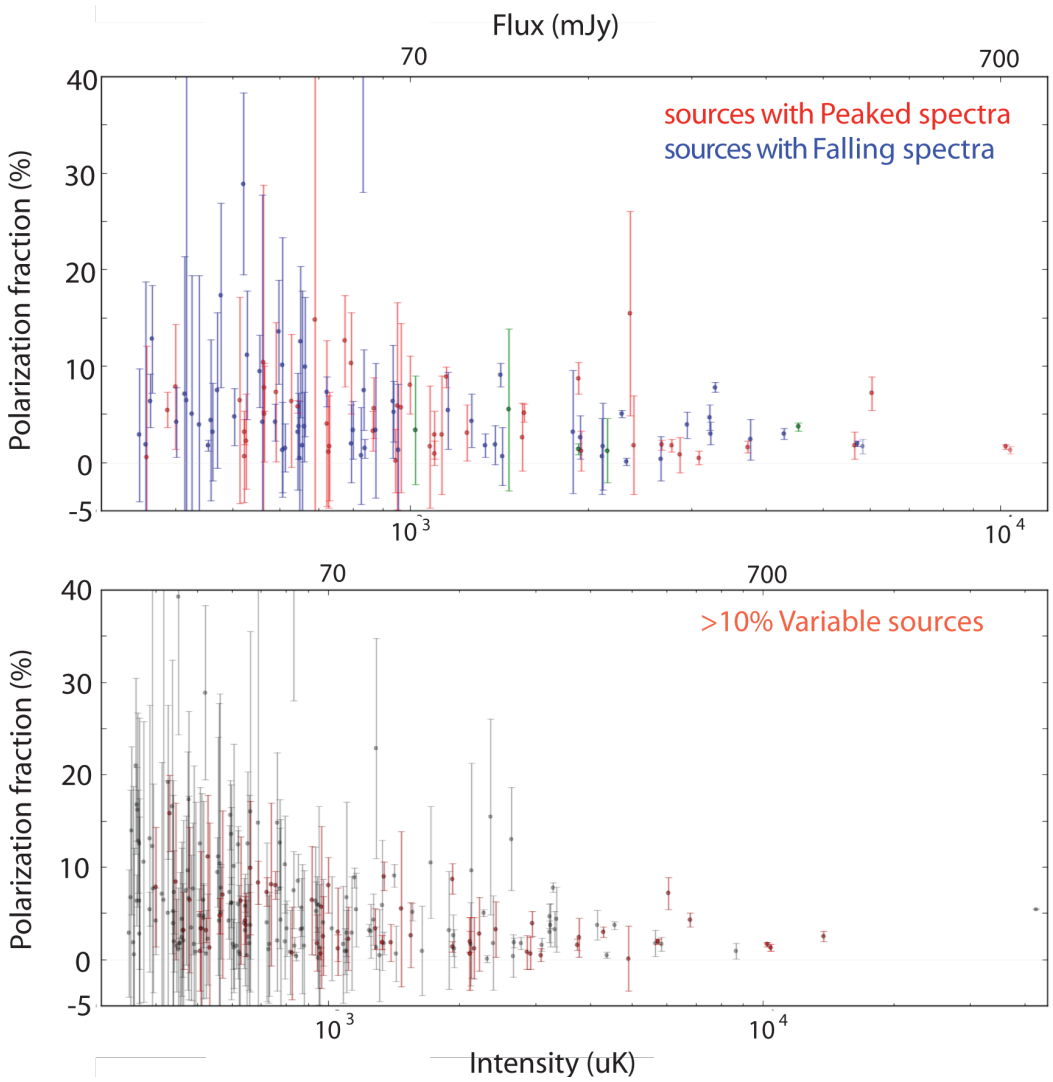

Figure 6.24: Fractional Polarization versus total source flux. *top:* sources differentiated according to steepening (falling) and peaked spectra based on total flux. *bottom:* sources with total flux variability >10% differentiated from the rest.

of polarization is anticorrelated with the flux density for steep-spectrum sources, while no correlation was detected for flat-spectrum sources. In Figure 6.24, I present a comparison of the fractional polarization of sources with peaked versus falling spectra and based on measured source variability. No evidence of any differentiating trend was found. 1.4-148 GHz spectral indices are plotted against the 148 GHz source flux for ACTPol-VLA First cross-identified sources in the latest ACTPol Deep56 map (this map has not been analyzed yet for this work, see Figure 6.25). Note that the low flux source sample suffers from a selection bias.

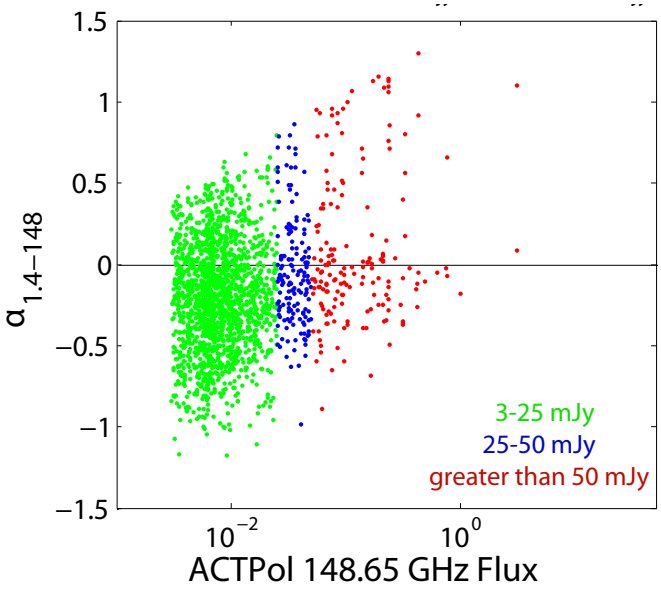

Figure 6.25: 1.4-148 GHz spectral indices are plotted against 148 GHz flux for ACTPol-VLA First cross-identified sources with 148 GHz flux density greater than 3 mJy. The low flux sample is incomplete and suffers from selection bias that favors sources with more negative spectral indices.

Measurements enabled by ACTPol and eventually AdvACT in five frequency bands over 25 to 280 GHz will constrain the spectral signature of thousands of point sources over a large enough frequency range to unambiguously distinguish between radio and dusty sources and help find new previously unidentified sources. In addition to the astrophysical implications, a better understanding of the SEDs and polarization of foreground radio sources would permit a better statistical analysis of their effect on the high-l power spectrum of CMB anisotropies, in particular the E $\times$ E power spectrum which is most sensitive to point sources.

CHAPTER 7

Conclusion and Outlook

In this concluding chapter, we highlight the first science results using ACTPol data; summarize the work presented in this thesis; briefly discuss Advanced ACTPol (AdvACT), the next generation upgrade to ACTPol; and comment on the applicability of some of the technologies we developed towards future experiments.

7.1 Early Science Results from ACTPol

Key science results have already been published using the ACTPol data. In the first season, ACTPol mapped four regions of the sky covering a total of 270 deg$^\circ$ with an angular resolution of 1.3' and achieved sensitivity between 11 and 17 μK-arcmin with three months of data. CMB temperature and polarization power spectra derived from the first season data are published in Naess et al. [237]. Representative maps and power spectra are shown in Figures 7.1 and 7.2. Detection of the gravitational lensing of the CMB temperature and polarization fields by large scale structure with a combined significance of 9.1σ obtained by cross-correlating the reconstructed convergence signal from the first season of ACTPol data with Cosmic Infrared Background (CIB) fluctuations measured using the Planck satellite are published in Engelen et al. [238]. A B-mode polarization lensing signal was found with a significance of 3.2σ. Evidence of the gravitational lensing of the CMB by dark matter halos obtained using ACTPol lensing convergence maps stacked at the locations of optically-selected CMASS galaxies from the SDSS-III/BOSS survey was presented in Madhavacheril et al. [239]. Measurements of the kinematic Sunyaev-Zel'dovich (kSZ) effect over the redshift range $z = 0.4-0.7$ using the first two seasons of ACTPol data together with the CMASS galaxy sample was presented in Schaan et al. [240]. Yet another way of measuring the kSZ effect using the ACTPol CMB temperature data to evaluate the mean pairwise baryon momentum associated with the positions of bright galaxies in the BOSS

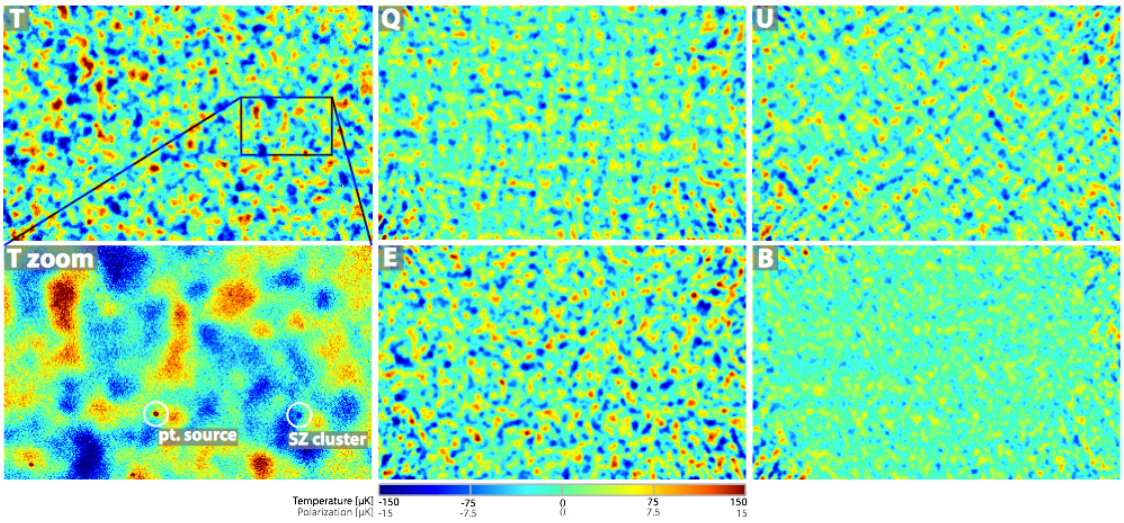

Figure 7.1: Example maps from the region 29.65° < RA < 40.49°, -7.60° < Dec < -0.68°, in the center of ACTPol patch D6. Panels 1,2,3,5,6 (left to right, top to bottom) show T, Q, U, E and B respectively. Panel 4 is a zoom on a 2.79° x 1.73° subregion of the T map, showing the full map resolution. The maps have been bandpass filtered to maximize signal-to-noise ($240 < l$ for temperature, $260 < l < 1370$ for polarization). The visible patterns in the Q and U maps are consistent with a sky dominated by E-mode polarization, as can be seen in the derived E and B maps. The B map is consistent with noise except for a faint m = 0 (constant declination) ground residual. The circled galaxy cluster candidate, ACT-CL J0205.2-0439, is within 2' of a CFHTLS cluster candidate with photometric redshift z = 1.1 and three concordant galaxies with spectroscopic z = 0.97 found in the VIMOS Public Extragalactic Survey. The circled point source may be associated with FBQS J0209-0438, a quasar at z = 1.128. Figure taken from S.K. Naess et al [237].

DR11 Large Scale Structure catalog was presented in Bernardis et al. [241].

Sky coverage and observation time have been rapidly increasing every season and tremendous advances have been made by the collaboration in the last couple of years in terms of understanding the various systematic effects and developing more efficient analysis methods. Power spectra and lensing measurements using data from the second season of ACTPol observations will soon be published. The first ACTPol publications highlighted above is only the beginning of what promises to be an exciting journey towards advancing our knowledge of the origins and evolution of our Universe.

7.2 ACTPol, AdvACT, and Beyond

Achieving the sensitivity required for measurement of the faint CMB polarization signal requires large arrays of well optimized detectors. The first 148 GHz ACTPol array PA1,

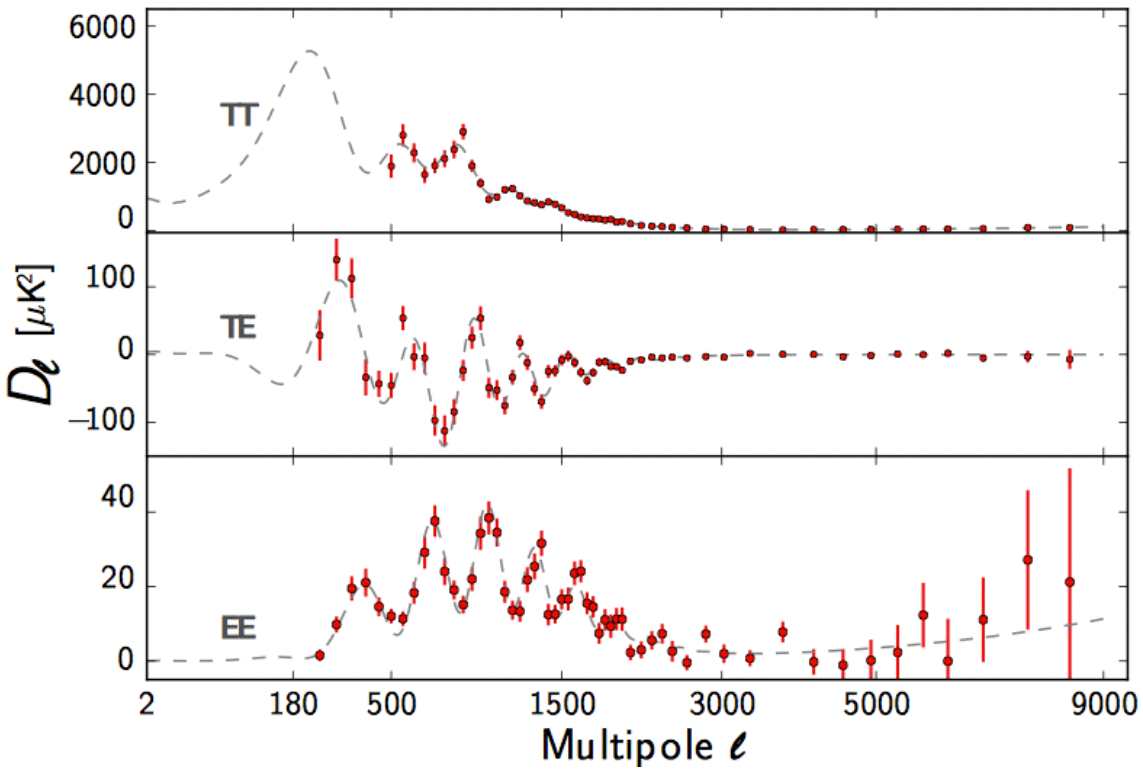

Figure 7.2: The ACTPol TT, TE, and EE power spectra, together with the best-fitting ΛCDM cosmological model and foreground components. Six acoustic peaks are seen in the E-mode polarization, out of phase with the temperature peaks and with the TE correlation pattern predicted by the standard model. Figure taken from S.K. Naess et al [237].

deployed in 2013, achieved sensitivity of 20 $\mu K\sqrt{s}$ in its first season and electrical yield of $\sim$ 50%. The design of the second array PA2 was similar to PA1 and was deployed in 2014. Aided by the valuable lessons learned from PA1, PA2 achieved a sensitivity of 16 $\mu K\sqrt{s}$ in its first season and a substantially higher electrical yield of $\sim$70%. We presented the design of our horn coupled multichroic polarimeters implemented for the first time on the ACTPol multichroic array, which we call PA3, in Chapter 3. Upon deployment in June 2015, it became the first multi-color array to be fielded for CMB observations [87, 158]. Although the optical efficiency of detectors on one of the six sub-arrays is lower than expected, the array is still the most sensitive among all ACTPol arrays, with a preliminary net sensitivity $<$10 $\mu K\sqrt{s}$. The PA3 array also has the highest electrical yield of the three ACTPol arrays, 86%, helped by advanced assembly techniques [234]. Figure 7.3 shows temperature maps of Centaurus A from six hours of observation with the PA3 array at 90 and 150 GHz. Figure 7.5 shows preliminary maps from observations with the first ACTPol multichroic array. In Chapter 2, we described a new approach for AR coating silicon lenses that is applicable for millimeter and sub-millimeter wavelengths and can be expanded to wider bandwidths by

adding additional layers. This technology was successfully demonstrated in the ACTPol experiment.

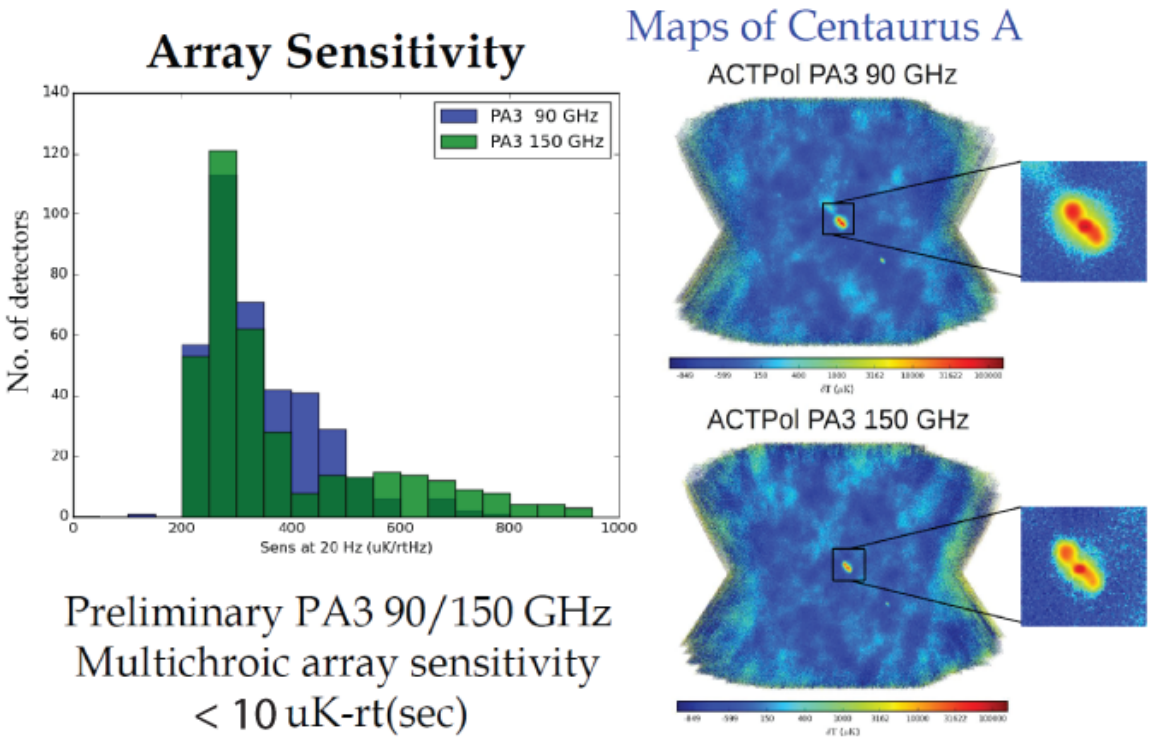

Figure 7.3: *left:* ACTPol PA3 multichroic array NEP (Noise Equivalent Power). Figure courtesy: S. P. Ho. *right:* Temperature maps of Centaurus A made from six hours of PA3 data Figure courtesy: M. Lungu.

AdvACT [69] is a staged upgrade over three years of ACTPol's three existing detector arrays and their optics. The new detector arrays, building on the instrumentation development for the ACTPol multichroic array, will be more densely packed dichroic arrays in aggregate spanning five frequency bands from 25 GHz to 280 GHz with an upgraded read-out system implementing a novel multiplexing technique [235]. Processes development for fabrication on 150 mm silicon wafers [159] by our collaborators at NIST, Boulder increases the focal plane real estate by moving from six, 75 mm sub-wafers to a single 150 mm wafer comprising each array. These developments, along with more compact pixel designs, facilitate denser detector packing essentially doubling the per-array detector count from ACTPol resulting in an increase in mapping speed and consequently sensitivity. Improvements in detection efficiency achieved by switching from SiO_x to a lower dielectric loss SiN_x insulator layer also contributes to increase in sensitivity. Switching from MoCu to AlMn transition edge sensors (TES) [160] helped achieve excellent uniformity and parame-

ter control. At the time of writing this thesis, July 2016, the first ACTPol 148 GHz detector array has now been replaced with the first AdvACT high frequency (HF) multichroic array. Continually rotating silicon half-wave plates being developed in the McMahon lab will be employed to modulate incoming polarization signals for improved control of polarized systematic effects. This will enable AdvACT to access angular scales corresponding to multipole l as low as ~ 50. Spline-profiled feedhorns have been developed [236] for the high frequency AdvACT arrays as an alternative to stacked silicon platelet ring-loaded corrugated feeds where wafer thickness and feature size make them more difficult to fabricate.

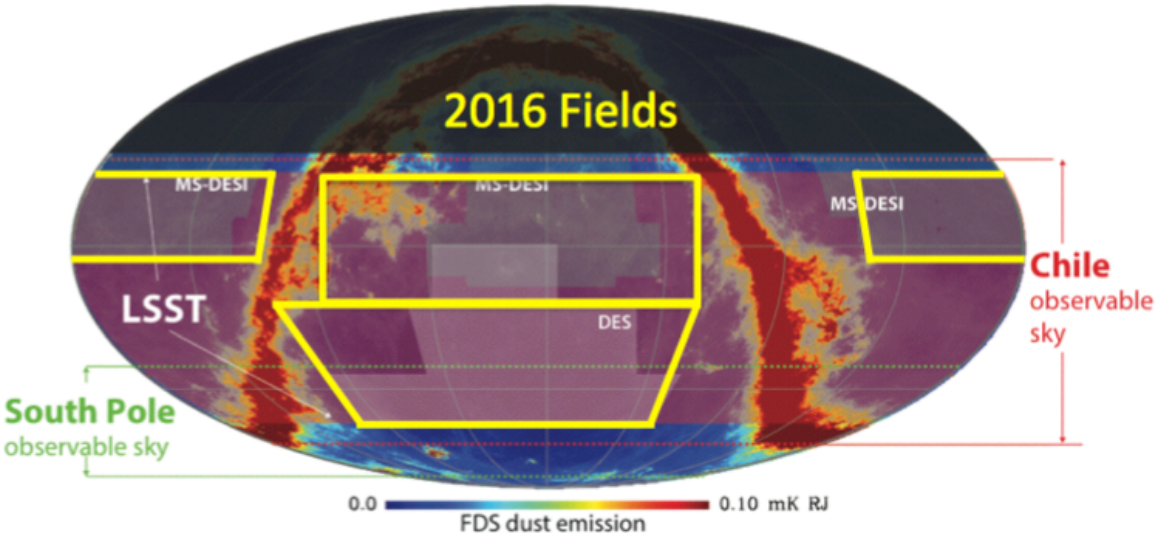

Figure 7.4: Sky coverage of AdvACT. The yellow boxes are the tentative patches to be mapped by AdvACT during the current observing season. Sky coverage of some other astronomical surveys are shown by the shaded regions to highlight the overlap. Figure courtesy: AdvACT Collaboration.

We presented a method to characterize the passbands of the deployed detectors in Chapter 4. A newer FTS is being built that will enable more accurate measurements of the effective central frequencies of the AdvACT instrument to various sources, which will be critical in constraining the foregrounds to the level required to meet the science goals of AdvACT. The highly sensitive detector arrays, multi-frequency foreground mitigation, and excellent control of systematics will enable search for B-modes from inflationary gravitational waves at tensor-to-scalar ratios $r \sim 0.01$. There are two dominant sources of polarized galactic foregrounds: dominant at frequencies below 90 GHz is synchrotron emission from cosmic rays interacting with magnetic fields, while at frequencies above 150 GHz, spinning dust grains produce polarized thermal emission. With both low bands (26 and 38 GHz) and a high band (230 GHz), AdvACT can clean both synchrotron and dust foregrounds, making

it capable of independently detecting the inflationary B-mode signal in both the cleanest CMB bands, i.e., 90 and 150 GHz. Given its large sky coverage, AdvACT will be able to make measurements in multiple spatially separated patches on the sky to confirm that the signal is isotropic and test it against the spatial variation of foreground amplitude. A detection of the inflationary gravitational waves would transform our understanding of the early universe and open a window into high energy physics at the GUT scale. AdvACT will also improve constraints on many cosmological parameters through measurements of the primary anisotropies, enable determination of the sum of neutrino masses Σm_ν to 0.03 eV, advance our understanding of dark energy through the detection of the kinematic SZ effect with high significance and the detection of a large, high-purity catalogue of galaxy clusters through the thermal SZ effect. In Chapter 6, we presented a study of the polarization properties of the extragalactic sources detected in the ACTPol maps from observations during the first two seasons. AdvACT will identify many thousands of high-redshift lensed sources down to the $\sim$ mJy level at millimeter wavelengths, providing a data set that will allow accurate modeling of the radio source contamination in measurements of the CMB anisotropy power spectra, especially at small angular scales. These could also serve as targets for follow up by powerful radio telescopes to study evolution of young star-forming galaxies. The unique combination of large sky coverage, excellent resolution (1.3' at 145 GHz, 7.1' at 28 GHz), and sensitivity to multiple colors with 1000s of detectors, is set to make AdvACT the most powerful observatory to measure the secondary CMB anisotropies. Overlapping with a number of astronomical surveys at a range of wavelengths (see Figure 7.4), AdvACT is the only instrument that can amplify the LSST, HSC and SDSS-III ground-based measurements of dark energy with both its lensing and cluster data.

Since the first measurement of CMB anisotropies by the COBE satellite, the focal plane of CMB observatories have evolved from containing a few individually manufactured detectors (e.g. WMAP [242]) to designs in which the entire usable focal plane is tiled with monolithic-arrays (e.g. ongoing and upcoming ground based observatories). This has been enabled by tremendous progress in millimeter-wavelength detector technology. Today, CMB observatories have access to arc-minute scales from the ground (ACT, SPT), while the most recent satellite mission Planck mapped the CMB with resolution of $\sim$7' from space. Further improvement in instrumental capability depends on developing detector technologies with even higher sensitivity and immunity to systematic effects, and optical designs with larger diffraction-limited fields of view. CMB detector technology has hit the photon background noise limit, which means that the only way to further increase sensitivity is to increase the number of detectors, achievable, for e.g., by installing larger

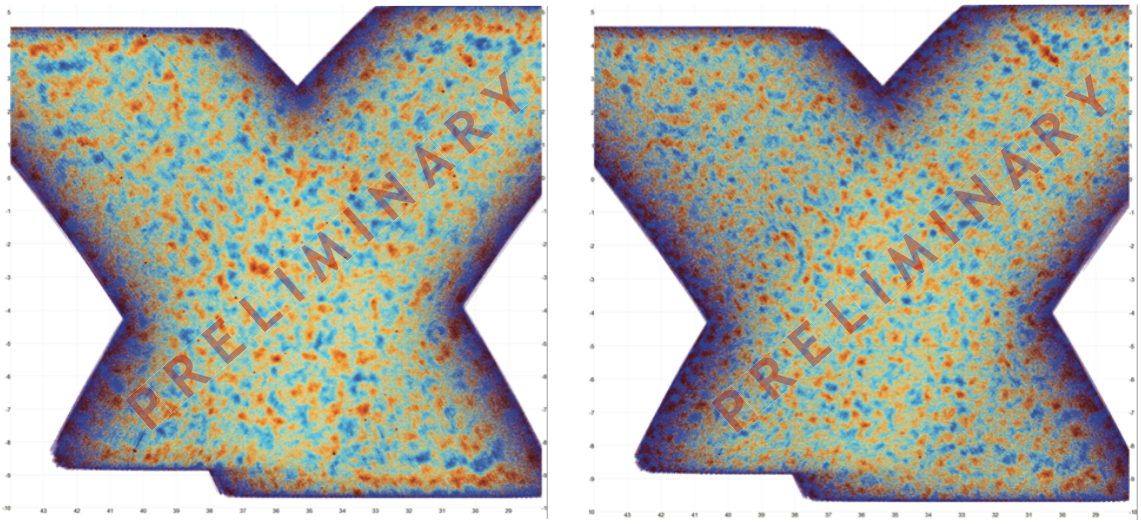

Figure 7.5: Preliminary 90 GHz (left) and 150 GHz (right) maps of a 15° × 15° patch centered at RA ∼36° and Dec ∼-3° made from observations with the ACTPol multichroic array. The color scale is restricted to ±250 μK. Figure courtesy: S.K. Naess

focal planes, or denser packing of pixels. Other avenues for increasing sensitivity are by improving the detection efficiency, or implementing multi-color pixels.

Several detector technologies are being pursued towards this end, including lenslet-coupled sinuous-antenna devices (e.g. SPT-3G [243]), beam-defining slot antenna arrays (e.g. BICEP [244]), and multichroic MKID arrays (e.g. [245]). Our collaboration has been developing integrated corrugated feed-horn coupled polarimeter arrays consisting of pixels that are simultaneously sensitive to two frequency bands [86, 87]. Detection of the faint B-mode signal will require unprecedented sensitivity, exquisite control over instrumental systematics, and unambiguous foreground characterization (as demonstrated by the joint BICEP Planck analysis [60]). Our approach achieves control over beam systematics through the use of proven corrugated feeds, while improving sensitivity and effectively subtracting foregrounds through multi-color pixels. This technology is adaptable to sub millimeter wavelength instruments broadening its potential impact on future CMB and far-infrared space observatories.

A study in 2009 concluded that dense logarithmically spaced spectral bands (as many as 10) providing increased spectral resolution over the frequency range $\sim 40 < \nu < 200$ - 300 GHz [246] are needed to characterize and remove various complicated polarized foregrounds. With ACTPol, we have demonstrated dichroic pixels to more efficiently populate the diffraction-limited field of view at each frequency and thus increase sensitivity. How-

ever, the optimum aperture size and/or close-packed pixel spacing to achieve maximum mapping speed is frequency dependent. Therefore, for a multichroic pixel with a single fixed physical aperture size, there is little advantage in spanning frequencies greater than a 2.25:1 bandwidth, as the departure from the optimal aperture size near the band edges results in diminishing returns in terms of improvements in mapping speed. AdvACT will employ five frequency bands in the range 25-280 GHz using dichroic pixels split over bandwidths: 125-280, 70-170, and 24-47 GHz. This approach can be expanded to double the number of spectral bands by splitting each of the AdvACT bands into two resulting in quadruplexed four-color pixels. This can be achieved, for e.g., by adding a second set of diplexers at the output of the first diplexers to split each band into two (see Figure 7.6). The hit in efficiency for subdividing the bands this way has been verified to be negligible by means of simulations. However, this would require that many of the detector components be redesigned and made more compact in order to accommodate the extra circuit components without driving the pixel size bigger and away from the optimum aperture. These pixels can then be scaled to higher frequencies.

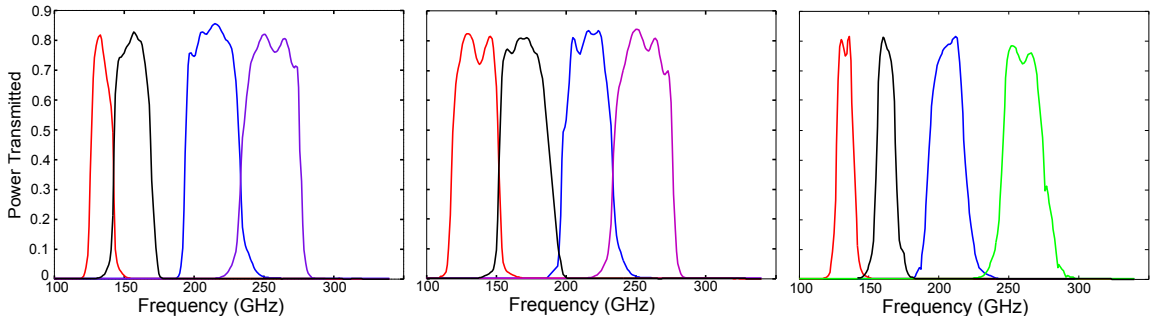

Figure 7.6: Example simulated passbands for some four-color pixels as described in text. The filter designs can be easily adjusted to allow varying extents of overlap between the bands which could enable better spectral characterization of complicated foregrounds that are not defined by a simple power law. For a ground observatory, the atmospheric lines need to be avoided, whereas a space mission would have no such constraints.

The CMB community is planning a Stage IV (CMB-S4) ground-based observatory that would field $\sim 10^6$ detectors. Multiple Crossed-Dragonne telescopes [247] incorporating silicon reimaging optics would be a possible configuration for CMB-S4. The four-color pixels described in the previous paragraph could be an option worth considering. While advancement in detector technology is making increasingly small angular scale measurements of CMB anisotropies possible from the ground, measurements at multipole $l < \sim 50$ have not yet been demonstrated from the ground. When it comes to detecting the infla-

tionary B-mode signal, while polarization modulation facilitated by Half-Wave Plates and Variable-delay Polarization Modulators [248] could make large angular scales ($l < 80$) [32] accessible from the ground, a satellite mission (e.g., LiteBird [249]) would be eventually necessary to prove Inflation beyond doubt. The two major motivations for a satellite mission are (1) extensive characterization of dust foregrounds which would include measurements at frequencies above 300 GHz (not accessible from the ground because of the atmosphere), and (2) accessing the largest angular scales to measure both the reionization and recombination peaks in the B-mode signal. Since size and mass are major factors determining feasibility and cost of a space mission, an instrument incorporating broadband (5:1 bandwidth) silicon reimaging optics feeding a single focal plane efficiently tiled with monolithic arrays (e.g., EPIC-IM concept [150]) consisting of several scaled versions of four-color pixels could be an interesting option. The large-aperture wide-bandwidth AR coated silicon lenses we developed (see Chapter 2) could be extended to realize broader bandwidth (e.g., 5:1 bandwidth). Implemented in the form of refractive cold reimaging optics, this technology could magnify the usable field of view compared to plastic lenses, as well as provide a compact real image of the primary mirror that could be used as a cold Lyot stop to control stray radiation. These technologies could be first tested on balloon based sub-orbital payloads necessary to make the case for a satellite mission.

The next decade is going to be really exciting for CMB research. Next generation instruments will enable an extensive search for B-modes from inflationary gravitational waves down to much lower tensor-to-scalar ratios; measurement of the temperature and polarization anisotropies at finer angular scales will improve constraints on many cosmological parameters; large sky coverage will open up exciting avenues for cross-correlating CMB with large scale structure surveys; and our understanding of the nature and properties of dark energy and neutrinos will certainly be improved. Thus, CMB observations are set to play a key role in advancing our knowledge of the origin and evolution of our Universe.

APPENDIX A

Design Tolerances for the Two-layer AR Coating

The manufacturing tolerances for the eight types of machining errors shown in Figure A.1 were evaluated based on a fiducial design. These include: (1) errors in the pitch, δp; (2) errors in the centering of the deeper groove relative to the shallow groove, δc; (3) errors in the kerf widths, δk_1, δk_2; (4) slopes in the walls of the grooves parameterized by δ_{S1} and δ_{S2} which represent the distance the upper and lower groove tilt inward at the groove bottom if the mean width is fixed; (5) errors in the depth of either grooves δd_1, δd_2, (6) differences in the depth of grooves in the two orthogonal directions assuming the correct mean depth are parameterized δd_{LR_1} for the upper and δd_{LR_2} for the lower groove; (7) application of this coating to a surface tilted at an angle ϕ relative to the bottom edge of the saw and where the depth of each groove is measured at the center of the groove (e.g., the effect of applying this coating at the edge of a curved lens); and (8) rows of broken posts. The tolerance to variation in the refractive index of the silicon substrate, δn_{Si} was also evaluated. The tolerances for these parameters were quantified based on a fiducial model similar to what was fabricated but with straight walled pillars using HFSS simulations in which the parameters in each family were varied separately. For the majority of these effects the results were distilled to a band averaged reflection at 15° angles of incidence. The sensitivity to each parameter was quantified as the displacement needed to bring about a 3 dB increase in reflectance. For the case of tilted surface and for broken posts the results of a small number of simulations were evaluated and compared to the fiducial performance. In the remainder of this section we discuss these results.

Pitch: Variations in the pitch change the effective index of both layers. Figure A.2 shows the band averaged reflectance as function of variation in the pitch. Variations between -3 μm and 3.5 μm lead to increases in the reflectance of less than 3 dB over the fiducial design. Therefore we find a conservative tolerance for the pitch is $\delta p < 3$ μm ($\delta p/p < 0.0075$).

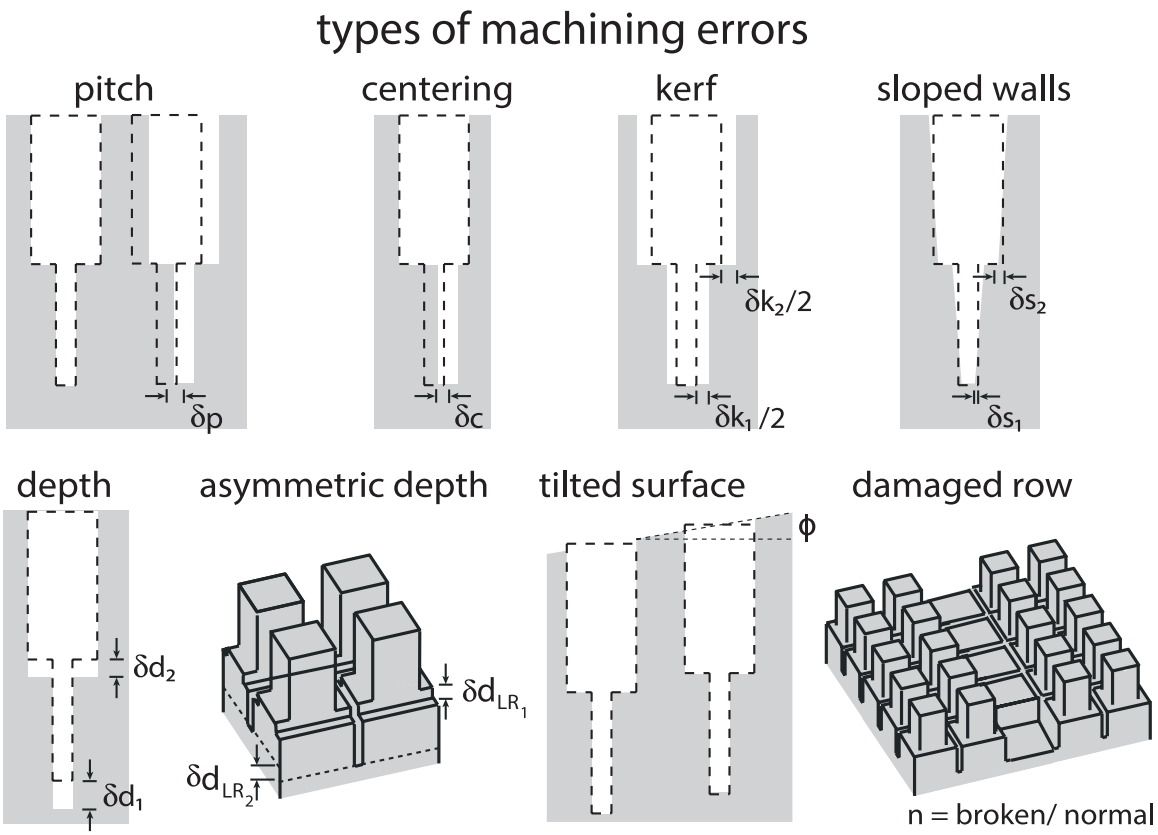

Figure A.1: This figure shows the families of machining errors considered in the tolerance analysis and described in the text. The dashed lines show the target shape for the grooves and that for the pillars while the white space in the grey represents the material as actually cut. Therefore difference between the dashed region and the white region represent machining errors. For the asymmetric depth and damaged row errors the sketches show the geometry of the errors.

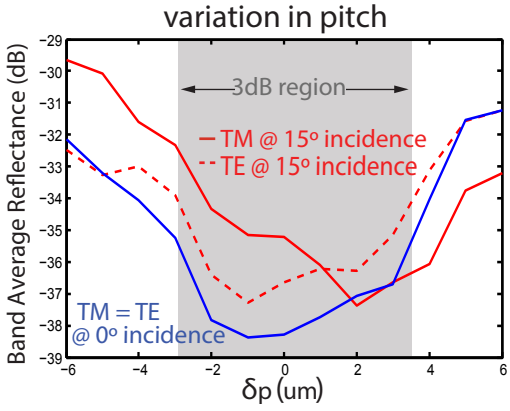

Figure A.2: The band averaged reflectance at a 15° angle of incidence as a function of changes in the pitch. The grey region shows range for which the performance is within 3 dB of the fiducial design.

Centering: The performance was insensitive to errors in the centering of the deeper grooves within the shallower grooves. A displacement of 20 µm degraded the reflectance by substantially less than 1 dB. This is consistent with both layers of pillars behaving as layers with a constant effective index of refraction. The only requirement on the centering is that the cuts that form the lower groove do not remove material in the upper pillars.

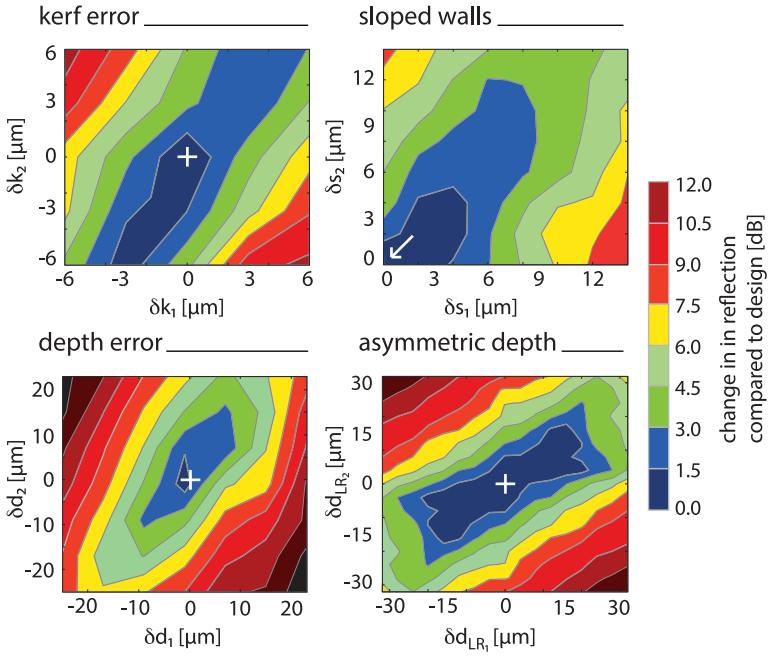

Figure A.3: This figure shows the impact of errors in the kerf, slopes in the sidewalls, overall depth errors, and asymmetric differences in depth between the two orthogonal cuts. The color scale presents the degradation in reflection at 15° incidence compared to the simulations in Figure 2.6. The fiducial design is at the coordinate (0,0) in all the plots as highlighted by a "+" or arrow. The outer edge of the light blue contour (see label) represents 3 dB degradation. The horizontal (vertical) axis represents errors in the inner (outer) layer of the coating for the labeled parameters.

Kerf: The upper left panel of Figure A.3 presents the impact of errors in the kerf. This plot shows that controlling δk_1 and δk_2 to 3 µm insures a less than 3 dB degradation in performance. It is notable that the impact of varying both parameters in the same direction (e.g., $\delta k_1 = \delta k_2$) has little impact on the performance. We have chosen the fiducial design to be near the high end of the most favorable region to make the manufacture relatively immune to blade wear, which could have (but did not) narrow the kerf width as machining proceeds.

Sloped Walls: The upper right panel of Figure A.3 presents the impact of slopes in the walls left behind by the dicing saw. Conservative estimates for the 3 dB tolerance for these

two parameters are 6 μm for δs_1 and 3 μm for δs_2. Sloping both layers by a similar amount results in negligible degradation.

Depth: The lower left panel of Figure A.3 presents the impact of depth errors. The 3 dB tolerances for these parameters are 7.5 μm for δd_1 and 10 μm for δd_2. This difference can be understood by the fact that the index of refraction is higher in layer 1. Expressed in terms of optical path length the sensitivities would be identical.

Asymmetric Depth: The lower right panel of Figure A.3 presents the impact of asymmetric depth. The 3 dB tolerances for these parameters are 15 μm for δd_{LR_1} and 12 for δd_{LR_2} for asymmetry in directions common to both grooves. This error also affects the 90° rotational symmetry of the geometry resulting in birefringence but the cross-polarization can be no larger than the absolute reflection.

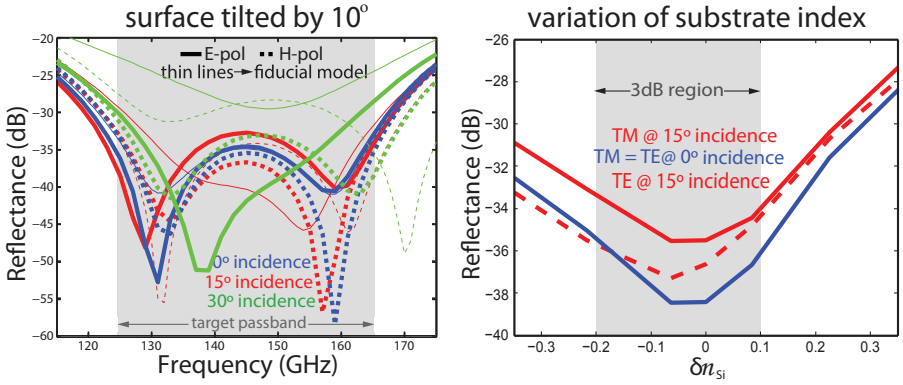

Figure A.4: *Left:* The simulated impact of having the surface of the lens tilted by 10°. *Right:* The simulated impact of variation in the refractive index of the silicon substrate.

Application to tilted surfaces: The left panel of Figure A.4 compares the performance of this coating applied to a surface tilted by 10° compared with the performance when applied to a flat surface. Fortuitously, this effect improves performance at large angles of incidence and has little effect at small angles. Therefore this shows that applying this coating by making grooves parallel to the lens symmetry axis of a curved lens will produce acceptable performance.

Groups of broken posts: Assessing the impact of the broken posts is not straight forward because the region and extent of illumination varies between the three lenses. The degradation due to broken posts would thus be a function of the effective aperture area of the lenses

and the location of the defects in addition to the total area affected. Accurately quantifying this is beyond the scope of this work. Qualitatively, the degradation would be negligible if the fraction of total area affected is small and more importantly, the length scale of the individual affected areas is smaller than the wavelength of incident light. Simulating the impact of broken posts is computationally difficult. Therefore we resorted to a simplified model consisting of a unit-cell containing seven posts in a row with one broken off completely. This is equivalent to having one seventh of the posts destroyed. In the fabricated lenses the fraction of broken posts was well 1 per few thousand on the first lens and substantially less in subsequent lenses. This pessimistic case produces band averaged reflections below 2% which is acceptable though it does produce non-trivial cross-polarization. We used simulation to estimate that keeping the number of broken posts below 1/700 would result in a negligible degradation in the overall performance of the coating.

Index: Variation in the refractive index of the silicon substrate also changes the effective index of both layers. The right panel of Figure A.4 shows the band averaged reflectance as function of variation in the index. Variations in n_{Si} between -0.2 and 0.1 lead to increases in the reflectance of less than 3 dB over the fiducial design. Therefore we find that a conservative tolerance for the index is $\delta n_{Si} < 0.1$ ($\delta n_{Si}/n_{Si} < 0.03$). This tolerance is weaker than that imposed by the optical design.

The 3dB sensitivities derived in this section are summarized in Table A.1. The band averaged reflectivity of the fiducial design is -31 dB ($\sim 0.1\%$) at 15° incidence which is significantly better than the requirements for the system.

Comparison of these requirements to machining capabilities reveals that the kerf width, sloped walls, depth, and asymmetric depth represent challenges for manufacture. Metrology on test wafers demonstrated that the 180 μm blades repeatedly achieved the target kerf width while the narrow 40 μm blades showed significant, but repeatable variation in machining. Therefore, we performed metrology of cuts on a test wafer to verify the kerf of the thin blade prior to cutting the lens and used careful machine setup to bring the kerf within a range of +2/-6 μm with slope less than 4 μm. Given the covariance of the depth errors, we required the depths to be within 25 μm for errors in directions common to both groove depths and 5 μm for variations in opposite directions. This requirement also served to set the asymmetric depth requirement. These tolerances provide performance better than -23 dB (0.5%) in band averaged reflections at 15 degree angles of incidence.

Table A.1: A summary of the 3 dB sensitivities for all parameters described in the text.

machining error	parameter	sensitivity	tolerance (units of p)
pitch (p)	δp	3	7.5×10^{-3}
centering	δc	†	NA
kerf	δk_1	3	7.5×10^{-3}
	δk_2	3	7.5×10^{-3}
sloped walls	δs_1	6	1.5×10^{-2}
	δs_2	3	7.5×10^{-3}
depth	δd_1	7.5	1.9×10^{-2}
	δd_2	10	2.5×10^{-2}
asymmetric depth	δd_{LR_1}	15	3.8×10^{-2}
	δd_{LR_2}	12	3×10^{-2}
tilted surface	ϕ	‡	NA
damaged row	r	$\sim 1/700$	NA
index	δn	0.1	NA

† don't hit the edges of the top layer
‡ actually improves the performance

APPENDIX B

Design of the plastic lenses for the reflectometer setup

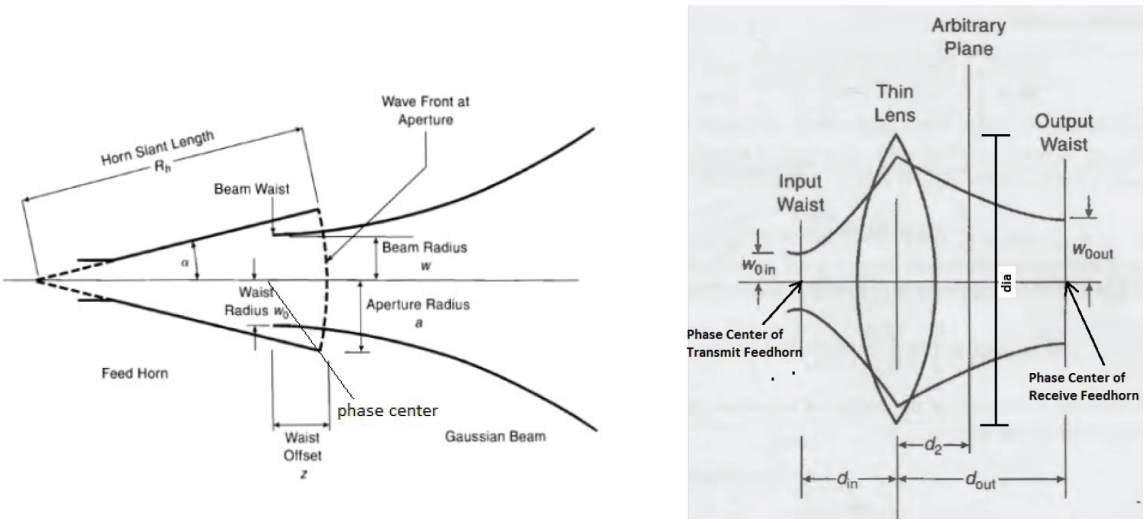

Figure B.1: *left*: parameters for a Gaussian beam diverging from a feed horn *right* a Gaussian beam propagating through a lens. Figures taken from Quasioptical Systems: Gaussian Beam Quasioptical Propogation and Applications, Paul F. Goldsmith [135]

The design of the focusing lenses for the reflectometer setup shown in Figure 2.18 is based on the theory of propagation of Gaussian beams. An in-depth discussion of this can be found in [135]. The relevant parameters defining the design are labelled in Figure B.1 and the relevant equations are as below:

$$
\begin{aligned}
z_c &= \frac{\pi w_{oin}^2}{\lambda}, \\
\frac{d_{out}}{f} &= 1 + \frac{d_{in}/f - 1}{(d_{in}/f-1)^2 + z_c^2/f^2}, \\
w_{oout} &= \frac{w_{oin}}{[(d_{in}/f-1)^2 + z_c^2/f^2]^{0.5}}
\end{aligned}
\tag{B.1}
$$

where, w_{oin} is the beam waist radius at the phase center of the feed, calculated from the dimensions of the feed [135]. The point of phase center (from where the radiation seems to emanate) usually lies near the aperture slightly deep into the horn, but the precise location of this point is frequency dependent. Table below lists the values of the parameters for two types of feeds, WR-6 and WR-10, for a few different frequencies, and for chosen d_{in} = 120 mm and d_{in} = 350 mm. The plastic (UHMWPE) plano-convex lenses, with focal lengths equal to d_{in} and d_{out} were manufactured by the Princeton Physics Machine Shop.

$$\frac{1}{f_{thin\ lens}} = -C_{thin\ lens} = \frac{n_2 - n_1}{n_1}\left(\frac{1}{R_2} - \frac{1}{R_1}\right) \tag{B.2}$$

Freq GHz	WR	w_{oin} mm	d_{in} mm	w_{oout} mm	d_{out} mm	Dia_{lens} mm †	$f_{thin\ lens}$ mm ††
110	10	3.3	120	10.0	349	128	92.3
75	10	4.1	120	12.5	347	150	92.6
110	6	3.0	120	9.0	355	142	91.6
170	6	2.5	120	7.5	353	109	91.9

† diameter of the lens such that $> 99\%$ of the radiated power passes through it
†† effective focal length according to the thin lens equation (Equation B.2), $n_2 \sim 1.51$ and $n_1 = 1$

APPENDIX C

AR coatings on plastic

Each of the three ACTPol optical paths have a vacuum window, at the Gregorian focus of the ACT telescope (focal ratio of 2.5), through which the cryostat opens to the sky. It is made of ∼6.9 mm thick Ultra-High Molecular Weight Polyethylene (UHMWPE). For the first two single frequency ACTPol arrays, a single layer expanded teflon (commercially known as Zitex) quarter-wave anti-reflection coating with thickness optimized for the band-center was sufficient to reduce reflections to $< 1\%$ over the frequency band of interest. However, for the dichroic 90/150 GHz array spanning from 75 to 170 GHz frequency range, such a single layer coating would not be ideal. Though we used a similar coating designed to behave as a quarter-wave coating at $\sim$ 120 GHz for the first ACTPol dichroic array, eventually we would want a better anti-reflection coating. To achieve this, we explored several options, a summary of which is presented below along with reflection measurements of the current Zitex coated window.

We measured the reflection from a piece of Zitex used for AR-coating the ACTPol UHMWPE vacuum window and found that the index that best fit the measured reflection was $\sim$ 1.32, whereas the quoted index of the material was 1.2. The measurement, shown in Figure C.1, was made using the same reflectometer setup used to measure the reflection from the ACTPol silicon lenses and compared to HFSS simulations with $n_{zitex} = 1.32$. We also measured the reflection from the actual Zitex-coated UHMWPE window prior to deployment. The thickness of Zitex optimized for the dichroic array was 0.43 mm. We found that the measurement best matched simulation when we assumed $n_{zitex} = 1.32$ and found that the band averaged reflection was $\sim 2.5\%$ over our two bands of interest. For the future, we note that a simple two-layer coating composed of teflon and Zitex would reduce the band average reflection below 1.5%, verified by HFSS simulation as shown in Figure C.2.

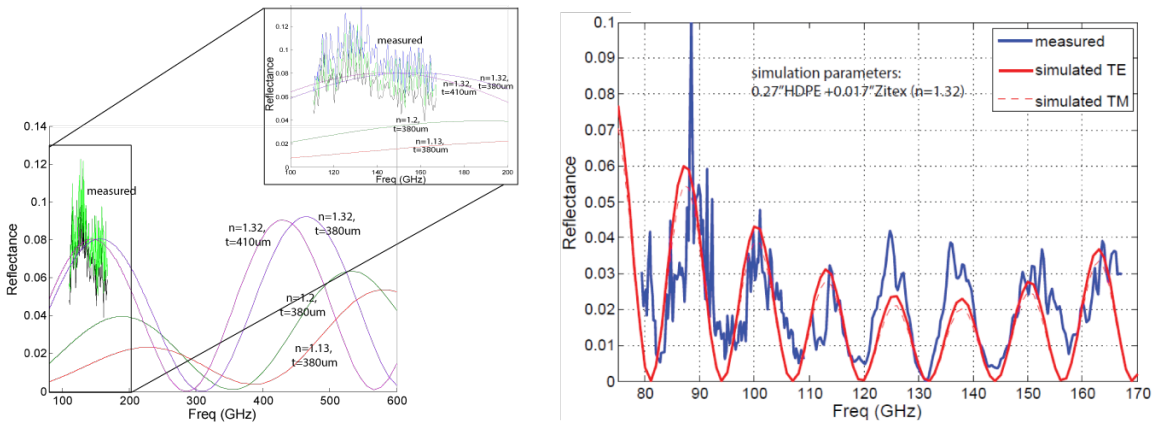

Figure C.1: *left:* Measured reflection from a ∼380 µm thick sheet of the Zitex used for AR-coating the UHMWPE vacuum window compared to simulations with different index and thickness parameters. The blue, green, and black curves correspond to three different measurements. *right:* Measured reflection from the ACTPol PA3 vacuum window made of UHMWPE and AR-coated with Zitex. Simulated reflection (assuming $n_{zitex} = 1.32$) is also plotted for comparison.

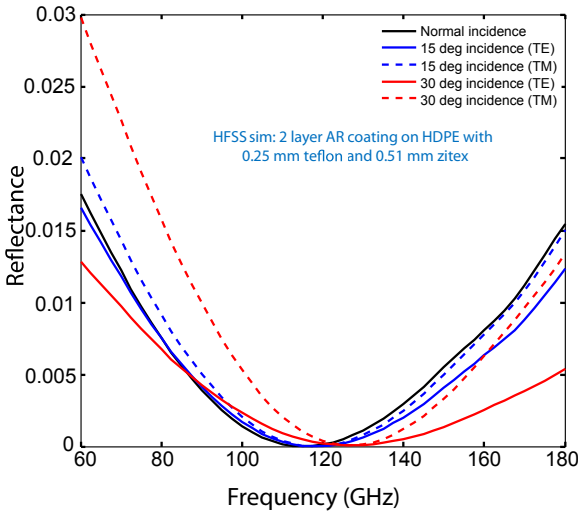

Figure C.2: Simulated reflection from a two-layer AR coating on HDPE composed of teflon and Zitex

Given the lower refractive index of UHMWPE ($n \sim 1.51$), a two-layer AR coating conceptually similar to the one for the 150 GHz silicon lenses, would be good enough to reduce the reflections below 1% over 75-170 GHz (see Figure C.4). However, our goal was to simplify the AR-coating procedure as well as reduce the time it would take to cut this coating. So, we designed some alternative approaches for AR coating UHMWPE. Figure C.3 shows one such design that we prototyped on HDPE. This involved drilling holes using a custom made stepped-cylindrical drill bit. It turned out that as the plastic cooled down after the drilling, the holes would shrink in size, thereby, effectively increasing the fill fac-

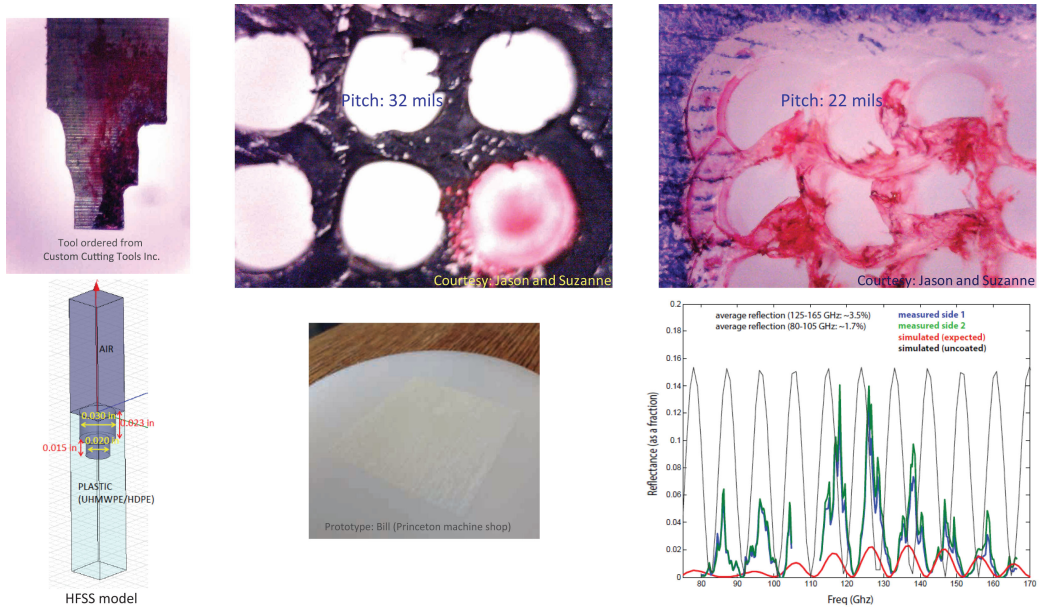

Figure C.3: *top left:* Cross-section of a custom drill bit for drilling holes on HDPE to make an AR-coating. *top middle:* Zoomed-in photo of a prototype made at the Princeton Physics machine shop with a pitch of 32 mils. *top right:* Zoomed-in photo of a prototype made at the Princeton Physics machine shop with a pitch of 22 mils. *bottom left:* Simulated model in HFSS. *bottom middle:* Photo of a 2x2 inch square section of the prototype with the 22 mil pitch. *bottom right:* Measured reflection of the same, when compared to simulation, is significantly higher.

tor. In order to compensate for this, we tried reducing the pitch of the features. The extent to which the pitch had to be reduced meant that the drilling tool diameter was now larger than the pitch which led to all kinds of random deformations of the plastic. The measured reflections shown in the bottom right panel of Figure C.3 confirmed that this approach was not working. Figure C.4 shows two other geometries simulated using HFSS that could potentially work as acceptable AR coatings on the UHMWPE window and would involve cutting/drilling with a single tool. The two-layer coating which would need two different tools would be much more complicated and time-consuming, and hence not being considered. It is shown just for comparing the simulated reflections between the various designs.

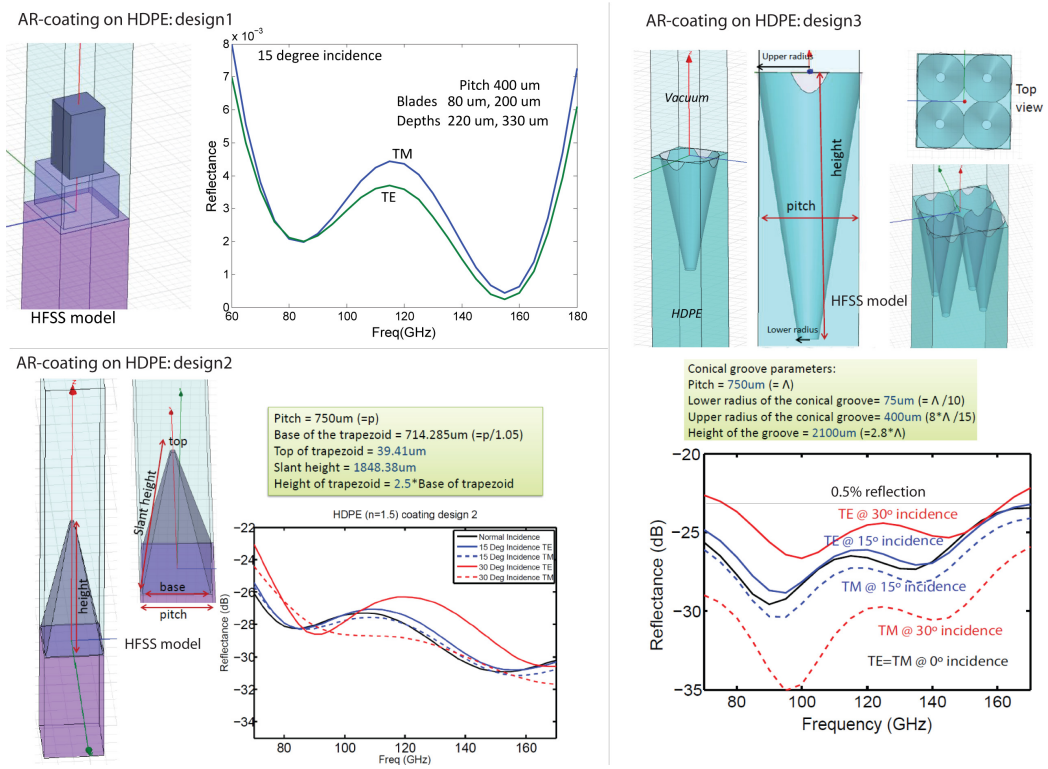

Figure C.4: Three alternative AR coating designs for HDPE along with simulated reflections: (*top left:*) design1: a two-layer coating very similar to that for the silicon lenses, (*bottom left:*) design2: cutting grooves in perpendicular directions with a tool having a triangular cross-section might be easier. (*right:*) design3: conical holes drilled into HDPE.

APPENDIX D

Mitered Bends in CPW and MS Transmission Lines

The transmission lines on which the signal is routed from the OMT to the TES detectors need to be bent several times. This introduces a discontinuity which changes the line characteristic impedance, adding a shunt capacitance. This could lead to unwanted reflections of the signal ultimately leading to loss in efficiency. In addition, the effective length of the transmission line containing bends becomes shorter than the centerline length as electromagnetic waves like to take shortcuts. At frequencies of our interest, the effect of the shunt capacitance is not a significant one. However, if the transmission line that needs to be bent is part of a circuit element, for e.g., CPW-to-MS transition, stub filter, then the change in the effective length needs to be carefully modeled and corrected for in the component design. The effects of bends in transmission lines could be minimized by mitering or curving the transmission lines. We simulated the effects of different ways of bending our microstrip transmission line in SONNET to estimate the change in effective length as well as to find the best mitering scheme that minimizes reflection in our frequencies of interest. Our findings are summarized in Figures D.1 and D.2.

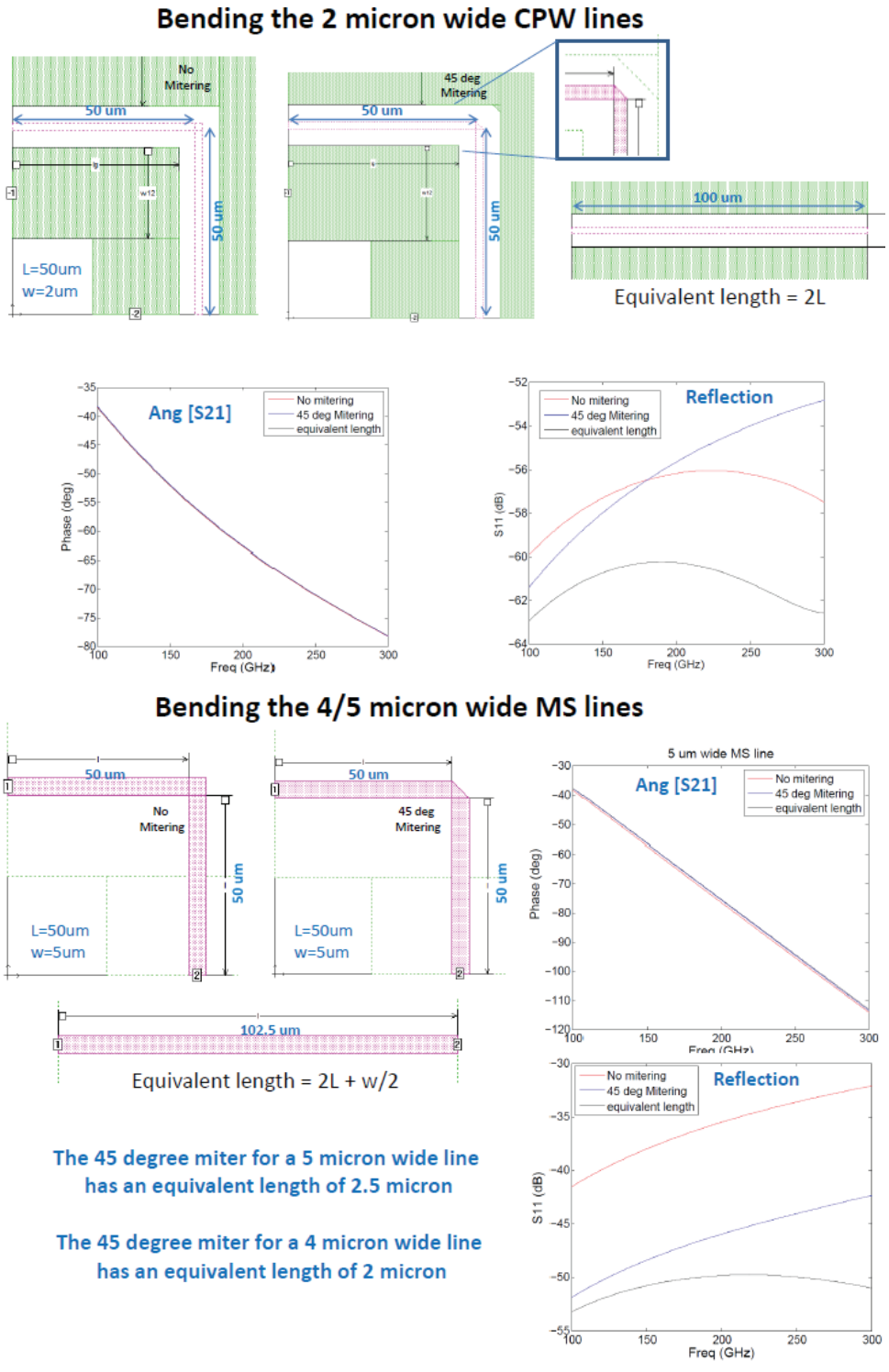

Figure D.1: Mitering of 90° bends in our CPW and MS lines.

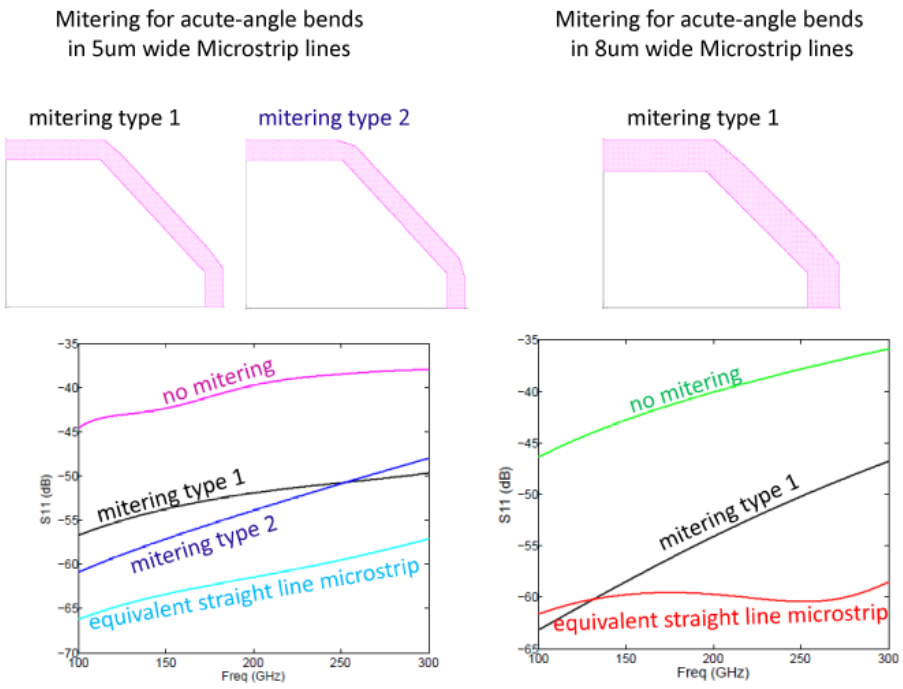

Figure D.2: Mitering of acute angle bends in our CPW and MS lines.

APPENDIX E

Crosstalk between pairs of traces in the array wiring layout

This note describes a simple method to estimate the crosstalk between neighboring pairs of traces in the detector array wiring layout, when there is no criss-cross between the two traces in a pair. This method requires several assumptions and simplifications which are mentioned in the appropriate places. The following steps were followed to arrive at an estimate of the induced current in a pair of traces due to the current flowing through the nearest neighboring pair:

· calculate the mutual inductance between two pairs of conductors and the self inductance of a single rectangular conductor loop

· with the help of a circuit model of the TES bias circuit, estimate the induced current in a pair of traces due to a small time varying current flowing through its nearest neighboring pair

E.0.1 Mutual and Self Inductance

The magnetic field due to a straight current carrying wire at a distance r from the center of the wire is given by

$$B = \frac{\mu_o I}{2\pi r} \tag{E.1}$$

The magnetic field due to the pair 1 conductors (blue) in Figure E.1 (right) at a distance r along the x axis is

$$B = \frac{\mu_o I}{2\pi}[\frac{1}{(r-s)} - \frac{1}{r}] \tag{E.2}$$

where, $s = 13$ μm is the separation between any two adjacent conductors. The radius of each conductor is $w = 4$ μm. The flux through the area covering the pair 2 conductors

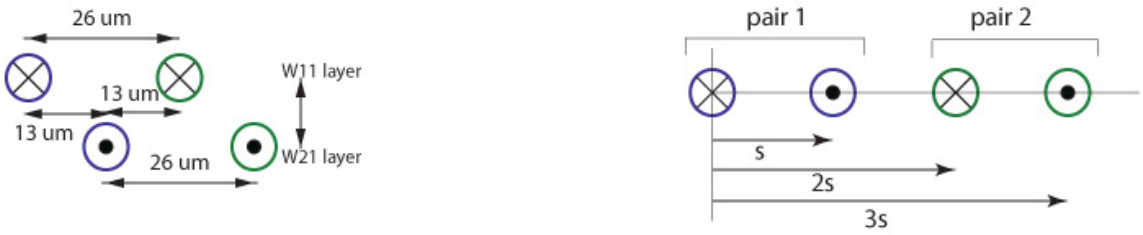

Figure E.1: *Left:* Two neighboring pairs of traces (blue and green). Each pair consists of two traces - one each on the two wiring layers on the wafer. *Right:* A simplified case of the figure on the left where the separation between the two wiring layers is ignored. This is an assumption to simplify the calculation of the mutual inductance between the two pairs.

(green) due to the above magnetic field is

$$\begin{aligned}\phi &= \frac{\mu_o I}{2\pi}\int_L\int_{2s+4}^{3s-4}[\frac{1}{(r-s)}-\frac{1}{r}]\,dr dl \\ &= \frac{\mu_o IL}{2\pi}[\ln(r-s)-\ln r]_{2s+4}^{3s-4} \\ &= \frac{\mu_o IL}{2\pi}\ln(\frac{630}{578})\end{aligned} \tag{E.3}$$

The mutual inductance between pairs 1 and 2 is

$$M_{12} = \frac{\phi}{I} = \frac{\mu_o L}{2\pi}\ln(\frac{630}{578}) \tag{E.4}$$

Assuming $L = 13000$ µm (assumption related to the total length of a trace),

$$M_{12} \sim 2.25\times10^{-10}\ H = 0.225\ nH \tag{E.5}$$

Approximating a single pair of traces as a rectangular loop, the self inductance of the loop can be similarly computed to be

$$L_{11} = L_{22} = \frac{\mu_o \ln(a/w)L}{\pi} \sim 6.2\times10^{-9}\ H = 6.2\ nH \tag{E.6}$$

E.0.2 Estimate of the crosstalk

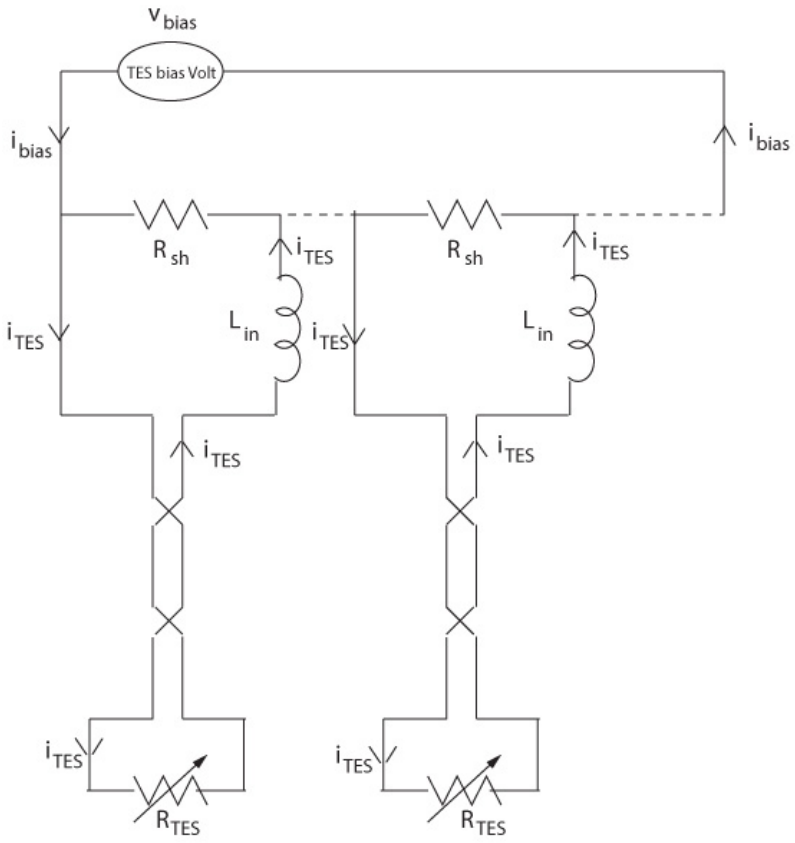

Figure E.2: A circuit model of the TES biasing circuit with the criss-crossed traces.

From Figure E.3, applying circuit rule to loops 1 and 2,

$$i_{1,TES}R_{TES} + (\,L_{in} + L_{11})[\frac{di_{1,TES}}{dt}] + M_{12}[\frac{di_{2,TES}}{dt}] + v_{1s}e^{j\omega t} = v_{1b} \tag{E.7}$$

$$i_{2,TES}R_{TES} + (\,L_{in} + L_{22})[\frac{di_{2,TES}}{dt}] + M_{21}[\frac{di_{1,TES}}{dt}] + v_{2s}e^{j\omega t} = v_{2b} \tag{E.8}$$

To solve the above pair of coupled differential equations, assumed a general form for $i_{1,TES}$ and $i_{2,TES}$:

$$\begin{aligned} i_{1,TES} &= i_{1b} + i_{1s}e^{j\omega t} \\ i_{2,TES} &= i_{2b} + i_{2s}e^{j\omega t} \end{aligned} \tag{E.9}$$

Substituting Equation E.9 into E.7 and E.8, we get

$$i_{1b}R_{TES} + i_{1s}e^{j\omega t}(R_{TES} + j\omega a) + j\omega b\, i_{2s}e^{j\omega t} = v_{1b} - v_{1s}e^{j\omega t} \tag{E.10}$$

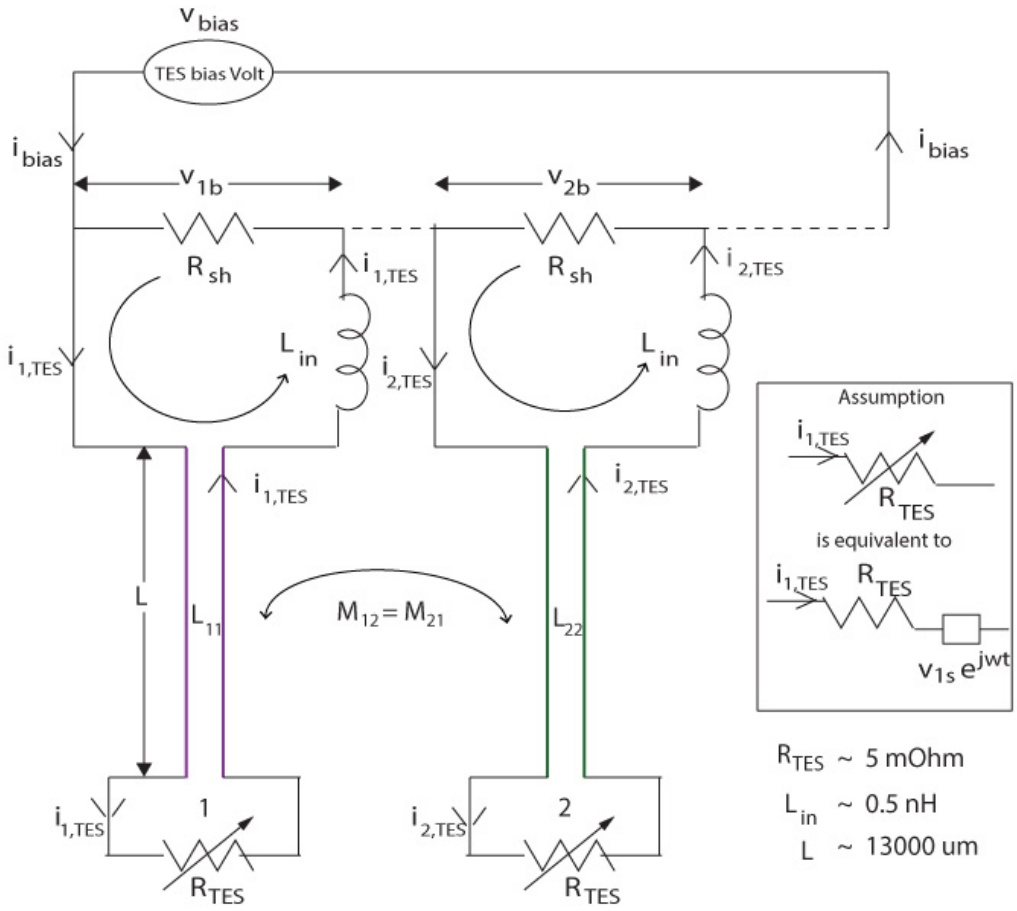

Figure E.3: A circuit model of the TES biasing circuit without the criss-cross. The two neighboring pairs of traces between which the crosstalk is calculated are marked purple and green. For ease of computation, the voltage drop across the variable TES resistance is approximated as: product of a constant resistance, R_{TES} times the current i_{TES} plus a time varying voltage $v_{1s}e^{j\omega t}$ as shown in the inset.

$$i_{2b}R_{TES} + i_{2s}e^{j\omega t}(R_{TES} + j\omega a) + j\omega b\, i_{1s}e^{j\omega t} = v_{2b} - v_{2s}e^{j\omega t} \tag{E.11}$$

where, $a = L_{in} + L_{11} = L_{in} + L_{22}$ and $b = M_{12} = M_{21}$

Writing Equation E.10 and E.11 in matrix form,

$$\begin{bmatrix} (R_{TES} + j\omega a) & j\omega b \\ j\omega b & (R_{TES} + j\omega a) \end{bmatrix} \begin{bmatrix} i_{1s}e^{j\omega t} \\ i_{2s}e^{j\omega t} \end{bmatrix} = \begin{bmatrix} v_{1b} - i_{1b}R_{TES} - v_{1s}e^{j\omega t} \\ v_{2b} - i_{2b}R_{TES} - v_{2s}e^{j\omega t} \end{bmatrix}$$

(E.12)

Solving the above equation for i_{1s} using Cramer's rule, we get

$$i_{1s}e^{j\omega t} = \frac{\begin{vmatrix} (v_{1,bias} - i_{1b}R_{TES}) - v_{1s}e^{j\omega t} & j\omega b \\ (v_{2,bias} - i_{2b}R_{TES}) - v_{2s}e^{j\omega t} & (R_{TES} + j\omega a) \end{vmatrix}}{\begin{vmatrix} (R_{TES} + j\omega a) & j\omega b \\ j\omega b & (R_{TES} + j\omega a) \end{vmatrix}}$$

(E.13)

But, $(\ v_{1,bias} - \ i_{1b}R_{TES}) = (\ v_{2,bias} - \ i_{2b}R_{TES}) = 0$ (equating the constant (DC) terms on both sides of Equation E.10 and E.11). Therefore Equation E.13 reduces to

$$i_{1s} = \frac{\begin{vmatrix} -\ v_{1s} & j\omega b \\ -\ v_{2s} & (R_{TES} + j\omega a) \end{vmatrix}}{\begin{vmatrix} (R_{TES} + j\omega a) & j\omega b \\ j\omega b & (R_{TES} + j\omega a) \end{vmatrix}}$$

(E.14)

Similarly,

$$i_{2s} = \frac{\begin{vmatrix} (R_{TES} + j\omega a) & -\ v_{1s} \\ j\omega b & -\ v_{2s} \end{vmatrix}}{\begin{vmatrix} (R_{TES} + j\omega a) & j\omega b \\ j\omega b & (R_{TES} + j\omega a) \end{vmatrix}}$$

(E.15)

The induced current, $i_{1,ind}e^{j\omega t}$ in loop 1 due to a small time varying component $i_{2s}e^{j\omega t}$ in loop 2, is given by:

$$i_{1,ind} = (\ i_{1s,b=M_{12}} - \ i_{1s,b=0}) \tag{E.16}$$

where,

$$\begin{aligned} (\ i_{1s,b=0}) &= \frac{-\ v_{1s}(R_{TES} + j\omega a)}{(R_{TES}^2 - \omega^2 a^2 + 2j\omega R_{TES}a)} \\ (\ i_{1s,b=M_{12}}) &= \frac{-\ v_{1s}(R_{TES} + j\omega a) + \ v_{2s}j\omega b}{(R_{TES}^2 - \omega^2 a^2 + 2j\omega R_{TES}a + \omega^2 b^2)} \\ (\ i_{2s,b=0}) &= (\ i_{1s,b=0}) \text{ under the assumption: } \ v_{1s} = \ v_{2s} \end{aligned} \tag{E.17}$$

Using $L_{in} = 0.5\,nH$, $a = L_{in} + L_{11} = L_{in} + L_{22} = 6.7\,nH$, $b = M_{12} = M_{21} = 0.225\,nH$, $v_{2s} = v_{1s}, R_{TES} = 5\ m\Omega$, we get the magnitude of the ratio $|\frac{i_{1,ind}}{i_{2s,b=0}}|$ as plotted in Figure E.4 as a function of frequency. The ratio $|\frac{i_{1,ind}}{i_{2s,b=0}}|$ asymptotically approaches $\frac{b}{(\ b+\ a)} \sim 0.033$ in the large ω limit.

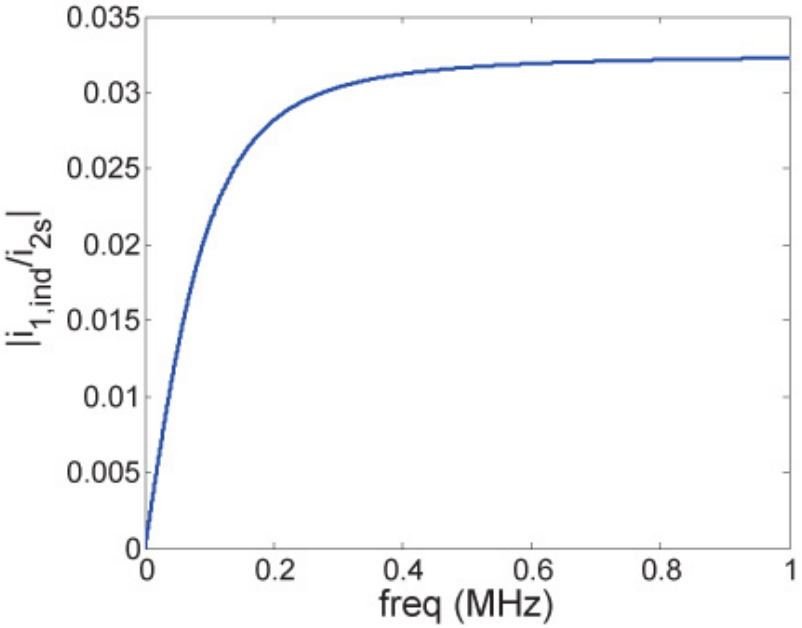

Figure E.4: Ratio of induced current to the time varying component of the current in the neighboring pair as a function of frequency.

BIBLIOGRAPHY

[1] Alpher R. A., Bethe H., and Gamow G., "The origin of chemical elements", The Physical Review, **73**, Iss. 7, pp. 803-804 (1948)

[2] Alpher, R. A. and Herman, R. C., "Remarks on the Evolution of the Expanding Universe", Physical Review, vol. **75**, Iss. 7, pp. 1089-1095 (1949)

[3] Partridge, R. B., "3K: The Cosmic Microwave Background Radiation", New York: Cambridge University Press (1995)

[4] A. A. Penzias and R. W. Wilson, "A Measurement of Excess Antenna Temperature at 4080 Mc/s", The Astrophysical Journal, vol. **142**, pp. 419-421 (1965)

[5] Dicke, R. H., Peebles, P. J. E., Roll, P. G., and Wilkinson, D. T., "Cosmic Black-Body Radiation", Astrophysical Journal, vol. **142**, p. 414-419 (1965)

[6] Kolb, E. and Turner, M., "The Early Universe", Redwood City, CA: Addison- Wesley Publishing Company (1990)

[7] A. H. Guth, "The inflationary universe: A possible solution to the horizon and flatness problems", Physical Review D, Volume **23**, Number 2, 347-356 (1981)

[8] A. Albrecht and P. J. Steinhardt, "Cosmology for grand unified theories with radiatively induced symmetry breaking", Physical Review Letters, **48**: 1220 (1982)

[9] M. Trodden, "Electroweak baryogenesis", Reviews of Modern Physics, **71**:1463 (1999)

[10] C. L. Bennett et al., "First year Wilkinson Microwave Anisotropy Probe (WMAP) observations: Preliminary maps and basic results", The Astrophysical Journal, **148**: 1 (2003)

[11] J. C. Mather et al, "A preliminary measurement of the Cosmic Microwave Background spectrum by the Cosmic Background Explorer (COBE) satellite", The Astrophysical Journal Letters, vol. **354**, pp. L37-L40 (1990)

[12] Fixsen, D. J., Cheng, E. S., Gales, J. M., Mather, J. C., Shafer, R. A., and Wright, E. L., "The Cosmic Microwave Background Spectrum from the Full COBE FIRAS Data Set", Astrophysical Journal v. **473**, p. 576 (1996)

[13] "Cosmic Microwave Background Anisotropy", theory.physics.helsinki.fi/~cpt/Cosmo12.pdf

[14] G. F. Smoot et al, "Structure in the COBE differential microwave radiometer first-year maps", The Astrophysical Journal Letters, vol. **396**, pp. L1-L5 (1992)

[15] Sachs R. K. and Wolfe A. M., "Perturbations of a cosmological model and angular variations of the Microwave Background", The Astrophysical Journal, **147**: 73-90 (1967)

[16] Silk J., "Cosmic black-body radiation and galaxy formation", The Astrophysical Journal, **151**: 459-471 (1968)

[17] Hu, W. and Dodelson, S., "Cosmic Microwave Background Anisotropies", Ann. Rev. Astron. Astrophys. **40**: 171-216 (2002)

[18] R. A. Sunyaev and I. B. Zeldovich, "Microwave Background Radiation as a Probe of the Contemporary Structure and History of the Universe", Annual Review of Astronomy and Astrophysics, vol. **18**, pp. 537-560 (1980)

[19] J. E. Carlstrom, G. P. Holder, and E. D. Reese, "Cosmology with the Sunyaev-Zel'dovich Effect", Annual Review of Astronomy and Astrophysics, vol. **40**, pp. 643-680 (2002)

[20] N. Hand et al., "Evidence of Galaxy Cluster Motions with the Kinematic Sunyaev-Zel'dovich Effect", Physical Review Letters **109**, 041101 (2012)

[21] Rees, M. J., "Polarization and Spectrum of the Primeval Radiation in an Anisotropic Universe", Astrophysical Journal, vol. **153**, p. L1 (1968)

[22] Chandrasekhar, S., "Radiative Transfer", New York: Dover Publications (1960)

[23] Arthur Kosowsky, "Seeing Sound Waves in the Early Universe", arxiv.org/abs/astro-ph/9811163, RAP-238

[24] Marc Kamionkowski, "Statistics of cosmic microwave background polarization", Phys. Rev. D, Vol. **55**, Iss. 12, 7368 (1997)

[25] M. Zaldarriaga and U. Seljak, "An All Sky Analysis of Polarization in the Microwave Background", Phys. Rev., vol. **D55**, pp. 1830-1840 (1997)

[26] Shun Saito, Kiyotomo Ichiki, and Atsushi Taruya, "Probing polarization states of primordial gravitational waves with CMB anisotropies", JCAP **0709**: 002 (2007)

[27] Wayne Hu and Martin White, "A CMB polarization primer", New Astronomy **2**, 323-344 (1997)

[28] Crittenden, R., Davis, R. L., and Steinhardt, P. J., "Polarization of the Microwave Background Due to Primordial Gravitational Waves", Astrophysical Journal Letters v. **417**, p. L13 (1993)

[29] Marc Kamionkowski, Arthur Kosowsky, and Albert Stebbins,"A Probe of Primordial Gravity Waves and Vorticity", Phys. Rev. Lett. **78**, 2058 (1997)

[30] U. Seljak and M. Zaldarriaga, "Signature of Gravity Waves in Polarization of the Microwave Background", Phys. Rev. Lett., vol. **78**, pp. 2054-2057 (1997)

[31] Daniel Baumann et. al., "CMBPol: A Mission to Map our Origins", AIP Conf.Proc. **1141**: 3-9 (2009)

[32] T. Essinger-Hileman et al, "CLASS: The Cosmology Large Angular Scale Surveyor", Society of Photo-Optical Instrumentation Engineers (SPIE) Conference Series, vol. **9153**, p. 1 (2014)

[33] Justin Lazear et. al., "The Primordial Inflation Polarization Explorer", Proceedings of SPIE Volume **9153**, Astronomical Telescopes + Instrumentation (2014)

[34] M. Zaldarriaga and U. Seljak, "Gravitational Lensing Effect on Cosmic Microwave Background Polarization", Phys. Rev. D, vol. **58**, p. 023003 (1998)

[35] W. Hu and T. Okamoto, "Mass Reconstruction with Cosmic Microwave Background Polarization", The Astrophysical Journal, vol. **574**, no. 2, p. 566 (2002)

[36] John Kovac,"Detection of Polarization in the Cosmic Microwave Background using DASI", Thesis (2003)

[37] Kaplinghat, M., Knox, L., and Song, Y., "Determining Neutrino Mass from the CMB Alone", Phys. Rev. Lett. **91**: 241301 (2003)

[38] Hu, W. 2002, "Dark synergy: Gravitational lensing and the CMB", Phys. Rev. D, **65**: 023003 (2002)

[39] Coulson, D., Crittenden, R. G., and Turok, N. G., Physical Review Letters, **73**, 2390 (1994)

[40] C. B. Netterfield et al., "A Measurement of the Angular Power Spectrum of the Anisotropy in the Cosmic Microwave Background", Astrophys. J., **474**, 47 (1997)

[41] S. Hanany et al, "MAXIMA-1: A Measurement of the Cosmic Microwave Background Anisotropy on Angular Scales of 10^{-5}", The Astrophysical Journal Letters, vol. **545**, no. 1, p. L5 (2000)

[42] N. W. Halverson et al, "Degree Angular Scale Interferometer First Results: A Measurement of the Cosmic Microwave Background Angular Power Spectrum", The Astrophysical Journal, vol. **568**, no. 1, p. 38 (2002)

[43] A. Miller et al, "The QMAP and MAT/TOCO Experiments for Measuring Anisotropy in the Cosmic Microwave Background", The Astrophysical Journal Supplement Series, vol. **140**, pp. 115-141 (2002)

[44] W. C. Jones et al, "A Measurement of the Angular Power Spectrum of the CMB Temperature Anisotropy from the 2003 Flight of BOOMERANG", The Astrophysical Journal, vol. **647**, no. 2, p. 823 (2006)

[45] G. Hinshaw et al, "Nine-year Wilkinson Microwave Anisotropy Probe (WMAP) Observations: Cosmological Parameter Results", The Astrophysical Journal Supplement Series, vol. **208**, no. 2, p. 19 (2013)

[46] Planck Collaboration, "Planck 2015 Results. XIII. Cosmological Parameters", submitted to Astronomy and Astrophysics, arxiv.org/abs/1502.01589 (2016)

[47] E. M. Leitch et al, "Measurement of polarization with the Degree Angular Scale Interferometer", Nature, vol. **420**, no. 6917, pp. 763-771 (2002)

[48] C. Bischoff et al, "New Measurements of Fine-Scale CMB Polarization Power Spectra from CAPMAP at Both 40 and 90 GHz", The Astrophysical Journal, vol. **684**, no. 2, p. 771 (2008)

[49] C. Pryke et al, "Second and Third Season QUaD Cosmic Microwave Background Temperature and Polarization Power Spectra", The Astrophysical Journal, vol. **692**, no. 2, p. 1247 (2009)

[50] D. Barkats et al, "Degree-scale Cosmic Microwave Background Polarization Measurements from Three Years of BICEP1 Data", The Astrophysical Journal, vol. **783**, no. 2, p. 67 (2014)

[51] QUIET Collaboration, "Second Season QUIET Observations: Measurements of the Cosmic Microwave Background Polarization Power Spectrum at 95 GHz", The Astrophysical Journal, vol. **760**, no. 2, p. 145 (2012)

[52] QUIET Collaboration, "First Season QUIET Observations: Measurements of Cosmic Microwave Background Polarization Power Spectra at 43 GHz in the Multipole Range 25-475", The Astrophysical Journal, vol. **741**, no. 2, p. 111 (2011)

[53] A. T. Crites et al., "Measurements of E-Mode Polarization and Temperature-E-Mode Correlation in the Cosmic Microwave Background from 100 Square Degrees of SPTpol Data", The Astrophysical Journal, Volume **805**, Number 1 (2014)

[54] Planck Collaboration, "Planck intermediate results. XXX. The angular power spectrum of polarized dust emission at intermediate and high Galactic latitudes", AA **586**, A133 (2016)

[55] A. van Engelen et al, "The Atacama Cosmology Telescope: Lensing of CMB Temperature and Polarization Derived from Cosmic Infrared Background Cross-correlation", The Astrophysical Journal, vol. **808**, no. 1, p. 7 (2015)

[56] The Polarbear Collaboration, "A Measurement of the Cosmic Microwave Background B-mode Polarization Power Spectrum at Sub-degree Scales with POLARBEAR", The Astrophysical Journal, vol. **794**, no. 2, p. 171 (2014)

[57] D. Hanson et al, "Detection of B-Mode Polarization in the Cosmic Microwave Background with Data from the South Pole Telescope", Physical Review Letters, vol. **111**, no. 14, p. 141301 (2013)

[58] P. A. R. Ade et al, "Detection of B-Mode Polarization at Degree Angular Scales by BICEP2", Phys. Rev. Lett., vol. **112**, p. 241101 (2014)

[59] BICEP2 and Keck Array Collaborations, "BICEP2/Keck Array V: Measurements of B-mode Polarization at Degree Angular Scales and 150 GHz by the Keck Array", The Astrophysical Journal, vol. **811**, p. 126 (2015)

[60] P. A. R. Ade et al, "Joint Analysis of BICEP2/Keck Array and Planck Data", Phys. Rev. Lett., vol. **114**, p. 101301 (2015)

[61] Planck Collaboration, "Planck intermediate results. XIX. An overview of the polarized thermal emission from Galactic dust", AA **576**, A104 (2015)

[62] KECK Array and BICEP2 Collaborations, "BICEP2 / Keck Array VI: Improved Constraints On Cosmology and Foregrounds When Adding 95 GHz Data From Keck Array", Phys. Rev. Lett. **116**, 031302 (2016)

[63] R. Gusten, L. A. Nyman, P. Schilke, K. Menten, C. Cesarsky, and R. Booth, "The Atacama Pathfinder EXperiment (APEX) - a new submillimeter facility for southern skies", Astronomy and Astrophysics, vol. **454**, pp. L13-L16 (2006)

[64] A. Wootten and A. Thompson, "The Atacama Large Millimeter/Submillimeter Array", Proceedings of the IEEE, vol. **97**, no. 8, pp. 1463-1471 (2009)

[65] The Polarbear Collaboration, "The new generation CMB B-mode polarization experiment: POLARBEAR", 2010 Rencontres de Moriond proceedings (2010)

[66] M. Niemack et al, "The Atacama B-mode Search: An Experiment to Probe Inflation by Measuring the Cosmic Microwave Background Polarization", in American Astronomical Society Meeting Abstracts, vol. **213**, p. 480.05 (2009)

[67] R. J. Thornton et al., "The Atacama Cosmology Telescope: The polarization-sensitive ACTPol instrument", submitted to the Astrophysical Journal, arxiv.org/abs/1605.06569 (2016)

[68] M. D. Niemack et al, "ACTPol: A polarization-sensitive receiver for the Atacama Cosmology Telescope", Proc. SPIE, vol. **7741**, p. 77411S (2010)

[69] S. W. Henderson et al., "Advanced ACTPol cryogenic detector arrays and readout", Journal of Low Temperature Physics, Special Edition LTD 16, Pages 1-8 (2016)

[70] R. Keisler et al., "A measurement of the damping tail of the cosmic microwave background power spectrum with the South Pole Telescope", The Astrophysical Journal, **743**(1): 28 (2011)

[71] Jonathan L. Sievers et al., "The Atacama Cosmology Telescope: Cosmological parameters from three seasons of data. Journal of Cosmology and Astroparticle Physics", **10**: 060 (2013)

[72] Blake D. Sherwin et al., "Evidence for dark energy from the cosmic microwave background alone using the Atacama Cosmology Telescope lensing measurements", Physical Review Letters, **107**(2): 021302 (2011)

[73] Matthew Hasselfield et al., "The Atacama Cosmology Telescope: Sunyaev-Zel'dovich selected galaxy clusters at 148 GHz from three seasons of data", Journal of Cosmology and Astroparticle Physics, **07**: 008 (2013)

[74] E.-M. Mueller, F. de Bernardis, R. Bean, and M. D. Niemack, "Constraints on Gravity and Dark Energy from the Pairwise Kinematic Sunyaev-Zel?dovich Effect", The Astrophysical Journal, vol. 808, no. 1, p. 47 (2015)

[75] Christopher P Ahn et al., "The ninth data release of the Sloan Digital Sky Survey: first spectroscopic data from the SDSS-III Baryon Oscillation Spectroscopic Survey", The Astrophysical Journal Supplement Series, **203**(2): 21 (2012)

[76] D. S. Swetz et al, "Overview of the Atacama Cosmology Telescope: Receiver, Instrumentation, and Telescope Systems", The Astrophysical Journal Supplement Series, vol. **194**, no. 2, p. 41 (2011)

[77] J. W. Fowler et al, "Optical design of the Atacama Cosmology Telescope and the Millimeter Bolometric Array Camera", Appl. Opt., vol. **46**, no. 17, pp. 3444-3454 (2007)

[78] M. D. Niemack, "Towards dark energy: Design, development, and preliminary data from ACT", Ph.D. dissertation, Princeton University (2008)

[79] R. Datta et al, "Large-aperture wide-bandwidth antireflection-coated silicon lenses for millimeter wavelengths", Appl. Opt., vol. **52**, p. 8747 (2013)

[80] P. A. R. Ade, G. Pisano, C. Tucker, and S. Weaver, "A review of metal mesh filters", Millimeter and Submillimeter Detectors and Instrumentation for Astronomy III. Proceedings of the SPIE, Volume **6275**, id. 62750U (2006)

[81] Precision Cryogenics, http://www.precisioncryo.com/

[82] Janis Research Company, http://www.janis.com/

[83] K. W. Yoon et al, "Feedhorn-Coupled TES Polarimeters for Next-Generation CMB Instruments", in American Institute of Physics Conference Series, vol. **1185**, pp. 515-518 (2009)

[84] J. McMahon et al, "Planar Orthomode Transducers for Feedhorn coupled TES Polarimeters", AIP Conference Proceedings, vol. **1185**, no. 1, pp. 490-493 (2009)

[85] J.J. McMahon, et al., "Multi-chroic Feed-Horn Coupled TES Polarimeters", Journal of Low Temperature Physics, **167**, 879-84 (2012)

[86] R. Datta et al., "Horn Coupled Multichroic Polarimeters for the Atacama Cosmology Telescope Polarization Experiment", J. Low Temp. Phys., Volume **176**, Issue 5, pp 670-676 (2014)

[87] R. Datta et al., "Design and Deployment of a Multichroic Polarimeter Array on the Atacama Cosmology Telescope", J. Low Temp. Phys., Volume **184**, Issue 3, pp 568-575 (2016)

[88] James J Bock, J Gundersen, Adrian T Lee, P L Richards, and E Wollack, "Optical Coupling", Journal of Physics: Conference Series, vol. **155**, no. 1, p. 012005 (2009)

[89] J. A. Chervenak et al, "Superconducting multiplexer for arrays of transition edge sensors", Applied Physics Letters, vol. **74**, p. 4043 (1999)

[90] K. D. Irwin et al, "Time-division SQUID multiplexers", AIP Conf. Proc. **605**, 301 (2002)

[91] Piet A. J. de Korte et al, "Time-division superconducting quantum interference device multiplexer for transition-edge sensors", Rev. Sci. Instrum. **74**, 3807 (2003)

[92] D. Bintley et al., "Commissioning SCUBA-2 at JCMT and Optimising the Performance of the Superconducting TES Arrays", Journal of Low Temperature Physics, **167**, 152-60 (2012)

[93] M.D. Niemack et al., "A Kilopixel Array of TES Bolometers for ACT: Development, Testing, and First Light", Journal of Low Temperature Physics, **151**, 690-6 (2008)

[94] S. Padin et al., "South Pole Telescope optics", Applied Optics **47**, 4418-28 (2008)

[95] S. Hanany, M. D. Niemack, and L. Page, "CMB Telescopes and Optical Systems", Planets, Stars and Stellar Systems, Volume 1: Telescopes and Instrumentation (2012)

[96] Hemant Kumar Raut, V. Anand Ganesh, A. Sreekumaran Nair, and Seeram Ramakrishna, "Anti-reflective coatings: A critical, in-depth review", Energy Environ. Sci., **4**, 3779 (2011)

[97] J. Lau et al., "Millimeter-wave antireflection coating for cryogenic silicon lenses", Applied Optics, **45**, 3746-51 (2006)

[98] R.E. Collin, "Field Theory of Guided Waves", McGraw-Hill, New York, pp. 749-786 (1990)

[99] D.R. Smith and J.B. Pendry, "Homogenization of metamaterials by field averaging", (invited paper), Journal of the Optical Society of America B, Vol. **23**, No. 3, pp. 391-403 (2006)

[100] Ari H. Sihvola, "Electromagnetic Mixing Formulas and Applications", Electromagnetic Wave Series, Vol. **47**, Institution of Engineering and Technology, London, United Kingdom (2008)

[101] P.-S. Kildal, K. Jakobsen, and K. Sudhakar Rao, "Meniscus-lens-corrected corrugated horn: a compact feed for a Cassegrain antenna", IEE Proc. **131**, 390-4 (1984)

[102] Cohn S. B., "Lens Type Radiators: Antenna Engineering Handbook", McGraw-Hill, N.Y. (1961)

[103] P.B. Clapham and M.C. Hutley, "Reduction of Lens Reflection by 'Moth Eye' Principle", Nature, Vol. **244**, pp. 281-282 (1973)

[104] B.S. Thornton, "Limit of the moth's eye principle and other impedance-matching corrugations for solar-absorber design", Journal of the Optical Society of America, Vol. **65**, No. 3, pp. 267-270 (1975)

[105] M.E. Motamedi, W.H. Southwell, and W.J. Gunning, "Antireflection surfaces in silicon using binary optics technology", Applied Optics, Vol. 31, No. 22, pp. 4371-4376 (1992)

[106] J. Zhang, et al., "New artificial dielectric metamaterial and its application as a terahertz antireflection coating", Applied Optics, **48**, 6635 (2009)

[107] K.-F. Schuster, et al. "Micro-machined Quasi-Optical Elements for THz Applications", Sixteenth International Symposium on Space Terahertz Technology, held May 2-4, 2005 at Chalmers University of Technology. Gteborg, Sweden., p. 524-528 (2005)

[108] P. Han et al., "Application of Silicon Micropyramid Structures for Antireflection of Terahertz Waves", IEEE Journal of Selected Topics in Quantum Electronics, Vol. **16**, No. 1 (2010)

[109] M. Shimon et al., "CMB Polarization Systematics due to Beam Asymmetry: Impact on Inflationary Science", Phys. Rev. **D77**: 083003 (2008)

[110] A. MacKay, "Proof of Polarization Independence and Nonexistence of Crosspolar Terms for Targets Presenting n-Fold (n $>$ 2) Rotational Symmetry with Special Reference to Frequency-Selective Surfaces", Electron. Lett., vol. **25**, no. 24, pp. 1624-1625 (1989)

[111] S. Rytov, "The electromagnetic properties of finely layered medium", Soviet Physics JETP **2**, 466-475 (1956)

[112] S. Biber, et al., "Design of Artificial Dielectrics for Anti-Reflection-Coatings", 33rd European Microwave Conference, Munich (2003)

[113] D.L. Brundrett, E.N. Glytsis, and T.K. Gaylord, "Homogeneous layer models for high-spatial-frequency dielectric surface-relief gratings: conical diffraction and antireflection designs", Applied Optics, Vol. **33**, No. 13, pp. 2695-2706 (1994)

[114] T.K. Gaylord, W.E. Baird, and M.G. Moharam, "Zero-reflectivity high spatial-frequency rectangular-groove dielectric surface-relief gratings", Applied Optics, Vol. **25**, No. 24, pp. 4562-4567 (1986)

[115] D.E. Aspnes, "Local-field effects and effective-medium theory: A microscopic perspective", Am. J. Phys. **50**, 704 (1982)

[116] D.E. Aspnes, "Bounds on Allowed Values of the Effective Dielectric Function of Two-Component Composites at Finite Frequencies", Physical Review B, Vol. **25**, No. 2, pp. 1358-1361 (1982)

[117] W.G. Egan and D.E. Aspnes, "Finite-wavelength effects in composite media", PRB, Vol. **26**, No. 10, pp. 5313-5321 (1982)

[118] A. Wagner-Gentner, et al. "Low loss THz window", Infrared Physics and Technology, **48**, 249-253 (2006)

[119] G. Matthaei, L. Young, E. M. T. Jones, "Microwave Filters, Impedance-Matching Networks and Coupling Structures", McGraw-Hill, New York, pp. 300-304 (1964)

[120] D. H. Raguin and G. M. Morris, "Analysis of antireflection-structured surfaces with continuous one-dimensional surfaces profiles", Applied Optics, Vol. **32**, No. 14, pp. 2582-2598 (1993)

[121] Jackson J. D., "Classical Electrodynamics", John Wiley & Sons Inc. (1998)

[122] "Ansoft High Frequency Structure Simulator (HFSS) software package", http://www.ansys.com/Products/Simulation+Technology/Electromagnetics/High-Performance+Electronic+Design/ANSYS+HFSS

[123] "Workshop 9-1: Unit Cell Analysis (Infinite Array)", http://www.ece.uprm.edu/~rafaelr/inel6068/HFSS/HFSS_Antenna_v2015_v1/workshop_instructions_trainee/ANSYS_HFSS_Antenna_W09_1_Unit_Cell.pdf

[124] S. Orfanidis, "Electromagnetic waves and antennas", Chapter 5 http://www.ece.rutgers.edu/~orfanidi/ewa/ch05.pdf, Chapter 6 http://www.ece.rutgers.edu/~orfanidi/ewa/ch06.pdf

[125] Nu-Tek Precision Optical Corporation, http://www.nu-tek-optics.com

[126] T. Duffar, "Crystal Growth Processes Based on Capillarity: Czochralski, Floating Zone, Shaping and Crucible Techniques", Wiley, Blackwell (2010)

[127] J. Krupka, et al., "Measurements of Permittivity, Dielectric Loss Tangent, and Resistivity of Float-Zone Silicon at Microwave Frequencies", IEEE Transaction on Microwave Theory and Techniques, vol. **54**, No. 11, pp. 3995-4000 (2006)

[128] M. N. Afsar and H. Chi, "Millimeter wave complex refractive index, complex dielectric constant, and loss tangent of extra high purity and compensated silicon", International Journal of Infrared and Millimeter Waves, vol. **15**, pp. 1181-1188 (1994)

[129] V. V. Parshin, et al. "Silicon as an Advanced Window Material for High Power Gyrotrons", Int. Journal of Infrared and Millimeter Waves, vol. **16**, no. 5, pp. 863-877 (1995)

[130] P. Yeh, "Optical Waves in Layered Media", Wiley, New York (1988)

[131] F. Gervais, "High-Temperature Infrared Reflectivity Spectroscopy by Scanning Interferometry", Electromagnetic Waves in Matter, Part I, Vol. **8** (Infrared and Millimeter Waves), K. J. Button, eds. (Academic Press, London), pp. 284–287 (1983)

[132] M. Van Exter and D. Grischkowsky, "Optical and Electronic Properties of Doped Silicon from 0.1 to 2 THz", Applied Physics Letters, Vol. **56**, No. 17, pp. 1694-1696 (1990)

[133] Y. Okada and Y. Tokumaru, "Precise determination of lattice parameter and thermal expansion coefficient of silicon between 300 and 1500K", J. Appl. Phys., Vol. **56**, No. 2, pp. 314-320 (1984)

[134] B. I. Shklovskii and A. L. Efros, "Electronic Properties of Doped Semiconductors", Berlin, Germany, Springer, ch. 4 (1984)

[135] Paul F. Goldsmith, "Quasioptical Systems: Gaussian Beam Quasioptical Propogation and Applications", Wiley-IEEE Press (1997)

[136] Darin Rosen, et al., "Epoxy-based broadband anti-reflection coating for millimeter-wave optics", Applied Optics Vol. **52**, Issue 33, pp. 8102-8105 (2013)

[137] Li, YunZhou, Bin Cai, and Yiming Zhu., "Fabrication of anti-reflective microstructure at terahertz frequency by using Chinese acupuncture needles", Optics letters **40**.12: 2917-2920 (2015)

[138] Matsumura, Tomotake, et al., "Millimeter-wave broadband antireflection coatings using laser ablation of subwavelength structures", Applied optics **55**.13: 3502-3509 (2016)

[139] K. Smith et al., "Gravitational Lensing", CMB Polarization Workshop: Theory and Foregrounds: CMBPol Mission Concept Study. AIP Conference Proceedings, Volume **1141**, pp. 121-178 (2009)

[140] W. Hu, "Weak lensing of the CMB: A harmonic approach", Phys.Rev. D **62**, 043007 (2000)

[141] D. Hanson et al., "Detection of B-Mode Polarization in the Cosmic Microwave Background with Data from the South Pole Telescope", Phys. Rev. Lett. **111**, 141301 (2013)

[142] The POLARBEAR Collaboration, "A Measurement of the Cosmic Microwave Background B-Mode Polarization Power Spectrum at Sub-Degree Scales with POLARBEAR", Astrophysical Journal, **794**: 171 (2014)

[143] P. A. R. Ade et al., "BICEP2. II. EXPERIMENT AND THREE-YEAR DATA SET", The Astrophysical Journal, Volume **792**, Number 1, 62 (2014)

[144] A. van Engelen et al., "The Atacama Cosmology Telescope: Lensing of CMB Temperature and Polarization Derived from Cosmic Infrared Background Cross-Correlation", The Astrophysical Journal, Volume **808**, Number 1, 7 (2015)

[145] E. Grace et al., "ACTPol: on-sky performance and characterization", Proc. SPIE **9153**, Millimeter, Submillimeter, and Far-Infrared Detectors and Instrumentation for Astronomy VII, 915310 (2014)

[146] Stephen Padin, "Mapping speed for an array of corrugated horns", Applied Optics Vol. **49**, Issue 3, pp. 479-483 (2010)

[147] Y. Takeichi, T. Hashimoto and F. Takeda, "The ring-loaded corrugated waveguide", IEEE Transactions on Microwave Theory and Techniques **MTT-19**, Volume **19**, Issue 12, 947-950 (1971)

[148] A. Kogut et al., "PAPPA: Primordial Anisotropy Polarization Pathfinder Array", New Astron. Rev., v **50**, pp 1009-1014 (2006)

[149] R. Knoechel and B. Mayer, "Broadband printed circuit 0° /180° couplers and high power inphase power dividers", IEEE **MTT-S** International Microwave Symposium Digest, p. 471 (1990)

[150] J. Bock et al., "Study of the Experimental Probe of Inflationary Cosmology (EPIC)-Intemediate Mission for NASA's Einstein Inflation Probe", arxiv.org/abs/0906.1188 (2009)

[151] NI AWR Design Environment, http://www.awrcorp.com/products/microwave-office

[152] J. Britton et al., "Corrugated Silicon Platelet Feed Horn Array for CMB Polarimetry at 150 GHz", Proc. of SPIE, Millimeter, Submillimeter, and Far-Infrared Detectors and Instrumentation for Astronomy V, Vol. **7741**, 77410T-1 (2010)

[153] B. W. Maxfield and W. L. McLean, "Superconducting Penetration Depth of Niobium", Phys. Rev., Vol. **139**, Iss. 5A, A1515?A1522 (1965)

[154] Jia-Shen G. Hong and M. J. Lancaster, "Microstrip Filters for RF / Microwave Applications", John Wiley & Sons (2004)

[155] David M. Pozar, "Microwave Engineering", Wiley (2011)

[156] G. Cataldo et al, "Infrared dielectric properties of low-stress silicon nitride", Optics Letters, Vol. **37**, No. 20, pp. 4200-4202 (2012)

[157] V. Belitsky, C. Risacher, M. Pantaleev, and V. Vassilev, "Superconducting Microstrip Line Model Studies at Millimeter and Sub-millimeter Waves and their Comparison", 14th International Symposium on Space Terahertz Technology, Int. J. Infrared Milli Waves **27**: 809 (2006)

[158] S. P. Ho et al., "The First Multichroic Polarimeter Array on the Atacama Cosmology Telescope: Characterization and Performance", J Low Temp Phys **184**: 559 (2016)

[159] S. M. Duff et al., "Advanced ACTPol Multichroic Polarimeter Array Fabrication Process for 150 mm Wafers", J Low Temp Phys **184**: 634 (2016)

[160] D. Li et al., "AlMn Transition Edge Sensors for Advanced ACTPol", J Low Temp Phys **184**: 66 (2016)

[161] David T. Chuss, S. Harvey Moseley, Giles Novak, and Edward J. Wollack, "A Martin-Puplett Architecture for Polarization Modulation and Calibration", Proceedings of SPIE, Volume **5492**, Part 3, Pages 1487-1497 (2004)

[162] David A. Naylor, T. Alan Clark, and Gary R. Davis, "Polarizing Fourier transform spectrometer for astronomical spectroscopy at submillimeter and mid-infrared wavelengths", Proceedings of SPIE, Vol. **2198**: 703-714 (1994)

[163] A. Kogut et al., "The Primordial Inflation Explorer (PIXIE): A Nulling Polarimeter for Cosmic Microwave Background Observations", JCAP **1107** 025 (2011)

[164] Motion Control, Aerotech Inc., https://www.aerotech.com

[165] Reinhard Beer, "Remote Sensing by Fourier Transform Spectrometry", John Wiley & Sons, Page 15 (1992)

[166] Optical Design Software — CODE V — Synopsys, https://optics.synopsys.com/codev/

[167] Sacek, Vladimir, "6.5. Strehl ratio", Notes on amateur telescope optics, (2006)

[168] Crystran's Rough Guide to Aspheric Surfaces, www.crystran.co.uk/userfiles/files/aspheric-lens-design.pdf

[169] Eccosorb HR-10, www.lairdtech.com/products/eccosorb-hr

[170] Tslots, by Futura Industries, http://www.tslots.com

[171] McMaster-Carr: Item No. **3110K93**, Close-Up Infrared Heater, Round, 4-7/8" Diameter, 1 Element, 120V, 500 Total Watts

[172] LabJack, Measurement & Automation, https://labjack.com

[173] L. Mertz, "Auxiliary computation for Fourier spectrometry", Infrared Physics, Vol. **7**, 17-23 (1967)

[174] C. D. Porter and D. B. Tanner, "Correction of Phase Errors in Fourier Spectroscopy", International Journal of Infrared and Millimeter Waves, Vol. **4**, No. 2 (1983)

[175] Werner Herres and Joern Gronholz, "Understanding FTIR Data Processing", www.ccmr.cornell.edu/wp-content/.../2/.../Understanding_FTIR.pdf

[176] Avishai Ben-David and Agustin Ifarraguerri, "Computation of a spectrum from a single-beam Fourier-transform infrared interferogram", Applied Optics, Vol. **41**, No. 6, 1181 (2002)

[177] L. Page et al., "First Year Wilkinson Microwave Anisotropy Probe (WMAP) Observations: Beam Profiles and Window Functions", Astrophys. J. Suppl., **148**: 39 (2003)

[178] L. Page et al., "The Optical Design and Characterization of the Microwave Anisotropy Probe", Astrophys. J., **585**, 566-586 (2003)

[179] J. Dunkley et al., "The Atacama Cosmology Telescope: likelihood for small-scale CMB data", JCAP **2013**, 07, 025 (2013)

[180] Dicke R H., "The measurement of thermal radiation at microwave frequencies", Rev. Sci. Instr., **17**:268-75 (1946)

[181] W. V. T. Rusch and P. D. Potter, "Analysis of Reflector Antennas", New York, Academic Press (1970)

[182] J. W. M. Baars, R. Lucas, J. G. Mangum, and J. A. Lopez-Perez, "Near-Field Radio Holography of Large Reflector Antennas", IEEE Antennas and Propagation Magazine, Vol. **49**, No. 5 (2007)

[183] Pedro Antonio Fluxa Rojas et al., "Far Sidelobe Effects From Panel Gaps of the Atacama Cosmology Telescope", Proc. SPIE **9914**, Millimeter, Submillimeter, and Far-Infrared Detectors and Instrumentation for Astronomy VIII, 99142Q (2016)

[184] T.A. Marriage et al., "The Atacama Cosmology Telescope: Extragalactic Sources at 148 GHz in the 2008 Survey", Astrophysical Journal, **731**, 100 (2011)

[185] J. D. Vieira et al.,"Extragalactic Millimeter-wave Sources in South Pole Telescope Survey Data: Source Counts, Catalog, and Statistics for an 87 Square-degree Field", Astrophysical Journal, vol. **719**, 763-783 (2010)

[186] L.M. Mocanu et al, "Extragalactic Millimeter-wave Point Source Catalog, Number Counts and Statistics from 771 $\deg^2$ of the SPT-SZ Survey", The Astrophysical Journal, Volume **779**, Number 1 (2013)

[187] Danica Marsden et al., "The Atacama Cosmology Telescope: Dusty Star-Forming Galaxies and Active Galactic Nuclei in the Southern Survey", Mon. Not. R. Astron. Soc., **439** (2), 1556-1574 (2014)

[188] de Zotti, G., Massardi, M., Negrello, M., Wall, J., "Radio and millimeter continuum surveys and their astrophysical implications", The Astronomy and Astrophysics Review, Volume **18**, Issue 1-2, pp. 1-65 (2010)

[189] James Hough, "Polarimetry: a powerful diagnostic tool in astronomy", News and Reviews in Astronomy and Geophysics, **47** (3): 3.31-3.35 (2006)

[190] I. Agudo, C. Thum, H. Wiesemeyer, and T. P. Krichbaum, "A 3.5 mm Polarimetric Survey of Radio-Loud Active Galactic Nuclei", The Astrophysical Journal Supplement Series, Volume **189**, Number 1 (2010)

[191] M. Lopez-Caniego et al, "Polarization of the WMAP Point Sources", Astrophysical Journal, **705**, 868-876 (2009)

[192] L. Page et al., "Three Year Wilkinson Microwave Anisotropy Probe (WMAP) Observations: Polarization Analysis", Astrophys. J. Suppl. **170**: 335 (2007)

[193] R.A. Battye, I.W.A. Browne, M.W. Peel, N.J. Jackson, C. Dickinson, "Statistical properties of polarized radio sources at high frequency and their impact on CMB polarization measurements", Mon. Not. R. Astron. Soc., **413** (1): 132-148, (2011)

[194] E. L. Wright et al., "Five-Year Wilkinson Microwave Anisotropy Probe Observations: Source Catalog", The Astrophysical Journal Supplement, Volume **180**, Issue 2, pp. 283-295 (2009)

[195] Anna Sajina, Bruce Partridge et al., "High Frequency Radio Spectral Energy Distributions and Polarization Fractions of Sources in an Atacama Cosmology Telescope Survey Field", Astrophysical Journal, **732**: 45, 19 pp (2011)

[196] QUIET Collaboration: K. M. Huffenberger et al., "The Q/U Imaging Experiment: Polarization Measurements of Radio Sources at 43 and 95 GHz", The Astrophysical Journal, Volume **806**, Number 1 (2014)

[197] N. Whitehorn et al, "Millimeter Transient Point Sources in the SPTPol 100 Square Degree Survey", Submitted to: Astrophys. J., arxiv.org/abs/1604.03507 (2016)

[198] Carlstrom, J. E., et al., "The 10 Meter South Pole Telescope", Publ. Astron. Soc. Pac.**123**: 568-581 (2011)

[199] J.S. Farnes, B.M. Gaensler, and E. Carretti, "A Broadband Polarization Catalog of Extragalactic Radio Sources", Astrophysical Journal Supplement Series, **212**: 15, 29 pp (2015)

[200] Planck Collaboration, "Planck intermediate results VII. Statistical properties of infrared and radio extragalactic sources from the Planck Early Release Compact Source Catalogue at frequencies between 100 and 857 GHz", Astronomy and Astrophysics, Volume **550**, A133 (2013)

[201] Planck Collaboration, "Planck 2015 results. XXVI. The Second Planck Catalogue of Compact Sources", Accepted by A&A, http://arxiv.org/abs/1507.02058 (2016)

[202] Lueker, M. et al., "Measurements of Secondary Cosmic Microwave Background Anisotropies with the South Pole Telescope", Astrophys. J. **719**: 1045-1066 (2010)

[203] Fowler, J. W., et al., "The Atacama Cosmology Telescope: A Measurement of the 600 ¡ l ¡ 8000 Cosmic Microwave Background Power Spectrum at 148 GHz", ApJ, Volume **722**, Number 2, 1148 (2010)

[204] Lin, Y.-T., Partridge, B., Pober, J. C., Bouchefry, K. E., Burke, S., Klein, J. N., Coish, J. W., and Huffenberger, K. M., "Spectral Energy Distribution of Radio Sources in Nearby Clusters of Galaxies: Implications for Sunyaev-Zel'dovich Effect Surveys", ApJ, **694**, Number 2, 992 (2009)

[205] Sehgal, Neelima et al., "Simulations of the Microwave Sky", The Astrophysical Journal, Volume **709**, Issue 2, pp. 920-936 (2010)

[206] Vanderlinde, K. et al., "Galaxy Clusters Selected with the Sunyaev-Zel'dovich Effect from 2008 South Pole Telescope Observations", The Astrophysical Journal, Volume **722**, Issue 2, pp. 1180-1196 (2010)

[207] L. Toffolatti et al, "Extragalactic Source Counts and Contributions to the Anisotropies of the Cosmic Microwave Background. Predictions for the Planck Surveyor mission.", Mon. Not. R. Astron. Soc., **297**, 117-127 (1998)

[208] Luigi Toffolatti et al, "Extragalactic source contributions to arcminute-scale Cosmic Microwave Background anisotropies", Astronomy and Astrophysics, **438**, 475 (2005)

[209] M. Tucci, Luigi Toffolatti, Gianfranco De Zotti, and Enrique Martinez-Gonzalez, "High frequency predictions for number counts and spectral properties of extragalactic radio sources. New evidence of a break at mm wavelengths in spectra of bright blazar sources", Astronomy and Astrophysics, Volume **533**, A57 (2011).

[210] M. Tucci and Luigi Toffolatti, "The Impact of Polarized Extragalactic Radio Sources on the Detection of CMB Anisotropies in Polarization", Hindawi Publishing Corporation Advances in Astronomy, **2012**, Article ID 624987 (2012)

[211] Louis, T. et al., The Atacama Cosmology Telescope: Two-Season ACTPol Spectrum and Parameters", In preparation

[212] Max Tegmark and Angelica de Oliveira-Costa, "Removing Point Sources from CMB Maps", Astrophysical Journal Letters, **Vol. 500**, No. 2 (1998)

[213] Serkowski, K., "Statistical Analysis of the Polarization and Reddening of the Double Cluster in Perseus", Acta Astronomica, Vol. **8**, p.135 (1958)

[214] J. F. L. Simmons and B.G. Stewart, "Point and interval estimation of the true unbiased degree of linear polarization in the presence of low signal-to-noise ratios", Astronomy and Astrophysics, **142**, 100-106 (1985)

[215] S. Plaszczynski, L. Montier, F. Levrier, and M. Tristram, "A novel estimator of the polarization amplitude from normally distributed Stokes parameters", Mon. Not. R. Astron. Soc., **439**, 4048-4056 (2014)

[216] J. L. Quinn, "Bayesian analysis of polarization measurements", Astronomy and Astrophysics, **538**, A65 (2012)

[217] D. Maier, C. Tenzer, and A. Santangelo, "Point and Interval Estimation on the Degree and the Angle of Polarization. A Bayesian approach", Publications of the Astronomical Society of the Pacific Vol. **126**, No. 939, pp. 459-468 (2014)

[218] J. M. Stil, B.W. Keller, S.J. George, and A.R. Taylor, "Degree of Polarization and Source Counts of Faint Radio Sources from Stacking Polarized Intensity", The Astrophysical Journal, Volume **787**, Number 2 (2014)

[219] L. Montier et al, "Polarization measurement analysis I. Impact of the full covariance matrix on polarization fraction and angle measurements", Astronomy and Astrophysics, **574**, A135 (2015)

[220] L. Montier et al, "Polarization measurements analysis II. Best estimators of polarization fraction and angle", Astronomy and Astrophysics, **574**, A136 (2015)

[221] Mesa, D. et al., "Polarization properties of extragalactic radio sources and their contribution to microwave polarization fluctuations", Astronomy and Astrophysics, v. **396**, p. 463-471 (2002)

[222] M. Tucci, E. Martinez-Gonzalez, L. Toffolatti, J. Gonzalez-Nuevo, and G. De Zotti, "Predictions on the high-frequency polarization properties of extragalactic radio sources and implications for polarization measurements of the cosmic microwave background", Mon. Not. R. Astron. Soc., **349**, 1267-1277 (2004)

[223] Taylor, A. R. et al., "Radio Polarimetry of the ELAIS N1 Field: Polarized Compact Sources", The Astrophysical Journal, Volume **666**, Issue 1, pp. 201-211 (2007)

[224] Grant, J. K. et al., "The DRAO Planck Deep Fields: The Polarization Properties of Radio Galaxies at 1.4 GHz", The Astrophysical Journal, Volume **714**, Issue 2, pp. 1689-1701 (2010)

[225] Subrahmanyan, R., Ekers, R. D., Saripalli, L., and Sadler, E. M., "ATLBS: the Australia Telescope Low-Brightness Survey", Monthly Notices of the Royal Astronomical Society, Volume **402**, Issue 4, pp. 2792-2806 (2010)

[226] C.A. Hales, R.P. Norris, B.M. Gaensler, and E. Middelberg, "ATLAS 1.4 GHz Data Release 2–II. Properties of the faint polarized sky", Mon. Not. R. Astron. Soc. **440** (4): 3113-3139 (2014)

[227] E. M. Sadler et al., "The properties of extragalactic radio sources selected at 20 GHz", Mon. Not. R. Astron. Soc. **371**: 898-914 (2006)

[228] T. Murphy et al., "The Australia Telescope 20 GHz Survey: the source catalogue", MNRAS, vol. **402**, 2403-2423, (2010)

[229] Becker, R. H., White, R. L., and Helfand, D. J., "The FIRST Survey: Faint Images of the Radio Sky at Twenty Centimeters", ApJ, **450**, 559 (1995)

[230] Helou, G. and Walker, D. W., "Infrared astronomical satellite (IRAS) catalogs and atlases. Volume 7: The small scale structure catalog", Volume **7**, p.1-265 (1988)

[231] Gianfranco De Zotti et al, "Predictions for high-frequency radio surveys of extragalactic sources", Astronomy and Astrophysics, Volume **431**, Number 3, 893-903 (2005)

[232] M. Tucci, E. Martinez-Gonzalez, P. Vielva, and J. Delabrouille, "Limits on the detectability of the CMB B-mode polarization imposed by foregrounds", Mon. Not. R. Astron. Soc., **360**, 926-934 (2005)

[233] L.P.L. Colombo and E. Pierpaoli, "Estimates of unresolved point source contribution to WMAP 5", Mon. Not. R. Astron. Soc., **407**, 247-257 (2010)

[234] C. G. Pappas, "Assembly, Characterization and Operation of Large Scale TES Detector Arrays for ACTpol", Thesis (2016)

[235] S. W. Henderson et al., "Readout of two-kilopixel transition-edge sensor arrays for Advanced ACTPol", Proc. SPIE. **9914**, Astronomical Telescopes + Instrumentation Conference: Millimeter, Submillimeter, and Far-Infrared Detectors and Instrumentation for Astronomy VIII (2016)

[236] S. M. Simon, "Cosmic Microwave Background Polarimetry with ABS and ACT: Instrumental Design, Characterization, and Analysis", Thesis (2016)

[237] Sigurd Naess et. al., "The Atacama Cosmology Telescope: CMB Polarization at $200 < l < 9000$", Journal of Cosmology and Astroparticle Physics, **10**: 007 (2014)

[238] A. van Engelen et al., "The Atacama cosmology telescope: Lensing of CMB temperature and polarization derived from cosmic infrared background cross-correlation", The Astrophysical Journal, Vol. **808**, Issue 1, pp. 7 (2014)

[239] Mathew Madhavacheril et al., "Evidence of Lensing of the Cosmic Microwave Background by Dark Matter Halos", Physical Review Letters, Vol. **114**, Issue 15, pp. 151302 (2014)

[240] E. Schaan et al., "Evidence for the kinematic Sunyaev-Zel'dovich effect with ACTPol and velocity reconstruction from BOSS", Phys. Rev. D **93**, 082002 (2016)

[241] F De Bernardis et al., "Detection of the pairwise kinematic Sunyaev-Zel'dovich effect with BOSS DR11 and the Atacama Cosmology Telescope", arXiv.org/abs/1607.02139 (2016)

[242] C.L.Bennett et al., "The Microwave Anisotropy Probe Mission", ApJ, **583**: 1-23 (2003)

[243] B. A. Benson et al., "SPT-3G: A Next-Generation Cosmic Microwave Background Polarization Experiment on the South Pole Telescope", Proc. SPIE **9153**, Astronomical Telescopes + Instrumentation, arxiv.org/abs/1407.2973 (2014)

[244] P. A. R. Ade et al., "Antenna-coupled TES bolometers used in BICEP2, Keck array, and SPIDER", The Astrophysical Journal, Volume **812**, Number 2 (2015)

[245] B. R. Johnson et al., "Polarization Sensitive Multi-Chroic MKIDs", Proc. SPIE **9914**, Millimeter, Submillimeter, and Far-Infrared Detectors and Instrumentation for Astronomy VII, 99140X (2016)

[246] J. Dunkley et al., "CMBPol Mission Concept Study: Prospects for polarized foreground removal", American Institute of Physics Conference Series, volume **1141**, pages 222-264 (2009)

[247] M. D. Niemack, "Designs for a large-aperture telescope to map the CMB 10x faster", Applied Optics **55**, 1688-96 (2016)

[248] N. J. Miller et al., "Recovery of Large Angular Scale CMB Polarization for Instruments Employing Variable-delay Polarization Modulators", ApJ **818**, 151 (2016)

[249] T. Matsumura et al., "Mission design of LiteBIRD", Journal of Low Temperature Physics, Volume **176**, Issue 5-6, pp 733-740 (2014)